Cyprus University of Technology
Faculty of Engineering and Technology

Doctoral Dissertation

COMPUTATIONAL MODELING OF NANOINDENTATION ON EMERGING MATERIALS: AUXETICS, HARD THIN FILMS AND COHESIVE-FRICTIONAL SOLIDS

Demetris Photiou

Limassol, June 2019

CYPRUS UNIVERSITY OF TECHNOLOGY

FACULTY OF ENGINEERING AND TECHNOLOGY

DEPARTMENT OF MECHANICAL ENGINEERING AND
MATERIALS SCIENCE AND ENGINEERING

Doctoral Dissertation

COMPUTATIONAL MODELING OF NANOINDENTATION ON EMERGING MATERIALS: AUXETICS, HARD THIN FILMS, AND COHESIVE-FRICTIONAL SOLIDS

Demetris Photiou

Limassol, June 2019

Approval Form

Doctoral Dissertation

COMPUTATIONAL MODELING OF NANOINDENTATION ON EMERGING MATERIALS: AUXETICS, HARD THIN FILMS AND COHESIVE-FRICTIONAL SOLIDS

Presented by

Demetris Photiou

Supervisor: Georgios Constantinides, Assistant Professor, CUT

Signature ____

Member of the committee: Anastasios V. Georgiades, Associate Professor, CUT

Signature ____

Member of the committee: Triantafyllos Stylianopoulos, Assistant Professor, UCY

Signature ____

Cyprus University of Technology

Limassol, June 2019

Copyrights

The approval of the dissertation by the Department of Mechanical Engineering and Materials Science and Engineering does not imply necessarily the approval by the Department of the views of the writer.

Acknowledgements

I would like to express my special appreciation to my advisor, Professor Georgios Constantinides. He acted as mentor for me, playing an important role in my academic and scientific development through a relationship that is characterized by unconditional trust and mutual respect and care. His contributions in the field of mechanics of materials and his unflagging interest of the progress of this work have been priceless. I am grateful for his discussions, ideas and suggestions to make my Ph.D. experience stimulating and productive.

I would especially like to thank Professor Ernestos Sarris for his guidance and support to the field of numerical implementation and analysis software. I gained a lot from his vast computational knowledge and research ideas. The passion and enthusiasm he has for his research is contagious and motivational for me. Furthermore, I would like to thank my examination committee members, Professor Tasos Georgiades for his valuable guidance and inspiring discussions, and Professor Triantafyllos Stylianopoulos for his availability and constructive feedback.

I would like to acknowledge the personnel of Research Unit for Nanostructured Materials Systems for the continuous encouragement and inspirational discussions; Professor Pantelis Kelires, Loukas, Marios, Petros, Nikoletta and Constantinos. I would also like to thank all the faculty and staff of the Department of Mechanical Engineering and Materials Science and Engineering at Cyprus University of Technology, for providing a wonderful teaching and supportive environment in this department. Specially thanks to Professor Andreas Anayiotos for his availability and willingness to help and support me over the years.

I devote my heartiest appreciation to my parents and sister for their boundless love, moral support and guidance.

And last but not least, I would like to express my deepest love to my wife Maria, who has been by my side throughout this Ph.D., living every single minute of it, and without her support and encouragement, I would not have been able to complete much of what I have done and become who I am. The last word goes for Constantinos, my baby boy, who has given me the extra strength and motivation to get things done, and for being such a good little baby that past 10 months! This thesis is dedicated to them.

To my wife, Maria,

and son, Constantinos

ABSTRACT

Nanoindentation has evolved into a ubiquitous tool for the mechanical characterization of materials at small scales. Several mechanical metrics are routinely extracted, the most common of which are the elastic modulus and the hardness of the indented material. Perhaps, even more importantly than the capability for nanoscale mechanical characterization, is the fact that it provided experimentalists with an unprecedented access to fundamental material physics. This enabled a refined understanding of the underlying mechanisms that yield the macroscopic mechanical response of materials and enabled materials scientists and engineers in developing models and routes for tailor-made synthesis of materials for specific applications. This capability, however, triggered the uncontrolled utilization of nanoindentation in virtually all material systems: metals, ceramics, polymers, composites, biomaterials, thin films, etc. The initial framework of data analysis, however, was developed for metals and it is not necessarily suitable for other materials systems. The utilization of nanoindentation into more complex systems requires the incorporation of the peculiarities of the constitutive relations of the material characteristics and geometrical details into the analysis.

This thesis deals with the computational (finite element) modeling of nanoindentation on a variety of emerging materials systems. The three material types studied herein are: (a) auxetic, (b) hard thin films, and (c) cohesive-frictional solids. Auxetics are materials that possess a negative Poisson’s ratio and exhibit the counter-intuitive response of expanding laterally when stretched. This intriguing response provides auxetic systems several augmented characteristics among of which is an enhancement in indentation resistance. Hard thin films are nowadays widely used as protective coatings from mechanical/contact loads or corrosive environments or for additional functionalities like sensing capabilities or biocompatibility. Cohesive-frictional materials are solids with a pressure-sensitive yield criterion. Several important materials fall within this category among them cement-based composites (the most widely used solids on earth), shales (the material in which the majority of hydrocarbon resources is stored) and bulk metallic glasses (one of the most promising advanced metals with enhanced strength and ductility characteristics). The focus of this thesis is twofold: On one hand it aims in deciphering the underlying physics of these materials systems when indented by rigid probes and on the other hand to develop the necessary framework for experimentalists to properly interpret the obtained data, plan their experimental protocol accordingly or develop strategies for material optimization.

Keywords: nanoindentation; contact mechanics; finite element method; auxetics; thin films; cohesive-frictional materials

ΠΕΡΙΛΗΨΗ

Η τεχνική της νανοδιείσδυσης ή νανοσκληρομέτρησης έχει εξελιχθεί σε ένα απαραίτητο εργαλείο μηχανικού χαρακτηρισμού υλικών σε μικρή κλίμακα. Με τη χρήση της συγκεκριμένης δοκιμής, μπορούν να προσδιοριστούν διάφορες μηχανικές ιδιότητες, οι συνηθέστερες εκ των οποίων είναι το μέτρο ελαστικότητας του Young και η σκληρότητα. Πέρα από τη δυνατότητα μηχανικού χαρακτηρισμού υλικών στη νανοκλίμακα, σημαντικότερο είναι το γεγονός ότι η συγκεκριμένη τεχνική παρέχει μία άνευ προηγουμένου πρόσβαση στη θεμελιώδη κατανόηση της φυσικής των στερεών υλικών. Το γεγονός αυτό επιτρέπει την ακριβέστερη κατανόηση των μηχανισμών στους οποίους εδράζει η μακροσκοπική μηχανική απόκριση των υλικών και δίδει τη δυνατότητα σε επιστήμονες και μηχανικούς υλικών στο να αναπτύξουν μοντέλα και διαδικασίες για στοχευμένη σύνθεση υλικών για συγκεκριμένες εφαρμογές. Η δυνατότητα αυτή πυροδότησε την ευρεία χρήση της τεχνικής νανοδιείσδυσης σε σχεδόν όλα τα συστήματα υλικών: μέταλλα, κεραμικά, πολυμερή, σύνθετα, βιοϋλικά, λεπτά υμένια, κλπ. Ωστόσο, πρέπει να επισημανθεί ότι ενώ το αρχικό πλαίσιο ανάλυσης δεδομένων αναπτύχθηκε για μέταλλα, αυτό δεν είναι απαραιτήτως κατάλληλο για άλλα συστήματα υλικών. Η χρήση της τεχνικής σε πιο πολύπλοκα συστήματα απαιτεί την ενσωμάτωση των ιδιαιτεροτήτων των καταστατικών εξισώσεων των υλικών και τις ιδιαιτερότητες των γεωμετρικών τους στοιχείων στην ανάλυση.

Η παρούσα διατριβή εξετάζει την υπολογιστική μοντελοποίηση της νανοσκληρομέτρησης σε μια ποικιλία αναδυόμενων συστημάτων υλικών. Στόχο αποτελεί, αφενός η κατανόηση της φυσικής συγκεκριμένων συστημάτων όταν αυτά υπόκεινται σε φορτία επαφής και αφετέρου η ανάπτυξη του αναγκαίου πλαισίου για πειραματικούς ερευνητές για ορθή ερμηνεία των μηχανικών δεδομένων ή ακόμα και για σωστό προγραμματισμό του πειραματικού πρωτοκόλλου. Τα συστήματα που μελετήθηκαν περιλαμβάνουν: (α) αυξητικά υλικά, (β) σκληρά λεπτά υμένια, και (γ) υλικά με συνοχή και εσωτερική τριβή. Αυξητικά είναι τα υλικά που διαθέτουν αρνητικό λόγο Poisson και επιδεικνύουν την αντισυμβατική συμπεριφορά του να επεκτείνονται πλευρικά όταν εφελκύονται. Αυτή η ενδιαφέρουσα απόκριση τους προσδίδει βελτιωμένα χαρακτηριστικά εν σχέση με τα μη-αυξητικά υλικά, ανάμεσα των οποίων είναι και η ενισχυμένη αντίσταση στη διείσδυση. Τα σκληρά λεπτά υμένια χρησιμοποιούνται ευρέως ως προστατευτικές επικαλύψεις από μηχανικά φορτία ή διαβρωτικά περιβάλλοντα ή για πρόσθετες λειτουργίες, όπως ικανότητες αίσθησης και βιοσυμβατότητα. Τα υλικά με συνοχή και εσωτερική τριβή είναι στερεά με κριτήριο διαρροής εξαρτώμενο από την υδροστατική πίεση. Αρκετά σημαντικά υλικά εμπίπτουν στην κατηγορία αυτή, ανάμεσά τους τα υλικά με βάση το τσιμέντο (τα πιο ευρέως χρησιμοποιούμενα στερεά στη γη), σχιστόλιθοι (υλικό στο οποίο είναι αποθηκευμένη η πλειονότητα των υδρογονανθράκων) και μεταλλικοί ύαλοι (ένα από τα πιο υποσχόμενα προηγμένα μέταλλα με ενισχυμένη αντοχή όσο και ολκιμότητα).

Λέξεις κλειδιά: νανοδιείσδυση; μηχανική επαφών; μέθοδος πεπερασμένων στοιχείων; αυξητικά υλικά; λεπτά υμένια; υλικά με συνοχή και εσωτερική τριβή

TABLE OF CONTENTS

LIST OF TABLES

LIST OF FIGURES

LIST OF ABBREVIATIONS

a	Radius of contact
A_c	Area of contact
C	Constraint factor
c	Cohesion
d	Vector of nodal displacements
E	Elastic modulus
E_{eq}	Equivalent elastic modulus (coating and substrate)
${E_{eq}}^*$	Reduced equivalent elastic modulus (coating and substrate)
E_f	Elastic modulus of coating
${E_f}^*$	Reduced elastic modulus of film
E_i	Elastic modulus of indenter
E_r	Reduced modulus
E_s	Elastic modulus of substrate
${E_s}^*$	Reduced elastic modulus of substrate
F	Vector of nodal stress
$f(\rho)$	Axi-symmetric shape of indenter
G	Shear modulus
H	Hardness
h	Indentation depth
h_c	Contact depth
h_e	Elastic displacement during unloading
h_f	Residual penetration depth when indenter is fully unloaded
h_s	Elastic displacement of sample without any contact with indenter

K	Bulk modulus or stiffness matrix
P	Indenter's load
p_c	Normal pressure
p_m	Mean contact pressure
P_{max}	Maximum load of indenter
R	Indenter's radius
S	Contact stiffness
u	Displacements
u_r	Radial displacement
u_z	Normal displacement
W_e	Elastic work
W_p	Plastic work
W_t	Total work
Y	Yield strength
Y_c	Compressive yield strength
Y_f	Coating's yield strength
Y_s	Substrate's yield strength
z	Height (polar coordinates)

Greek Symbols

α	Effective indenter's angle
γ	Correction factor for frictionless indentation
γ^{ad}	Correction factor for adhesive indentation
ε	Normal strain or intercept factor
ε_l	Longitudinal strain

ε_{pl}	Plastic equivalent strain
ε_t	Transverse strain
θ	Polar angle (polar coordinates) or indenter’s semi angle
μ	Friction coefficient
v	Poisson’s ratio
v_i	Poisson’s ratio of indenter
v_f	Poisson’s ratio of film
v_s	Poisson’s ratio of substrate
ρ	Radial distance (polar coordinates)
σ	Stress
σ_r	Radial stress
σ_z	Normal stress
σ_{eff}	Von-Mises stress
τ	Shear stress
Φ	Weight function
φ	Angle of friction
ψ	Plasticity index

Part I

GENERAL PRESENTATION

Chapter 1

Introduction

Instrumented indentation is widely used in measuring the mechanical properties of all types of materials. While it was initially developed for determining the elastic modulus and hardness of metals [1–3], it quickly evolved into a nanomechanical platform for characterizing many types of materials: ceramics where indentation is used for estimating the mechanical properties at low/high temperatures [4,5], polymers in which dynamic measurements are commonly used to obtain the dynamic moduli [6,7], composites in which indentation can provide nanomechanical maps in space with micrometer resolutions [8,9], and advanced materials like biomaterials, where fluid cell indentation can probe the mechanical properties of the sample in hydrated conditions [10].

The theoretical foundations for analyzing indentation data were laid by Hertz through his pioneering work on the contact between two elastic bodies [11]. Subsequently, Sneddon used the method initially proposed by Boussinnesq to extract a relationship between the load and displacement for axisymmetric indenters [12,13]. In 1970s, the indentation technique became very popular due to technological advancements and the development of instrumented nanoindentation platforms that were capable of inducing loads with sub-mN resolution and monitoring displacements in the sub-nm regime. In parallel to technological advancements, many theoretical/computational studies were initiated to develop the analysis framework for the interpretation of nanoindentation data [1,14–16]. Most notably in 1992, the study of Oliver and Pharr [2] was established as a general methodology for estimating the elastic modulus and hardness of materials at very small scales, bypassing the need for directly measuring the area of contact, that was traditionally performed post-indentation in hardness tests. The proposed framework makes the implicit assumption that the indented material is isotropic, bulk and homogeneous and the indenter is significantly stiffer than the indented material, such as indenter deformations are of secondary importance. Recent advancements in materials science synthesis and nanotechnology delivers novel material systems with complex microstructures and constitutive responses that need to be accounted for when nanoindentation is used.

The overarching themes of this thesis are: first, the examination of proposed models of axisymmetric indenter into elastic half-space materials and their application on advanced systems by performing parametric studies via finite element modeling, and secondly, the quantification and development of protocols for experimentalists in order to obtain reliable measurements on such advanced systems.

1.1 Problem Statement and Research Background

During an indentation test a controlled load is applied through a diamond indenter on the surface of the sample under investigation. The applied load (P) and resulting penetration depth (h) are continuously monitored in the process ($P - h$ curves). Proper interpretation of nanomechanical experiments relies on accurate modeling the contact mechanics problem. The peculiarities of the indented materials' response or the geometrical and mechanical properties of the used probe should be exclusively accounted for in the data analysis process.

Through an inverse application of advanced models, the mechanical properties of the sample can be extracted. There are several analytical approaches for completing this step most of which have focused on the indentation modulus (E_r) and hardness (H) of the material:

$$E_r = \frac{\sqrt{\pi}}{2}\frac{S}{\sqrt{A_c}} \tag{1.1}$$

$$H = \frac{P_{\max}}{A_c} \tag{1.2}$$

where S is the unloading slope at maximum depth ($h_{\max}$), $S = dP/dh|_{h_{\max}}$, and A_c is the area of contact at maximum load ($P_{\max}$). E_r and H, under certain circumstances, can be converted to the elastic modulus [2,17] and strength characteristics [18–20] of the indented system. In the case of a rigid indenter E_r relates to the plane stress modulus of the material:

$$E_r = \frac{E}{(1-\nu^2)} \tag{1.3}$$

Directly or indirectly most analysis methods make use of the analytical solution of an axisymmetric indenter being pushed against a semi-infinite, linear elastic half-space. In fact, Equation (1.1) can be directly derived from the linear elastic solution [2,16] and it has proven to hold true for any indenter that can be described as a solid of revolution [21]. Impressively enough, the equation is still valid even if the material exhibits an elastic-plastic response with the only required provision being that the area of contact is properly accounted for in the analysis [22]. In other words all plasticity phenomena are incorporated into the area of contact and provided that this is accurately captured, Equation (1.1) continues to hold.

The methodologies that have been developed over the years are primarily valid for metallic materials and do not include the particular characteristics of other materials/geometries. Here, in this thesis, we investigate these issues through finite element analysis for the understanding and exploitation of nanoindentation testing. Analytical solutions are primarily restricted to the simple linear elastic domains and therefore preclude a direct interpretation of experimental data which usually includes highly non-linear phenomena, like extensive plasticity or time-dependent phenomena. The advent of computational methods, like finite element analysis provides an unprecedented opportunity for an in-depth investigation of all these complex phenomena and the generation of algorithms for data analysis and mechanical properties extraction.

1.2 Research Objectives

The major objective of this thesis is to resolve various open issues regarding nanoindentation testing using finite element method. More precisely:

Objective 1: *Study the behavior of auxetic materials under indentation tests and investigate the validity of the existing analytical solutions.* Auxetic materials compose a new class of materials that their response to tensile loading leads to an increase in volume. We aim to decode and understand this innovative response under various indentation characteristics (friction, various indenter angles, etc.). Moreover, correction factors have been proposed in the literature to account for the ill-posed boundary conditions assumed in the analytical solution. These studies, however, focused on the positive Poisson's ratio regime and have neglected auxetic systems. Here, we use the finite element method to propose correction factors for the conical and spherical indentation response of elastic auxetic materials. Finally, we aim to investigate the influence of plastic strains in the shear strengthening mechanisms that auxetic materials exhibit. We ultimately want to define the conditions under which indentation hardness enhancement is displayed.

Objective 2: *Investigate the indentation response of coated systems by developing scaling relationships and analysis parameters for the extraction of thin film properties.* A basic requirement to apply nanoindentation theory is that material is assumed to be homogeneous. In the case of thin films, where there is a strong interaction at the interface between the coating and the substrate, this statement is no longer valid. In order to measure the mechanical properties of the film only, a commonly used rule is to limit the maximum indentation depth to less than 10% of the film's thickness. However, this empirical rule cannot be applied to very thin films, for which very low indentation depths are needed, due to current experimental resolutions. Through numerical modelling we investigate several experimental factors including the substrate characteristics, scaling parameters and the effect of elastic moduli mismatch on the overall indentation response. Finally, we propose experimental guidelines for the accurate predictions of coating's properties.

Objective 3: *Develop a numerical framework that allows application of nanoindentation testing in cohesive-frictional materials.* Such materials are characterized by a yield criterion that is pressure sensitive. The focus here, is to explore through nanoindentation simulations the link between hardness, cohesion and internal angle of friction.

These three objectives provide a state-of-the-art motivation for modeling indentation-based contact mechanics of advanced material systems. Their outcome can serve for the quantitative modeling and analysis of non-linear material/geometries, or as a guide to experimentalists for developing rigorous testing and data analysis protocols.

1.3 Thesis Outline

This thesis is divided into five major parts. The scope, methodology and originality of this study are presented in the first part, Chapter 1. The second part of this thesis presents an overview of nanoindentation; Chapter 2 reviews the fundamental tools and analytical solutions of instrumented nanoindentation, which introduce the theoretical background to the reader for the upcoming sections while Chapter 3 focuses on the numerical modeling of indentation technique through dimensional analysis and finite element simulations.

The third part of this thesis focuses on the indentation resistance of auxetic material systems. Chapter 4 introduces the reader to the physical origins of auxeticity, their unique characteristics and their potential applications, including some existing products in the market. In addition, a numerical study on a composite auxetic structure is performed as a case study to demonstrate the enhanced mechanical response that auxetic materials exhibit compared to their conventional counterparts. Chapter 5 presents a numerical study on the conical and spherical indentation on elastic auxetic materials. The effect of contact friction, cone geometry is evaluated in detail and correction factors are proposed that enhance the predictive capabilities of the analytical solution. Chapter 6 extends the indentation response to account for elastoplastic von-Mises auxetic materials, under frictionless and adhesive contact.

The fourth part of this thesis deals with the indentation response of hard material systems: hard coatings and cohesive-frictional materials. Chapter 7 presents the experimental parameters and gives a state-of-the-art literature review about the indentation modeling of thin film systems. Finite element analysis of stiff coatings on soft substrates are performed in Chapter 8, where numerical data is validated and parametric analysis is performed. Chapter 9 deals with the indentation behavior of cohesive-frictional materials. The effect of cohesion and angle of friction is investigated in order to capture their combined response and a link between hardness and strength properties is proposed.

Finally, Chapter 10 (fifth part) summarizes the main results and conclusions from this thesis and proposes future perspectives that are foreseen, backed with some preliminary results.

Part II

BACKGROUND MATERIAL

Chapter 2

Indentation Mechanics

Chapter 2 of this thesis presents the indentation mechanics and subsequent analysis on homogeneous, isotropic solids. The physics involved during an indentation process are directly linked to the continuum theory of contact mechanics. The analytical solutions of Hertz's theory and the contact between an axisymmetric indenter and an elastic half space are presented in detail. In general, this Chapter will serve as a guide for the upcoming sections, by introducing several fundamental aspects of nanoindentation analysis.

2.1 Introduction

Instrumented indentation has been developed into a standardized tool for nano- and micro-mechanical characterization of materials [1–3,16,23,24]. It was initially introduced for sub-micron metallic material volumes but it has expanded its application range into studying virtually all classes of material systems: metals [25], ceramics [26], polymers [27–29] and composites [8,30–32].

This type of test consists of a controlled loading through an indenter tip of known properties and geometry by penetrating perpendicular into the surface of the sample under investigation. The advantage of this technique is that it can continuously record small loads (10^{-6} N) and penetrations (10^{-10} m) with high accuracy and precision. The analysis of indentation test relies on the conversion of the experimental reading of indenter load (P) and penetration depth (h), to mechanical metrics like hardness, elastic modulus, creep modulus, energy dissipation, and more. The validity of these metrics depends largely upon the analysis procedure used to analyze the experimental data. Commercially available indentation instruments run automated analysis procedures and therefore the mechanical properties are directly provided to the users. At first glance, these numbers may be a good estimation regarding the response of indented material, however, routine analysis of indentation data can lead to significant errors. For accurate interpretation of results, one must understand the fundamental principles of contact mechanics.

In this chapter, the general principles of contact mechanics (elastic and elastic-plastic) will be addressed within the concept of spherical and conical indentation and their link with experimental observations will be presented.

2.2 Historical Background

Indentation testing was initially developed for hardness measurements. The idea of these measurements was established by mineralogists in the form of scratch hardness. This method depends on the ability of a material to be scratched by or to scratch another material [18]. In 1812, the German mineralogist Frederich Mohs [33] selected ten mineral materials as standards and proposed an arbitrary hardness scale, from 1 (softer – talc) to 10 (harder – diamond). Even though this hardness scale is nonlinear and dimensionless, it has been widely used by mineralogists. An alternative method which is based on the Mohs scale, consists of using a diamond stylus to scratch, under a predefined load, the surface of a material. Then, the hardness of the material is related with the size of the residual scratch imprint; the smaller the scratch the harder the material. However, this procedure is not suited for measuring the hardness of materials, due to the complication of the results; elastic, plastic and frictional properties of the surfaces. In nowadays, experimentalists use scratch tests to evaluate mainly the adhesion strength and friction coefficient of thin film systems.

In 1900, the Swedish metallurgist Brinell [34] introduced the Brinell test, where the hardness of a material was defined by penetrating hard spherical balls (tungsten carbide and diamond) into metals. The imprint on metal’s surface was measured to extract the Brinell hardness number, by dividing the maximum indentation load with the area of the imprint. In 1908, Meyer expressed the indentation hardness as the ratio of the maximum applied force, to the projected area of contact, which is a useful normalized parameter

[35]. Beyond the use of spherical indenters, conical diamond indenters for hardness test were first introduced by Ludwick in 1908 [36]. Thereafter, a large variation of conical and pyramidal indenters has been introduced in the field due to their advantage of producing similar imprint impressions at different indentation depths (geometrical similarity), and also, that they produce faster plastic deformation inside the surface of the material of interest; Rockwell indenter – sphero-conical [37], Vickers indenter – four sided, square base pyramid, Berkovich indenter – three sided pyramid [38].

In contrast to the measurement of hardness which only requires knowledge of the maximum indentation load and the residual imprint after load removal, the evaluation of the material's elastic modulus requires continuous information of the penetration depth during the test. In the 1970s, due to the mature knowledge of nanotechnology and microelectronics, depth-sensing indentation techniques were introduced that allowed a continuous control and recording of the indenter's displacement into the material's surface, during loading and unloading steps [14–16,39,40]. This development motivated the research community to identify techniques for the design and analysis of mechanical properties of materials at small volumes, such as thin films and nanocomposites.

2.2.1 Indentation Testing

A typical nanoindentation test consists of (at least) two phases: a loading and an unloading phase. To extract the mechanical properties of a material, the applied load P and the resulting penetration depth h are continuously recorded and represented in a $P-h$ graph as illustrated in Figure 2-1. During the loading portion of the experiment, and depending on the indenter's geometry, the material usually undergoes elastoplastic deformation. When load is removed the tested material attempts to regain its original form, which in most materials is hardly possible because of the plastic deformation. However, there is a degree of recovery and is achieved due to the recovery of internal elastic deformations. The beginning of the unloading portion of the $P-h$ curve relates to the contact stiffness $S=dP/dh$, which is an index of the resistance of material to the elastic deformation and leads on the estimation of the elastic modulus [2,13]. As shown in Figure 2-1, the net area which is enclosed by the experimental data symbolizes the plastic work W_p (heat in plastic deformation and elastic stored energy due on residual stresses) and the area under P_{max}

and at the right of W_p represents the elastic work W_e (elastic recovery of the deformed surface). In purely elastic cases, loading and unloading paths lay on a single curve.

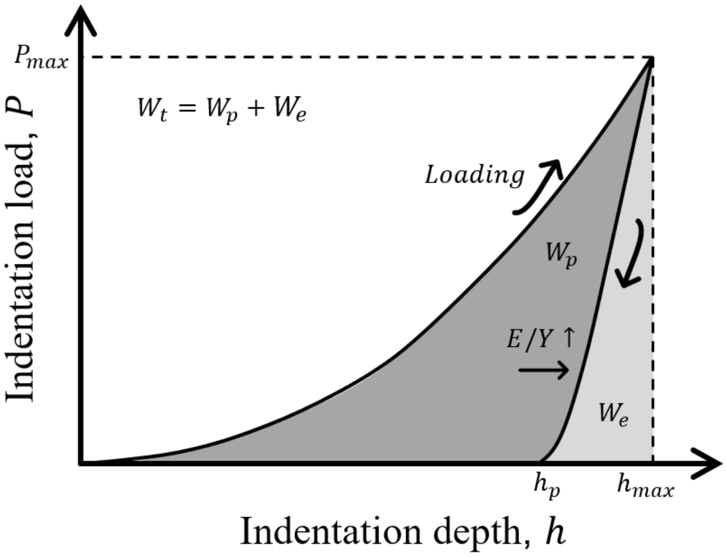

Figure 2-1: Schematic illustration of a typical $\boldsymbol{P-h}$ response of an indented material.

The area under the loading curve is the total work provided to the system W_t:

$$W_t = \int_{h=0}^{h_{max}} P_{loading}(h)dh\,; \;\; W_t = W_p + W_e \tag{2.1}$$

From the above equation, one can define the plasticity index ψ of a material, which characterizes the relative plastic/elastic behavior when it goes through external stresses and strains as:

$$\psi = \frac{W_p}{W_p + W_e} \tag{2.2}$$

where $\psi = \emptyset$ for a fully elastic behavior ($W_p = 0$) and $\psi = 1$ for a fully plastic behavior ($W_p = 0$).

The quality of nanoindentation data is strongly dependent on the load and displacement measurements. For practical considerations, any error that may derive from instrument calibrations, like thermal drift or frame compliance, must be considered and excluded from calculations. The experimentally employed methodology also depends on the physical mechanisms of the tested material. For polymers or other materials tested near their melting temperature, one must consider the influence of creep in the loading response. Respectively, for a thin film system, one must exclude the influence of the substrate from the global response.

The extraction of mechanical properties is achieved by applying continuum scale mechanical models (see Chapter 2.4) to derive mainly two quantities: indentation hardness H and indentation modulus E^* of the indented material:

$$H = \frac{P_{max}}{A_c} \tag{2.3}$$

$$E^* = \frac{1}{2}\frac{\sqrt{\pi}}{\sqrt{A_c}}\frac{dP}{dh} \tag{2.4}$$

where P_{max} is the maximum applied load and A_c is the projected area of contact.

All quantities required to determine H and E_r are directly obtained from the $P - h$ curve, with the exception of the projected area of contact A_c, which either can be estimated using atomic force microscopy measurements of the residual imprint or can be extrapolated from the $P - h$ curve using analytical techniques; this is detailed below.

2.3 Geometric Characteristics of Indenters

The most common indenters in nanoindentation tests are pyramidal, conical and spherical. These probes must be chosen with reference to the sample response. In practice, pyramidal indenters are preferred for thin films testing, since they produce a faster and more contained plastic response on the coatings, in contrast to spherical indenters, which are characterized by smooth transitions from elastic to plastic regimes. Furthermore, tips with sharp geometry can be used to investigate fracture toughness of coatings or employed in scratch tests. Despite the high stiffness of the probes (diamonds are commonly used), with daily use probes may lose their sharpness (increase of their tip radius), worn and deform on experiments in hard samples. The indentation characteristics of the most common probes are summarized in Table 2-1.

Table 2-1: Indentation characteristics for various indenter tips.

Indenter type	Projected contact area	Semi angle θ (deg)	Effective angle θ (deg)	Intercept factor ε
Sphere	$A = 2\pi R h_c - \pi {h_c}^2$	--	--	1
Berkovich	$A = 3\sqrt{3}{h_c}^2 \tan^2\theta$	65.27°	70.3°	0.75
Vickers	$A = 4{h_c}^2 \tan^2\theta$	68°	70.3°	0.75
Cone	$A = \pi {h_c}^2 \tan^2 a$	α	α	0.72

2.3.1 Geometrical Similarity

Conical and pyramidal indenters are characterized by the property of geometrical similarity; the ratio of the radius of circle of contact to the depth of penetration depth a/h remains constant independently of indenter's load, which results constant strain within the indented material. This behaviour is illustrated in Figure 2-2 (a) where von-Mises distribution and legend values for an elastic material remain constant independently of the indentation depth. Geometrical similarity remains unaffected from material properties as shown in Figure 2-2 (b), (d), where contour plots of equivalent plastic strains pressure distribution are plotted for elastoplastic materials of E/Y = 400 and E/Y = 40 in various indentation depths. In addition, hardness of bulk elastoplastic material – extracted from sharp indentation – doesn't depend on the maximum load or the depth of indentation, if conditions of fully plastic zone under the tip are generated, see Figure 2-2 (c).

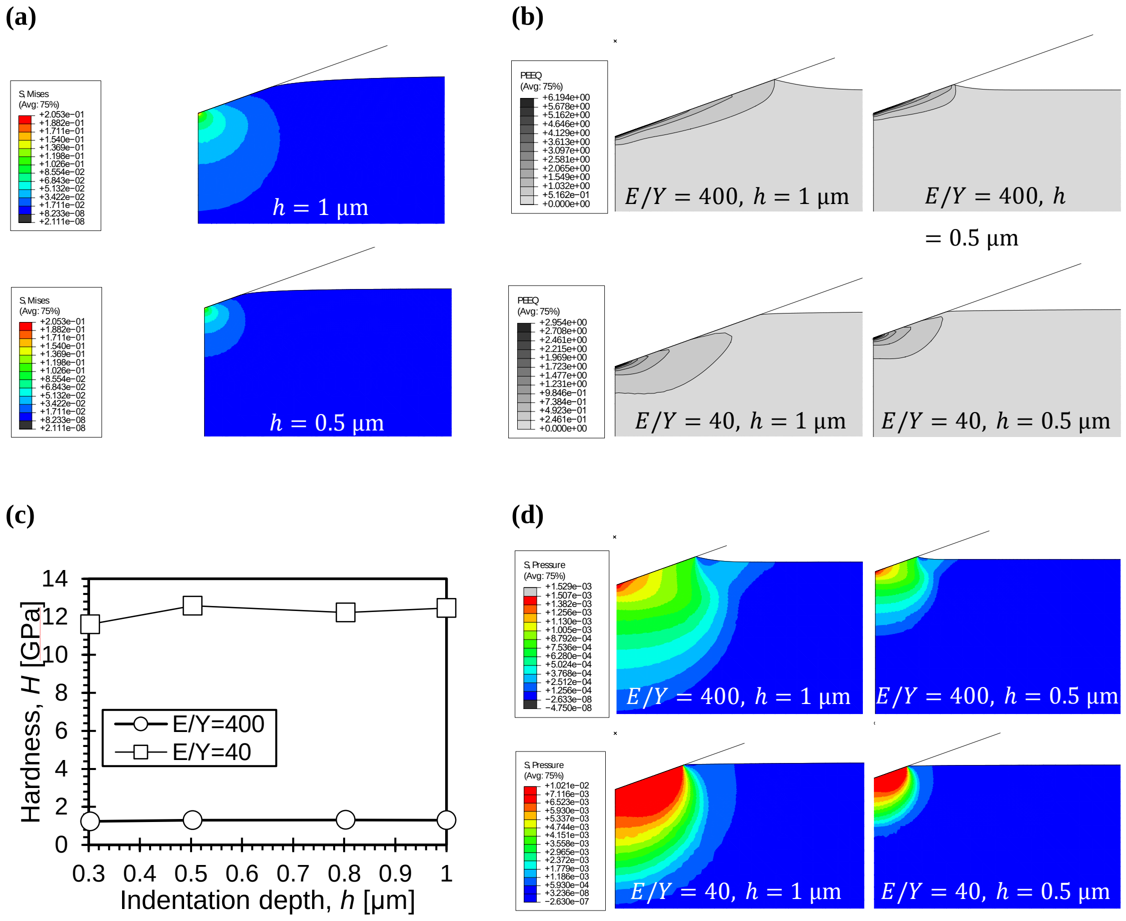

Figure 2-2: Evidence of geometric similarity via (a) elastic material simulations, and elastic-perfect plastic material through (b) equivalent plastic strains, (c) hardness values, (d) pressure contours.

On the other hand, during the loading of a spherical probe into a material, the radius of contact increases more rapidly than the resulting penetration depth, Figure 2-3 (a). In order to capture the geometric similarity (in the case of sphere) one must maintain a constant a/R where R is the radius of the indenter. This quantity is called indentation strain and it will be the governing parameter for the spherical numerical analyses in this report. The dependence of geometrical similarity on indentation strain is captured in Figure 2-3, where indentation simulations have been applied on elastic material E = 250 GPa and v = 0.2 using spheres of R = 8.5, 10, 25 μm. Von-Mises stresses distribution is similar for all three cases, although their size ranges with the indentation strain; for R = 8.5, von-Mises stresses obtain their highest values. This response reflects on the numerical $P - h$ curves of the material, where the highest indentation resistance is again obtained for R = 8.5, Figure 2-3 (b).

By estimating a constant indentation strain a/R (regardless of the sphere size) and then calculating the hardness values, as shown in Figure 2-3(c), it is observed that hardness is strictly dependent on a/R which drives the response of spherical indentation and is independent from indentation depth and the size of sphere.

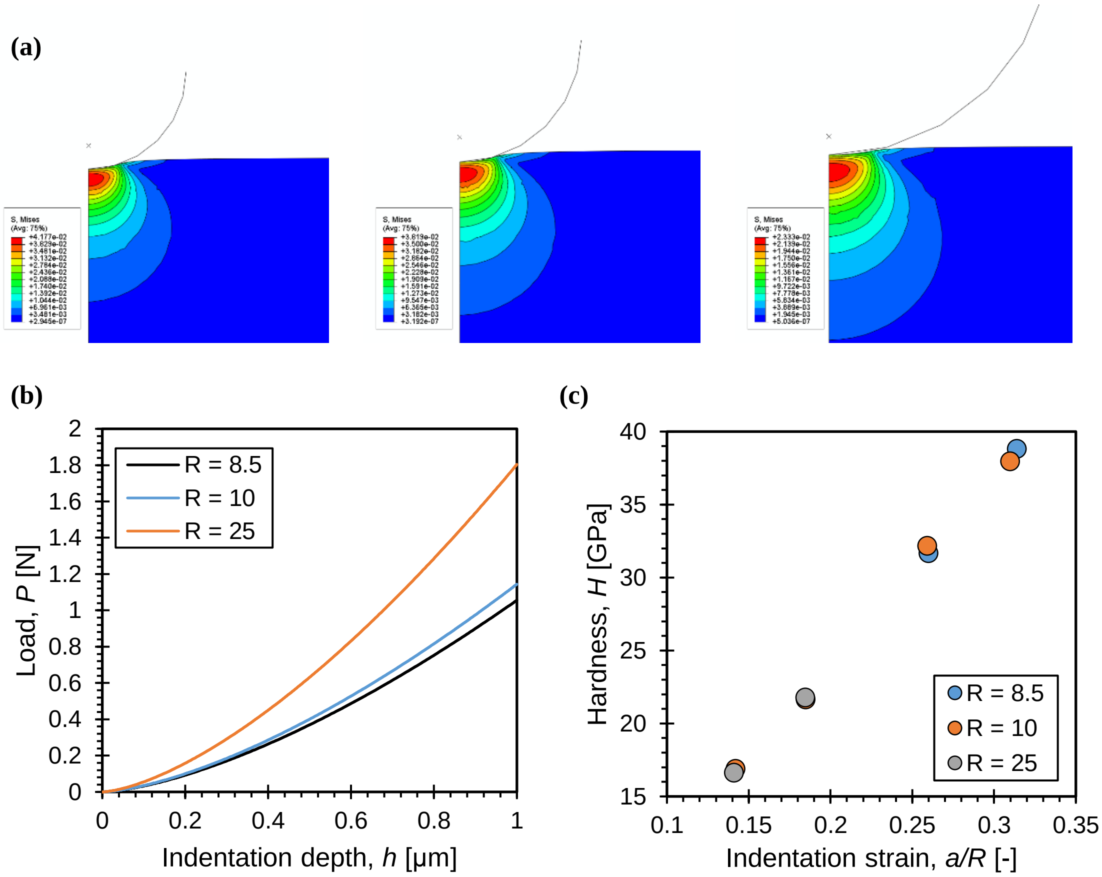

Figure 2-3: (a) Generated von-Mises stresses of spherical indentation for three sphere radii ***R*** = 8.5, 10, 25 μm, (b) Load/displacement curves for under various ***R***, (c) Hardness response as a function of indentation strain defines geometric similarity for spherical indenter.

2.3.2 Effective Cone Angle

The triangular pyramid Berkovich indenter is the most common tip for performing nanoindentation experiments, due to its geometry (Figure 2-4) which leads in high plastic strains and zones inside the sample and, from experimental point of view, it's easier to measure the area of contact when the edges of the pyramid are readily detectable in the impression. Therefore, it is suitable for indentations in metals, ceramics, super-hard materials and thin films. In addition, conical indenters can generate large plastic zones under the surface of contact too, however it is not so feasible to calculate the area of the impression. Another practical consideration is that pyramidal indenter is easier to be manufactured than conical.

However, from analytical – computational point of view, conical indenters are axisymmetric and thus the indentation problem becomes two dimensional and easier to model. In respect to finite element analysis and the analytical solutions for axisymmetric indenters, pyramidal geometries are modeled as cones with equivalent effective angles such as to maintain the same projected area of contact with depth of penetration. It is observed from Table 2-1 that the projected area of contact of an ideal Berkovich indenter $A = 24.56{h_c}^2$, for a Vickers indenter $A = 24.5{h_c}^2$ and for a conical indenter $A = \pi {h_c}^2 \tan^2 a$, which corresponds (for the two cases) in an equivalent angle a of 70.3°.

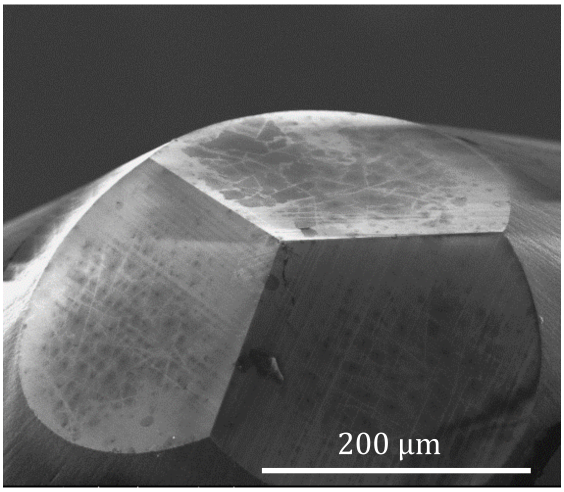

Figure 2-4: Scanning Electron Microscopy (SEM) image in the secondary electron's mode of a triangular pyramid Berkovich indenter. Some impurities are observed on its surface which are due to debris and/or dust.

2.4 Indentation Theory

The analytical approach of solving an indentation problem goes back to 1881, where the German physicist Heinrich Hertz [11] studied the contact between elastic solids and introduced a linear elastic solution for the contact between two spheres. Then, in 1885, Boussinesq solved the problem of contact between two linearly elastic isotropic solids by implementing methods of potential theory. Later, Sneddon proposed solutions of the axisymmetric Boussinesq problem, by solving the contact problem for rigid conical indentation with elastic half-space in 1948, and a general solution in 1965 for any arbitrary axisymmetric indenter [41].

The importance of indentation techniques drastically changed after the technological advancements in 1970s, that led to the development of depth-sensing indentation tests [16,40]. By recording the applied load and indenter's displacement into material surface, the elastic modulus of the indented material can be extrapolated by analyzing the slope of the unloading curve $S = dP/dh$. In 1992, Oliver and Pharr, published a methodology for analyzing indentation data and extracting mechanical characteristics of the indented material that circumvented the need for directly measuring the area of contact; this publication is currently one of the most cited in the field of materials science and engineering. Oliver and Pharr showed that there is a unique relationship between the elastic contact stiffness S, the projected area of contact A_c and the indentation modulus E^*, for all axisymmetric indenters [2]. What follows is a historical background and critical examination of the studies that contributed to the development of indentation analysis.

2.4.1 Elastic Contact: Hertz Theory

The basic analysis for extracting the elastic stiffness of materials from nanoindentation experiments is mainly based on Hertz theory, who while studying the optical interference between two glass lenses, he observed elasticity effects due to pressure forces. Thus, Hertz began developing his theory and in 1882 he studied the contact stresses between two elastic bodies of revolution. When the second body is considered to have an infinite radius ($R = \infty$), one can approach the indentation of a sphere into an elastic half-space [41].

Hertz analytical solution has been based on the following assumptions: the surfaces are continuous and non-conforming (the area of contact is much smaller than the characteristic radius of the body), each body is considered as elastic half-space due to the small radius of curvature of the contacting bodies compared to the radius of the circle of contact, the bodies are in frictionless contact (no traction forces), the strains and stresses are small; the dimensions of each body are small in comparison with the radius of the circle of contact. Turning that assumptions into spherical indentation conditions, the radius of the first body, reduces to $R = R_i$ where R_i is the indenter tip radius, as illustrated in Figure 2-5.

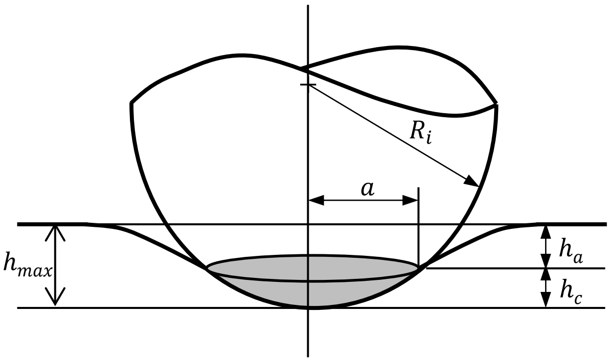

Figure 2-5: Schematic of indentation contact between spherical indenter and material, where $\boldsymbol{a}$ is the radius of the circle of contact, $\boldsymbol{h_{max}}$ is the maximum penetration depth, $\boldsymbol{R}$ is the indenter tip radius, $\boldsymbol{h_c}$ is the contact depth and $\boldsymbol{h_a}$ is the depth of the circle of contact from the specimen free surface.

The resulting stress and displacement distribution that is generated from the indentation contact are extremely important in reviewing the underlying physics that control their nanomechanical response. For the case of spherical indentation, the normal pressure distribution was given by Hertz as:

$$\frac{\sigma_z}{p_m} = -\frac{3}{2}\left(1 - \frac{r^2}{a^2}\right)^{\frac{1}{2}}, \qquad r \leq a \tag{2.5}$$

where p_m is the mean contact pressure, r is defined as the radial distance and a is the radius of circle of contact. From the above equation it can be concluded that at the center of contact, the normal pressure distribution maximizes its value, $\sigma_z = 1.5p_m$, and is zero at the edge of contact radius, $r = a$. This is graphically depicted in Figure 2-6.

Regarding normal and radial displacements of points on the surface of contact between the two solid bodies, as a result of the above pressure distribution, Hertz showed that:

$$u_z = \frac{1 - v^2}{E}\frac{3}{2}p_m\frac{\pi}{4a}(2a^2 - r^2), \qquad r \leq a \tag{2.6}$$

$$u_z = \frac{1-v^2}{E}\frac{3}{2}p_m\frac{1}{2a}\left[(2a^2-r^2)\sin^{-1}\frac{a}{r}+r^2\frac{a}{r}\left(1-\frac{a^2}{r^2}\right)^{1/2}\right], \qquad r > a \tag{2.7}$$

$$u_r = -\frac{(1-2v)(1+v)}{3E}\frac{a^2}{r}\frac{3}{2}p_m\left[1-\left(1-\frac{r^2}{a^2}\right)^{\frac{3}{2}}\right], \qquad r \le a \tag{2.8}$$

$$u_r = -\frac{(1-2v)(1+v)}{3E}\frac{a^2}{r}\frac{3}{2}p_m, \qquad r > a \tag{2.9}$$

where E is the elastic modulus of the indenter.

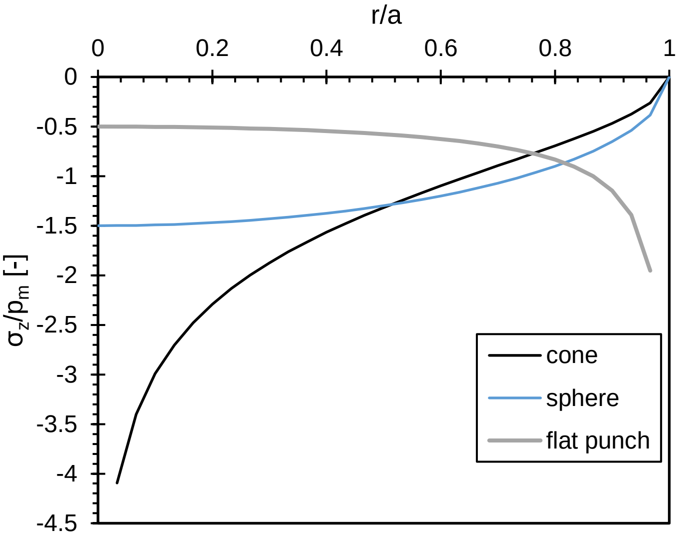

Figure 2-6: Comparison of pressure profiles for sphere, cone and flat punch geometries with equal contact radius.

Hertz's analysis resulted in the following equations:

$$a = \left[\frac{3PR}{4E_r}\right]^{1/3} \tag{2.10}$$

$$h = \left[\left(\frac{3}{4E_r}\right)^2\frac{P^2}{R}\right]^{1/3} \tag{2.11}$$

$$p_m = \frac{P}{\pi a^2} = \left(\frac{4E_r}{3\pi}\right)\frac{a}{R} \tag{2.12}$$

where P is the applied load, R is the radius of the spherical indenter and h corresponds to the axial distance. E_r is the reduced (also termed combined) modulus of the indenter and the sample given by:

$$\frac{1}{E_r} = \frac{(1-v^2)}{E} + \frac{(1-v_i^2)}{E_i} \tag{2.13}$$

where E, v and E_i, v_i are the elastic modulus and Poisson's ratio of the sample and the indenter respectively. Note that in the case, the indenter is much stiffer than the sample, $E_i \gg E$, indenter is assumed to be rigid and that turns Equation (2.13) to:

$$\frac{1}{E_r} \approx \frac{(1-v^2)}{E} \tag{2.14}$$

Substituting Equation (2.10) into (2.11), results:

$$h = \frac{a^2}{R} \tag{2.15}$$

By assuming a rigid indenter, then $h = u_{z|r=0}$. For rigid and non-rigid indenters Hertz showed that the contact depth h_c is exactly one half of the maximum depth h_{max}:

$$h_c = \frac{1}{2} h_{max}, \;\; u_{z|r=a} = \frac{1}{2} u_{z|r=a} \tag{2.16}$$

2.4.2 Axisymmetric Rigid Indentation on an Elastic Half-Space

The main focus of contact mechanics is the determination of size and exact shape of the contact area. Unlike classical mechanics problems, the contact zone is unknown so that areas where displacements (in the contact region), and those where forces (free surface) are prescribed are not known *a priori*. This renders the analysis intrinsically non-linear, since the surface boundary conditions must be formulated under restrictions of a point z that is either situated in the contact zone or in the stress-free area. The contact problem between a rigid axisymmetric indenter and an infinite half-space is shown in Figure 2-7 and is described by the following set of equations, written in polar coordinates (ρ, θ, z):

$$div\, \sigma = 0 \tag{2.17}$$

$$\sigma = F(\varepsilon) \tag{2.18}$$

$$\varepsilon = \frac{1}{2}(\nabla u + \nabla^t u) \tag{2.19}$$

$$P = -\int_{\rho=0}^{a}\int_{\theta=0}^{2\pi}\sigma_{zz}(\rho,\theta,0)\rho d\rho d\theta \tag{2.20}$$

$$u_z(\rho,\theta,0) = -h + f(\rho), \qquad \rho < \alpha \tag{2.21}$$

$$\sigma_{\rho z}(\rho,\theta,0) = 0, \qquad \rho > 0 \tag{2.22}$$

$$\sigma_{zz}(\rho,\theta,0) = 0, \qquad \rho > a \tag{2.23}$$

where P is the applied load, in direction z, $f(\rho)$ defines the axi-symmetric shape of the indenter, and a is the contact radius. Equation (2.17) is the static equilibrium condition (neglecting body forces), Equation (2.18) provides the stress-strain relation of the indented material (here linear isotropic elastic), Equation (2.19) links linearized strain to displacements and the remaining relations (Equations (2.20) - (2.23)) are the boundary conditions (similar with Hertz theory) for the total load (Equation (2.20)), the vertical displacement in the contact region (Equation (2.21)), the zero shear stress on the surface (Equation (2.22)) which includes the frictionless contact condition and the stress-free boundary condition outside the contact zone (Equation (2.23)).

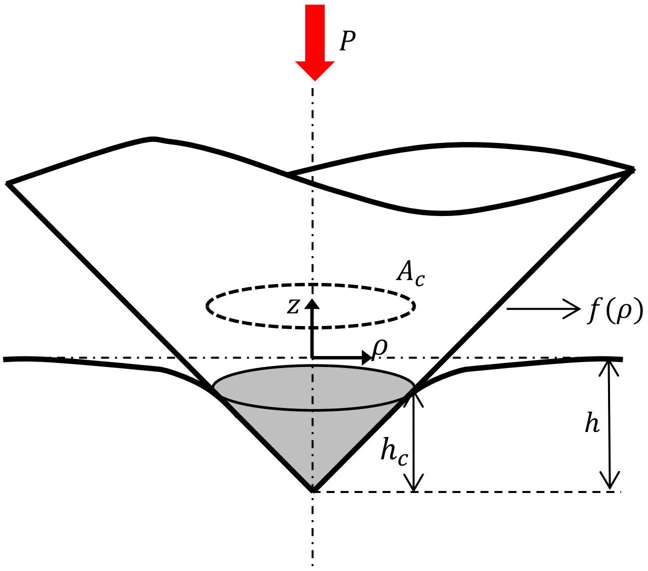

Figure 2-7: The contact problem between a rigid axisymmetric indenter and an infinite half-space, where $\boldsymbol{P}$ defines the applied load, $\boldsymbol{h}$ the penetration depth, $\boldsymbol{h_c}$ the contact depth, $\boldsymbol{A_c}$ the projected area of contact, $\boldsymbol{f(\rho)}$ the axi-symmetric shape of the indenter in the z direction.

The profiles of specific axisymmetric indenters (Equation (2.21)) are presented in Table 2-2.

Table 2-2: Vertical displacements of axisymmetric indenters (Equation (2.21)).

Probe Type	Vertical displacements u_z
Flat punch	$u_z = -h, f(\rho) = 0$
Spherical	$u_z = -h + \rho^2/(2R)$
Conical	$u_z = -h + \rho \cot a$

There are several ways of solving the above set of equations, the more traditional one being the method developed by Lee and Radok [42], and further formalized by Sneddon [13,43] which consists in performing on all problem equations two dimensional Fourier transforms in the directions of the surface coordinates x and y. In the case of axi-symmetry, this integral transform is called a Hankel transform on the polar coordinates ρ and θ which are transformed into a variable θ of dimension L^{-1}. The area of contact is circular by symmetry and its projected radius a is kept as an unknown. It turns out that the equations written with a new set of non-physical coordinates can be solved analytically in the transformed space. Finally, the integral transforms are performed backwards to return to the original problem. Following this procedure, the expressions for h and P for an isotropic half-space read:

$$h = \alpha \int_{\rho=0}^{\alpha} \frac{f'(\rho)d\rho}{\sqrt{a^2 - \rho^2}} \tag{2.24}$$

$$P = 2\frac{E}{1-\nu^2} \int_{\rho=0}^{\alpha} \frac{\rho^2 f'(\rho)d\rho}{\sqrt{a^2 - \rho^2}} \tag{2.25}$$

where f is any smooth convex function, and f' stands for its derivative with respect to ρ. In respect of an axisymmetric indentation with a cone of semi-apex angle of θ Equations (2.24) and (2.25) provide explicit relations of depth and load as a function of the contact radius:

$$h = \frac{\pi}{2}\frac{\alpha}{\tan\theta} \tag{2.26}$$

$$P = \frac{\pi}{2}\frac{E}{1-\nu^2}\tan\theta\, h^2 \tag{2.27}$$

As expected from dimensional analysis, P is scaled with h^2, which provides an interesting insight into the nonlinear nature of the contact problem: for each increment of load, both the area of contact and the depth of indentation increase. Similarly, a and h are linearly related and can define the contact depth as the distance measured on the z-axis between the indenter tip and the contact edge. From Equation (2.26) we obtain the following relation:

$$h_c = \frac{\alpha}{\tan\theta} = \frac{2}{\pi}h \tag{2.28}$$

Equation (2.28) suggests that the elastic indentation always produces sink-in. In fact, provided that the material remains purely elastic the contact depth to indentation depth ratio will always be a constant at $h_c/h = 2/\pi = 0.64$. Furthermore, if one rewrites P and h in Equations (2.26) and (2.27) as a function of the projected area of contact $A_c = \pi a^2$, then one obtains:

$$h = \frac{\sqrt{\pi}}{2}\frac{\sqrt{A_c}}{\tan\theta} \tag{2.29}$$

$$P = \frac{1}{2}\frac{E}{1-\nu^2}\frac{A_c}{\tan\theta} \tag{2.30}$$

Equation (2.30) suggests that the hardness of the material is constant and independent of the depth of penetration:

$$H = \frac{P}{A_c} = \frac{1}{2\tan\theta}\frac{E}{1-\nu^2} \tag{2.31}$$

The solution presented above implicitly relies on the restriction posed on vertical displacements at the contact interface described by Equation (2.21). The radial movements of the surfaces are neglected, leading to deformed surfaces that essentially ‘penetrate’ the indenter during loading [44], resulting in inaccuracies on the predicted load and interfering with any experimental analysis protocol that relies on the above analysis. The accuracy of Equations (2.27), (2.28) and (2.31) will be numerically scrutinized in Chapter 4.

2.5 Analyzing Load – Displacement Curves

The mode of deformation (elastic, plastic, fracture, phase transformation, viscous behaviour) during an indentation test can be extracted directly from the shape of $P - h$ curve. An experimentalist must consider the estimated response of a material, for example the ratio between E/Y, temperature effects for polymer materials, indentation load for coating systems load profile, appropriate selection of indenter shape, in order to design a reliable indentation test. In addition, nowadays, through special set-up of indentation instruments, impact and friction tests can be applied, therefore prior understanding of the physics of an interested material, is a crucial factor to properly design characterization experiments.

A typical $P - h$ curve is shown in Figure 2-8, which represents the indentation response on quartz. Loading curve is described by Kick's law as:

$$P = Ch^m \tag{2.32}$$

where C is a constraint factor (a function of material's properties and indenter geometry) and m is a power law exponent, which has been shown to be constant and dependent only on indenter's geometry (K.L. Johnson 1985): m = 1 for flat punch, m = 1.5 for parabolid of revolution and m = 2 for conical geometry.

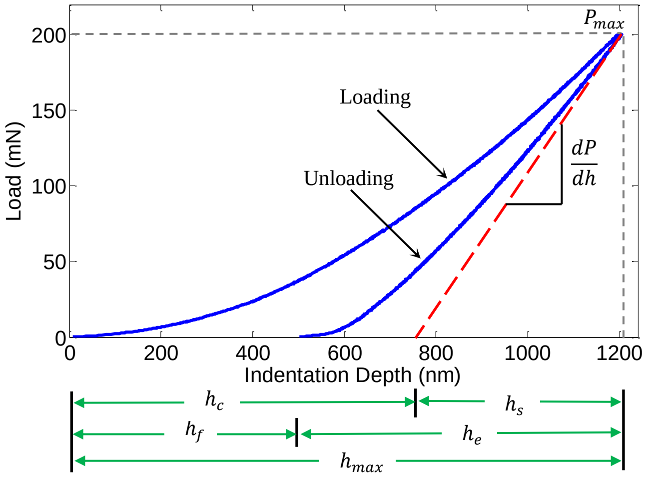

Figure 2-8: Indentation test, $\boldsymbol{P - h}$ curve, on fused silica using Berkovich pyramidal indenter with a maximum load of 200 mN. Experimental data are being obtained from Nanotest Platform 2 of Micromaterials Systems Ltd, in the Micro/Nano Mechanics of Materials lab at CUT.

From the unloading curve, the elastic modulus of material can be calculated, assuming the response to be purely elastic. For a conical indenter, Bulyshev et al. [16] proposed an equation which relates the slope at the beginning of the unloading S, the reduced modulus E^* and the projected area of contact A_c:

$$S = \frac{dP}{dh} = \frac{2}{\sqrt{\pi}} E_r \sqrt{A_c} \tag{2.33}$$

where S is the experimentally measured stiffness of the upper portion of the unloading data. It has been proven that Equation (2.33) holds true for any indenter shape that can be described as a solid of revolution [21].

The contact stiffness S and projected area of contact A_c are always linked to the experimental parameters through the methodology proposed by Doerner and Nix [1] and later improved by Oliver and Pharr [2]. In the first work, the authors suggested that the initial part of unloading curve is almost linear based on the assumption that projected contact area remains unchanged during unloading. This statement is only true for flat punch indentation (m = 1) and in such cases the unloading data can be described through:

$$P = S(h - h_c) \tag{2.34}$$

where h_c is the true contact depth. In the case of indentation testing on hard materials, where usually the obtained $P - h$ curve is characterizing with large elastic recovery during unloading, the above equation failed to properly fit indentation data. Oliver and Pharr introduced another method which takes account the nonlinearity of unloading curve by experimental findings on hard metals and ceramics.

2.6 Oliver and Pharr Method

In Oliver and Pharr approach, the load-displacement data from unloading path is fitted to a power-law equation as:

$$P = A(h - h_f)^m \tag{2.35}$$

where h_f is the final depth/imprint depth and is illustrated in Figure 2-8, $(h - h_f)$ is the elastic displacement, A and m are fitting parameters and can be determined by least squares fittings. The exponent m was experimentally found to vary in the range of $1.2 \leq m \leq 1.6$ which demonstrates that the indenter behaves more like a paraboloid of revolution (m = 1.5) due to “effective indenter shape”; for detailed exposition the reader is referred to the work of Oliver and Pharr (2004). Hence the contact stiffness is calculated by:

$$S = \frac{dP}{dh} = mA(h_{max} - h_f)^{m-1} \tag{2.36}$$

Furthermore, they utilized Sneddon’s solution (Sneddon 1965) of a rigid axisymmetric probe penetrating an elastic half-space, to propose a model for the calculation of elastic modulus and hardness by nanoindentation technique. The total penetration depth h_{max} during loading is defined as:

$$h_{max} = h_c + h_s \tag{2.37}$$

where h_s is the elastic recovery depth. It is in practice observed that h_{max} is experimentally measured and h_s must be calculated. Sneddon’s analysis (Sneddon 1965) for a conical indenter, suggests that h_s can be estimated through:

$$h_s = \frac{\pi - 2}{\pi}(h_{max} - h_f) \tag{2.38}$$

and for a conical indenter:

$$h - h_f = 2\frac{P}{S} \tag{2.39}$$

Thus, h_s results as:

$$h_s = \varepsilon \frac{P_{max}}{S} \tag{2.40}$$

where

$$\varepsilon = \frac{2}{\pi}(\pi - 2) \tag{2.41}$$

an intercept factor, which its values are given in

Table 2-1 for each indenter. The contact depth is computed by combining Equations (2.37) and (2.40):

$$h_c = h_{max} - \varepsilon \frac{P_{max}}{S} \tag{2.42}$$

The above equation implies that the contact depth is always smaller than the maximum depth which corresponds to sink-in behavior (Figure 2-9). The main assumption of the O&P method is that the deformed shape outside the area of contact is elastic. Although, in actual conditions, materials characterized by small values of work-hardening and high values of E/Y, exhibit pile-up phenomena $h_c > h_{max}$, due to the softer material right next to contact. Consequently, under this behavior O&P approach overestimates the mechanical properties of materials, through the underestimation of the contact depth h_c.

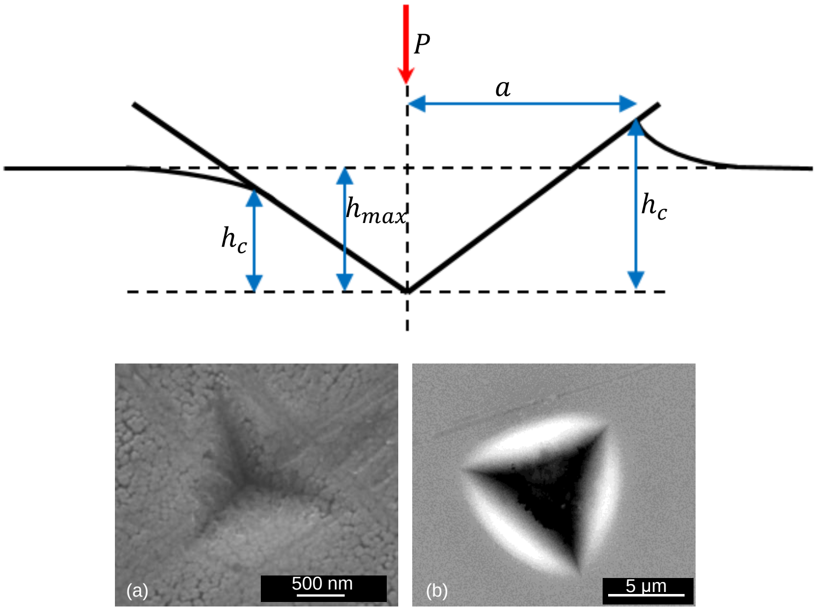

Figure 2-9: Graphical representation of sink-in and pile up phenomena and SEM images which show residual imprints left on surfaces after Berkovich indentation. (Photiou et al. 2016).

Oliver and Pharr expressed the contact area through an area function that relates the cross-sectional area of the indenter at contact depth:

$$A_c = f(h_c) \tag{2.43}$$

Key player in analyzing nanoindentation data, is the accurate measurement of the projected contact area in order to determine the real mechanical properties of the samples. A major problem in nanoindentation testing is the limitation of direct measurement of the area of contact due to the size of the residual imprint which is commonly not accessible by optical microscopes. Nowadays, in situ scanning electron microscopy indentation instruments have been developed, which allow a real-time monitoring of the contact area, although due to several requirements must be fulfilled that relate with the compatibility of SEM operating environment.

There are several factors that lead to wrong calculation of the contact area; cracks, pile-up, worn tips, complex material deformation, etc. Oliver and Pharr suggested a methodology to indirectly measure the area function of indenters for precise determination of their geometry. This involves calculating the contact stiffness over a range of indentation depths, using a reference material – in most cases quartz SiO_2, which is known for its elastic isotropic behavior, and the independence of its mechanical properties with penetration depth. Using the measurements of S and the known E as inputs, one can solve Equation (2.3) as a function of $A(h_c)$, and therefore, for every indentation depth will be calculating the corresponding area of contact. Figure 2-10 (a), shows the experimentally obtained area function $A(h_c)$ for a Berkovich indenter and a best-fitted 5th order polynomial function. Figure 2-10 (b) shows the deviations of an ideal geometry with the actual calculated through the calibrations process. Significant errors, especially at low depths, could be incorporated into the analysis if this calibration is disregarded.

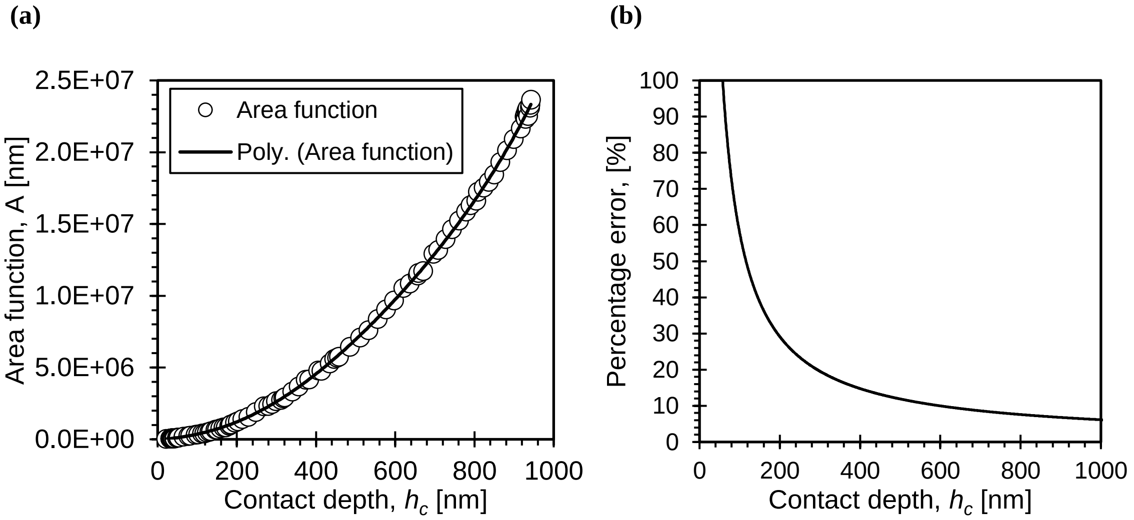

Figure 2-10: (a) Diamond area function of a Berkovich indenter generated through multi-depth indentations on quartz together with a 5th order polynomial fit, (b) percentage error deviation between the ideal and actual Berkovich geometry.

Usually experimentalists, due to the daily use of such instruments, obtain properties of indented materials, which are completely dependent on the user defined area function calibration and are not based on the understanding of the contact mechanics. This is the main reason that the O&P methodology has become so common, and that the research community attempts to adapt the approach to different deformation mechanisms; thin films, viscoelastic materials.

Since 1992, the advances in understanding of indentation mechanics, mainly through finite element simulations have improved the accuracy of the current methodology. In most cases the improvements are incorporated into multiplying correction factors that are inserted into Equations (2.3) and (2.4). For example, by applying finite element simulations King suggested correction factors β which account for the treatment of non-circular indenters as axisymmetric ones [45].

2.7 Chapter Summary

This chapter introduces the reader to the field of contact mechanics, a prerequisite for understanding the physical mechanisms at stake when a diamond indenter comes in contact with a material's surface during a nanoindentation test in order to access its mechanical properties. A historical background of the technique is presented and the underlying mechanical principles that allow converting indentation data into meaningful mechanical properties are outlined. The important concepts of experimental $P - h$ curves, self-similarity, and indentation strain are also shown and will be of significance in the developments of later chapters. The Oliver and Pharr methodology is described and critically examined, especially with respect to pile-up and sink-in phenomena.

Chapter 3

Finite Element Method in Nanoindentation Analysis

Finite element analysis is the primary tool that is extensively utilized within this thesis in addressing the indentation response of several advanced material systems. This chapter, therefore, serves as an introductory material to the finite element method that introduces the basic concepts of the technique and its application to nanoindentation testing.

3.1 Finite Element Modeling: Nonlinear Analysis

Finite element modeling (FEM) is a numerical technique for finding approximate solutions to boundary value problems of partial differential equations. FEM has been recognized in many engineering fields as it can solve complex and multi-physics engineering problems: solid mechanics, heat transfer, fluid dynamics and electromagnetism, to name a few. The finite element method consists of assuming the piecewise continuous function for the solution by minimizing the error between the real and the approximate solution. The accuracy of approximation depends on the combination of trial functions. The idea of FEM is to discretize the entire domain into simple subdomains, called finite elements, and then to apply the approximation solution (interpolating functions) on the element size. The finite elements relate to adjacent elements by sharing their nodes, thus adjacent elements have the same solution value at common nodes. The response of each element is expressed in terms of finite number of degrees of freedom characterized as the value of unknown functions, at a set of nodal points. Then, by assembling the collection of all element matrices, the response of the global matrix for the entire domain can be approximately computed. Boundary conditions are imposed, and a system of equations is obtained in a set of algebraic equations. Finally, additional computations are performed at selected elements based on the post-processing application.

Many phenomena in engineering exhibit non-linear responses, for example the relation between applied load and deflection of a beam that is fixed in one face. If in a structural system, relationships along displacements, strains and stresses are linear, then this system is defined as linear system. In case one of them is not linear, then the whole structure becomes non-linear. From a fundamental point of view finite element analysis results in a matrix equation that describes the behavior of several structural finite elements:

$$[F] = [K] \cdot [d] \tag{3.1}$$

where $[F]$ is the known vector of nodal loads, $[K]$ is the known stiffness matrix and depends on the geometry, material properties and boundary conditions – restraints, and $[d]$ is the unknown vector of nodal displacements. Linear systems can be solved using linear equations in the form of Equation (3.1) due that the stiffness matrix $[K]$ never changes while the model is deforming. On the other hand, for nonlinear systems, an applied load alters significantly the corresponding stiffness $[K]$. As a result, an iterative solution process is forced for the continuous restructuring of $[K]$, which increases the computational time in contrast, with the linear systems is which their analysis readily follows.

Non-linear systems can include up to three sources of nonlinearity: material nonlinearity, geometric nonlinearity and boundary nonlinearity which are represented in a comprehensive flowchart, Figure 3-1. In the case of material nonlinearity, material properties relate to the level of deformation/strain, in contrast to a linear material model in which the stress is proportional to strain. Some material models that tend to nonlinear behaviors are elastoplastic materials (von-Mises, Tresca, Mohr-Coulomb, Drucker-Prager, work-hardening models), hyperelastic (Blatz-Ko, Mooney-Rivlin, Ogden), viscoelastic, viscoplastic, creep, superelastic (i.e., nitinol response), etc. Geometric nonlinearity refers to cases where large deformations take place or in cases where model's shape change, and both result in changes to the stiffness matrix. In simple words, nonlinearity in geometry occurs in cases where the kinematic relationships (displacement, strains) are non-linearly dependent.

Finally, boundary nonlinearities occur when the imposed displacements or forces (boundary conditions) depend on the deformations of the structure and change during the analysis. Referring to Equation (3.1), the process of FEA is to solve the equation for the unknown displacements in the domain of the given boundary conditions. In such cases the boundary conditions also become unknowns to the problem. Contact problems are the most common applications of boundary nonlinearities. During an indentation test, when an indenter is in contact with a material, the contact boundary increases with material's deformation, resulting to a non-linear dependency between displacement and load.

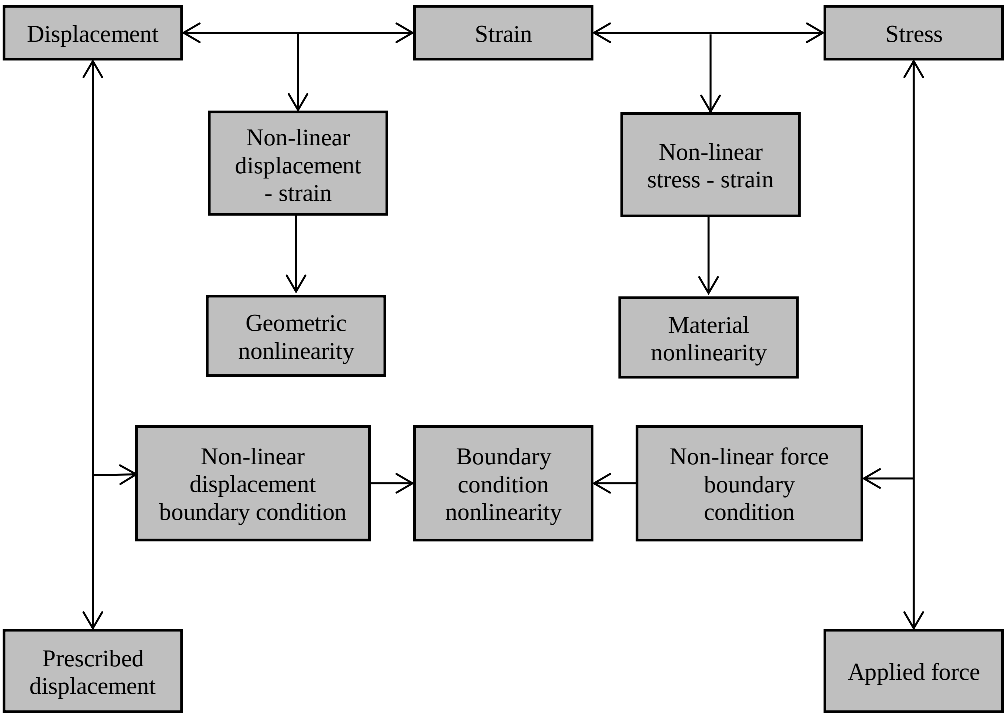

Figure 3-1: Flowchart of nonlinearity categories and their causes [46].

3.2 FEM of Nanoindentation Technique

The major limitation of analytical approaches in the nanoindentation technique is the accurate calculation of the contact area A_c, since they are based on elastic solutions and they don’t take account of the complex behavior that arises from material elastoplasticity, non-linear geometry, composite systems, anisotropic material response, time-dependent material response, and more. For this reason, FEM has become a useful tool for capturing and understanding the indentation contact. Furthermore, numerical simulations provide useful insights into the mechanics of contact which cannot be predicted or calculated in experiments. Such metrics include the stress and strain distribution within the indented material (or probe), size/shape/extent of plastic zones, elastic and plastic energies, reaction forces, and more.

The general concept of finite element modeling of nanoindentation technique is to define the mechanical properties of both the indenter and material as input parameters and then obtain a numerical load-displacement curve. As a result, comparison can be made between computational and experimental data. If the two curves are identical, the comparison can be very helpful in evaluating the estimation method of contact area, or the interpretation of the numerical results may further yield information which is not readily available through experiments.

Several finite element studies that are considered milestones within the indentation mechanics field are reported below:

- King showed that the assimilation of three-sided (Berkovich) and four-sided (Vickers) pyramidal indenters with an equivalent cone with a semi-apex angle that preserves the contact area function is accurate within 1–3% [47].
- Bhattacharya and Nix estimated the hardness at various points on the loading curve for bulk and thin film material systems [48].
- Larsson *et al.*, studied Berkovich indentation on elastic and elastoplastic solids and their numerical results were in excellent agreement with experimental findings [49].
- Bolshalkov *et al.*, studied material behavior during elastic-plastic indentation to quantify the influence of residual stresses on the indentation response [50,51].
- Many authors [44,52–54] have proposed correction factors to account for the radial displacements of the indented material which have been neglected in Sneddon’s analysis.
- Dao *et al.* and Chollacoop *et al.* developed both forward and reverse algorithms to estimate the yield strength and hardening exponent of the indented material, σ_y and n, utilizing the concept of representative stress and strain [55].

- Cheng and Cheng employed dimensional analysis and resulted in several dimensionless ratios that control the indentation response; the interdependencies of these dimensionless components has been subsequently studied using finite element modeling [56].
- Feng *et al.*, provided a closed-form analytical expression for the stress field around elastoplastic materials, through numerical conical indentations [57].
- Vandamme *et al.*, extracted the viscoelastic material response under conical indentation [29].
- Sarris and Constantinides, estimated elastic and plastic material properties for the conical indentation response of elasto-plastic materials of the Mohr-Coulomb type [58].
- Many authors have studied the indentation response of coating systems due to the combined response between thin film and substrate [59–61].

Finite element simulations will be widely used in this thesis to explore indentation mechanics in advanced material systems and to propose guideline procedures for the appropriate design and analysis of experiments.

3.3 Dimensional Analysis

Dimensional analysis is a powerful tool in the indentation field, both for experimentalists (for enhancing the design of experiment) and for modelers (for carefully selecting the range of values for parametric analysis). Here we will introduce various dimensionless sets that will enable the study of elastic and elastic-plastic materials from conical indentations. Generally speaking, the scope of dimensional analysis is to reduce the number of variables in a problem by enforcing dimensional homogeneity. Although this technique is primarily employed in fluid mechanics, it is a basic tool that can be used in all branches of engineering. The central theorem of dimensional analysis is the Buckingham Π theorem from which one selects the appropriate variables, the problem can be further reduced into dimensionless parameters significantly reducing the complexity of the probelm. This is further illustrated below.

3.3.1 Elastic Contact

For the case of elastic contact indentation, let's consider a 3D rigid conical indenter of semi cone angle θ indenting an elastic homogeneous solid. The contact is assumed frictionless and the surface of the solid is smooth. Now we need to select all the variables involved at the contact of the loaded indenter in the surface of the specimen. The load $[P]$ is chosen as a dependent variable, while Young's modulus $[E]$, Poisson's ratio $[v]$, penetration depth $[h]$ and indenter's semi angle $[\theta]$ as independent variables.

Thus:

$$P = f(E, v, h, \theta) \tag{3.2}$$

Dependent quantities in this case are stress $[\sigma]$ and strain $[\varepsilon]$ inside the sample. Therefore, as independent dimensions are chosen pressure and length. Applying Π theorem:

$\Pi_1 = [E]^a[h]^b[P] = \sigma^0\varepsilon^0$

where dimensions of $P = N = \sigma\varepsilon^2$

$\Pi_1 = [\sigma]^a[\varepsilon]^b[\sigma\varepsilon^2] = \sigma^0\varepsilon^0$

$\sigma: a + 1 = 0 => a = -1$

$\varepsilon: b + 2 = 0 => b = -2$

$\Pi_1 = [E]^{-1}[h]^{-2}[P] => \Pi_1 = \dfrac{P}{Eh^2}$

Therefore:

$$\frac{P}{Eh^2} = \mathit{\Pi}_1(v, \theta) \tag{3.3}$$

Equation (3.3) demonstrates that conical indenter's force P is proportional to the square of indenter's displacement h and that the dimensionless number P/Eh^2 is independent of the penetration depth, h. In fact, for a given semi-apex angle θ, which for Berkovich indenter equals 70.3°, it is only function of Poisson's ratio v.

3.3.2 Elastic-Plastic Contact

Dimensional analysis of a conical axisymmetric indenter with an elastic–perfectly plastic solid (von-Mises), requires in addition to the elastic case the consideration of the E/Y ratio which corresponds to an "elasticity/plasticity index".

$$\frac{P}{Eh^2} = \Pi_2\left(\frac{E}{Y}, v, \theta\right) \tag{3.4}$$

Similarly, the dimensionless number P/Eh^2 is independent of the penetration depth h, although, for a given semi-apex angle θ, it is function of E/Y ratio and Poisson's ratio v.

Similar dimensional analysis, gives information about the contact depth h_c:

$$\frac{h_c}{h} = \Pi_3\left(\frac{E}{Y}, v, \theta\right) \tag{3.5}$$

where it is obvious that the contact depth h_c is proportional to the penetration depth h and that the dimensionless number h_c/h is a function of E/Y and the Poisson's ratio v. In practice, when h_c/h is bigger than 1, pile-up phenomena occur, otherwise sink-in prevails.

During the unloading phase the load P also depends on the maximum indentation depth h_{max}, thus:

$$P = f_{unloading}(E, Y, v, h, \theta, h_{max}) \tag{3.6}$$

Dimensional analysis yields:

$$\frac{P}{Eh^2} = \Pi_4\left(\frac{E}{Y}, \frac{h}{h_{max}}, v, \theta\right) \tag{3.7}$$

The derivative of Equation (3.7) with respect to indentation depth h, results to the slope of the initial unloading curve, at h = h_{max} as:

$$\frac{1}{Eh_{max}} \frac{\mathrm{d}P}{\mathrm{d}h}\bigg|_{h=h_{max}} = \Pi_5\left(\frac{E}{Y}, v, \theta\right) \tag{3.8}$$

It is readily understood that the contact stiffness is a function, among other parameters, of the maximum indentation depth; a stiffening process takes place as the contact area between the indenter and the indented material increases.

3.3.3 Work of Indentation

As mentioned in Chapter 2 the net area which is enclosed by the experimental data symbolizes the plastic work W_p and the area under P_{max} and in the right of W_p represents the elastic work W_e (elastic recovery of the deformed surface). Therefore, the area under the loading curve is the total work $W_t = W_p + W_e$. Integrating that equation in the range of 0 to h_{max} yields:

$$W_t = \int_0^{h_{max}} P\,\mathrm{dh} = \frac{E h_{max}^3}{3} \Pi_1 \left(\frac{Y}{E}, v, \theta\right) \tag{3.9}$$

It results that the total work is proportional to h_{max}^3. Now, integrating load equation during unloading (in the range of h_f to h_{max}), the elastic work can be observed as:

$$W_e = \int_{h_f}^{h_{max}} P\,\mathrm{d}h = \frac{E h_{max}^3}{3} \Pi_6 \left(\frac{Y}{E}, v, \theta\right) \tag{3.10}$$

which is also proportional to h_{max}^3.

By calculating the ratio of plastic to total work, it can be seen that:

$$\frac{W_t - W_e}{W_t} = 1 - 3\frac{\Pi_6(Y/E, v, \theta)}{\Pi_1(Y/E, v, \theta)} \tag{3.11}$$

Cheng and Cheng [62] investigated the abovementioned correlation through finite element simulations and they resulted in a relationship between W_p/W_t and h_f/h_m for indenters with various angles. In conclusion, it becomes apparent that dimensional analysis yields a set of dimensionless ratios that reduces the number of free variables and contributes to the potential of simulating the indentation process and quantifying new relationships.

3.4 General Description of Numerical Model

In this thesis, finite element simulations were conducted using the commercially available software package ABAQUS [63] of Dassault Systèmes. For computational efficiency, pyramidal indenter geometries are modeled as cones with half-apex angle of θ=70.3° (see Chapter 2.3.2), to convert the indentation problem into 2D axi-symmetric, Figure 3-2. This conical angle ensures the same projected area of contact vs. contact depth relation ($A_c = f(h_c)$) as in Vickers and Berkovich pyramidal indenters which are commonly employed in experimental investigations. Previous numerical studies by King [45] showed that the assimilation of three-sided (Berkovich) and four-sided (Vickers) pyramidal indenters with a cone of equivalent semi-apex angle is accurate within 1-3%.

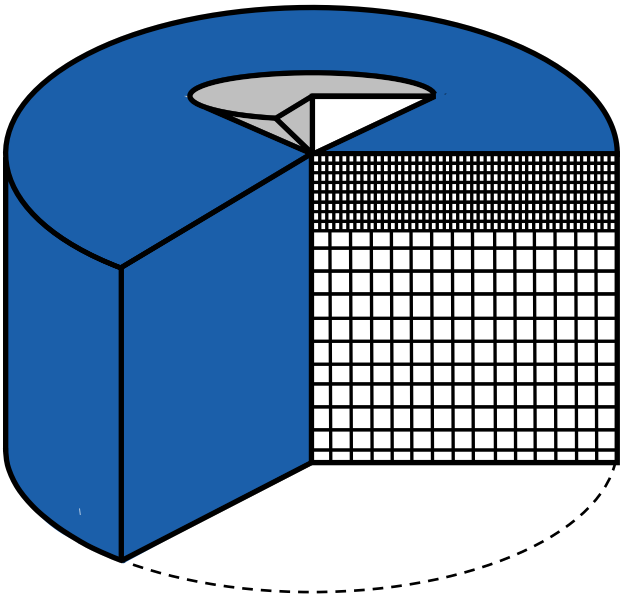

Figure 3-2: Schematic illustration of the general geometry modelled in this thesis.

The indenter is assumed to be rigid, which is a reasonable assumption given that most indenters are made out of diamond which has an elastic modulus that is much stiffer than most indented materials. Rigid indenter is always modeled as analytical rigid surface in 2D conditions. The only parameters that need to be defined for rigid surfaces are any translations and rotations of a single node which is stated as reference node and manipulates the behavior of the rigid surface. Therefore, the use of rigid surfaces is numerically effective since there is no need to calculate additional stresses and strains within the indenter.

Details of the model geometry are shown in Figure 3-3. The 'semi–infinite' half space is modeled as a 101×101 μm^2 domain characterized for elastic materials by Young's modulus (E) and Poisson's ratio (v), for elastic-perfect plastic materials (von-Mises) by E, v and yield stress (Y) and for cohesive-frictional materials by E, v, c and φ. The indentation simulations were restricted to depths below 1 μm, much smaller than the simulated domain such as to avoid any boundary effects. The continuum space is discretized using 4–node axisymmetric, isoparametric elements (CAX4–full integration).

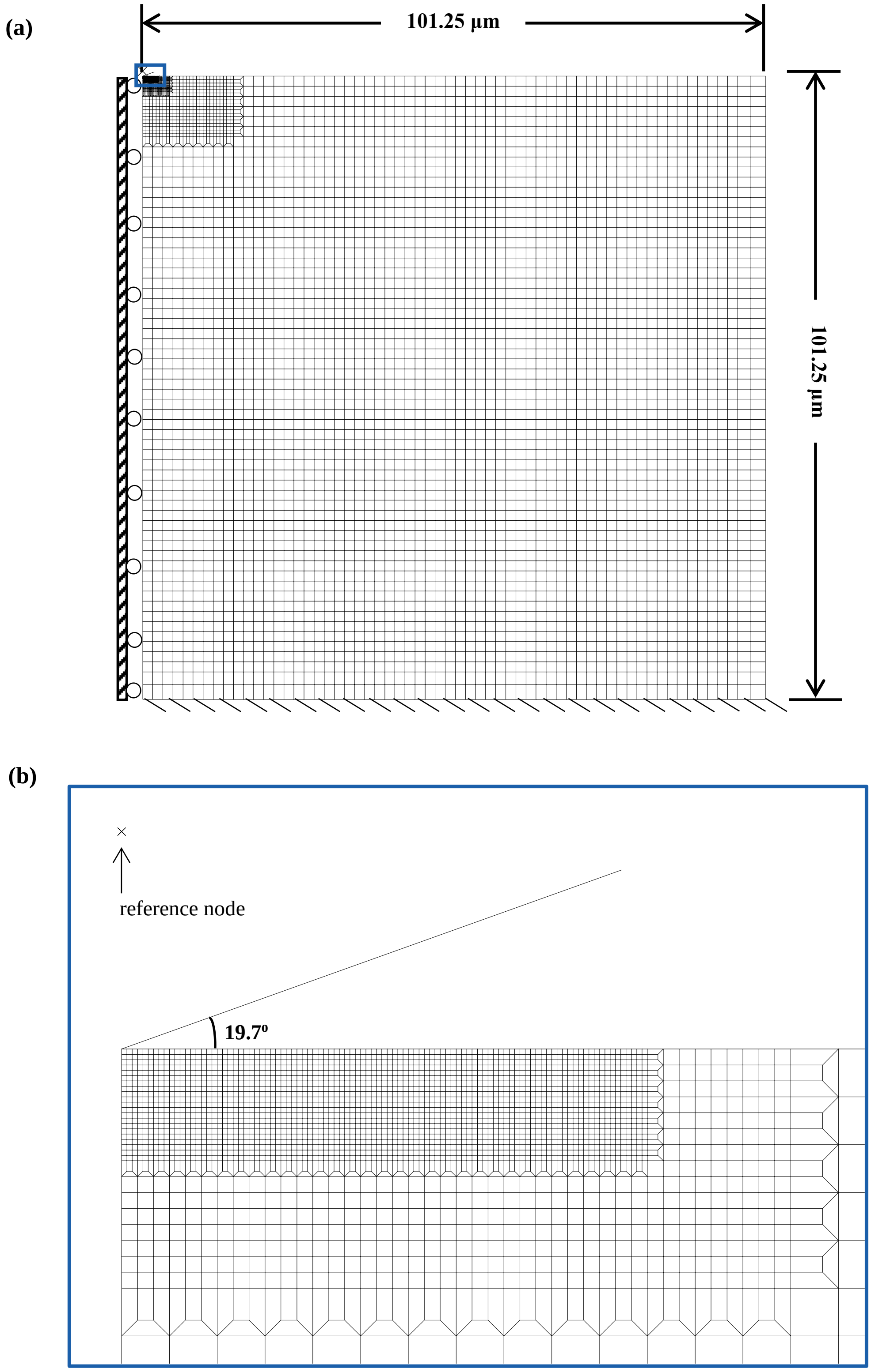

Figure 3-3: Details of (a) 2-dimensional axisymmetric finite element model of the conical indentation problem and characteristics of boundary conditions and mesh, (b) a portion of the finite element mesh that is near to the tip of indenter, cone’s effective angle and location of reference point.

The element size was continuously refined in five successive regions as approaching the indenter contact region for greater accuracy. A mesh sensitivity analysis was performed to ensure that the simulations results were insensitive to the mesh size (convergence study).

The contact detection was defined between the analytic rigid surface for the probe and an element-based surface for the contacting material, ensuring an accurate calculation of contact stresses at each node. The contact between them introduces moving boundary conditions which are often discontinuous and the contact to be solved, requires iterations for updating the model stiffness at every load increment. The contact formulation includes the use of a constrained enforcement method for the pair surfaces of the master (indenter) –slave (sample) and accounts for finite strain, rotations and sliding. This direct method of Lagrange multipliers attempts to strictly enforce a given pressure-overclosure behavior per constraint. Lagrange multipliers can add to the computational cost but also protect against numerical errors related to ill-conditioning that can occur if high contact stiffness is in effect. Any Lagrange multipliers associated with contact, are present only for active contact constraints so the number of equations will change as the contact status changes. By using this method, Lagrange multipliers are automatically selected based on the calculated stiffness. For nonlinear problems in ABAQUS, Newton-Raphson methodology is used to gain solutions for the incremental displacement by iteratively solving the linearized equation.

It is assumed that the loading rate is slow enough such as static friction can securely model the interface response. Simulations proceeded in two steps: the indenter was firstly subjected to a ramped vertical displacement, followed by an indenter retraction to the original position which corresponded to complete unloading at zero load. During this process the lower edge of the material was constrained vertically. Axisymmetric boundary conditions were used along the symmetry axis beneath the indenter region [64].

3.5 Procedure for Calculating the Area of Contact

For the appropriate calculation of hardness and elastic modulus, one needs to measure very precisely the projected area of contact, A_c. Experimentally, A_c can be explored either directly through the usage of a microscope instrument; optical for microindentation measurements and scanning electron microscope or atomic force microscope for nanoindentation measurements [65]. Indirect techniques are based mainly on the readings of penetration depth, contact depth and indenter geometry [2,3]. In extreme situations like roughness and pile-up, these techniques may not be effective and lead to inaccurate mechanical properties estimation.

On the other hand, in finite element simulations, the procedure for the calculation of projected area of contact is more straight-forward. In most cases, the contact area is determined using the contour at maximum load, as illustrated in Figure 3-4, based on the coordinates of the last contact node. The vertical distance from point 1 to point 2 defines the contact depth h_c, while the horizontal distance the contact radius a. Hence, element size in the contact region must be fine enough, in order to minimize contact area measurements with errors less than 2-3%.

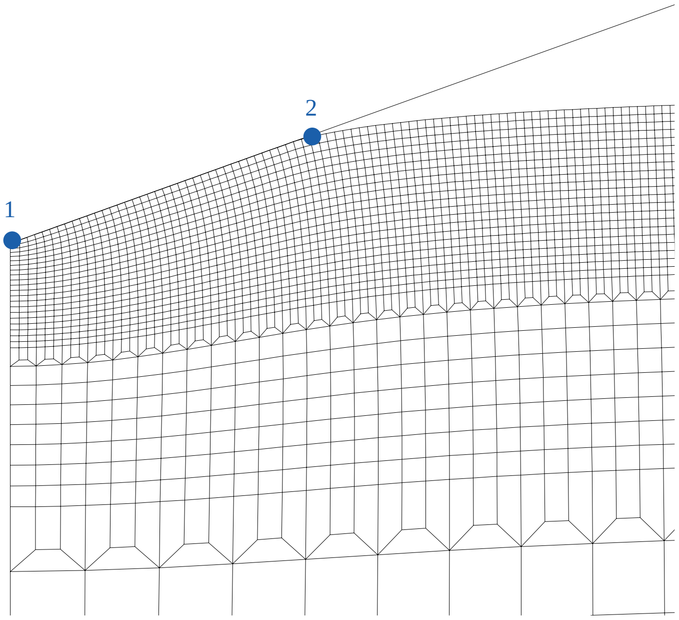

Figure 3-4: Numerical determination of projected contact area; vertical distance from point 1 to point 2 defines $\boldsymbol{h_c}$ and horizontal distance the contact radius $\boldsymbol{a}$.

A recently study [66] proposed that contact radius must be determined in the location where the contact pressure drops to zero [13]. Usually, in numerical indentation studies, contact pressure of the last contact node is non-zero. Thus, they suggest the estimation of the last contact node, from extrapolation value, for which the contact pressure results to zero. In Figure 3-5, the contact pressure distribution is plotted as function of radial distance for an elastic material with E = 200 GPa and v = 0.3, based on deformed and undeformed coordinates. Both curves are in an excellent agreement and they result for a contact radius of 380 nm (undeformed) and 362.3 nm (deformed). In comparison with the procedure that is described in Figure 3-4, the contact radius results at 357.2 nm, which is closed with the previous value (deviation 1.4%). In addition, in the study of Lee *et al.*, the ratio between minimum element size over maximum penetration depth was set at e/h_{max} = 0.1, while in our studies e/h_{max} = 0.05 – 0.025. Therefore, it is safe to follow either procedure for the numerical estimation of contact radius.

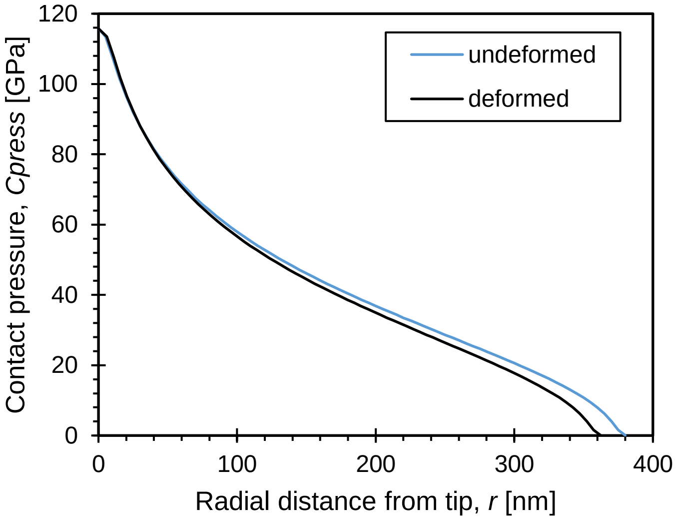

Figure 3-5: Numerical pressure distribution along radial direction for material with $\boldsymbol{E}$ = 200 GPa and $\boldsymbol{v}$ = 0.3. Blue line represents the undeformed radial distance while black line the deformed radial distance.

3.6 Comparison Between Experiment and Simulation

As a benchmark on the accuracy of finite element simulations predictions can be contrasted against experimental results. As illustrated in the flowchart of Figure 3-6, it is of great interest to evaluate the numerical results with respect to experimental measurements. The purpose of this procedure is to obtain two identical $P - h$ curves, experimental and numerical, and then through simulations to obtain useful information regarding stress and strain distributions, plastic zones, energies, etc. Hence, once the experimental load/displacement curve has been extracted, indentation parameters can be obtained; maximum indentation load P_{max}, maximum penetration depth h_{max}, contact stiffness $S = dP/dh$, contact depth h_c, hardness H, elastic modulus E and yield stress Y based on the methodology that is described in Chapter 2. Then, information $(E,\, v,\, h_{max})$

will be used as input data in order to structure the mechanical and geometrical response of the finite element model. Now, computational post-processing analysis yields a numerical $P - h$ response of the material, which must be compared and evaluated with the experimental one. If the two curves are in perfect agreement, then crucial results can be extracted based on numerical observations, or parametric studies can be designed based on specific targets. Otherwise, the numerical model should be re-evaluated and refined.

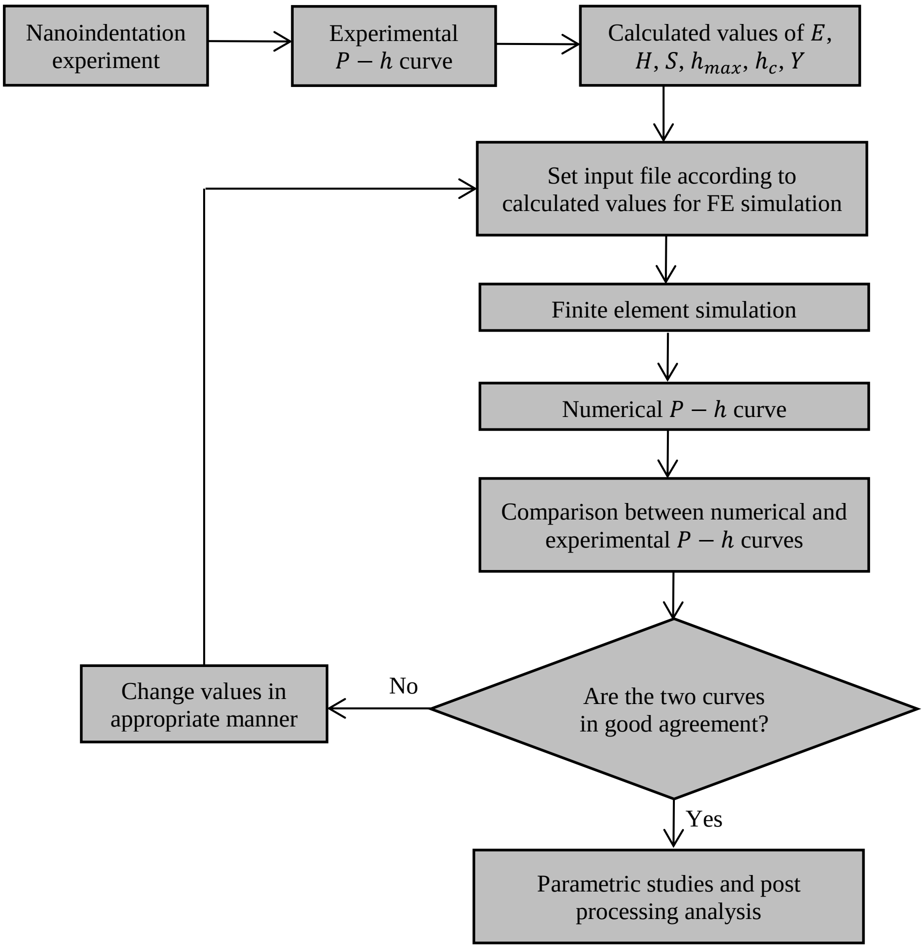

Figure 3-6: Flowchart diagram for the evaluation of a numerical model based on experimental measurements.

Figure 3-7 shows the comparison between the numerical (solid line) to experimental (dashed line) load – displacement results on fused silica, for the case of Berkovich indentation which is assimilated as cone of semi-angle 70.3º for simulation purposes. The experimental results of the elastic modulus have been used as inputs for the finite element model set up, where the yield stress of numerical material was estimated at $Y = H/1.9$

[57]. For the loading portion of $P - h$ curves, experimental and finite element results are nearly parallel with a small offset between them. However, this is not noteworthy since both curves result in the same maximum load value, where the hardness is extracted.

For the unloading portion, both results are laying on a single curve which gives the same contact stiffness value. The two curves start to deviate as they approach the horizontal axis, but this deviation has minimal effect on the indentation analysis procedure.

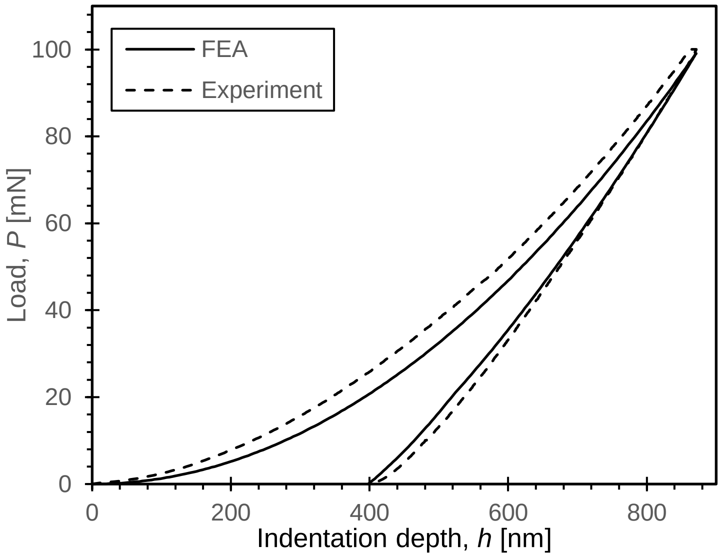

Figure 3-7: Load–displacement curves for sharp indentation on fused silica.

3.7 Effect of Plasticity on Indentation Response

The effect of generated plastic zones and material indentation response has been studied by "designing" elastic and elastic-perfectly-plastic materials. With the term perfect plasticity, we refer to a material that follows the von-Mises yield criterion and does not exhibit and hardening response beyond yielding. The von Mises criterion characterizes most metals and is described by:

$$\sigma_{eff} = \sqrt{\frac{(\sigma_1 - \sigma_2)^2 + (\sigma_2 - \sigma_3)^2 + (\sigma_3 - \sigma_1)^2}{2}} \tag{3.12}$$

where σ_{eff} is the von-Mises stress and σ_1, σ_2, σ_3 are the three principal stresses at a point. Yielding occurs when $\sigma_{eff} = Y$.

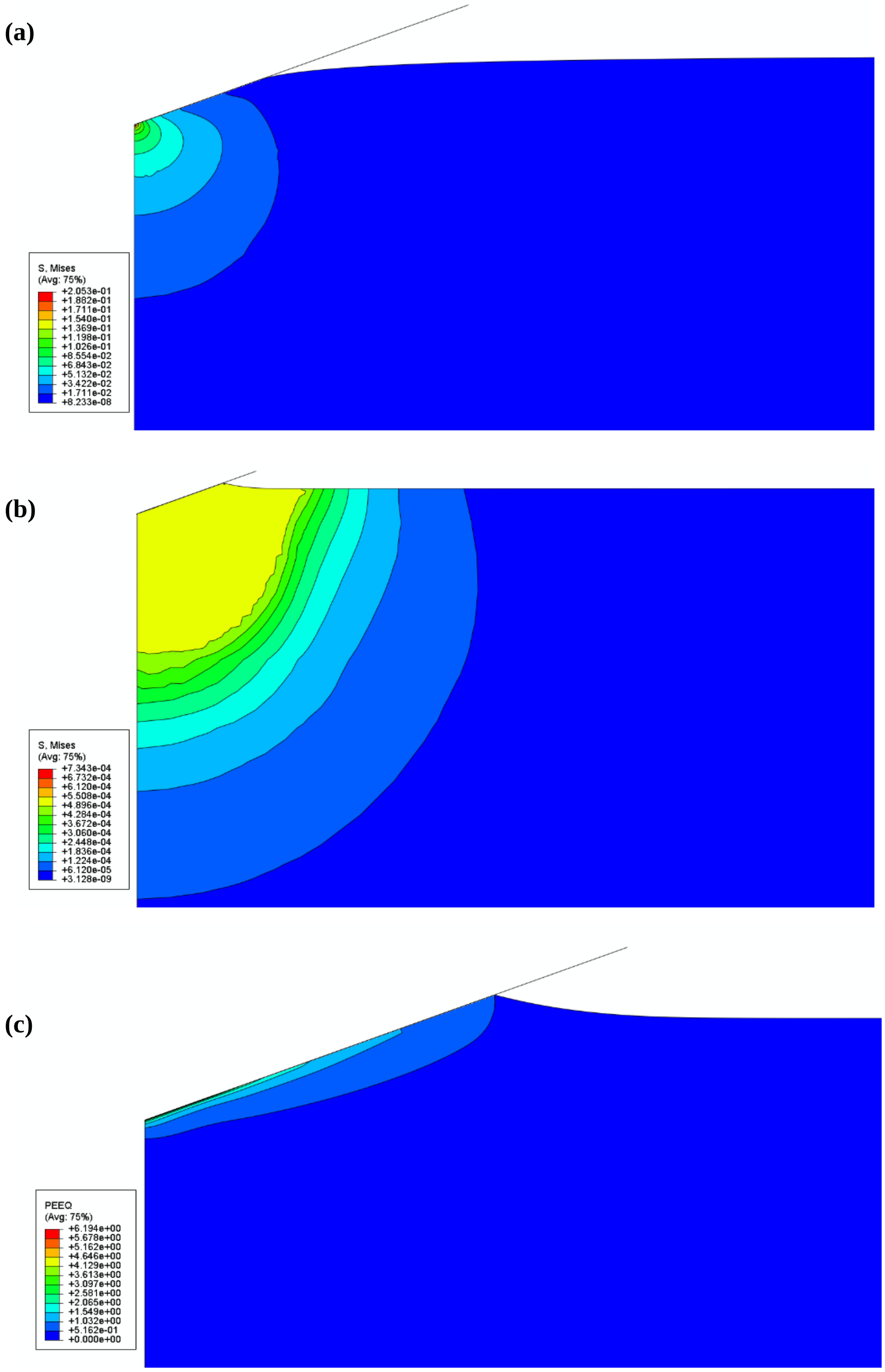

Figure 3-8: Contour plots in the fully loaded state for elastic and elastic-perfectly-plastic material with $\boldsymbol{E}$ = 200 GPa, $\boldsymbol{v}$ = 0.3 and $\boldsymbol{Y}$ = 500 MPa, where (a) shows von Mises stress distribution inside the elastic material; von Mises (b) and equivalent plastic strains (c) inside the elastic-perfectly-plastic material, accordingly.

Figure 3-8 (a)-(b) illustrate the generated von-Mises distributions under conical indentation for an elastic material with E = 200 GPa and v = 0.3 and an elastic-perfect-plastic material with E = 200 GPa, v = 0.3 and Y = 500 MPa, accordingly. Von-Mises stresses of elastic material are three order of magnitudes higher than that of the elastic-perfectly-plastic material. The reason is that elastic materials exhibit larger indentation resistance, they are stiffer in contrast to elastoplastic materials, where the domain factor cannot exceed the yield stress. In addition, this can be obtained from the extend of the stressed regions as indicated in from the stress distributions in both cases. In Figure 3-8 (c), the equivalent plastic strain distribution is illustrated, which highlights that plastic flow extends through the whole contact region and subsequently shifts the material's surface upwards and around the tip.

The differences in the indentation resistance between the two cases can be better demonstrated on a $P - h$ graph as presented in Figure 3-9 (a). Loading and unloading portions of the elastic material lay on a single curve, since there are no permanent deformations and all energy is recovered upon unloading. For that reason, elastic material exhibits larger indentation resistance with respect to an elastoplastic material which tends to dissipate energy once the yield criterion is satisfied, subsequently resulting in permanent plastic deformations. Figure 3-9 (b) demonstrates that elastic material response is accompanied by sink-in deformation of the material's surface, in contrast to the elastic-plastic material which tends to increase the contact area by displacing material around the tip, leading to pile-up phenomena.

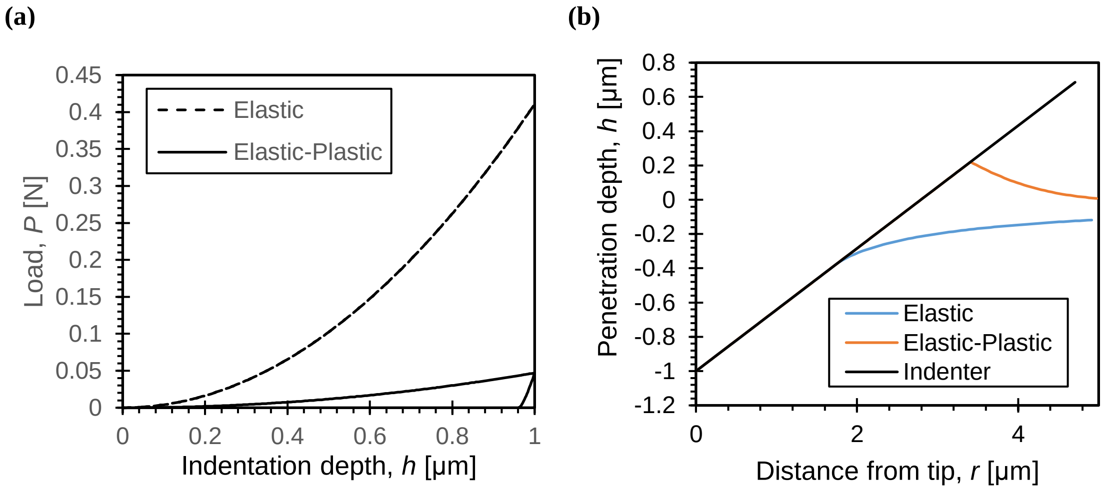

Figure 3-9: Post processing numerical analysis of (a) load – displacement curves and (b) profile imprints, for elastic and elastic-perfect plastic material with $\boldsymbol{E}$ = 200 GPa, $\boldsymbol{v}$ = 0.3 and $\boldsymbol{Y}$ = 500 MPa.

3.7.1 Indentation Imprint – Pile up Phenomena

As a preliminary discussion on the pile-up phenomenon, several materials have been studied, in order to link the E/Y ratio with sink-in or pile-up. Finite element simulations for conical indentation of elastic-plastic materials (Table 3-1) were performed and their $P - h$ responses, contact areas and surface profiles have been analyzed and extracted.

Table 3-1: Input data for various elasto-plastic materials.

Material	v [-]	E [GPa]	Y [MPa]	E/Y
Silver	0.37	71	55	1,291
6061 Aluminum alloy	0.33	69	62.05	1,112
AISI 1045 Carbon Steel	0.29	205	530	387
Ti_6Al_4V	0.34	113.8	880	129
PTFE	0.46	1.1	20	55
Silicon	0.28	190	7000	27
Fused Silica	0.17	72	4500	16

Figure 3-10(a) shows the results of dimensional group Π_3 for a large span of E/Y. For values of E/Y > 100, the material surfaces display pile-up phenomena and this phenomenon further enhances as E/Y increases. Results from the Oliver and Pharr methodology, Equation (2.42), are plotted against numerical findings, where both are in excellent agreement for materials that sink-in. For materials that exhibit pile-up response the Oliver and Pharr methodology is unable to accurately capture the contact area, potentially leading to inaccurate estimation of mechanical metrics like E and H.

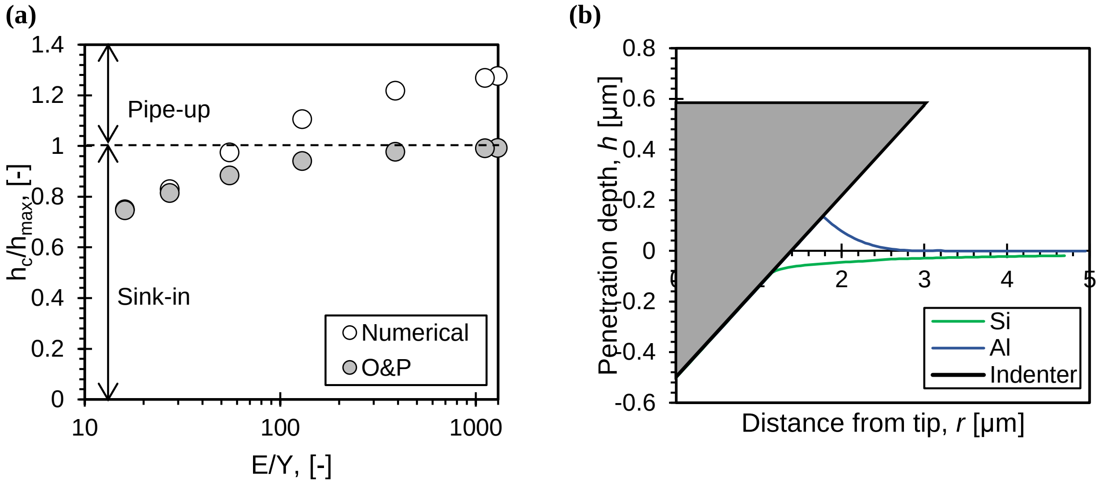

Figure 3-10: (a) Normalized contact depth for various $\boldsymbol{E/Y}$ materials. (b) Computational surface profiles at a state of fully load for silicon and aluminum materials.

Low E/Y materials, correspond to hard and highly elastic materials such as silicon, in which the generated plastic zones are small and all major deformation of the indented material is primarily elastic, therefore such materials exhibit sink-in response, Figure 3-10 (b). In the case of high E/Y −ratio (low indentation resistance) such as aluminum, the plastic zone is significantly extended and so the volume of the indented material around the contact, will tend to move the surface upward (pile-up).

3.8 Chapter Summary

This chapter dealt with numerical modeling of nanoindentation using the finite element method. The details of the numerical model have been presented and the procedure of extracting the projected area of contact has been analyzed. Dimensional analysis was performed in order to identify the major dimensionless factors of indentation testing. Indicative numerical studies of elastic and elastoplastic materials have been presented and the accuracy of the methodology has been proven against experimental data. Furthermore, the Oliver and Pharr methodology has been contrasted for a range of elastic-plastic von-Mises materials; pile-up phenomena tend to kick-in for $E/Y > 100$ and within this domain the O&P methodology gets inaccurate. The results presented in this chapter advocate towards the use of FEM in indentation testing for understanding the physical mechanisms and supporting the meaningful analysis of experimental data.

Part III

AUXETIC MATERIALS

Chapter 4

Auxetic Materials and Structures

Given the recent advances in materials synthesis and processing, a lot of enhanced materials with interesting microstructures and enhanced properties have been developed over the last years. Auxetic materials is a class of emerging solids having negative Poisson's ratio. These novel materials are gaining increasing interest in the scientific and technical sectors due to their attractive mechanical response. In contract to conventional materials ($v > 0$), auxetics exhibit enhanced indentation resistance, fracture toughness, impact resistance and uncommon mechanical response. These superior properties established auxetics as candidate materials for a broad range of applications, mainly in the biomedical and defense sectors. In this chapter we review the historical background of auxetic materials and structures, their relationship with microstructural architectures, synthesis routes and potential applications. Finally, we explore a computational study of a honeycomb auxetic and composite structure to motivate the research work that follows in Chapters 5 and 6.

4.1 Introduction

When conventional materials are stretched in one direction they tend to become thinner in the perpendicular directions. This characteristic behavior of the material is governed by one of the fundamental mechanical properties of materials; the Poisson's ratio, which for a conventional material possesses a positive value (v>0). However, thermodynamically the material is not restricted to have only positive v and negative values may also occur, meaning that the will undergo lateral expansion when stretch longitudinally. Materials that fall into this category have been termed auxetics, derived from the Greek word *Αυξητικός* meaning *to increase*.

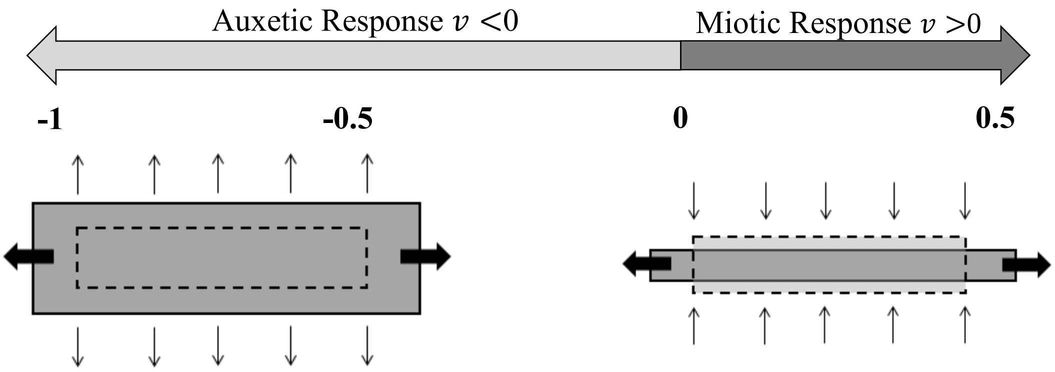

Figure 4-1: Tension behavior of materials under miotic ($\boldsymbol{v}$>0) and auxetic ($\boldsymbol{v}$<0) response.

Natural auxetic materials do exist; for example many cubic metals, arsenic, cadmium and a-cristobalite, and many biological materials (several tendons and tissues) have been found to be auxetic. Moreover, a wide range of other materials have been produced with tailored microstructural patterns to exhibit auxeticity, covering all major classes of materials. All those materials are of interest due to their interesting response under load and because they enhance other material properties, such as indentation resistance, volumetric strain energy dissipation, fracture toughness, porosity variation when stretched or compressed, enhanced energy absorption and different deformation pattern while bending. In the subsequent review, auxetic structures are discussed followed by a material summary and a brief discussion about the mechanical response of such materials.

4.2 What is Poisson’s Ratio?

Generally speaking Poisson’s ratio is the property of materials to expand or contract in directions perpendicular to the directions of compression or tension, respectively noted with v. Siméon Denis Poisson defined the ratio between transverse strain ε_t to longitudinal strain ε_l in the elastic loading direction as:

$$v = -\frac{\varepsilon_t}{\varepsilon_l} \tag{4.1}$$

The negative sign was inserted to account for the fact that most materials exhibit an opposing response, ending with a positive material constant v. French mathematician Augustin-Louis Cauchy proved theoretically that in order to characterize the elastic response of isotropic materials, one needs to define two independent moduli of elasticity. Hence, Poisson's ratio can differ from material to material. In the case of isotropic materials, v can be expressed in relation to bulk (K) and shear (G) modulus:

$$v = \frac{3K - 2G}{2(3K + G)} \tag{4.2}$$

It can be concluded from above equation that when K/G approaches 0, $v \rightarrow -1$ and when $K/G >> 0$, $v \rightarrow 0.5$. In Figure 4-2 the whole thermodynamically possible span range of Poisson's ratio is illustrated as a function of the ratio K/G. For most well-known solids, such as metals, ceramics and polymers, $0.25 < v < 0.35$. Rubbery materials undergo shear deformation but resist volumetric deformation, thus $K >> G$ and $0.4 < v < 0.5$. Auxetic materials with $v \approx -1$ exhibit opposite behavior to rubbery materials; they resist shear deformation and undergo volumetric deformation, hence $K << G$.

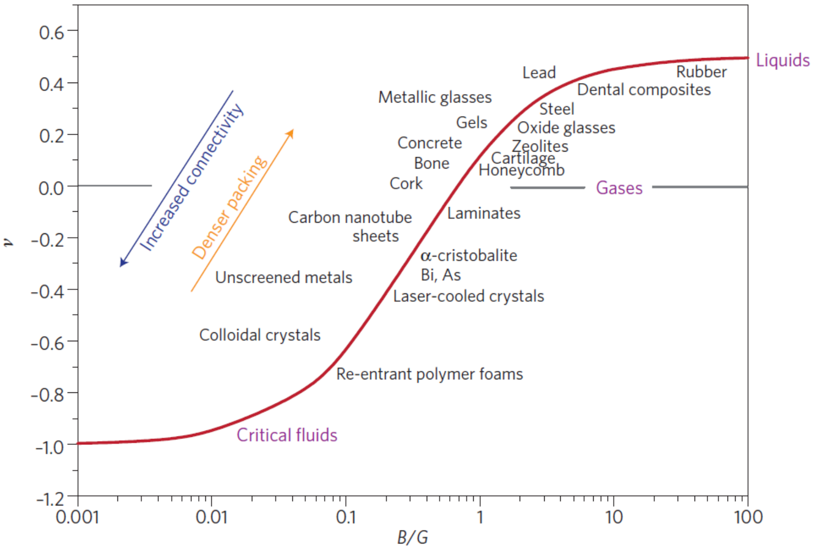

Figure 4-2: Span range of Poisson's ratio $\boldsymbol{v}$ as a function of the ratio between bulk and shear moduli for a wide range of isotropic classes of materials [67].

4.3 Auxetic Materials

The first experimental observation of a negative Poisson's ratio response was first reported by Voight in 1887, when he estimated the Poisson's ratio of pyrites as $v \approx$ -0.14. Nevertheless, the real interest in materials exhibiting negative Poisson's ratio (NPR) started 100 years later, when Lakes reported a re-entrant structure by permanently buckling the ribs of conventional hexagonal foam cells inward. In 1991, the term "auxetic" was introduced by Evans [68], referring to their response to expand laterally upon longitudinal tension.

Auxetic materials can be found in nature such as single crystals of a-cristobalite [69–72], pyrite [73], cubic elemental metals [74], zeolites [75–77], cadmium [78] and arsenic [79]. These materials demonstrate auxetic response when loaded in certain directions. In addition, many biological materials have been reported for their auxetic nature which is attributed to their fibrillar structures or other microstrucral architectures; these include cancellous bones [80], cow teat skin [81], cat skin [82], salamander skin [83] and membranes found in cytoskeleton of red blood cells [84].

In general, auxeticity is driven by the deformation mechanisms of specific structures, either microstructural or geometrical structures, such as rib hinging, bending, stretching and rotating. It has been found that the Poisson's ratio of auxetic materials is a scale independent property, from molecular level to macroscale, and depends entirely to the deformation mechanism. For example, identical rotational mechanism causes the auxetic response in zeolites (nanometer scale) and polymeric foams (millimeter scale).

This uncommon deformation pattern in combination with the ability to design a structural material with negative Poisson's ratio attracted the interest of the research community and led the development of auxetic metamaterials. As illustrated in Figure 4-3, the number of publications per year on the topic has increased to 230 in the last 30 years, which proves that auxetic materials and structures are an emerging class of materials with significant scientific interest. In addition to their novel deformation response, auxetic materials exhibit enhanced mechanical properties in contrast with their conventional counterparts, like increased shear modulus, indentation resistance, impact resistance, fracture toughness, acoustic damping, energy absorption.

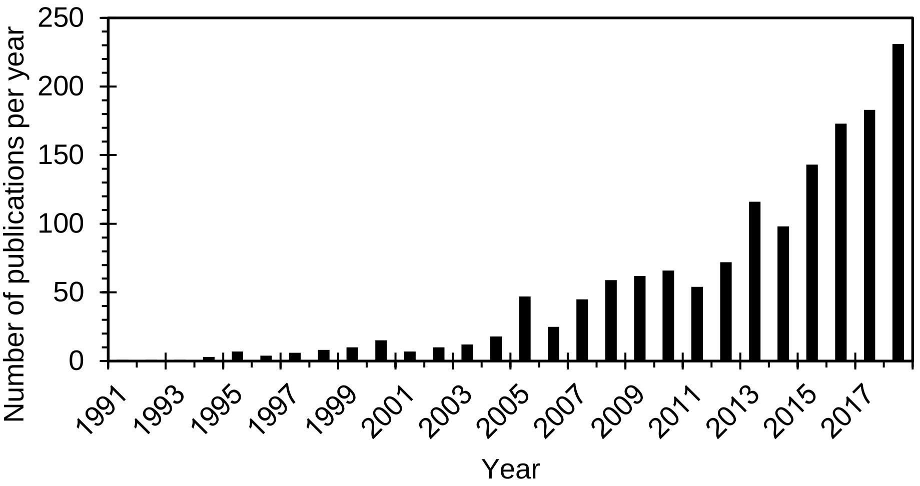

Figure 4-3: Number of publications on the topic of auxetics per year since 1990. Data extracted from Scopus search engine.

4.4 Types of Auxetic Structures

For manufacturing purposes, one must consider the internal structure of an auxetic material and its deformation mechanism, in order to "design" the macrostructure by tailoring the mechanical properties. The most common microstructures of cellular auxetics, which their deformation mechanism response drives the negative Poisson's ratio, are designated into re-entrant, chiral and rotating polygon units. Regardless of their different structure, Poisson's ratio is dominated by changes in internal areas. All these structures expand under tension (internal areas expand), while under compressive load, their internal areas tend to enclose. These microstructural effects are responsible for the macroscopically observed negative Poisson's ratio response.

4.4.1 Re-entrant Structures

The first re-entrant cellular structure was proposed by Gibson and Ashby in the form of honeycombs [85]. Re-entrants have been used widely to study the controlled mechanisms of auxetic effect. A variety of re-entrant structures can be found either in 3D or in 2D, and are formed by hexagonal, star shape, or arrowhead face cells, Figure 4-4. When these structures are subject to uniaxial tensile load, the cell ribs tend to increase (moving outward), resulting in the auxetic effect.

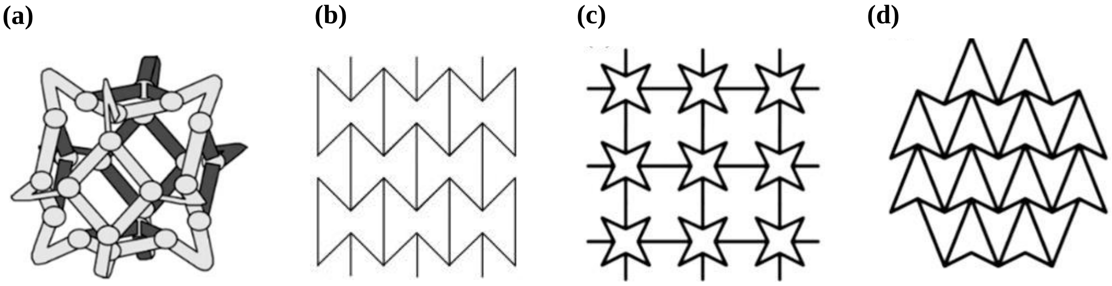

Figure 4-4: Schematic of re-entrant auxetic structures: (a) 3D auxetic cell, 2D (b) hexagonal, (c) star shape, (d) arrowhead face cells.

4.4.2 Chiral Structures

In 1991, Lakes proved that a non-centrosymmetric, chiral structure can produce a negative Poisson's ratio response [86]. As illustrated in Figure 4-5, the unit cell of this structure can be defined from a central node with six tangentially attached ribs/ligaments. When uniaxial load is applied, the nodes rotate accompanied by flexure of the ligaments, which rises the auxetic response in the transverse direction. With chiral structures, Poisson's ratio close to -1 can be obtained.

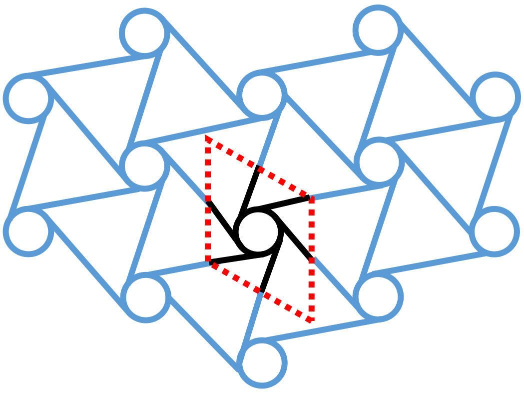

Figure 4-5: Typical chiral structure where the unit cell is highlighted by dotted lines.

4.4.3 Rotating Polygon Structures

Grima and Evans [87] presented a new structure that can achieve auxetic response, by involving the rotation of rigid squares joined with hinges at their vertices, Figure 4-6. Many authors extended the square geometry of this rotating mechanism to other polygon geometries in order to capture auxeticity: rotating tetrahedral [71], triangles [88–90], rectangles [91] and rhombi [92]. Furthermore, it has been proven that this is the dominant mechanism of the auxetic response of nature materials, such as zeolite and a-cristobalite. [93,94].

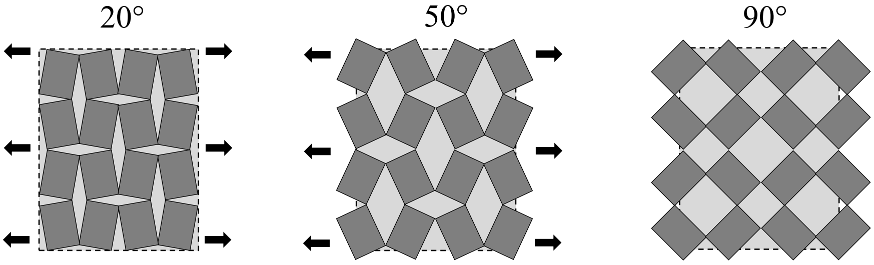

Figure 4-6: Rotating squares for auxetic behavior where (a) represents the relaxed struture and (b) the structure under horizontal tension load in which exhibits an auxetic response.

4.5 Novel Properties of Auxetic Structures

This counter-intuitive behavior described above is associated with several other beneficial effects and unique properties. The understanding of the physical mechanisms that drive their macroscopic response is crucial for the development of new and improved auxetic structures.

4.5.1 Indentation Hardness

During indentation on an auxetic material, the area under contact tends to densify in te longitudinal and transverse directions due to the compressive load that is generated at contact. Hence, this behavior leads to an increased indentation resistance, compared to the behavior of a conventional material, Figure 4-7 (a). By substituting Equation (2.27) in (2.3), one can derive that hardness scales as:

$$H \propto \left[\frac{E}{1-v^2}\right]^x \tag{4.3}$$

where x is a constant that depends on indenter's shape; for cone x=1 and for sphere x=2/3. Since for isotropic materials v extends from -1 to +0.5, as v moves closer to -1, the hardness of the material approaches infinity. This theoretical behavior of the normalized elastic hardness at $H/H_{v=0}$ is plotted in Figure 4-7 (b) for conical and spherical indenters, for various Poisson's ratio, and the deviation between the two curves is due to the indenter's geometrical profile and the resulting stress distribution. Under conical indentation, materials with $v = -0.9$ exhibit a fivefold increase of their hardness, in contrast to a threefold increase for the case of sphere.

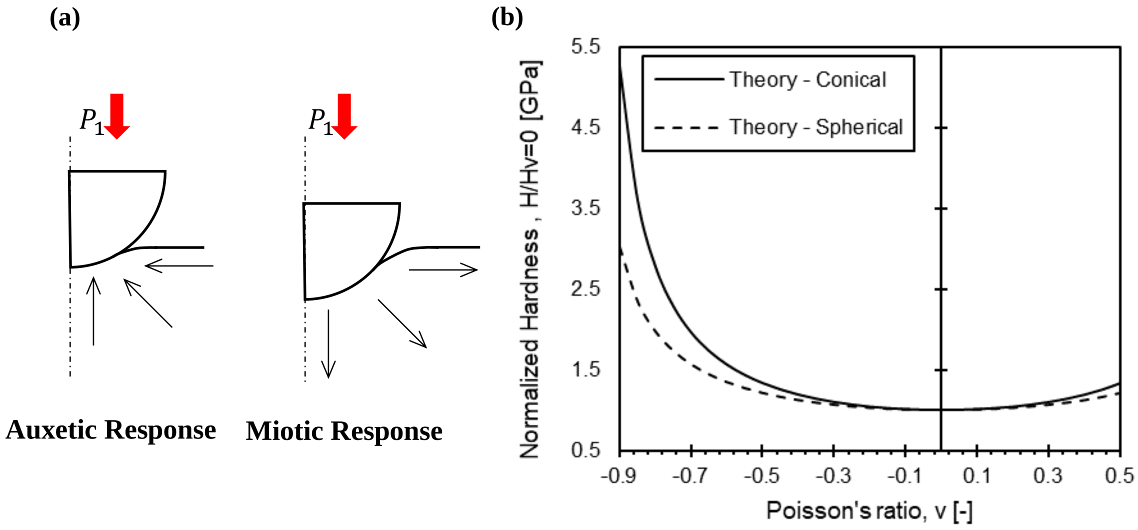

Figure 4-7: (a) Illustration of indentation resistance of conventional and auxetic materials, (b) evolution of normalized elastic indentation hardness $\boldsymbol{H/H_{v=0}}$ as function of $\boldsymbol{v}$.

A series of experimental studies have been reported in the literature; Alderson *et al.* [95] performed spherical indentation on ultra-high molecular weight polyethylene (UHMWPE) foams and resulted to an increase of indentation resistance by a factor of 2 on changing Poisson’s ratio value from 0 to -0.6. Chan and Evans [96] studied the response of polyurethane hexagonal (conventional) and re-entrant (auxetic) foams under spherical and cylindrical indenters, where they noted that for auxetics, the contact area increases due to their densifying mechanism in contrast with conventional material.

It should be emphasized that results presented in the above studies are affected by the microstructural architecture which can lead to significant amounts of anisotropy and plastic deformation. Materials with high porosities, like the foams described above, can change their mechanical response due to volumetric change ratio under pressure. When an auxetic foam is under compression, its elastic modulus increases with the increase in of densification. Furthermore, as the Poisson’s ratio approaches -1, the shear modulus approaches infinity, therefore materials become highly compressible (enlargement of density), but difficult to shear – anti-rubber material.

4.6 Applications of Auxetics

The only limitation of man-made auxetic materials is their association with increased porosity. Auxetics are, therefore, not yet ideal for structural applications, except if a pioneering new nanostructure would be fabricated, that through the incorporation of molecular entities would cause the macroscale response of material to be auxetic.

Taking advantage of the novel behavior of auxetic materials, a range of applications are suitable, from sports to medical field. Auxetic materials have the potential to be used in sports applications, for example; safety helmets, pads, gloves and mats due to their enhanced impact resistance and energy absorption for lighter components. In addition, auxetic products have been released in the sports sector by Under Armour [97] which developed apparel and shoes with auxetic skins to aid conformability and comfort, and Nike [98,99] which includes an architecture closed cell foam outsole with auxetic structure, Figure 4-8.

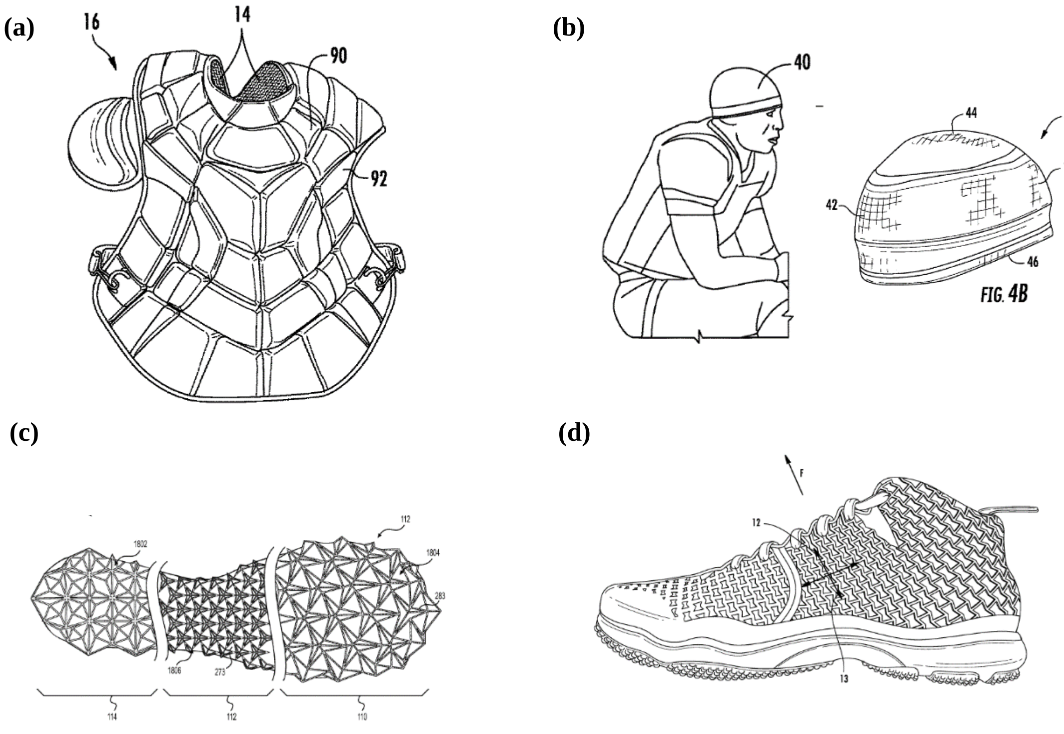

Figure 4-8: Registered patents related with auxetic products from Under Armour and Nike: (a) front view of apparel, (b) perspective and side view of a cap, (c) outer surface of an embodiment of a sole structure, (d) side view of footwear, including auxetic arrangements.

Auxetic systems of re-entrant structures or rotating polygons can offer a wide range of pore size and as a result, applications in filters as shown in Figure 4-9. Their unique pore-opening characteristics under deformation improve filter performance from macro to nano-scale. At the molecular level, auxetic polymeric materials could serve as excellent solution for drug-release and sensor applications [100–102].

A big effort in the field of auxetics is their usage in the biomedical field. Many authors studied the performance of auxetics for oesophageal stents [103,104], angioplasty stents [105,106] and annuloplasty rings [107]. The results are promising, due mainly to the ability of the material/strutcure to expand when stretched along with synclastic behavior and enhanced stiffness which minimize the generated stresses.

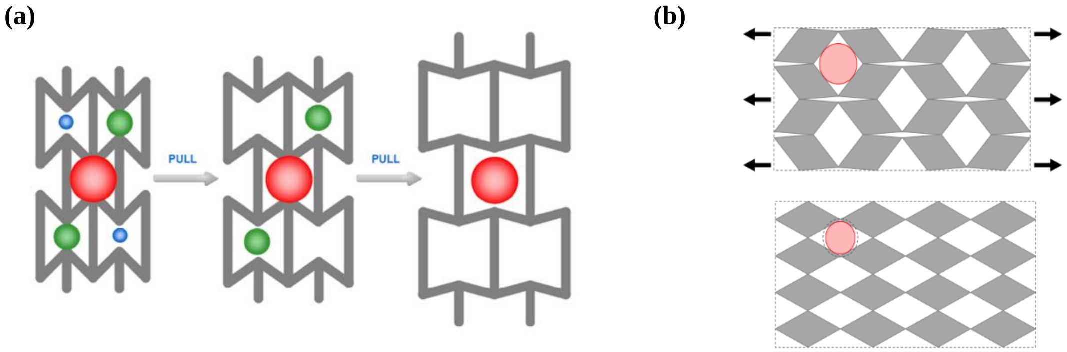

Figure 4-9: Smart filter application mechanisms by (a) re-entrant structures and (b) rotating rhombi network structures.

4.7 Numerical Response of Composites Plates in Re-entrant Structures

Auxetic cellular structures are highly recommended in the area of light-weight applications, due to their ability in achieving high stiffness and large surface to volume ratio. This property motivated the research community to the fabrication of auxetic composites, in order to combine the desirable auxeticity with additional beneficial properties of other materials. Auxetic material are used either as matrix structures in laminated composites due to their synclastic curvature properties, or as fiber reinforcements, in order to reduce the cracks between matrix and fiber. In this chapter, we suggest a design for composite plate with auxetic core, based on numerical results. The commercial software SolidWorks has been adopted to design the structure and perform the finite element analysis (FEA) of 3D re-entrant auxetic unit cell, auxetic structure and composite structure.

4.7.1 FEA on Re-entrant Honeycomb

An implicit finite element model for the validation design of re-entrant honeycomb plate has been built. In Figure 4-10, the unit cell of the auxetic structure is illustrated while the full size of structure is defined with 4 x 5 representative cells.

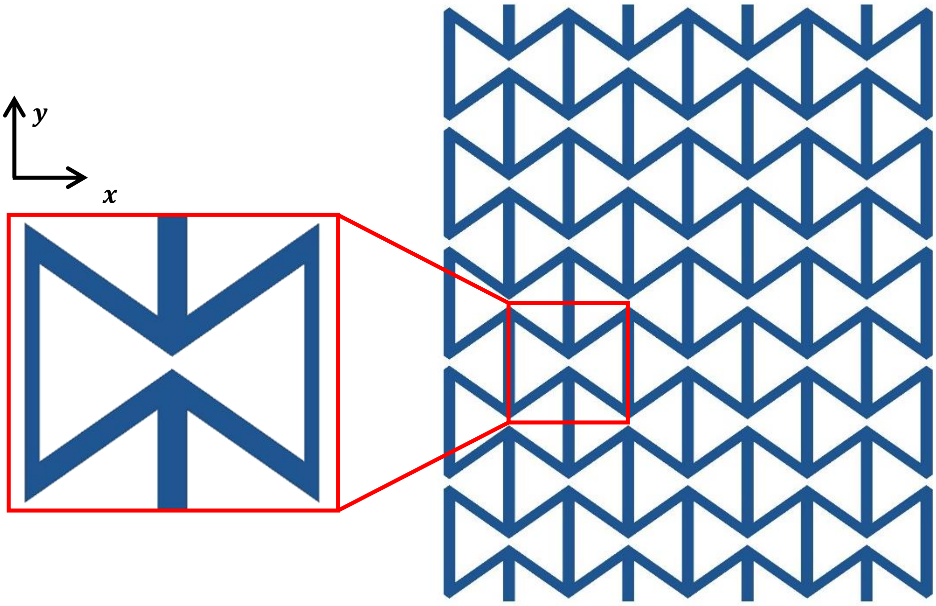

Figure 4-10: Model of unit cell of re-entrant honeycomb auxetic and the lattice of 4 x5 unit cells.

Parabolic tetrahedral solid elements have been used to construct the shape of the unit cell as shown in Figure 4-11(a). Detailed boundary conditions were established to calculate the auxetic response of the unit cell and re-entrant honeycomb structure. As shown in Figure 4-11(b) the tension of unit cell along the y direction has been modeled by displacement control condition. Nodes at the bottom surface of unit cell have been fixed along three directions, while nodes at rear face have been imposed at $\Delta z = 0$. In Figure 4-11(c), the boundary conditions of the re-entrant structure capture similar conditions with unit cell, except from the tension condition, where here an applied pressure has been imposed on the nodes at the top surface. A linear elastic material was chosen to characterize the response of the honeycomb with $E = 210$ GPa and $v = 0.28$. In addition, reference points have been defined in the models to extract average values of generated stresses, strains and displacements, to calculate the uniaxial behavior of the material and the Poisson’s ratio.

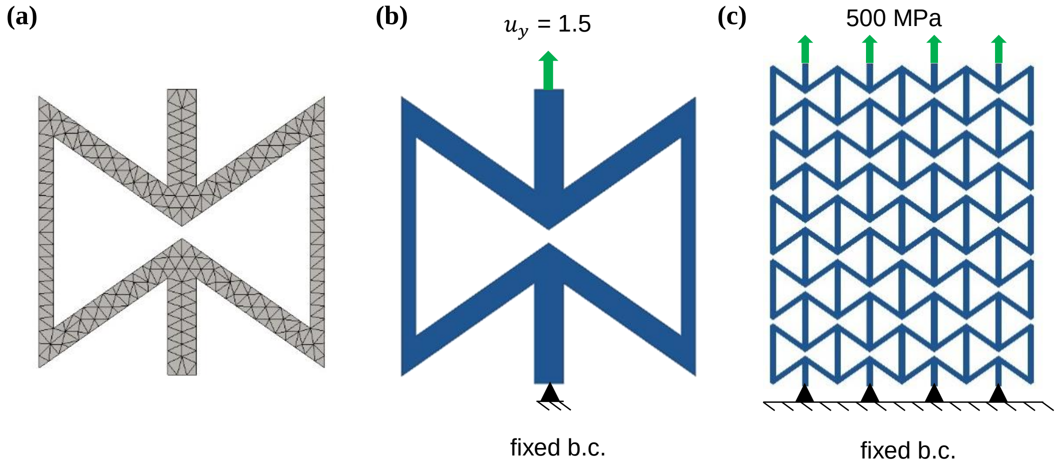

Figure 4-11: Numerical simulation models: (a) mesh model of unit cell, (b) displacement driven and boundary conditions used in unit cell, (c) load driven and boundary conditions used in honeycomb structure.

In Figure 4-12 the results of the simulated unit cell are presented. The maximum axial stresses are generated at four concave angles as expected. From Figure 4-12(b), which shows the corresponding axial displacements u_y, the lateral dimensions of the material expand rather than shrink, in response to the applied tensile load, which is characteristic of the auxetic behavior. Furthermore, as mentioned above, the Poisson’s ratio is not scale-dependent, therefore although the material at molecular lever is characterized by a positive v, the response of the structure at macroscale, supports a negative v, due to its deformation mechanism. Figure 4-12(c), (d) demonstrate the observed strains in ε_x and ε_y directions, accordingly. Analysis of these results and the slope between $\varepsilon_x/\varepsilon_y$ results in the Poisson’s ratio of the unit cell.

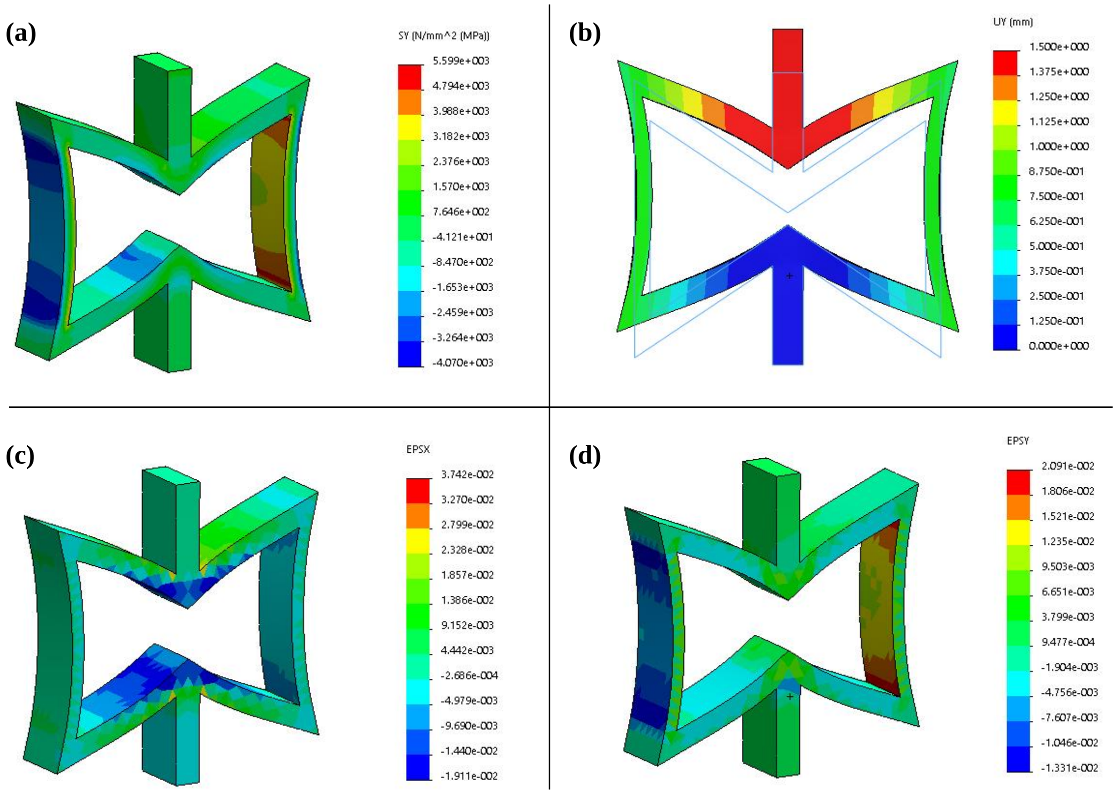

Figure 4-12: Elastic FEA results of the response of axial: (a) stresses, (b) displacements, (c) strains and (d) lateral strains.

Regarding the response of the honeycomb structure (Figure 4-13), results underlying auxetic response when tensile pressure is applied at the top face of the struts in y-direction.

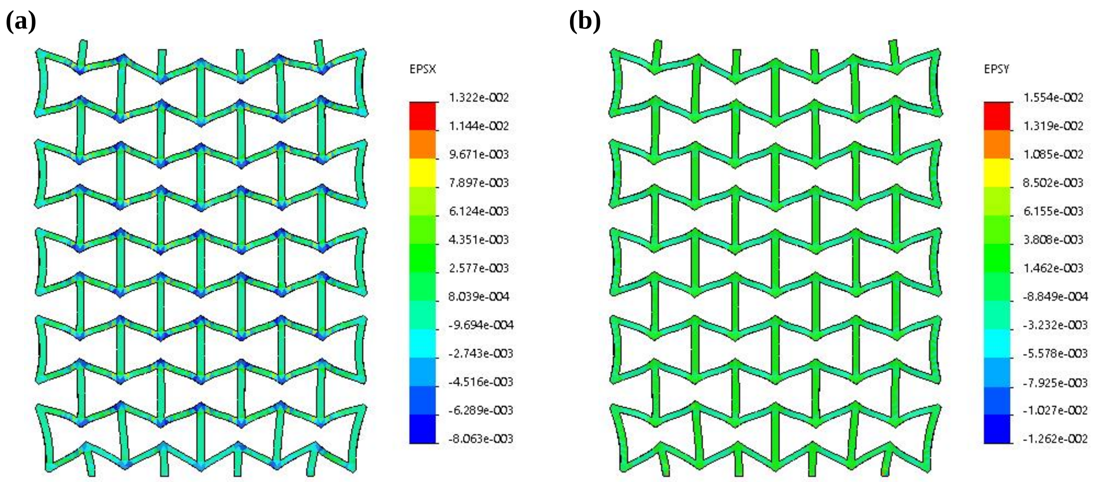

Figure 4-13: Strain field of the re-entract honeycomb structure. FEA results support the overall auxetic behavior when pressure is applied in $\boldsymbol{y}$-direction.

4.7.2 FEA on Sandwich Plate with Auxetic Matrix

Considering a sandwich plate with auxetic matrix, which has three layers of materials as illustrated in Figure 4-14. Top and bottom layers are elastic isotropic polymer material with E = 172 MPa and v = 0.439. The matrix material has a re-entrant honeycomb structure with E = 210 GPa and v = 0.28. The total thickness of the sandwich plate is 7 mm; h_1, h_3 = 1 mm and h_2 = 5 mm.

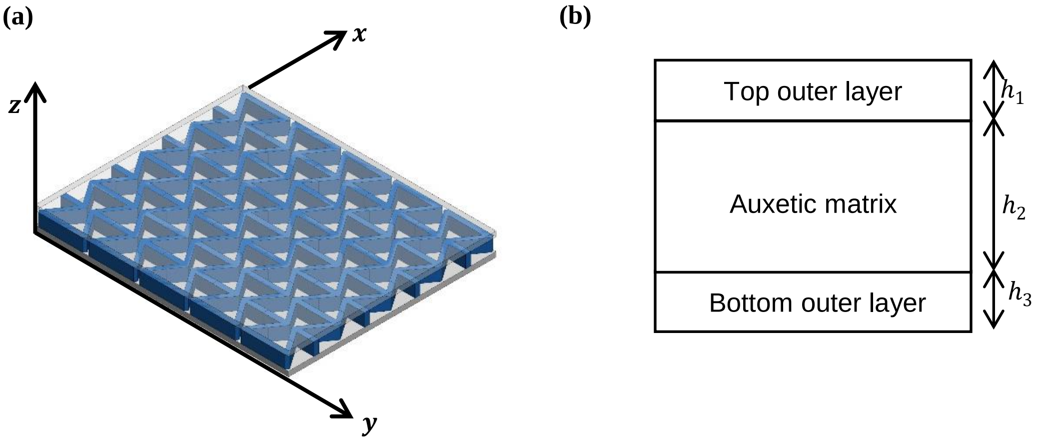

Figure 4-14: (a) CAD model of sandwich plate structure, and (b) discretization of composite structure.

Parabolic tetrahedral solid elements have been used to construct the shape of the composite unit cell and to characterize the interface between auxetic and plate materials, as depicted in Figure 4-15(a). Tension of unit cell was modeled by displacement control condition along the positive y-direction. Nodes at the bottom surface of unit cell have been fixed along three directions. For calculation purposes, we modeled only the half thickness (3.5 mm) and therefore we imposed symmetry conditions at the front face of the structure. Again, reference points have been defined in the models to extract average values of generated stresses, strains and displacements, to calculate the uniaxial behavior of the composite and the Poisson’s ratio. A mesh sensitivity analysis was carried out to ensure that the numerical solutions are mesh-independent.

The numerical response of the resulting axial displacements is shown in Figure 4-15(b). It is obvious that the elastic moduli mismatch discrepancy (E_{aux}/E_{plate} = 1220) affects the overall behavior of the structure. In addition, it seems that the composite structure exhibits an auxetic response under the current conditions.

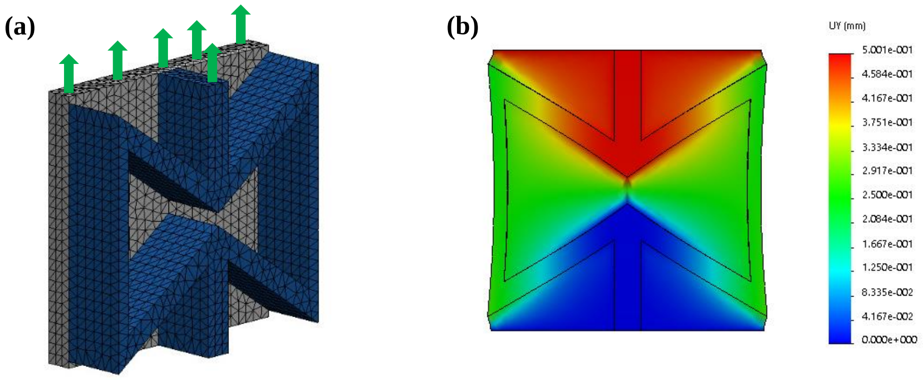

Figure 4-15: (a) Mesh model and boundary conditions of composite's unit cell, (b) computational axial strain results of composite structure.

Data in Figure 4-16(a) present the calculated axial stresses as a function of the axial strains. Auxetic curve exhibits a stiffening behavior in contrast to the plate's curve. That was expected, because of their moduli mismatch. Composite curve located between them and its slope, corresponds to E = 1.25 GPa. Figure 4-16(b) presents the transverse strain over the longitudinal strain in order to investigate the response of their Poisson's ratio. A linear fit was applied to the data (R = 0.997 – 0.9993) and their Poisson's ratio was calculated as: re-entrant structure v = -0.77 and composite structure v = -0.66.

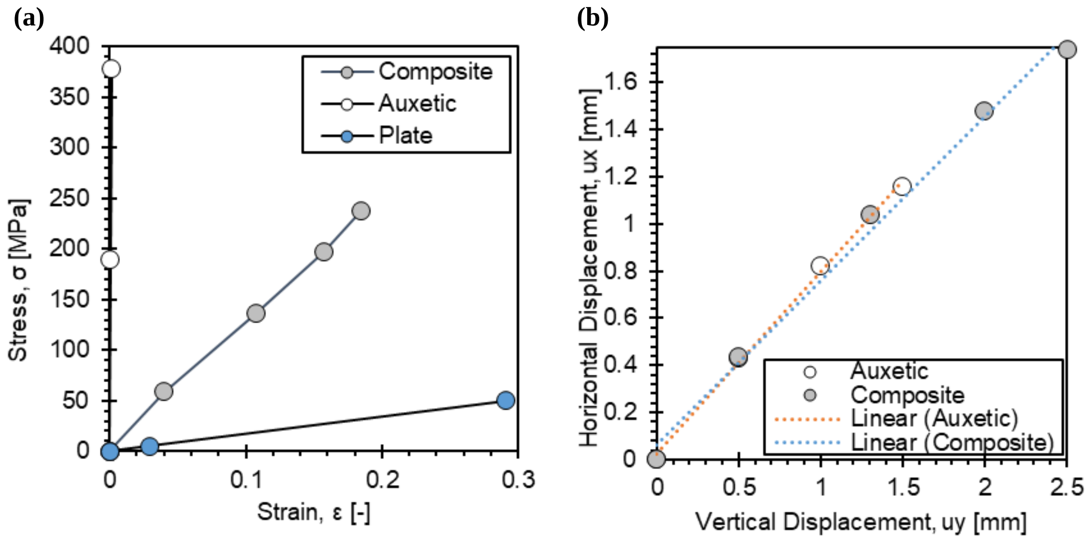

Figure 4-16: Numerical results of 3D auxetic and composite unit cells under uniaxial tensile tests: (a) nominal stress vs. nominal strain curve, (b) calculated lateral strain over axial strain for extracting Poisson's ratio value.

4.8 Chapter Summary

This chapter provided a brief review on auxetic materials and structures, including natural and man-made systems. It becomes apparent that auxetic response yields a superior mechanical response compared to their non-auxetic counterparts. Most of the synthesized auxetic structures are characterized by a significant amount of porosity, due to materials design purposes. Auxetics are an emerging class of materials with potential applications in the biomedical and sports industries. From a computational point of view, we have performed 3D finite element simulations in a sandwich auxetic panel and the numerical results demonstrate its superior mechanical response and motivate the need for future optimization studies that could lead to the design of new protective systems.

Chapter 5

Elastic Indentation Resistance of Auxetic Materials

This Chapter deals with the indentation resistance of auxetic materials. It has been reported in the literature that auxetic materials exhibit an enhanced indentation resistance, the origins of which have not been properly addressed. We here use the finite element method in order to investigate the origins and quantify this enhanced resistance. Furthermore, the theoretical solution that was presented in Section 2.4.2 of a rigid axisymmetric probe penetrating into a semi-infinite linear elastic half-space, becomes increasingly inaccurate for elastic indentations on auxetic materials ($\nu < 0$). We here correct the analytical solution for the entire possible span of Poisson's ratios.

5.1 Introduction

Several finite element studies [50,55,108–110] have pointed out that computational results deliver consistently higher values of the modulus of elasticity when calculated through Equation (2.33). A detailed analysis by Hay *et al*. [44] in their, by now, classic paper of 1999 has deciphered the origins of this discrepancy which has its roots on an inaccurate boundary condition used in the formulation of the mathematical problem that has been analytically solved. Through finite element modeling they have quantified this uncertainty and they have formulated analytical approximations for a correction factor γ for Equation (2.33) based on simple modifications of Sneddon's solution, which proved to be a function of the Poisson's ratio of the material (ν) and the cone semi apex angle (θ):

$$\gamma = 1 + \frac{(1-2\nu)}{4(1-\nu)\tan\theta} \tag{5.1}$$

$$\gamma = \pi \frac{\frac{\pi}{4} + 0.15483073 \cot\theta\,(1-2\nu)/4(1-\nu)}{\left(\frac{\pi}{2} - 0.83119312 \cot\theta\,(1-2\nu)/4(1-\nu)\right)^2} \tag{5.2}$$

Equation (5.1) is best suited for cube-corner indenters whereas Equation (5.2) for Berkovich/Vicker-type geometries. While correction factors have already been proposed [44,53,54], the majority of studies (with a few recent analytical exceptions [111,112]) have concentrated in the positive Poisson's ratio regime and have neglected an exciting and developing class of materials: the auxetic systems.

The aim of this particular study is twofold: on one side we aim to quantify the increased indentation resistance reported in the literature when indenting auxetic materials and identify through computational simulations the mechanisms that lead to this particular response. On the other hand, we aim to deal with the discrepancy caused by the existing analytical solution when indenting auxetic materials and extract correction factors that will eliminate any inaccuracies and will correct the analytical solution for the entire possible span of Poisson's ratios.

5.2 Finite Element Model

Two-dimensional axisymmetric finite element simulations are performed to investigate the elastic indentation response of cones and spheres on materials with various Poisson's ratios, with emphasis being placed on auxeticity. For the case of conical indentation, the indenter was modeled as a rigid cone with half-apex angle of θ=70.3°. This conical angle ensures the same contact depth vs. projected area of contact relation ($A_c = f(h_c)$) as in Vickers and Berkovich pyramidal indenters which are commonly employed in experimental investigations. Previous numerical studies by King [45] showed that the assimilation of three- (Berkovich) and four-sided (Vickers) pyramidal indenters with a cone of equivalent semi-apex angle is accurate within 1-3%. Details of the model geometry are shown in (Figure 5-1(a)). The ‘semi–infinite’ half space is modeled as a 101×101 μm^2 domain. The indentation simulations were restricted to depths below 500 nm, much smaller than the domain such as to avoid any boundary effects. The continuum space is discretized using 4–node axisymmetric, isoparametric elements (CAX4–full integration).

In the case of spherical indentation four indenter geometries were considered in order to cover a broad range of indentation strains; 5 µm, 8.5 µm, 10 µm, 25 µm and 50 µm. The ‘semi–infinite’ half space is modeled as a 101 × 101 mm^2 domain (see Figure 5-1(b)). All studies were performed to the same indentation depth, $h_{max} = 100$ µm, which is much smaller than the domain such as to avoid any boundary effects. The continuum space is represented by 4-node axisymmetric, CAX4 isoparametric elements.

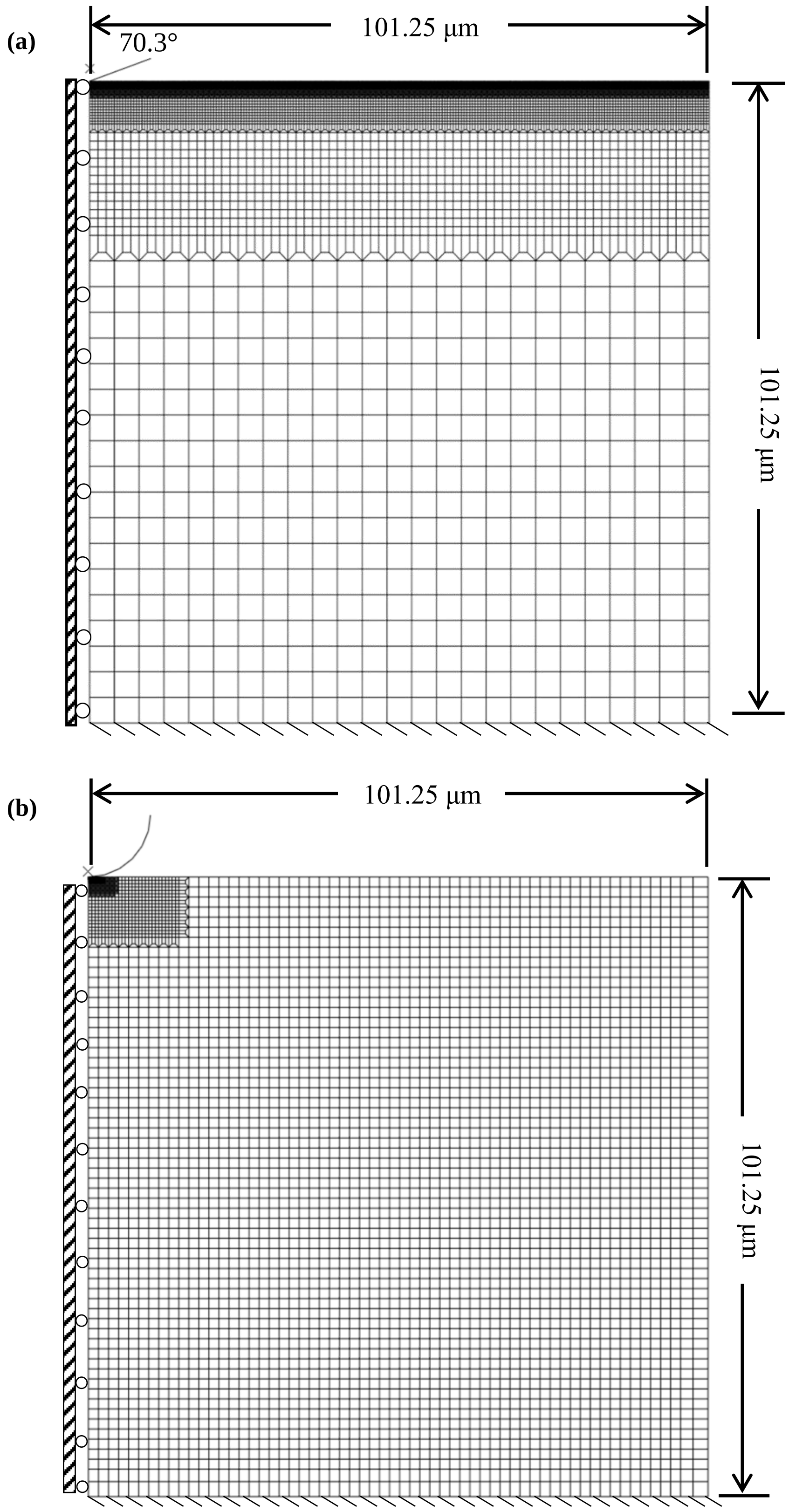

Figure 5-1: Schematic of the geometry modeled in this study with details of the mesh used for (a) conical and (b) spherical indentation.

The element size on both case studies was continuously refined in five successive regions as approaching the indenter contact region for greater accuracy. A mesh sensitivity analysis was performed to ensure that the simulation results were insensitive to the mesh size. Roller boundary conditions were applied on the axis of symmetry and fixed boundary conditions on the bottom surface of specimen. Frictional effects in the indenter–material interface were included in the analysis through an isotropic Coulomb model, in which the local shear stress τ_c is related to the local normal pressure p_c through $\tau_c = \mu p_c$ where μ is the friction coefficient between the indenter and the surface. We assume that the loading rate is slow enough such as static friction can securely model the interface response. Simulations proceeded in two steps: the indenter was firstly subjected to a ramped vertical displacement, followed by an indenter retraction to the original position which corresponded to complete unloading at zero load. During this process the lower edge of the material was constrained vertically. Axisymmetric boundary conditions were used along the symmetry axis beneath the indenter region [64].

5.3 Conical Indentation Resistance

Figure 5-2 shows the evolution of simulated $P - h$ responses for materials with an elastic modulus arbitrarily set to $E = 100$ GPa and various Poisson's ratios. The computational results suggest that the indentation resistance increases when $\nu \neq 0$. While a small increase is observed for positive Poisson's ratio the resistance of the material significantly increases as the Poisson's ratio moves into the negative regime (Figure 2(b)).

In order to better quantify the influence of ν on the material's ability to resist penetration we have calculated the elastic hardness of the material in the whole possible span of ν, $-1 \leq \nu \leq 0.5$. The physical meaning of hardness for elastic materials signifies their ability to resist penetration by a probe and relates to the average pressure generated beneath the indenter tip.

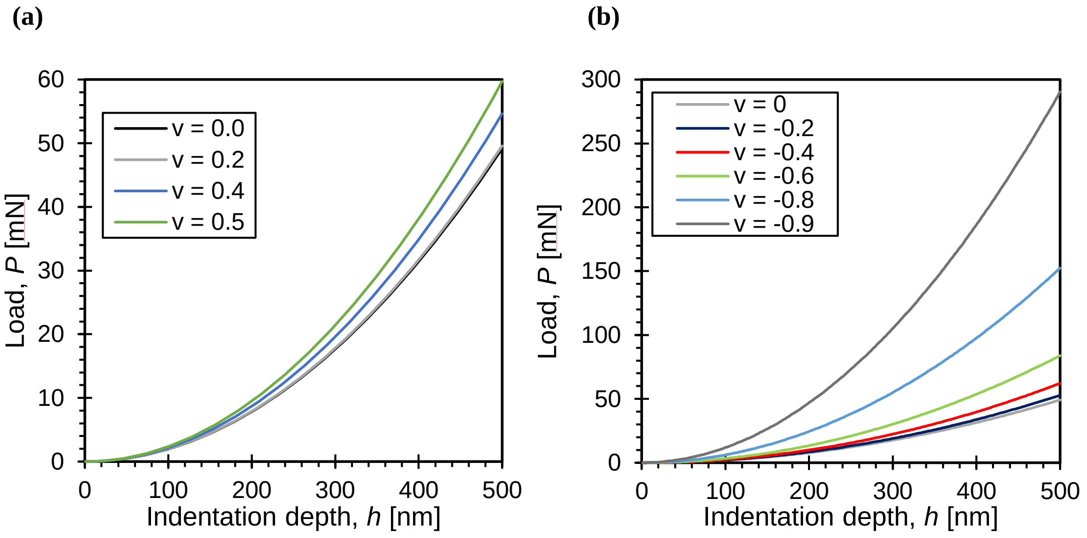

Figure 5-2: Conical indentation computational force-depth (P-h) responses for materials with E=100 GPa and v in the (a) positive (0 to 0.5) and (b) negative (-1 to 0) regime.

Data in Figure 5-3 corresponds to the normalized results by the hardness for $\nu = 0$ such as to present the relative amplification factor that the material experiences compared to the value at $\nu = 0$. Consistent with $P - h$ responses, the minimum possible resistance to penetration is provided for $\nu = 0$ and hardness increases for any deviation. The maximum within the positive regime is obtained for incompressible materials $\nu = 0.5$, $H/H_{\nu=0} = 1.17$ (numerical results). Of particular interest is the rapid amplification of hardness observed into the negative regime (auxetic materials) for which a sevenfold enhancement for the lowest ν simulated in this study ($H/H_{\nu=0} = 7.13$ for $\nu = -0.9$) is observed. The ability of the material to enhance its resistance to penetration is consistent with the experimental observations reported in [92, 113]. Before proceeding with a quantitative comparison between theory, simulations and experiments a few words on the nature of the indentation response of auxetic systems is due. In search of the physical mechanisms that lead to this amplified response we have investigated the interdependence of the elastic constants, the stress distributions beneath the indenter, and the contact depth evolution with Poisson's ratio.

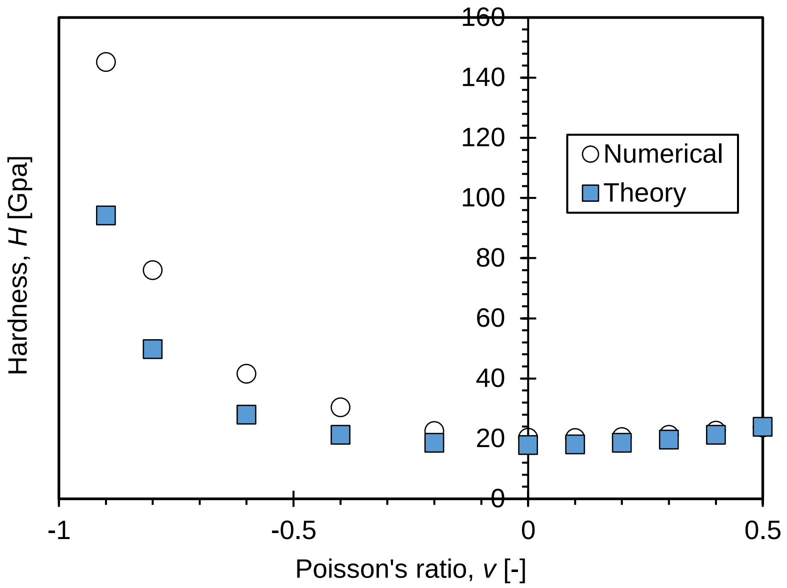

Figure 5-3: Normalized hardness for various Poisson's ratios on conical indentation.

Figure 5-4 assists the interpretation of the previously reported results by plotting the evolution of the three elastic constants (K, G,E_r) as a function of ν. The relations between K, G and ν are given by classical elasticity theory:

$$G = \frac{E}{2(1+\nu)}; \qquad K = \frac{E}{3(1-2\nu)} \tag{5.3}$$

The analytical solution (Equation (2.30)) suggests that the plane stress modulus, $E_r = E/(1-\nu^2)$, controls the indentation resistance of the material. It is evident that E_r experiences a minimum at $\nu = 0$ and increases for all other values. The increase is more significant in the negative Poisson's ratio domain especially for values of $\nu < -0.5$, below which E_r approaches the response of the shear modulus and together, thereafter, asymptotically increase to infinity as ν approaches -1. The transition to low ν values can therefore be interpreted as a shear-stiffening mechanism that also has implications on the indentation response. The limiting responses of the elastic constants are summarized below:

$$\nu \to 0.5\text{:}\ G \to \frac{E}{3}, K \to \infty, E_r \to \frac{4}{3}E \tag{5.4}$$

$$\nu \to -1\text{:}\ G \approx E_r \to \infty, K \to \frac{E}{9} \tag{5.5}$$

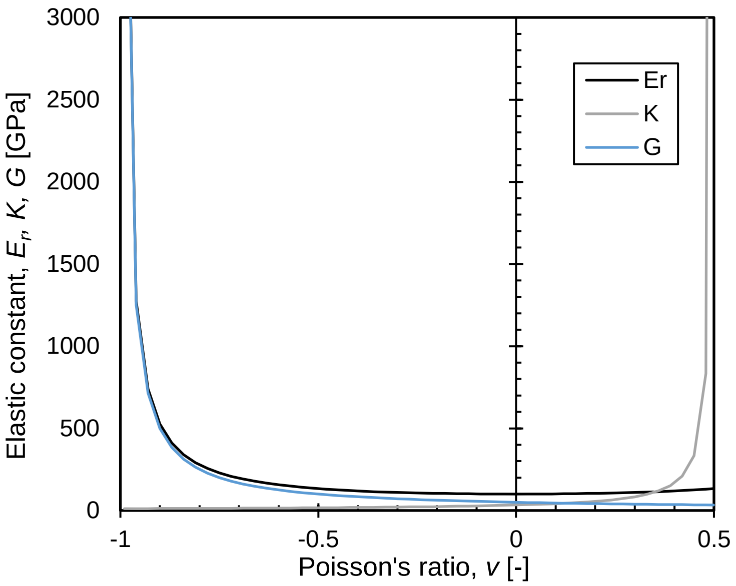

Figure 5-4: Evolution of elastic material constants as a function of the Poisson's ratio ($\boldsymbol{E}$ = 100 GPa).

Figure 5-5 shows the von Mises stress – which relates to the distortional energy of the material – profiles for the various Poisson's ratio materials. It appears that as ν reduces the resistance to penetration increases. This is manifested in (a) an increase in the absolute values of stresses generated within the indented material and (b) an increase in the normal stresses generated on the tip surface. These observations are consistent with the increase of maximum force required to penetrate lower Poisson's ratio materials to the same depth as observed in the simulated $P - h$ responses (see Figure 5-2).

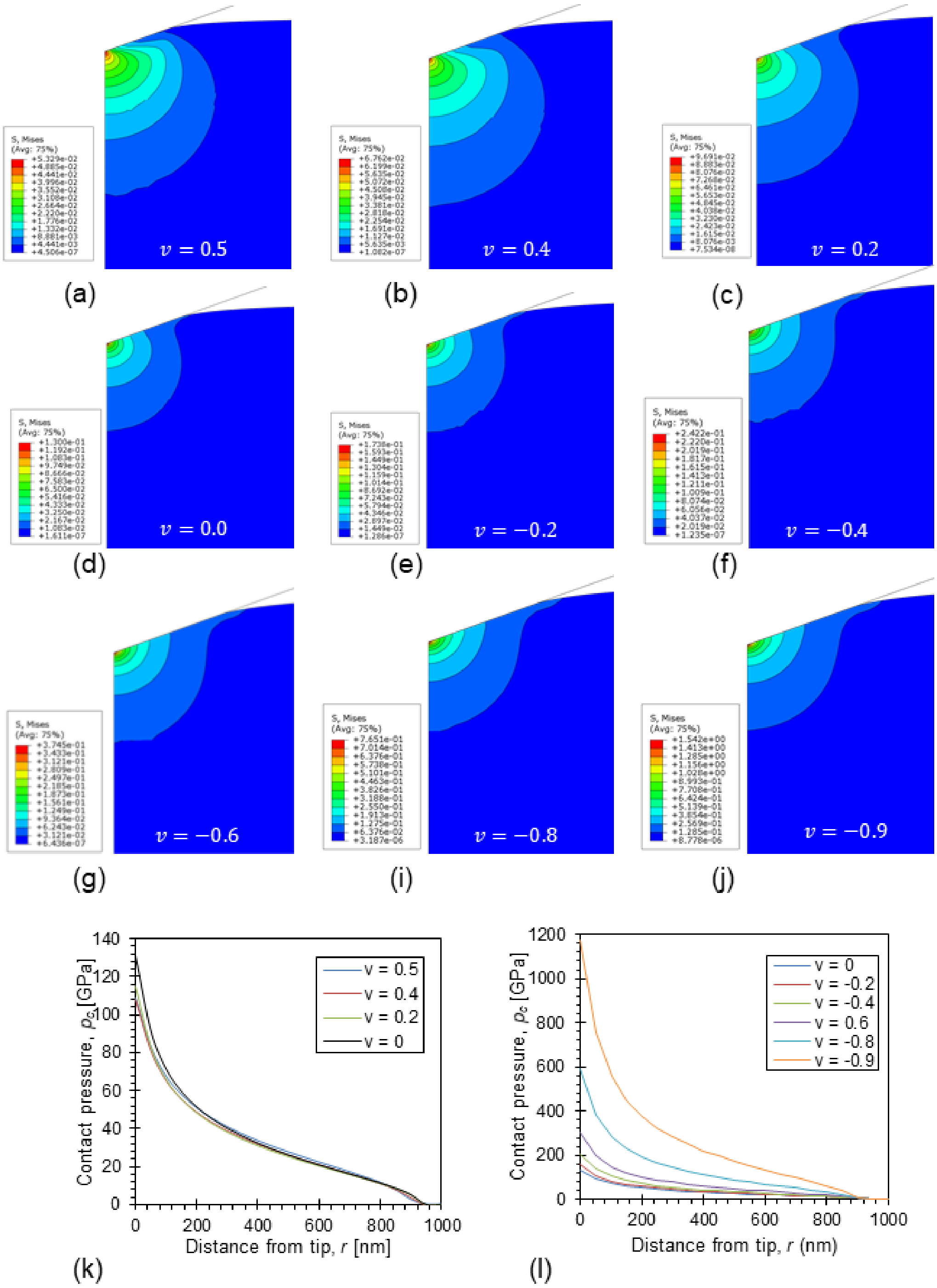

Figure 5-5: Von-Mises stress-profiles for the various Poisson's ratios (ν=0.5, 0.4, 0.2, 0, -0.2, -0.4, -0.6, -0.8, -0.9). The elastic modulus of the material is kept constant at ***E***=100 GPa.

Figure 5-6 indicates the numerically estimated contact depth normalized by the maximum indentation depth (here constant at $h = 500$ nm) for the various Poisson's ratio materials.

For positive Poisson's ratio materials $h_c/h_{\max}$ appears to be relatively constant and in close agreement with theoretical prediction $h_c/h_{\max} = 2/\pi = 0.64$ (to two decimal places). The response assumes identical values to the theoretical prediction as the material approaches an incompressible system (ν=0.5). In that particular case the physical problem converges to the assumed boundary conditions of the analytical solution. It is interesting to observe that as the Poisson's ratio moves into the negative regime (auxetic response) the normalized contact depth reduces, reaching a value of $h_c/h_{\max}$ =0.57 for ν =-0.9. This response which cannot be captured analytically due to the ill-posed boundary condition can probably be attributed to the tendency of the material to 'shrink' (reduce its volume) under the high compressive stresses generated by the tip, with a subsequent reduction in the contact area. This reduction of contact depth, and subsequently contact area, is in part responsible for the increased hardness observed in the negative Poisson's ratio regime.

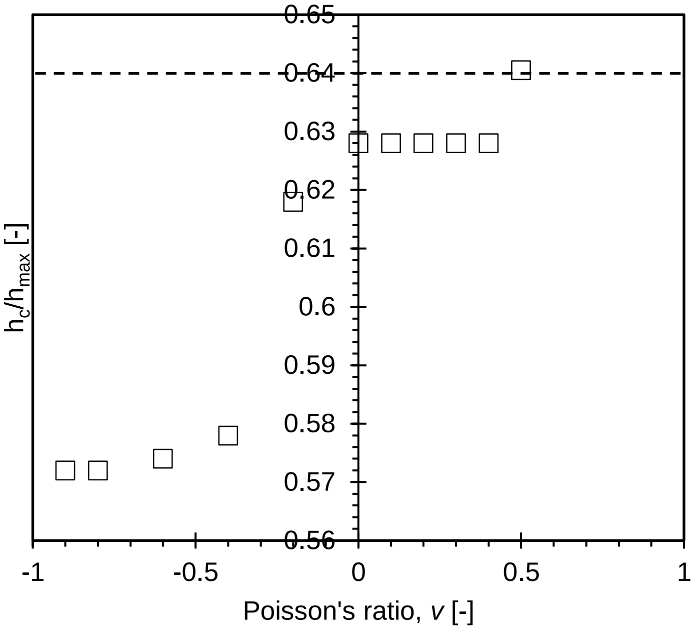

Figure 5-6: Normalized contact depth for various Poisson's ratios.

5.3.1 Correction Factor for the Analytical Solution

The simulated $P - h$ responses presented in Figure 5-2 can also be predicted by the analytical solution of Sneddon, Equation (2.27). Figure 5-7 contrasts the analytical and numerical results for the various Poisson's ratios. The discrepancy between the two increases as the Poisson's ratio decreases. This phenomenon has firstly been reported by Hay *et al* [44] in the positive Poisson's ratio regime and has been attributed to the ill-posed boundary conditions of the analytical problem formulation which results in a deformed material surface shape that penetrates into the indenter. In this section we compute the correction factor for the whole possible span of Poisson's ratios and we also investigate the effect of friction and indenter angles.

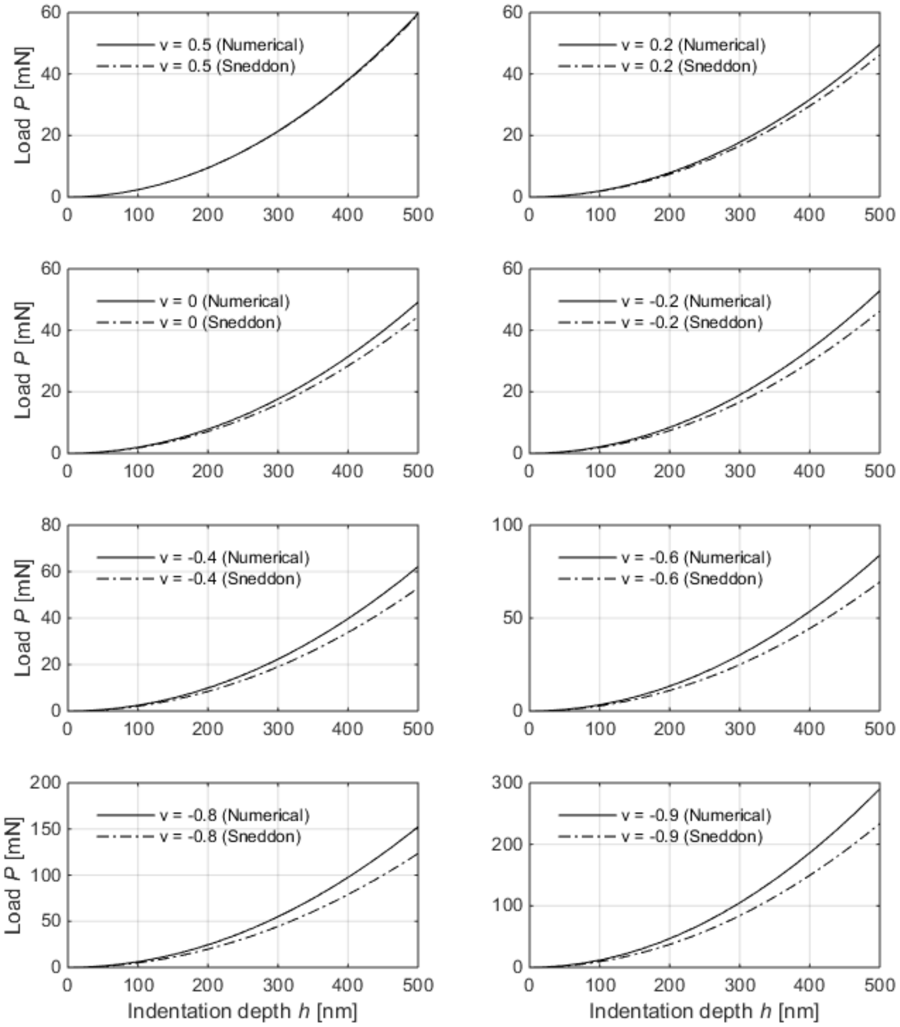

Figure 5-7: Analytical and computational force-depth (P-h) responses for materials with E=100 GPa and v in the range of 0.5 to -1.

It is interesting to note that the error observed in the load is constant throughout the depth of indentation suggesting that a multiplicative correction factor on Sneddon's equation will resolve the observed discrepancy. From a materials perspective it appears that the correction factor is independent of the elastic modulus of the material. We have checked the correction factor for three different elastic moduli, E=10 GPa, 100 GPa, 500 GPa, with nearly identical results. The most notable influence comes from the Poisson's ratio of the material (Figure 5-8). As ν reduces the discrepancy between the numerical results and the analytical solution increases, with higher deviations observed in the negative Poisson's ratio regime with values reaching up to 23% for the lowest possible ν that has been simulated in this study ($\nu = -0.9$). For positive ν the error is contained below 10% with the results between theory and simulations to converge when $\nu \rightarrow 0.5$ (incompressible media). The numerical results of Hay *et al* [44] and Poon *et al* [53] and the analytical formulation proposed by Hay *et al* are also presented in Figure 5-8 and compare favorably with our simulations, with the observed deviations being within 1% and could be potentially attributed to numerical details between the different studies.

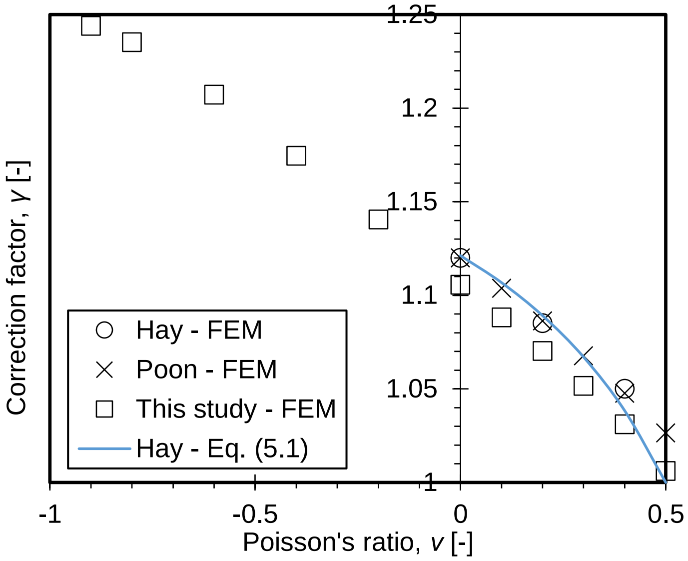

Figure 5-8: Correction factor for various Poisson's ratios.

5.3.2 Effect of Friction

The contact friction between the indenter and indented materials has been simulated at three different values: μ =0, 0.5, 1. Figure 10(a) suggests that the $P - h$ response remains mostly unaffected to the contact friction. A similar response is observed on the correction factor scaling function in which the presence of friction shifts the curve slightly upwards with the maximum observed deviation being in the order of 5% for the lowest simulated ν. The mathematical problem of adhesive contact by a flat punch has been treated by

Mossakovskii in 1954 (see references in [114]) who has later extended his solution to parabolic and spherical punches [115]. The geometry of cone, that pertains to our case, has been tackled by Spence [116]. More recently, building on the early mathematical developments of Mossakovksii, the results of adhesive (non-slip) indentation have been generalized to any probe that can be described by a monomial shape by Borodich and Keer, their results of which have been presented in a series of papers [17,114]. They concluded that the results on adhesive conical indentation on a semi-infinite half space are similar to the frictionless case but with a correction factor γ^{ad} that is introduced in the relation between the contact stiffness and the elastic modulus of the material (Equation (2.28)):

$$S = \frac{dP}{dh} = \gamma^{ad} \frac{2E}{1-\nu^2} \frac{\sqrt{A_c}}{\sqrt{\pi}} \tag{5.6}$$

where γ^{ad} is the correction factor for the case of adhesive (no-slip) contact of a rigid probe [114]:

$$\gamma^{ad} = \frac{(1-\nu)\ln(3-4\nu)}{1-2\nu} \tag{5.7}$$

Equation (5.7), which is included in Figure 5-9 compares well with the simulated results suggesting that the actual deformed geometry is much closer to the assumed boundary condition of the analytical solution resulting in significantly reduced discrepancies compared to the frictionless case.

In the case of spherical indentation the first studies of adhesive contact have been performed by Mossakovskii [115] and Spence [116]. Subsequentlty, a general result between adhesive contact of arbitrary curved axisymmetric convex indenters and elastic isotropic materials has been proposed by Borodich and Keer [114,117]:

$$\frac{\mathrm{d}h}{\mathrm{d}P} = \frac{1}{2\gamma^{ad} a E^*} \tag{5.8}$$

where γ^{ad} is the correction factor and for the case of no-slip contact for a rigid axisymmetric indenter results in Equation (5.7).

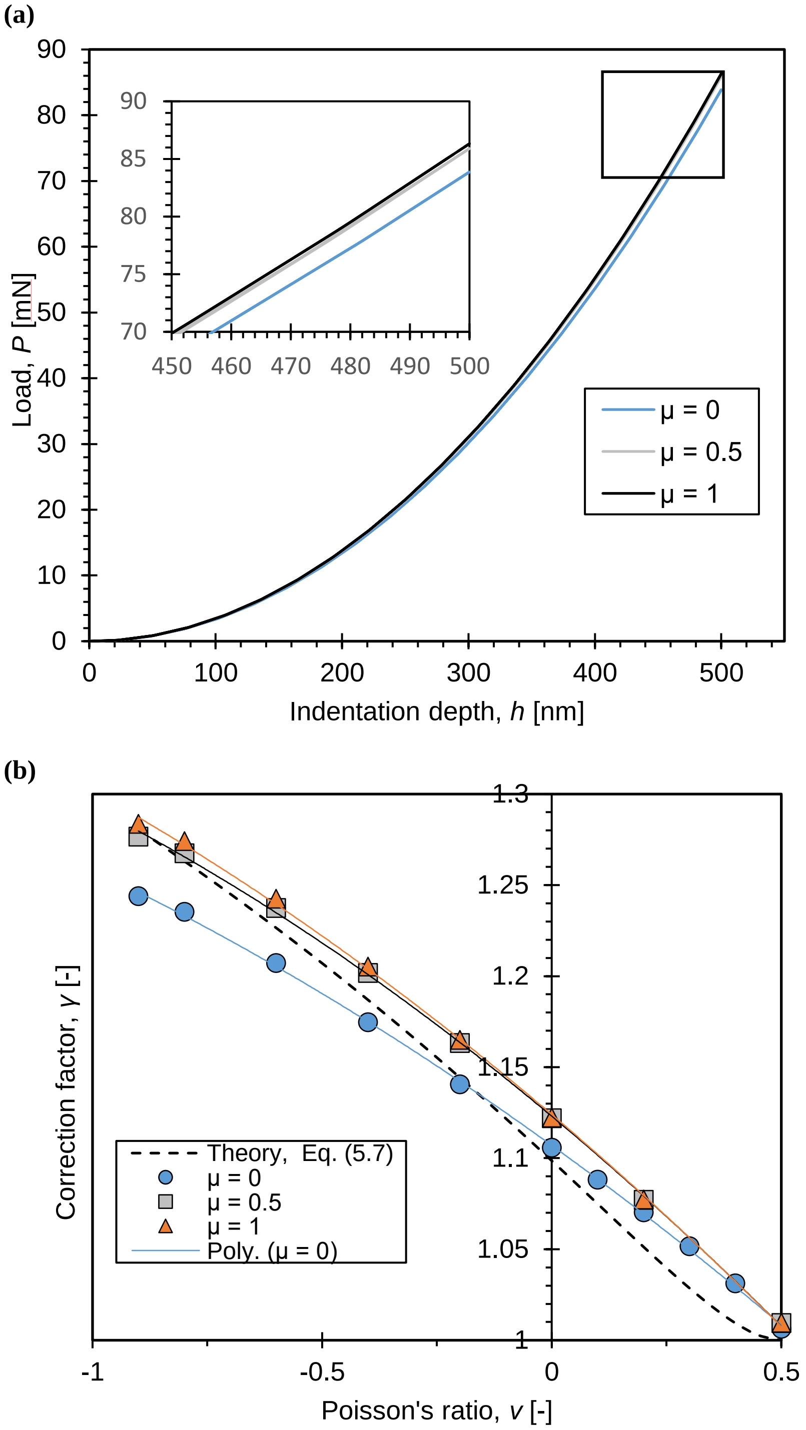

Figure 5-9: (a) P-h curves for three different coefficients of friction: $\boldsymbol{\mu}$ = 0, 0.5, 1. Inset represents a magnified region on the highest load/depth area. (b) The dependency of the correction factor on the Poisson's ratio is computed for three different coefficients of friction: $\boldsymbol{\mu}$ = 0, 0.5, 1. Solid lines represent polynomial fits.

5.3.3 Effect of indenter angle

Results on the correction factor for three different indenter geometries (θ=60°, 70.3°, 80°) are plotted in Figure 5-10(a). The results of Hay *et al* [44] for positive ν are also included for comparison. The data collected in this study is in excellent agreement with previously published results confirming the accuracy of the simulations. Furthermore, the data extends the correction factor into the negative regime in which the discrepancy becomes more severe. Overall, it appears that γ decreases with decreasing cone angle and/or increasing ν. All of the geometries converge to the theoretical solution for $\nu = 0.5$. The correction factor also vanishes as the cone angle approaches 90° consistent with the boundary condition of the analytical solution in which radial displacements are eliminated. The stress profiles for $\nu = -0.2$ and three different indenter geometries are shown in Figure 5-10(b) to 11(d). Since the load scales with the area of contact, blunt indenters, in which the area-to-depth scaling relation is more rapid, tend to offer more resistance to penetration. This however is accompanied with a load-spreading over a larger area and a subsequent smoothing/reduction of the stress distribution/intensity over the indenter-material contact region.

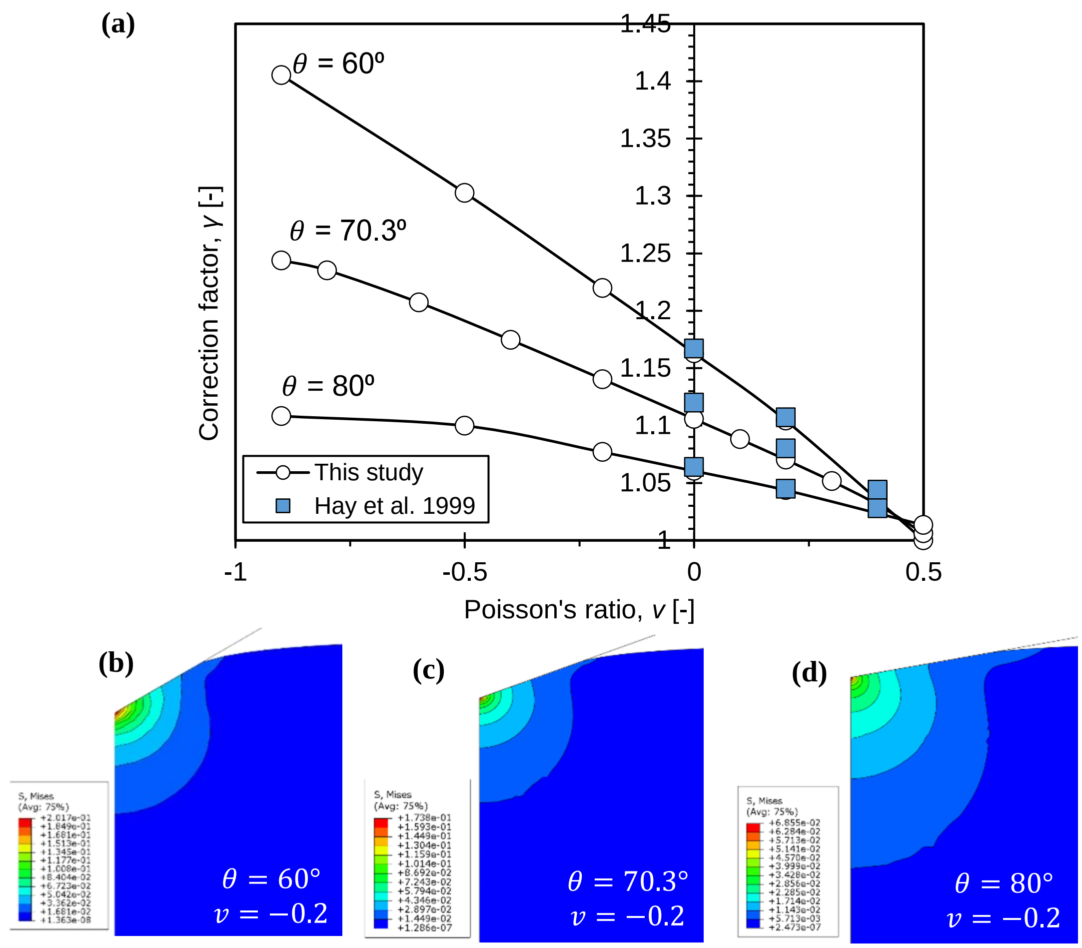

Figure 5-10: The dependency of the correction factor on the Poisson’s ratio is computed for three different cone half-apex angles: θ=60°, 70.3°, 80°. Solid lines represent polynomial fits.

5.3.4 Polynomial Correction Functions

The assumptions incorporated in the analytical solutions of a rigid axisymmetric probe being pushed against a semi-infinite linear elastic half-space become increasingly inaccurate for elastic indentations on auxetic materials ($\nu < 0$). The linear elastic solution for load (Equation (2.27)), contact stiffness (Equation (2.28)) and elastic hardness (Equation (2.31)) that form the basis for many experimental data analysis can be corrected to account for the effect of Poisson’s ratio, contact angle and contact friction. The polynomial correction functions $\gamma = f(\nu)$ calculated in this study and which can serve eliminate errors in experimental investigations are summarized in Table 5-1.

Table 5-1: Best fit polynomials for Poisson's ratio dependency of the correction factor γ.

Cone semi-apex angle, θ [º]	Friction Coefficient, μ [-]	Polynomial Fit
70.3	0	$\gamma=1.1070-0.1821\nu-0.0306\nu^2$; $R^2=0.9996$
70.3	0.5	$\gamma=1.1231-0.2106\nu-0.0406\nu^2$; $R^2=0.9995$
70.3	1	$\gamma=1.1240-0.2145\nu-0.0369\nu^2$; $R^2=0.9994$
80	0	$\gamma=1.0629-0.0842\nu-0.0357\nu^2$; $R^2=0.9960$
60	0	$\gamma=1.1633-0.3033\nu-0.0396\nu^2$; $R^2=0.9998$

5.4 Spherical Indentation Resistance

The previous sections of this chapter dealt with conical indentation. The remaining part of this chapter will be devoted to spherical indentation on elastic auxetic materials. Hay and Wolff [52] suggested a correction factor γ for the case of spherical indentation based on analytical and numerical results. Later on, Collin *et al.* [118] based on experimental data suggested a method for determining contact radius changes during loading for a/R < 0.25. In 2012, Collin [119] proposed a correction factor, based on numerical results for the estimation of contact radius during the unloading process.

Due to the breakdown of self-similarity (see Chapter 2.3.1) the indentation response with spherical indenters is rather more complex. In fact, for spherical indentation a correction factor γ depends on Poisson's ratio value and on the value of a/R. It must be noted that during loading of a spherical indenter, it's radius R increases faster than the penetration depth h. Dimensional analysis suggests that the loading portion of the curve will be a function of a/R in order to characterize constant imposed strain inside the material.

$$\frac{P}{Eh^2} = \Pi_{11}\left(\frac{a}{R}, v\right) \tag{5.9}$$

The load profile from Hertz's analysis, Equation (2.12) yields [52]:

$$P = \gamma\frac{4}{3}E^*\sqrt{R}h^{3/2} \tag{5.10}$$

$$\gamma = 1 + \frac{2}{3\pi}\left(\frac{1-2v}{1-v}\right)\frac{a}{R} \tag{5.11}$$

The accuracy of the above equation will be studied and evaluated for the indentation response of elastic auxetic materials.

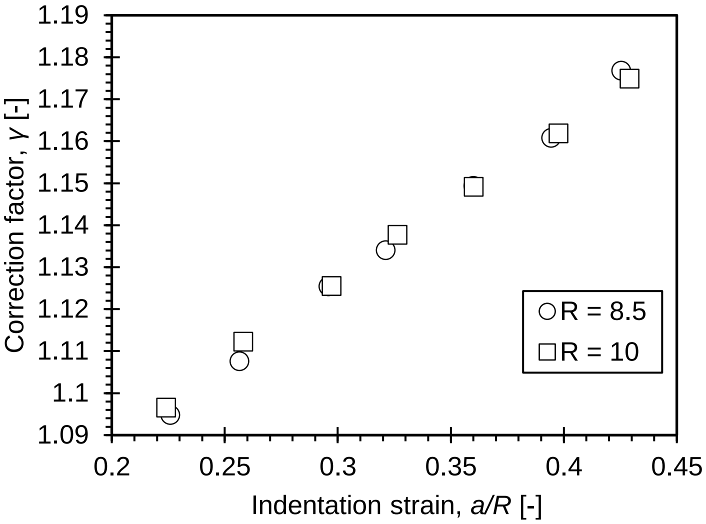

Figure 5-11: The zero effect of indenter size on correction factor.

The restriction on the boundary conditions of the vertical displacements on analytical solution, which allows the line of contact to be moved radially inwards, to “permeate” the indenter, is illustrated in Figure 5-12. For the case where a linear elastic material having a Poisson’s ratio of v = 0.5, numerical and analytical results are in excellent agreement, due that there is no influence of radial displacement (incompressibility). As the Poisson’s ratio decreases, the current limitation on the boundary conditions becomes significant and deviates from the real response of indented material.

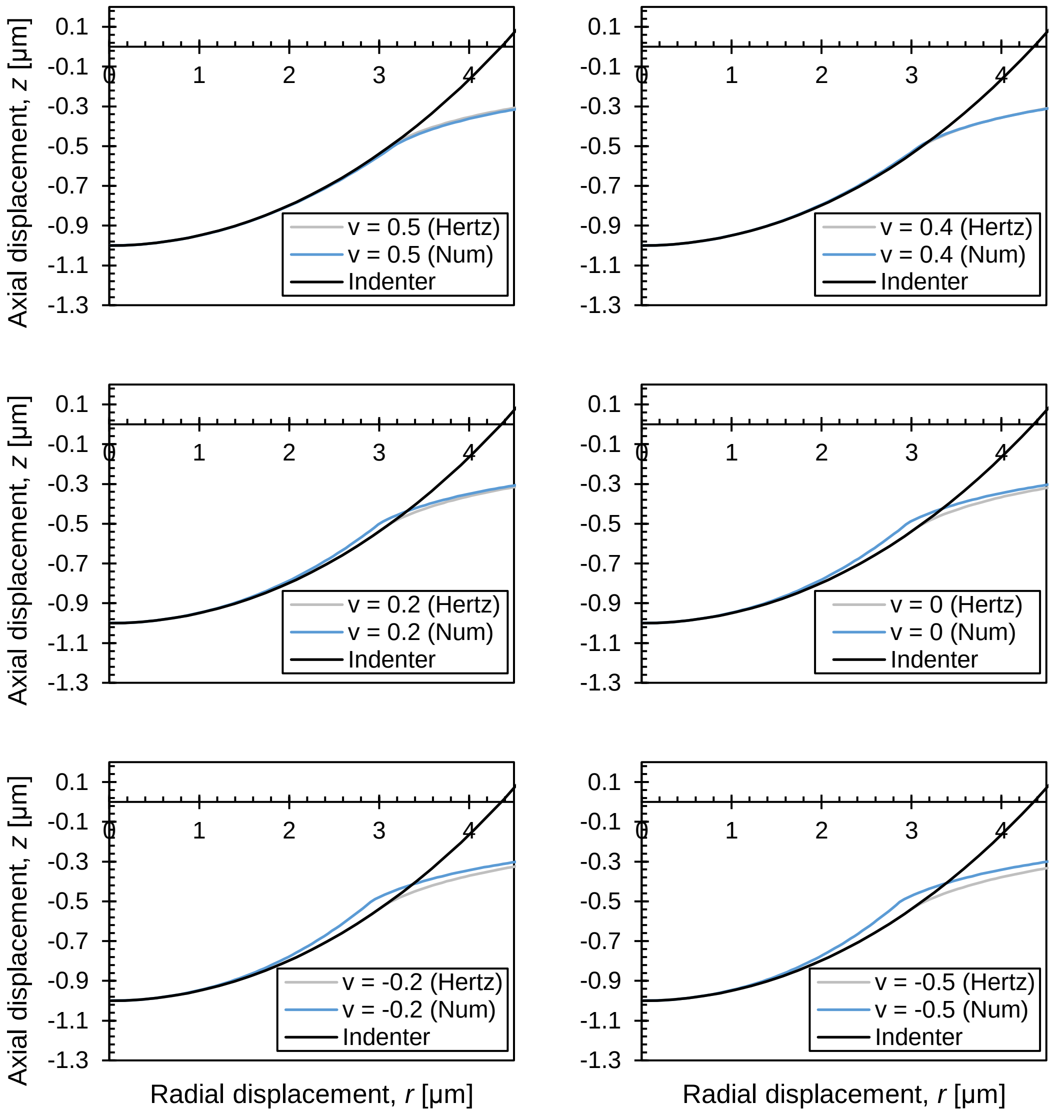

Figure 5-12: Effect of radial displacements on analytical solution for various Poisson's ratio values.

Numerical load (P) displacement (h) curves for conventional and auxetic materials are plotted in Figure 5-13. As evident, the materials tend to increase their indentation resistance, as their Poisson's ratio deviates from zero. The indentation resistance enhancement is more significant in the negative domain of Poisson's ratios, where a maximum of 6-fold increase is obtained for v = -0.9, which again underscores the unique mechanical behavior of auxetic materials. A similar response has been reported earlier for conical indenters and the origins of this enhancement has been traced to the shear stiffening mechanism that takes place for low v values and to the reduction of the contact area [120].

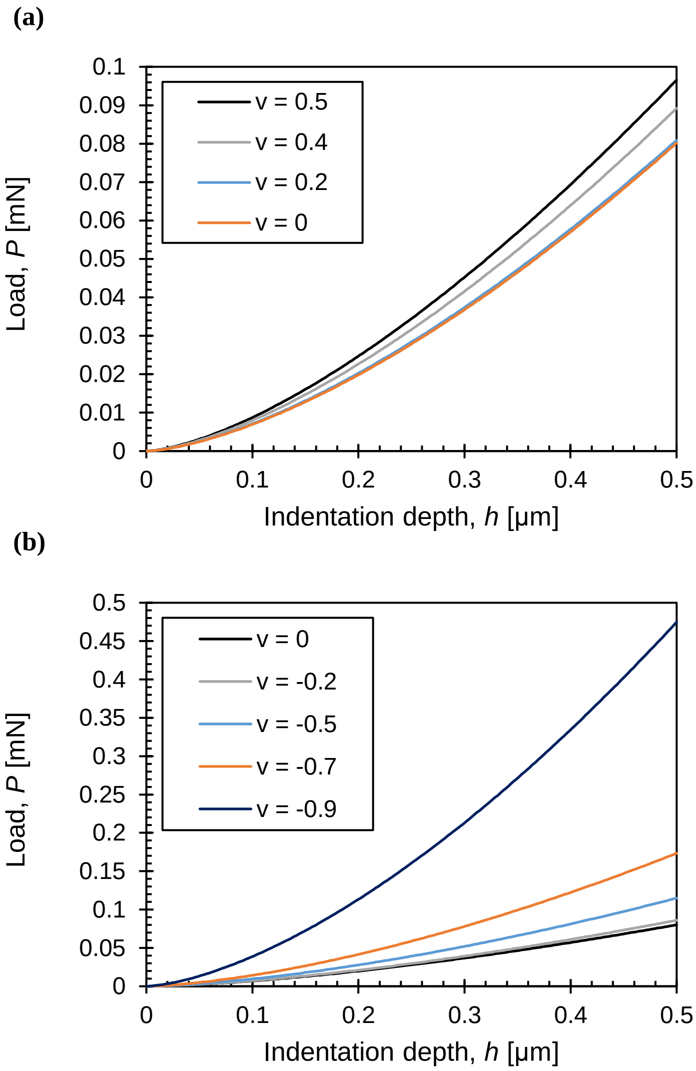

Figure 5-13: Computational force-depth (P-h) responses for materials with $\boldsymbol{E}$=250 MPa and $\boldsymbol{v}$ in the (a) positive (0 to 0.5) and (b) negative (-0.9 to 0) regime and for indenter's radius 1000 μm.

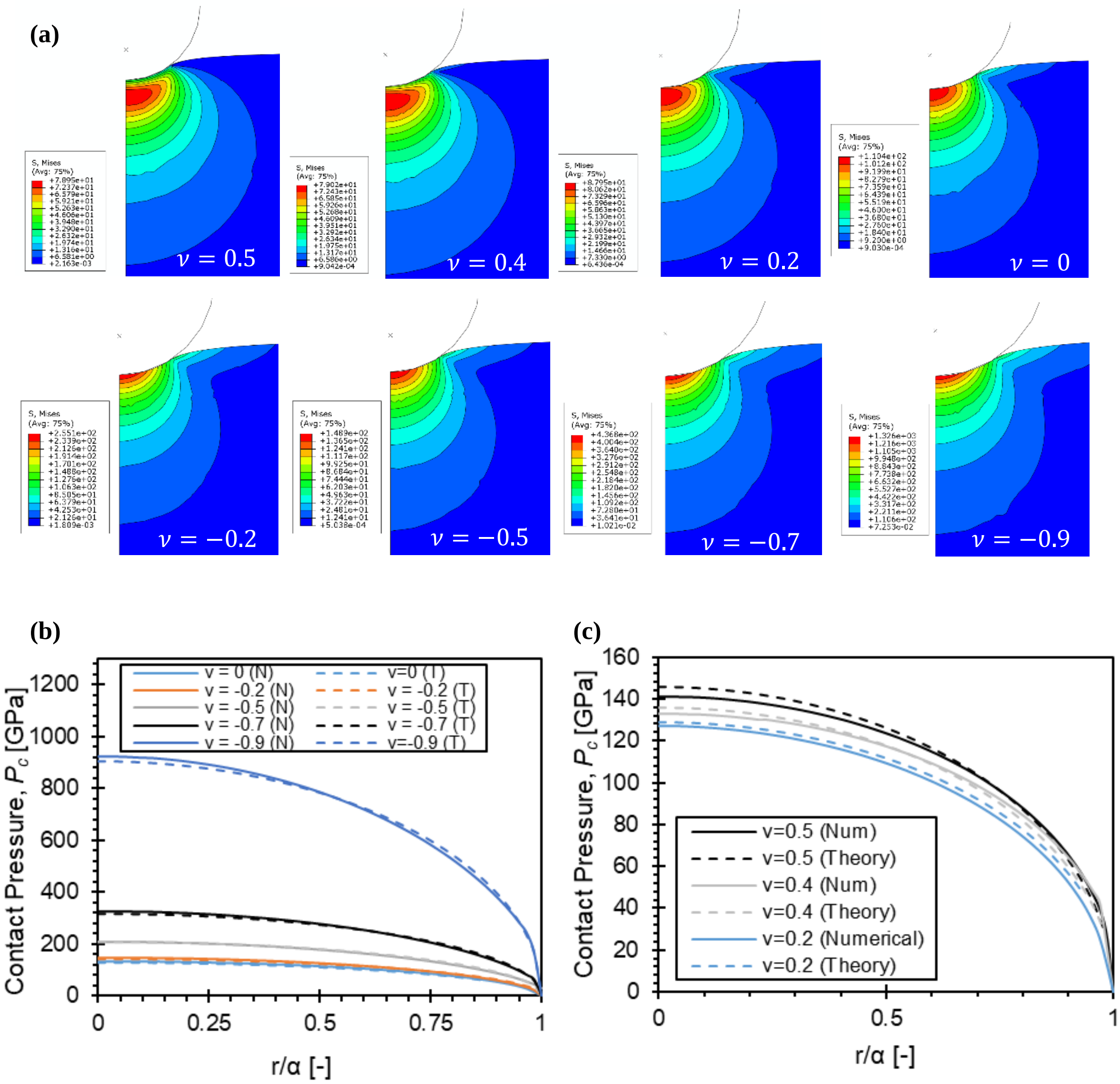

Figure 5-14: Von-Mises stress-profiles for the various Poisson's ratios ($\boldsymbol{\nu}$ = 0.5, 0.4, 0.2, 0, -0.2, -0.5, -0.7, -0.9). The elastic modulus of the material is kept constant at $\boldsymbol{E}$=250 MPa.

Figure 5-14 (a) shows the resulting von-Mises stresses that are generated within the material when the indenter is at maximum penetration depth, for the whole span of simulated Poisson's ratio materials. The stress values support the observation of an increased indentation resistance as the Poisson's ratio reduces. In addition, as the Poisson's ratio moves into its negative regime, the stresses tend to extent to the upper surface of the material, which is linked to the need of auxetics to reduce their lateral dimension – shrinking behavior, when they are subject to axial compressive stresses, subsequently activating a larger volume of the material. Figure 5-14 (b) and (c) present the corresponding computational and analytical normal stresses, which are generated in the indenter-material interface at maximum penetration depth. The computational results are in excellent agreement with the analytical solution suggesting that Equation (2.5) can be used with high accuracy in estimating the contact pressure distribution for the whole thermodynamically possible Poisson's ratio range.

As expected, any reduction of the contact area mirrors on the contact depth between the indenter and material, as shown in Figure 5-15(a), where the extracted deformation profiles of the above simulations at maximum indentation depth are plotted. It is evident that as the Poisson's ratio reduces the deviation from the analytical solution increases. Figure 5-15(b) quantifies this area reduction in terms of the effect of indentation strain on the ratio h_c/h_{max}, for all Poisson's ratio values tested herein. The analytical solution, Equation (2.16), suggests that h_c/h_{max} is constant and equals to 0.5. Nevertheless, this value is only verified for v = 0.5 and decreases as the Poisson's ratio reduces. The effect of large indentation strains coupled with the effect of shear stiffening at low v, "magnifies" the deviation from theoretical solution up to 20% for a/R=0.55 and v=-0.9.

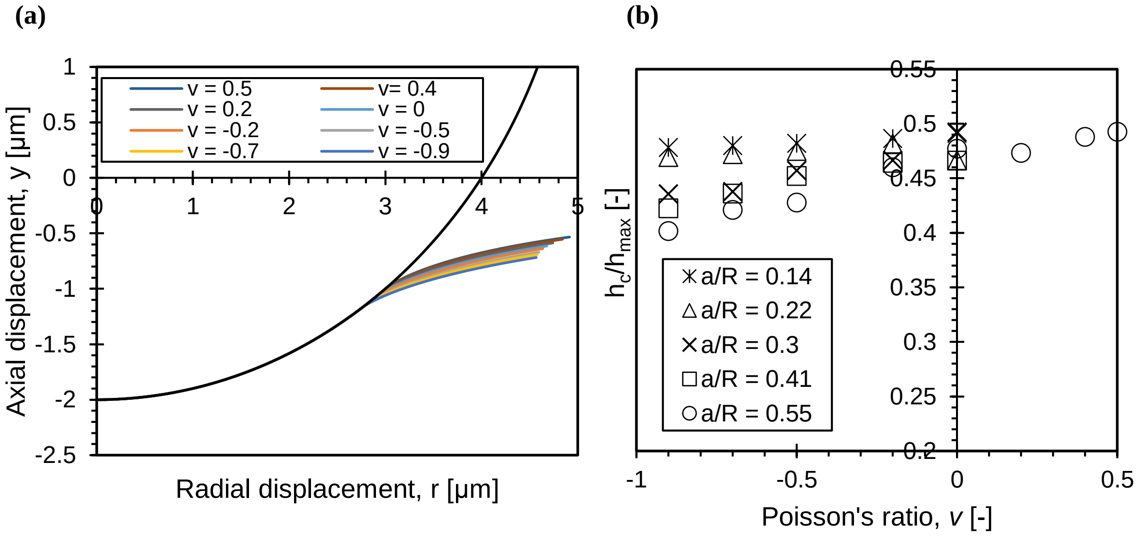

Figure 5-15: (a) Surface profiles at maximum depth of penetration and (B) normalized contact depth for various Poisson's ratios.

The combined actions of shear stiffening, contact area reduction and large indentation strains can be better demonstrated on the elastic hardness of auxetic materials. In nanoindentation technique, hardness is related with the mean pressure beneath the full load of indenter when it encounters the material:

$$H = \frac{P_{max}}{A_c} \tag{5.12}$$

In general, H describes the resistance to the indenter generated by the indented material and Equation (5.12) outlines that hardness is not exactly a pure property of a material, but a combined quantity of various mechanical properties (Equation (5.10)) and of geometrical properties, where the indenter's geometry plays a dominant role (subsequently A_c). If we substitute Equation (5.10) into Equation (5.12) results in:

$$H = \frac{P_{max}^{1/3}}{\pi}\left[\frac{3}{4}\left(\frac{1-v^2}{E}\right)R\right]^{-2/3} \tag{5.13}$$

Therefore, for constant indentation conditions; E, R, P_{max} or h_{max}, hardness is proportional to v in the form:

$$H \propto (1-v^2)^{-2/3} \tag{5.14}$$

The evolution of Equation (5.14) is illustrated in Figure 5-16, where normalized hardness at v = 0 is plotted for the investigated span of Poisson's ratio (-0.9 < v < 0.5). Hardness reaches a 3-fold enhancement at v = -0.9 and in general tends to increase as v moves into its negative regime. At this point, it must be noted that Equation (5.14) excludes any effect of the imposed indentation strain during the loading step of the indenter. Yoffe [121] showed that Hertz's Equation (5.10) is accurate for a/R < 0.1 and starts to deviates as $a/R \rightarrow 0.2$ and for $v \leq 0.3$. The numerical results of this study concern indentation strains in the order of ~0.15 < a/R < 0.55. Numerical data and theory exhibit similar evolution of their hardness which corresponds to the shear stiffening mechanism that governs in lower Poisson's ratio values. In addition, for constant Poisson's ratio values the numerical data show a discrepancy between different a/R values, reaching a maximum discrepancy of 23% for v = -0.9, where this phenomenon can be attributed to the increase of the imposed indentation strain inside the material. Furthermore, experimental results of Alderson *et al.* [95] which were performed with a spherical indenter are illustrated in Figure 5-16 and are in good agreement with our numerical curve of a/R = 0.55.

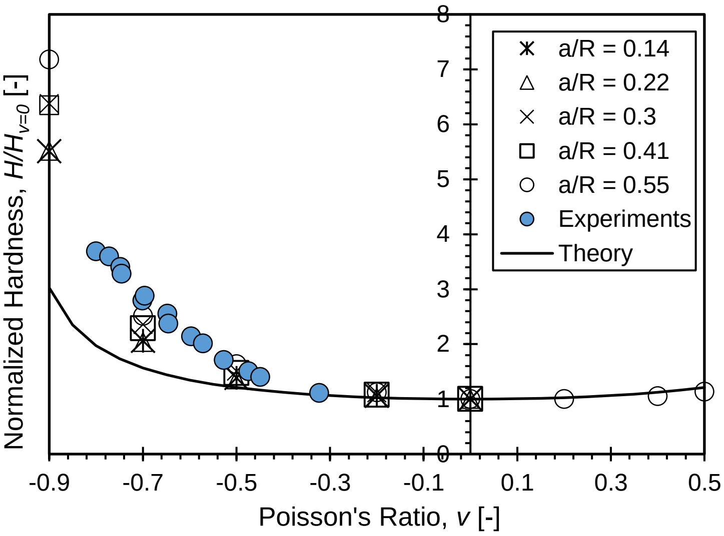

Figure 5-16: Normalized hardness at v = 0, for the whole span of Poisson's ratio.

5.5 Correction factor for the Analytical Solution

The analytical solution of Hertz, Equation **(2.12)**, has been evaluated on the numerical $P - h$ responses illustrated in Figure 5-17. Computational and analytical results are in excellent agreement when $v = 0.5$, incompressible material, where there is no any influence of radial displacement. As the Poisson's ratio reduces, the curves start to deviate, reaching an error of 36% for the lowest v of this study, which is related with the ill-posed boundary conditions of analytical solution.

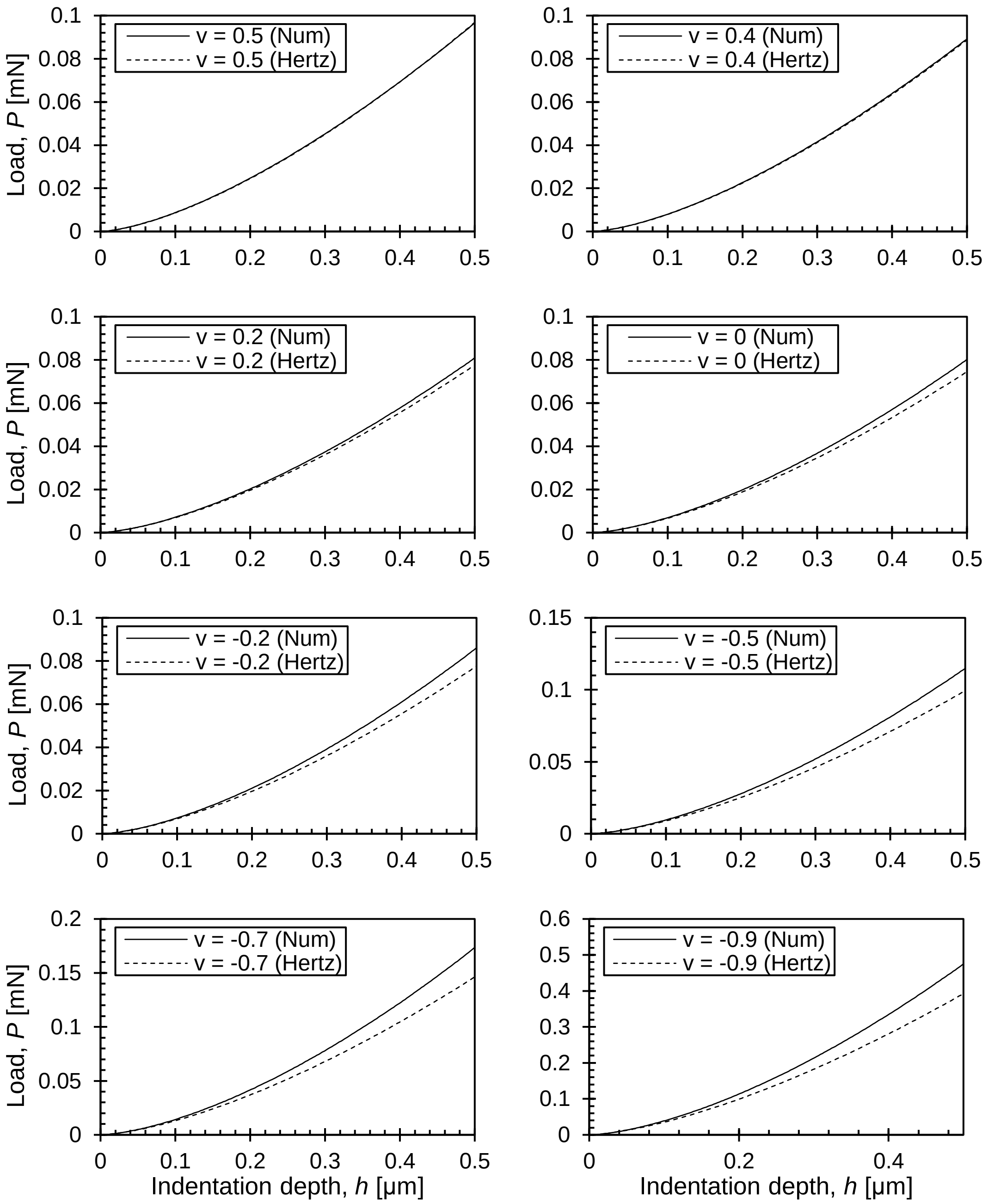

Figure 5-17: Evolution of numerical $\boldsymbol{P-h}$ responses in contrast with Hertz equation.

In spherical indentation, the error between analytical and numerical curve is not constant through the loading profile, as in the case of conical indentation. The computed values of γ indicate the coexistence of two independent parameters; Poisson's ratio and indentation strain (a/R). Figure 5-18 presents the computational correction factor of the current study with regards to the analytical expression of Equation (5.10). The two-data compare favorably with errors less than 6%. Moreover, it can be observed that while the Poisson's ratio decreases, the computational results increase more rapidly their slope, with respect to the analytical curves, which relates to the shear stiffening response of auxetic materials.

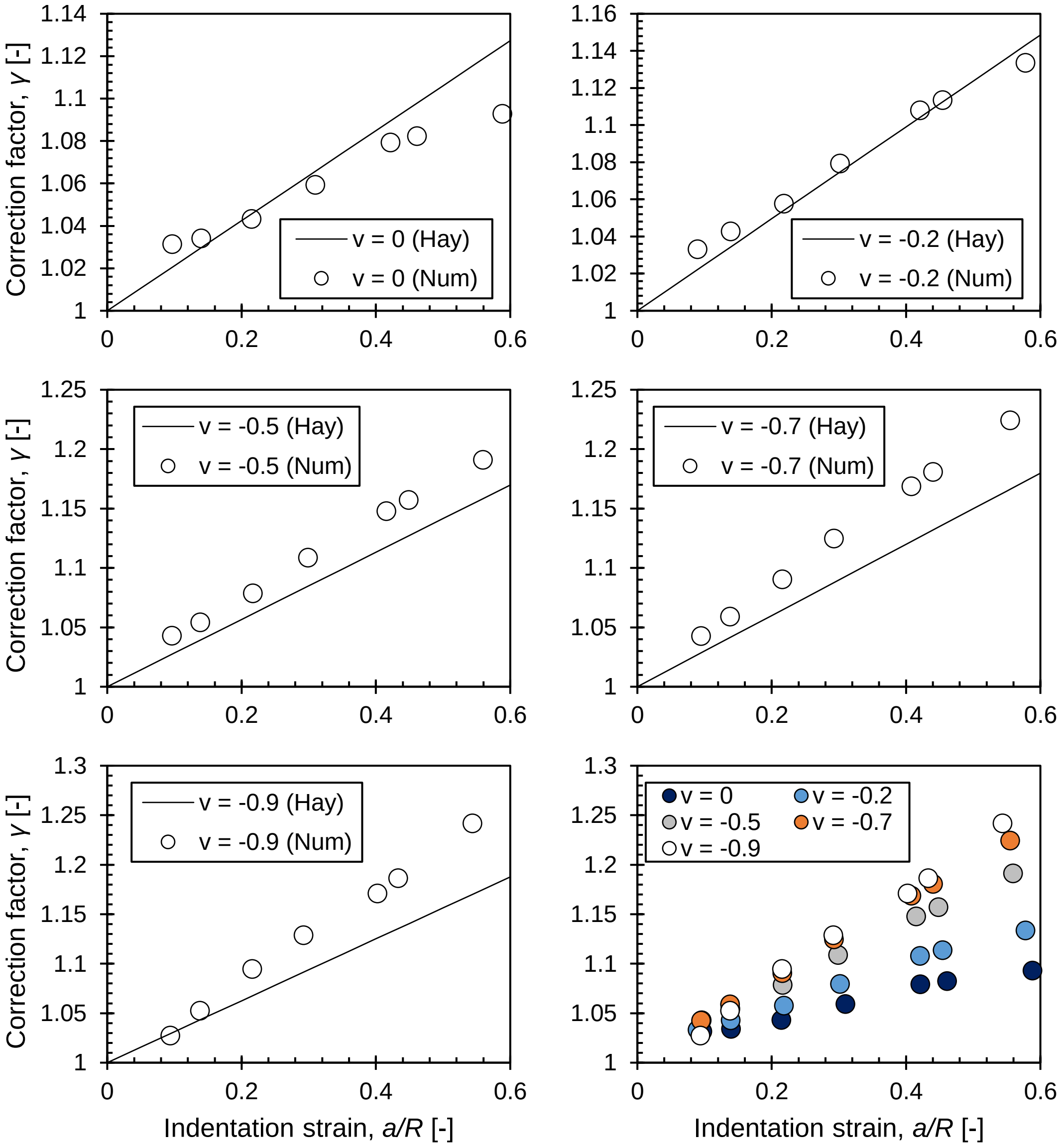

Figure 5-18: Correction factor γ for various Poisson's ratio as evolution of scaling factor a/R.

5.6 Effect of Friction

Conditions of fully adhesive contact between spherical indenter and auxetic materials have also been simulated (μ = 1) in our study. The presence of friction shifts the $P-h$ curve response of an auxetic material (E = 250 MPa, v = -0.5) compared to frictionless contact, upwards to a maximum of 5.7%. This small increase is arising from a further reduction of the contact area and from the increase of von-Mises stresses during the indentation, as observed in Figure 5-19.

Equation (5.8) is analogous to the Hertz-type contact, $\mu = 0$ (Equation (2.33)), and differs by a factor that depends entirely on Poisson's ratio. A no-slip contact means that there are no radial displacements during the loading, as analytical theory predicts, and analytical-numerical results starts to converge on a single curve for the case of conical indenters [122]. Although, in spherical indentation, the imposed indentation strain has been excluded from the analysis, therefore Equation (2.33) hold true only for low indentation strains, $a/R < 0.1$.

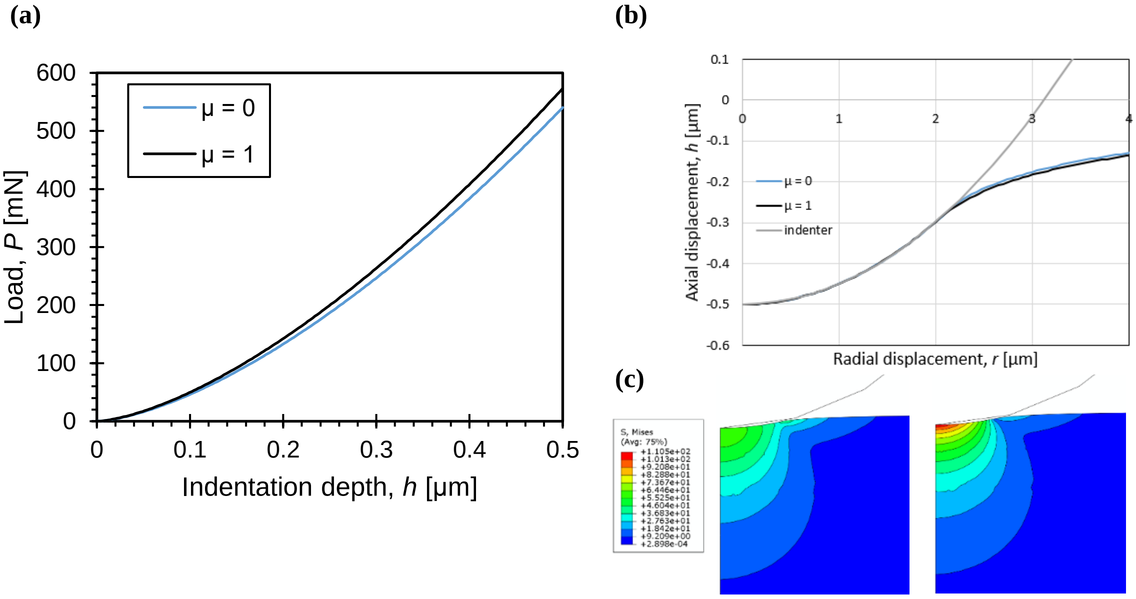

Figure 5-19: (a) $\boldsymbol{P - h}$ curve for two different coefficients of friction: $\boldsymbol{\mu}$ = 0, 1, with input parameters: $\boldsymbol{E} = 250$ **MPa**, $\boldsymbol{v} =$ -0.5 and $\boldsymbol{R} = 10$ **µm**, (b) surface profiles at maximum depth of penetration depth for frictionless and adhesive simulations and (c) corresponding von-Mises stresses.

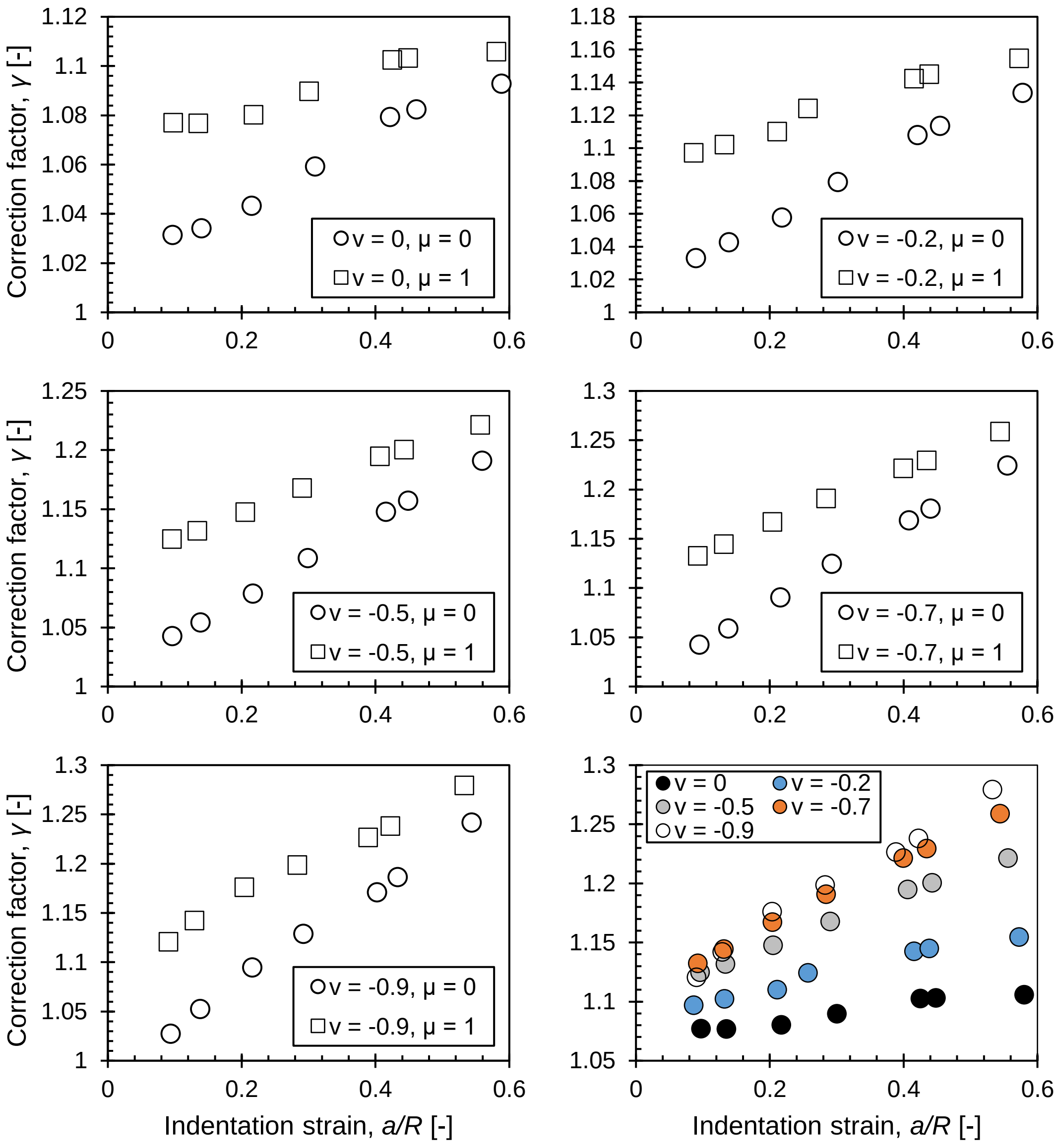

Figure 5-20: Correction factor γ of adhesive indentation for various Poisson's ratio as evolution of scaling factor a/R.

Comparable results have been extracted on the response of correction factor for adhesive contact, where an increase of 2-6% is observed, in comparison to frictionless contact. However, Figure 5-20 illustrates that friction is more significant for low a/R ratio and as a/R increases any friction effects start to become negligible, due to large strains that are generated throughout the indenter's penetration.

5.7 Concluding Remarks

Enhanced indentation resistance offered by auxetic systems can be traced to (a) the shear stiffening response which leads to increased required load for penetration and (b) the reduced area of contact that leads to higher stresses beneath the indenter tip. A literature search on available experimental indentation data on auxetic materials revealed a limited number of publications on the subject, all of which have used cylindrical or spherical indenters to probe the material. Strictly speaking, hardness is not a material property but rather a snapshot of material properties; it therefore depends on many factors among them the geometry of the tip. One should, therefore, not expect that the hardness of the material obtained with a spherical tip would correspond to the hardness of the material obtained with a conical tip. Nevertheless, theoretical solutions for both geometries exist that provide estimates of the amplification of elastic hardness as a function of the Poisson's ratio: $\frac{H}{H_{\nu=0}} = (1-\nu^2)^{-1}$ for cones and $\frac{H}{H_{\nu=0}} = (1-\nu^2)^{-2/3}$ for spheres.

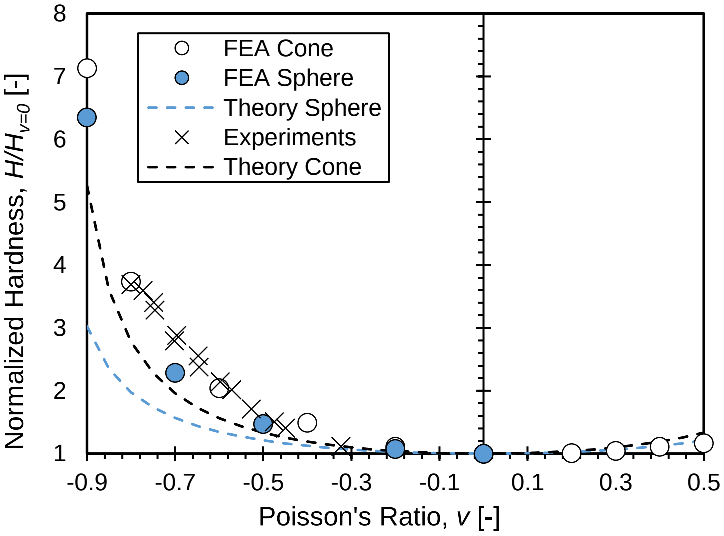

Figure 5-21: Theoretical, numerical and experimental results of normalized hardness for various Poisson's ratio materials.

The theoretical discrepancy between the hardness amplifications obtained by the two geometries is expected to increase as ν moves away from $\nu = 0$: for positive -0.5< ν <0.5 the maximum error is contained within ± 9% (due to symmetry), for ν = -0.6 it grows to 14% and for ν =-0.8 to 30%. Given the relatively small discrepancies (maximum of 14%) predicted within -0.6< ν <0.5 we decided to present the experimental data from spherical indentation and contrast them to the numerical results computed in this study, having in mind in parallel the limitations presented above. Alderson *et al* [95] performed spherical indentation data on auxetic polyethylene. The auxetic materials consisted of microporous ultra-high molecular weight polyethylene (UHMWPE) that have been fabricated through a three-stage thermal route [95]. Materials with Poisson's ratios down to -0.8 have been synthesized and tested under spherical (5mm diameter ball) indentation. Results with axial loads of 25, 50, 100 and 200 N have been presented. It was reported that high values of axial loads led to non-linear phenomena caused by large strains, plasticity and anisotropy. We here include the data collected with 25 N axial load which ensures the elastic response of the system. Experimental data, theoretical predictions and numerical simulations are plotted in Figure 5-21. It is interesting to note that the experimental data shows a hardness enhancement higher than the theoretical predictions of both conical and spherical indentation approaching the numerically simulated response. While this observation is encouraging regarding the validity of our results, additional experiments are required in order to confirm this scaling relation.

5.8 Chapter Summary

The linear elastic analytical solution of an axisymmetric probe indenting a semi-infinite half-space forms the backbone of most indentation data analysis protocols. It has been noted in the literature that the theoretical solution relies on a boundary condition that is ill-posed which leads to discrepancies from the actual response that depends, among other parameters, on the Poisson's ratio of the indented material. While correction factors have been proposed, prior studies have concentrated on the positive Poisson's ratio regime and have neglected an exciting and developing class of materials: the auxetic systems. The finite element method is used to simulate the conical and spherical indentation response of elastic materials with Poisson's ratios covering the whole thermodynamically possible range, $-1 \leq \nu \leq 0.5$. Consistent with theoretical predictions, the indentation resistance and hardness of auxetic materials is enhanced compared to their non-auxetic counterparts. The stress profiles and contact details are systematically analyzed and the increase in resistance is traced to the shear stiffening and the reduction of contact area compared to conventional materials. Furthermore, it is shown that the analytical linear elastic solution falls short in accurately describing the indentation response, especially for negative Poisson's ratio materials. In contrast to the theoretical prediction, the contact area reduces as the Poisson's ratio increases resulting in increased required force to penetrate the material and an enhanced pressure distribution beneath the indenter. The analytical solution is corrected for the whole ν range and best fit polynomials are proposed for ease-of-use (conical indentation). The effects of contact-friction, indenter cone-angle and plasticity are also studied and quantified.

In the specific case of spherical indentation, the imposed indentation strain a/R dominates the response of auxetic materials and yields to enhanced indentation resistance, in contrast to the response of conventional materials. Spherical indentation experiments depend entirely on the size of a/R, regardless of sphere's size or maximum penetration depth. In addition, for adhesive indentation contact, material's response remains mostly unaffected (up to 6%). Finally, the boundary conditions that used to derive the elastic characteristics of indentation contact, proved to be inaccurate, and therefore, for the precise analysis of indentation experiments on auxetic materials, ones have to apply corrections on Hertz's equation.

Chapter 6

Effect of Plasticity on Conical and Spherical Indentation

In Chapter 5 we focused on the elastic numerical indentation resistance of auxetic materials. We showed that elastic auxetic materials undergo shear stiffening mechanisms, especially for $v <$ -0.5. Also, during an indentation test, auxetics are being densified due to the generated compressive stresses which result to a contact area reduction. The combination of these two mechanisms, leads to an indentation enhancement by a factor of 1-6, which depend on indenter geometry and v. It is unclear however whether these benefits are retained when the material behaves elastoplastically. In this Chapter, the conical and spherical indentation response of elastic-perfectly plastic materials (of the von-Mises type) is computationally investigated. The effect of plastic work, contact friction and indenter shape on the overall response is quantified.

6.1 Finite Element Model

Two-dimensional axisymmetric finite element simulations are performed to investigate the elastic-plastic indentation response of cones and spheres on materials with various v and E/Y ratios, with emphasis being placed on auxeticity. Details of the model are given in Chapter 5.2. The indenter is modeled as a rigid cone with half-apex angle of θ = 60°, 70.3°, 80° and as a rigid sphere with radius of 250 μm.

It has been noted in the literature [95,113] from experimental results, that plasticity may influence the indentation resistance of auxetic materials and that hardness enhancement may become less significant but the mechanism and extent have not been investigated in detail. We here quantify the effect of plasticity through elasto-plastic finite element simulations. With reference to Figure 5-1 we have performed elastic-plastic simulations using both conical and spherical probes. Plasticity was modeled using the von Mises criterion, here expressed with respect to principal stresses:

$$\sigma_y = \sqrt{\frac{1}{2}[(\sigma_1 - \sigma_2)^2 + (\sigma_2 - \sigma_3)^2 + (\sigma_3 - \sigma_1)^2]} \tag{6.1}$$

Numerical details of the simulated materials are presented in Table 6-1. Dimensional analysis of an axisymmetric indenter with an elastic – perfectly plastic solid, requires in addition to the elastic case the consideration of the E/Y ratio which corresponds to an "elasticity/plasticity index". Dimensional analysis of von-Mises material suggests that the loading curves under conical and spherical indenter are correspondingly functions of:

$$P = Eh^2 \prod \left(\frac{E}{Y}, v, \theta\right) \tag{6.2}$$

$$P = Eh^2 \prod\nolimits_{sphere} \left(\frac{E}{Y}, \frac{a}{R}, v\right) \tag{6.3}$$

Table 6-1: Material properties used for the numerical simulations of conical and spherical (R = 250 μm) indentation.

θ [º]	E/Y [-]	E [GPa]	v [-]	Y [GPa]	h_{max} [μm]	μ [-]
70.3, 60, 80	0.25	100	0	400	0.5	0, 1
70.3, 60, 80	0.25	100	-0.2	400	0.5	0, 1
70.3, 60, 80	0.25	100	-0.5	400	0.5	0, 1
70.3, 60, 80	0.25	100	-0.7	400	0.5	0, 1
70.3, 60, 80	0.25	100	-0.9	400	0.5	0, 1
70.3, 60, 80	2.5	100	0	40	0.5	0, 1
70.3, 60, 80	2.5	100	-0.2	40	0.5	0, 1
70.3, 60, 80	2.5	100	-0.5	40	0.5	0, 1
70.3, 60, 80	2.5	100	-0.7	40	0.5	0, 1
70.3, 60, 80	2.5	100	-0.9	40	0.5	0, 1
70.3, 60, 80	25	100	0	4	0.5	0, 1
70.3, 60, 80	25	100	-0.2	4	0.5	0, 1
70.3, 60, 80	25	100	-0.5	4	0.5	0, 1
70.3, 60, 80	25	100	-0.7	4	0.5	0, 1
70.3, 60, 80	25	100	-0.9	4	0.5	0, 1
70.3, 60, 80	250	100	0	0.4	0.5	0, 1
70.3, 60, 80	250	100	-0.2	0.4	0.5	0, 1
70.3, 60, 80	250	100	-0.5	0.4	0.5	0, 1
70.3, 60, 80	250	100	-0.7	0.4	0.5	0, 1
70.3, 60, 80	250	100	-0.9	0.4	0.5	0, 1

6.2 Load – Displacement Curves of von-Mises Auxetic Materials

Figure 6-1 shows the evolution of numerical $P - h$ responses for a 70.3° conical indenter (Berkovich equivalent) and for materials with various v, E/Y ratios. For E/Y = 0.25 (see Figure 6-1 (a)), it is observed that the indentation resistance increases significantly as the Poisson's ratio decreases (v →-1) which is consistent with elastic results presented in Chapter 5 [122]. This mechanism is manifested in an increased contact stresses, hence material with v = -0.9 is demonstrating a significant resistance to penetration. As a result, the stresses beneath the probe exceed its yield point value, which leads to an elastoplastic response, in contrast with materials where $v >$ -0.9, exhibiting fully elastic responses. Figure 6-1 (b) presents numerical results of E/Y = 2.5, where the presence of elastoplastic zone is more pronounced in contrast with E/Y = 0.25. A similar response with respect to an increased indentation resistance is illustrated but not as enhanced as before. In fact, ss the E/Y ratio increases, numerical materials exhibit elastic-plastic behavior (Figure 6-1 (b) and (c)) where for E/Y = 25, the plastic region seems to dominate the responses. The shear stiffening mechanism begins to weaken, since the increase of indentation resistance as the v decreases is almost unaffected in contrast with E/Y = 0.25, 2.5. For E/Y = 250 all responses are characterized by fully plastic zones with minor differences in the indentation responses, among materials with different Poisson's ratios. In addition, the magnitude of indentation resistance decreases as v increases which leads to an inverse response Therefore, it seems that the shear stiffening mechanism is highly depended on the elastoplastic response of auxetic materials. To further quantify this observation the effect of plasticity is quantified in the following analysis.

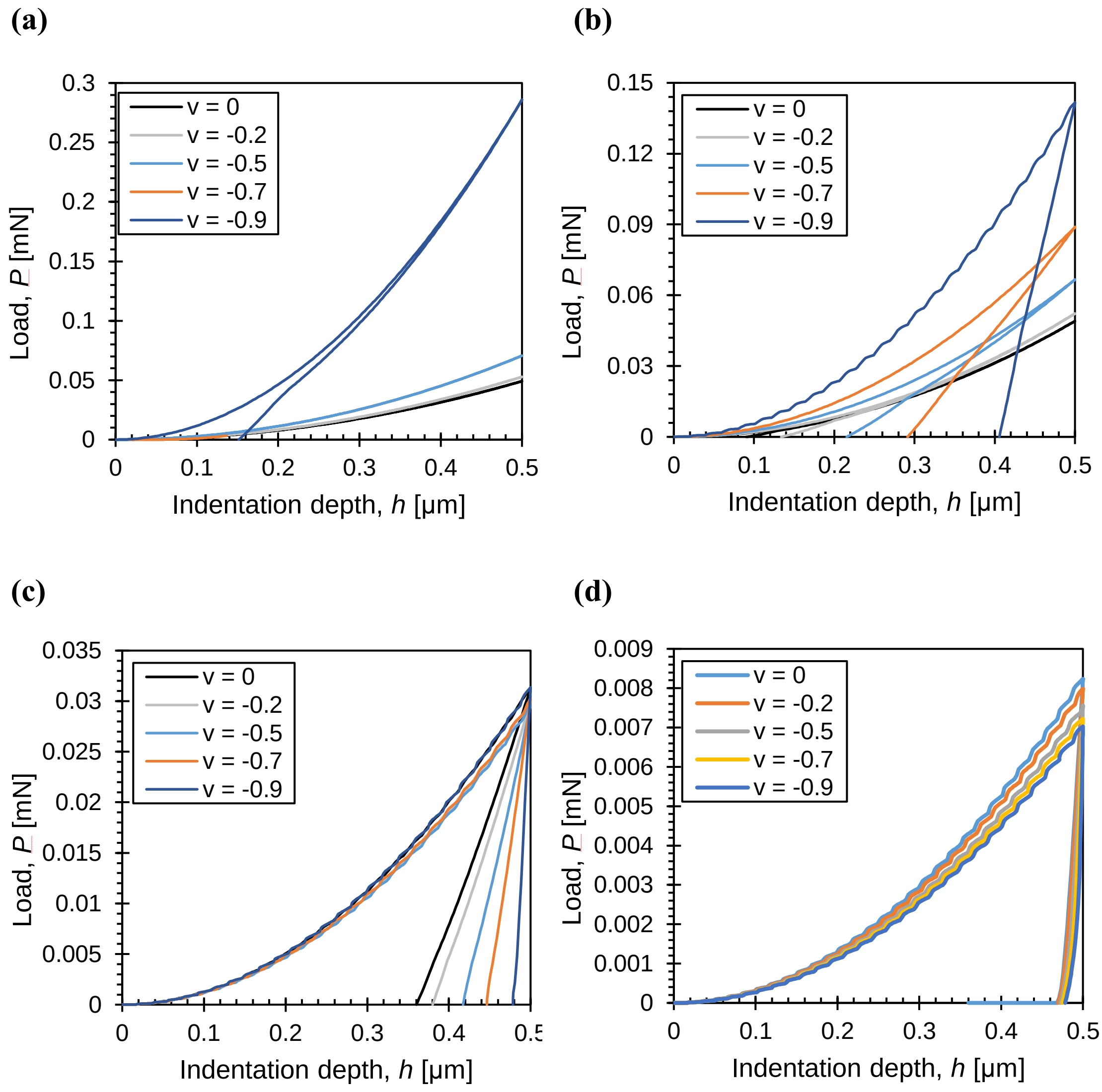

Figure 6-1: Resulting load-displacement curves obtained by elasto-plastic FE simulations with 70.3° cone indenter: (a) $\boldsymbol{E/Y}$=0.25, (b) $\boldsymbol{E/Y}$=2.5, (c) $\boldsymbol{E/Y}$=25, (d) $\boldsymbol{E/Y}$=250.

Figure 6-2 illustrates the evolution of plasticity index W_p/W_t with v. Materials of E/Y = 0.25 primarily show an elastic response, except for the case of v = -0.9 where the material undergoes minor elastoplasticity. Thereafter, as E/Y increases, the extend of the plastic zone inside the contact area increases significantly. Furthermore, for a fully plastic solid E/Y = 250, the relation of plasticity index for -0.9 $\leq v \leq$ 0 reaches a plateau, suggesting that irrespective of ν the material response is primarily plastic.

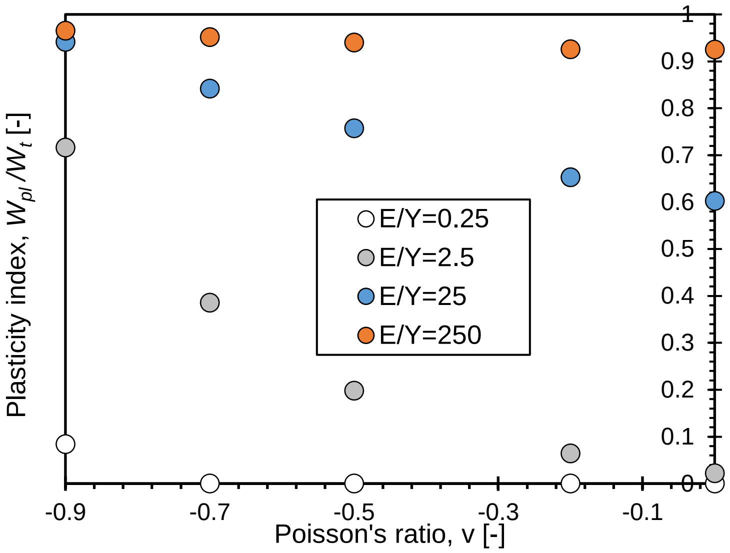

Figure 6-2: Plasticity index for various Poisson's ratio materials, under conical 70.3° indentation.

The findings of plasticity index can be evaluated in Figure 6-3, which captures the von-Mises stress (distortion energy) and equivalent plastic strain profiles for various v and E/Y solids at maximum indentation depth. For the case of E/Y = 2.5 the generated plastic strains grow under the indenter tip and progress through the whole area of contact as v decreases. The size of von-Mises stresses increase in magnitude and demonstrate profiles that tend to push the tip back when the Poisson's ratio approaches its lowest possible value, v → -1. These two observations support the shear stiffening mechanism and the tendency of an auxetic solid to densify which leads to a decrease of the contact area [122]. For the case of E/Y = 25 (see Figure 6-3 (b)) the plastic zone domain covers the whole surface of contact. The von-Mises stress profiles tend to spread in a larger area, eliminating the shear stiffening mechanism. For solids with E/Y = 250 the plastic strains cover (and extend beyond) the whole contact zone which support the results of numerical $P - h$ responses (Figure 6-1). Profiles of von-Mises stresses diverge from previous ones, which enhance the observation that the shear stiffening mechanism weakens with the existence of plastic deformation inside auxetic indented materials.

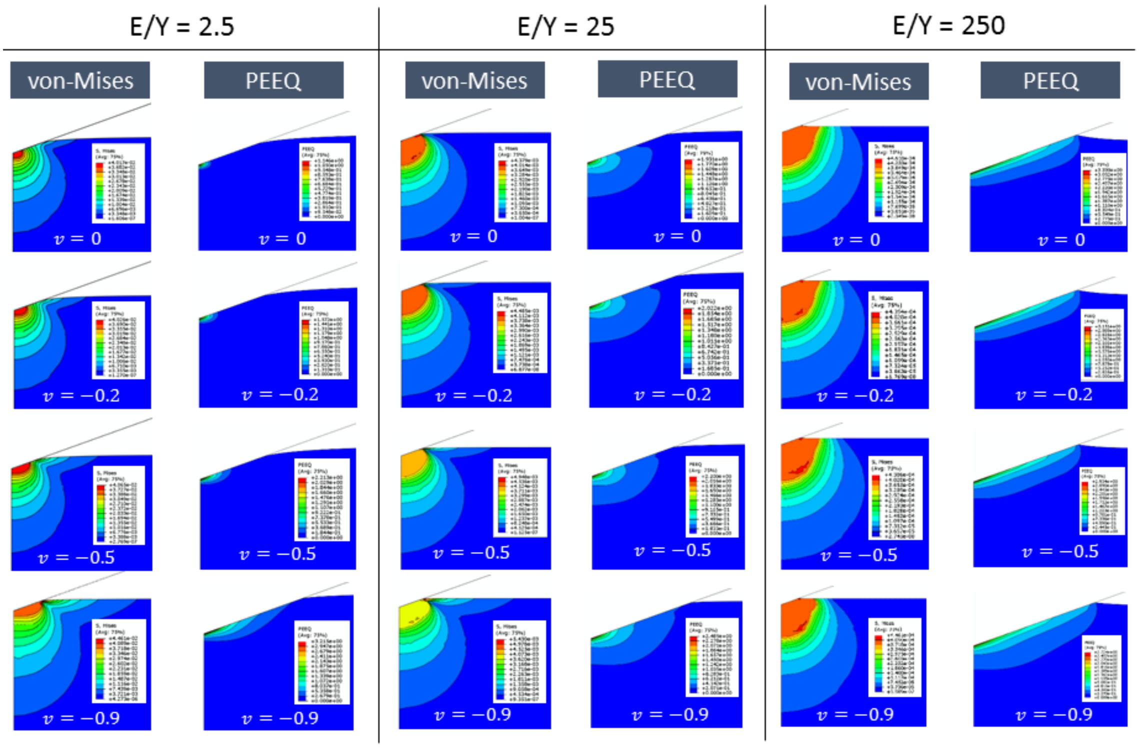

Figure 6-3: Evolution of resulting von-Mises stresses and equivalent plastic strains at maximum penetration depth of solids with (a) $\boldsymbol{E/Y}$ = 2.5, (b) $\boldsymbol{E/Y}$ = 25 and (c) $\boldsymbol{E/Y}$ = 250.

6.3 Effect of Indenter's shape

Normalized numerical $P - h$ curves for four different indenter geometries (cones with θ = 60˚, 70.3 ˚, 80˚ and sphere with R = 250 μm) on solids with E/Y = 2.5 and v = -0.7 are presented in Figure 6-4 (a). The data shown suggest that for spherical indentation the solid response is primarily elastic while for conical indentation the response is elastoplastic, with the degree of plasticity to increase as the cone angle decreases. This transition is quantified through the plasticity index which is presented in Figure 6-4 (b); it is evident that large plastic strains are attributed to low v and low θ values.

(a) **(b)**

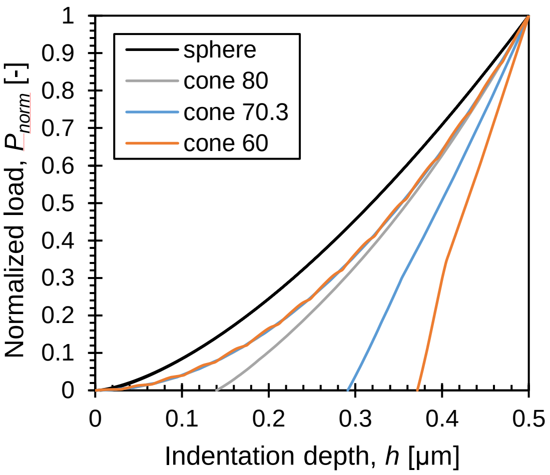

Figure 6-4: (a) Effect of indenter's shape on normalized $\boldsymbol{P-h}$ curves for materials with constant $\boldsymbol{E/Y}$=2.5 and $\boldsymbol{v}$=-0.7, (b) resulting indentation work.

Similar responses are obtained for the cases of E/Y = 25 and 250 which are summarized in Figure 6-5. Analogously for all E/Y, the plasticity index deviates similarly with v but the extend of deviation is much more pronounced for low E/Y ratios. Therefore, the shear stiffening mechanism is eliminated as plasticity kicks-in and dominates the contact response.

(a) **(b)**

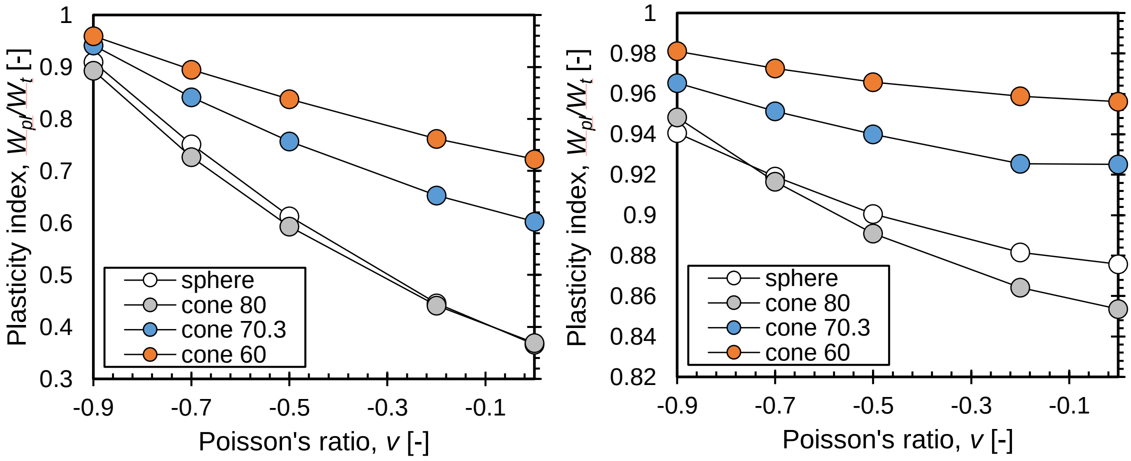

Figure 6-5: Plasticity index over Poisson's ratio of solids with (a) $\boldsymbol{E/Y}$=25 and (b) $\boldsymbol{E/Y}$=250.

Many authors tried to relate energy-based parameters to the hardness of materials [123–125]. Cheng and Cheng based on a scaling approach proposed a relationship between the ratio of elastic work to total work and the ratio of hardness to elastic modulus [56]. Jha *et al*., used the finite element method to relate the energy constants with indenter's geometry and indentation response of materials [126]. Lawn and Howes [127] correlated the elastic recoveries of several ceramic material as a function of indentation based energies as:

$$\frac{W_p}{W_t} = 1 - \left[\frac{1 - 3\left(\frac{h_p}{h_{max}}\right)^2 + 2\left(\frac{h_p}{h_{max}}\right)^3}{1 - \left(\frac{h_p}{h_{max}}\right)^2}\right] \tag{6.4}$$

Results on the plasticity index for three different indenter geometries (θ = 60°, 70.3°, 80°) are presented in Figure 6-6. The equation of Lawn and Howes (Equation (6.4)) is also included for comparison. The data collected in this study is in excellent agreement with the analytical equation confirming the accuracy of the simulations and the universality of the relationship of the plasticity index with h_f/h_{max} which appears to be independent of indenter angle and mechanical properties [62].

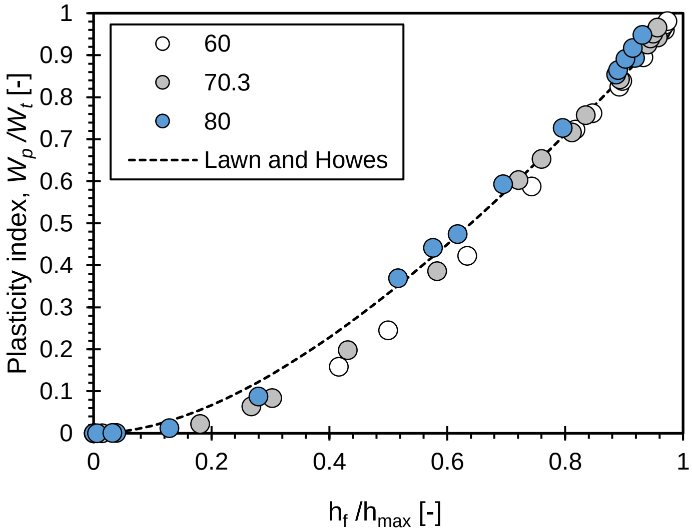

Figure 6-6: Plasticity index as function of $\boldsymbol{h_f/h_{max}}$.

6.4 Adhesive Elastoplastic Contact

The contact friction between indenters (both cones and sphere) and indented auxetic materials has been simulated at two different friction coefficient values: μ = 0, 1. Figure 6-7 suggests that the plasticity index response remains mostly unaffected to the contact friction. The presence of friction shifts the curves lightly upwards with the maximum observed deviation being on the order of 8% for a solid with E/Y = 2.5, v = -0.5 under conical indentation (θ = 60), in plasticity index values (0.35) which it can be considered satisfactory.

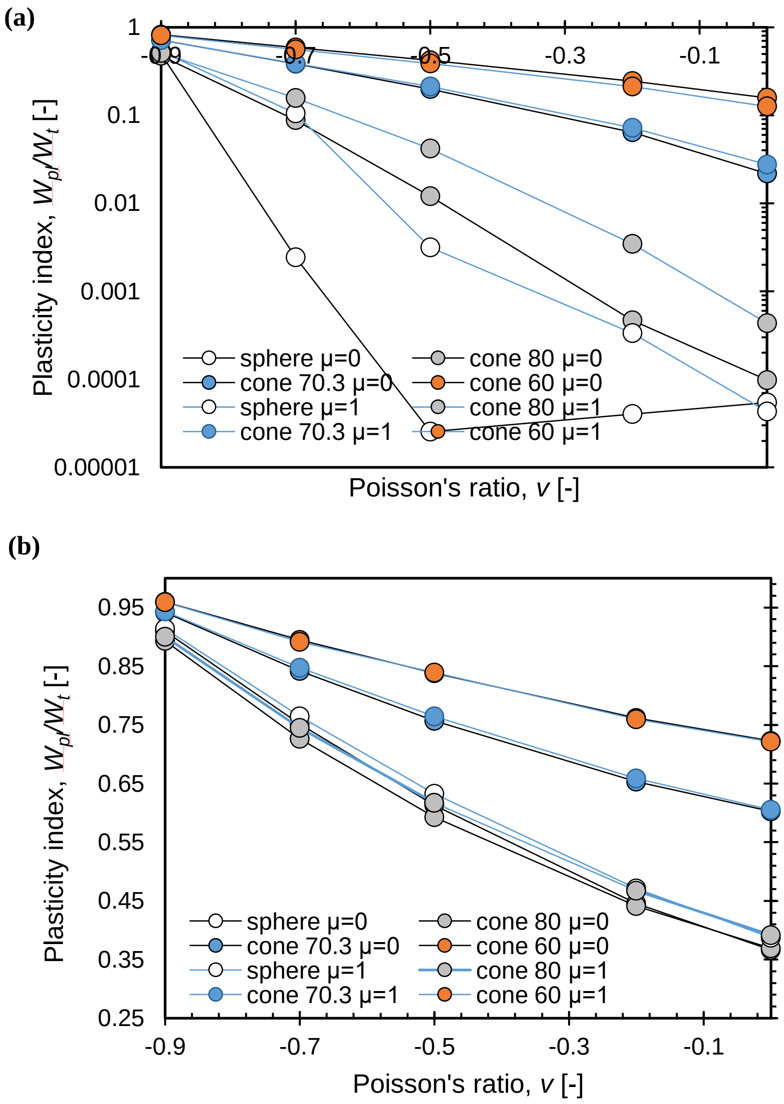

Figure 6-7: Effect of frictionless and adhesive contact for solids of various $\boldsymbol{v}$ and (a) $\boldsymbol{E/Y}$=2.5 and (b) $\boldsymbol{E/Y}$=25.

6.5 Indentation Hardness of von-Mises Auxetic Materials

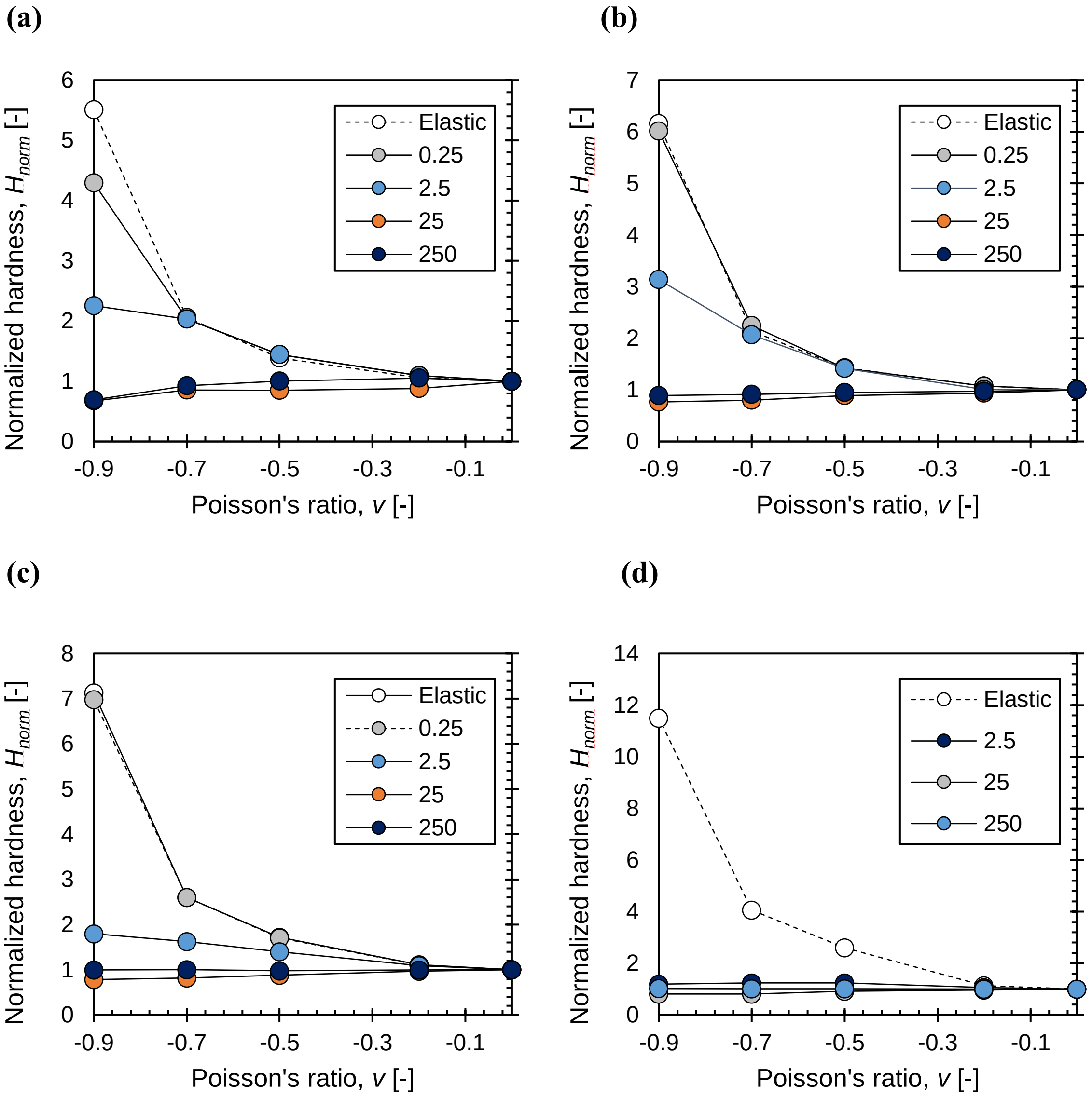

Figure 6-8: Normalized indentation hardness evolution as function of $\boldsymbol{v}$, for (a) sphere, (b) 80° cone, (c) 70.3° cone and (d) 60° cone indentation test.

Indentation resistance is related with the indentation hardness of materials. In Chapter 5, we have presented the enhancement in indentation hardness responses for elastic auxetic materials which led to amplification factors of 5.5 to 7. As shown in Figure 6-8, hardness enhancement is directly dependent to Poisson's ratio value and indenter's shape. For spherical indentation (constant indentation strain: a/R = 0.14), the hardness value increases by a factor of 5.5, while for conical indentation (θ = 60) hardness reaches a 12-

fold increase for v = -0.9 materials, as compared to the equivalent v = 0 material. On the other hand, for the case of elastoplastic auxetic materials, it is obvious that any existence of plastic deformation starts to weaken this advanced characteristics and for high plasticity indices values, materials even begin to soften. Hence, any enhancement on hardness, depends entirely on ensuring the elastic response of the auxetic material/structure. The detrimental effects of plasticity on this particular property of auxetic materials are also apparent in the case of spherical indentation, suggesting that the effect is independent of probe geometrical characteristics.

Figure 6-9 shows contour plots of the plastic strains resulting in conical indentation for three materials with different E/Y-ratio. One can observe that as the E/Y-ratio increases, plastic strains inside the material increase too and extend parallel to the probe surface subsequently leading to pile-up phenomena, which is another evidence of high percentage of plasticity within the material.

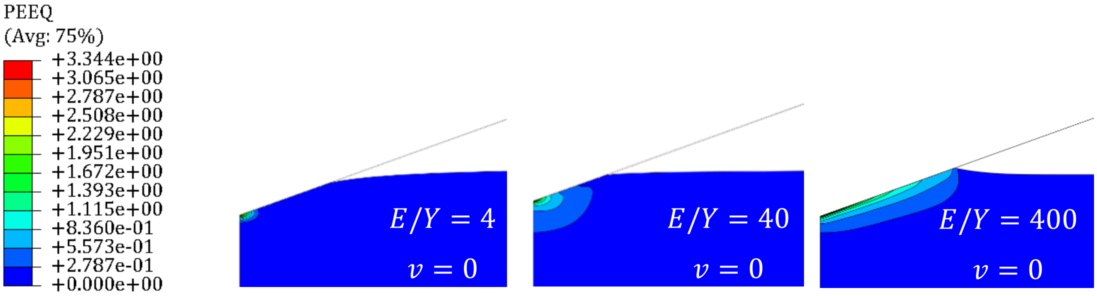

Figure 6-9: Plastic strains-profiles for various $\boldsymbol{E/Y}$ ratios (4, 40, 400). The Poisson's ratio of the material is kept constant at $\boldsymbol{v}$ = 0.

6.6 Chapter Summary

The effect of elastoplasticity on the indentation response of auxetic systems has been investigated and quantified. The indentation hardness enhancements reported in Chapter 5 for elastic auxetic materials are suppressed as plasticity of the indented material initiates. As the E/Y ratio increases the material tends to behave more plastically, the extend of plastic deformations become more pronounced and the indentation hardness enhancements are suppressed. An energy approach has been implemented in order to capture the ratio of plasticity index based on various Poisson's ratios, indenter geometries and adhesive/frictionless conditions. It is shown that as the material goes into full plasticity the auxetic material can even demonstrate a softening response, regardless of the Poisson’s ratio value. The dominant factor in the whole response appears to be the percentage of plastic work. Therefore, for applications where the mechanical auxetic materials are used as protective systems from indentation penetrations one needs to ensure that the material behaves primarily elastic in order to harness its full potential. This can be achieved in several ways, one of which is sandwiching the auxetic structure between two additional protective layers, as the panel geometry simulated in Chapter 4.

Part IV

HARD MATERIAL SYSTEMS

Chapter 7

Critical Review on Coating Systems

Over the past years, technological and industrial advances have led to the creation of more sophisticated synthesis techniques among them technologies for controlled and reproducible thin film deposition. Owning to their geometrical characteristics, in which the thickness of the film is usually much smaller than the other planar dimensions, thin film properties often differ when compared with their bulk counterparts; the investigation of their mechanical properties, therefore, becomes imperative. Thin films, nowadays, find applications in various sectors, ranging from magnetic information storage systems to coatings on biomedical implants [128,129]. With the rapid growth of thin film technology, a pressing need was created for quantitatively probing their mechanical properties. The study of the mechanical properties of thin films is of utmost importance, as possible underestimation of the mechanics, could lead to premature failures with all subsequent consequences. Nanoindentation is the most widely used method to determine the mechanical properties of materials at the submicron regimes. Recent advances allow load and deformation monitoring with nanoscale accuracy and precision. Using advanced models, the experimental data can be analyzed and converted to mechanical metrics like hardness, elastic modulus, creep modulus, energy dissipation and more [3,17,21,130]. The evaluation of the mechanical properties of coatings, however, is challenging owing to the complex interactions that take place between the film, substrate and their interface.

This chapter is devoted to the critical evaluation of the most prominent models for investigating the elastic modulus of thin films that could be found in the literature. After a screening of the existing literature models, the ones that are based on solid theory and reasoning are tested under variable conditions such as the mismatch ratio of the elastic moduli of the film to substrate (soft films on hard substrates and hard films on soft substrates), the film thickness, and the Poisson's ratio of the film and substrate.

7.1 Response of Coated Systems

Coating systems can be divided in four main categories: soft films on hard substrates (i.e. biomedical and electrical applications), hard on soft (protective and tribological applications), soft on soft (polymer coatings) and hard on hard (optical anti-reflection coatings). The proper characterization of these complex systems requires a thorough understanding of the corresponding properties of the coating-substrate, and the details of their interface.

Trends of experimental $P - h$ curves on coated systems reflect the cumulative mechanical response of the coating and the substrate. This relation varies and is also dependent on the interface between the two materials. Particularly in the case of hard coatings on soft substrates, there is a possibility that the substrate deforms plastically before the coating does. In such a scenario, the thin film will bent downwards due to the plastic deformation of the substrate, which will eventually result into compressive stresses in the film, potentially causing vertical cracks in the film. Also, if the substrate is characterized by a great level of work hardening, then the formation of the cracks will be stronger due to the interaction of two hard materials (Figure 7-1 (a)).

Turning to the case of soft coatings on hard substrates, there is a probability that the coating will deform plastically. Being "locked" between a very hard indenter and a hard substrate, it will tend to extrude from the edge, leading to pile-up phenomena and potentially to the delamination of the coating from the substrate (Figure 7-1 (b)).

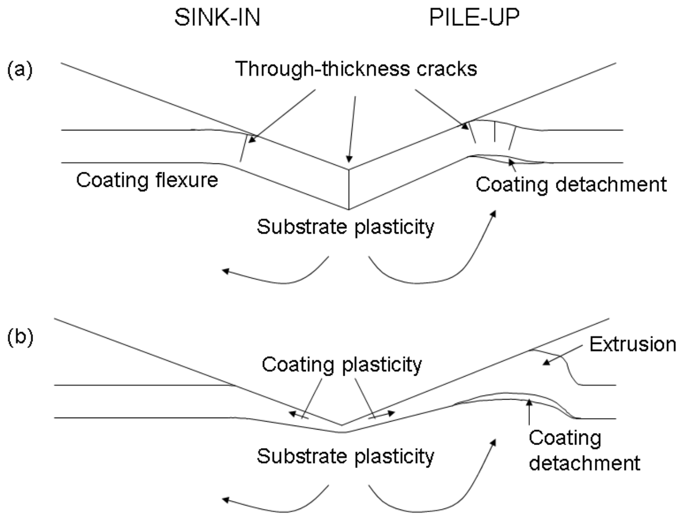

Figure 7-1: Physical mechanicsms in nanoindentation technique, corresponding on (a) hard on soft systems, and (b) soft on hard system [131].

We recall that the most widely used model for the evaluation of indentation data is the Oliver and Pharr approach [2]. A basic requirement in applying this method is that the sample is homogeneous and semi-infinite, meaning that the sample dimensions are much larger than the indentation depth. In the case of thin films the indentation depths could be comparable to the film thickness and subsequently there could be strong interactions at the interface between the coating and the substrate; thus the previous assumption of homogeneity is no longer valid.

To remedy this problem and measure "film-only" properties, Buckle [132] has empirically suggested restricting the depth of indentation to a small percentage of film's thickness such as to avoid any substrate interaction. In fact, it has been experimentally shown that for very low indentations, compared with the thickness of the film – less than 10%, the indenter doesn't 'feel' the substrate, thus accessing film-only properties. It was soon understood that this "rule of thumb" has no physical basis, especially for materials with high elastic modulus mismatch ratio; it was further appreciated that this model could potentially lead to erroneous results. Furthermore, there are cases where the deposited film is very thin, and therefore challenging for current experimental resolutions to achieve depths of penetration less than 10% of the film's thickness.

When the indenter penetrates into the coating's surface, the elastic regime extends into the substrate, especially if the coating is very thin. In the case of hard coatings on soft substrates, since substrate can yield in penetration depths, smaller than coating's thickness, it is obvious that using the 10% rule can result in significant errors. An indentation example is shown in Figure 7-2, where the indenter penetrates a hard and stiff coating (H = 25 GPa, E = 500 GPa, v = 0.35) that covers a softer substrate (H = 5 GPa, E = 100 GPa, v = 0.25). It is observed that the plastic strains are extended in the substrate even when the indentation depth is only a limited fraction of the film thickness and plasticity within the film is contained and has not traversed the whole of the film. A similar behavior is obtained even when the elastic modulus mismatch ratio is very small ($E_f/E_s > 0.3$).

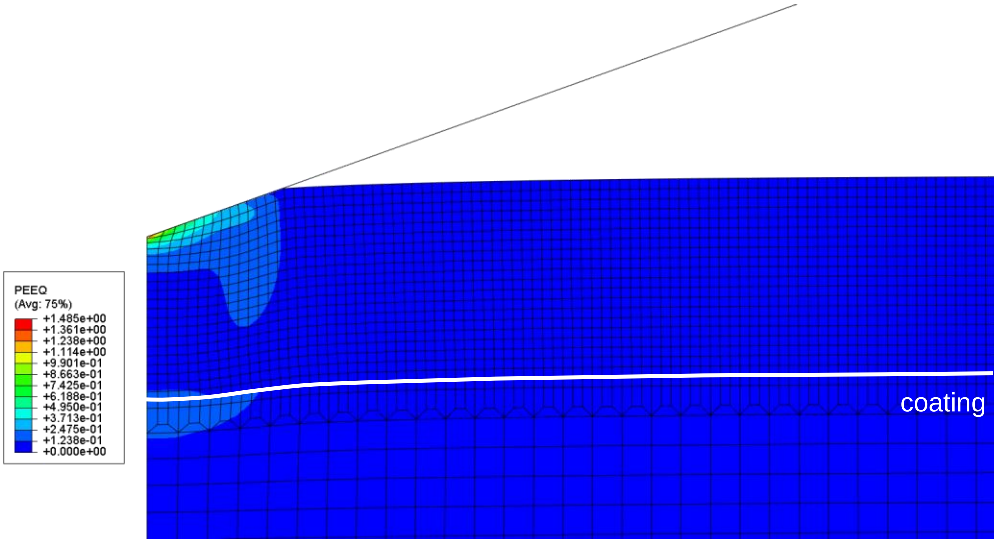

Figure 7-2: Finite element simulation of a hard coating on softer substrate. At penetration depth which corresponds on the 15% coating's thickness, we take significant errors in the measurement of coating's properties.

In order to model the substrate effect, Saha and Nix [133] based on Joslin's and Oliver's analysis [134] suggested some characteristics that are experimentally accessible. According to Equation (2.33) the experimental contact stiffness (S) can be related to contact area (A_c) and indentation modulus (E_r) as:

$$S = \beta \frac{2}{\sqrt{\pi}} E_r \sqrt{A_c} \tag{7.1}$$

where β is the correction factor based on indenter's geometry. The combination of Equation (2.30) and Equation (7.1) yields:

$$\frac{P}{S^2} = \frac{1}{\beta^2} \frac{\pi}{4} \frac{H}{{E_r}^2} \tag{7.2}$$

It becomes apparent that P/S^2 should be constant for a homogeneous material (Figure 7-3) since H, E_r and β are constants.

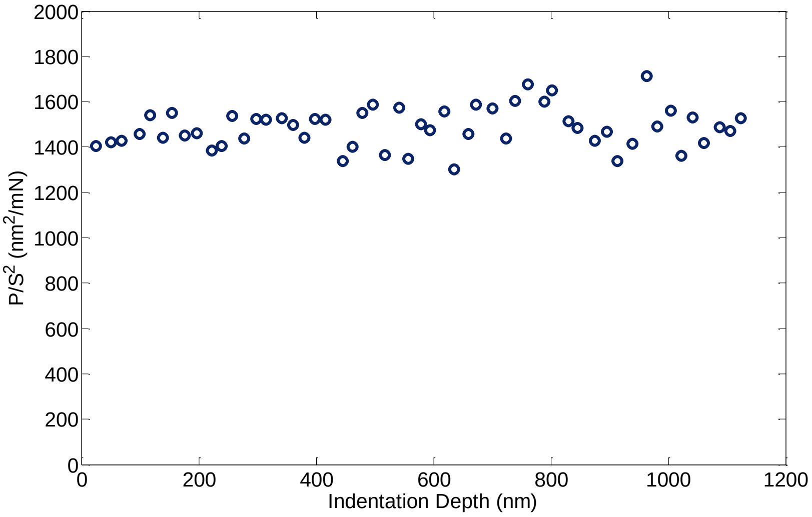

Figure 7-3: Plot of $\boldsymbol{P/S^2}$ of fused silica as a function of indentation depth, which is constant in all the range [135].

In contrast, in coating–substrate systems, the response of P/S^2 is different, due to the substrate's influence. From P/S^2 vs. indentation depth curves one can examine which property (H or E_r) is more affected by the substrate. Since P/S^2 is proportional to hardness H and inversely proportional to ${E_r}^2$, Saha and Nix [135] studied the response of Al coatings on four different substrates (aluminium, glass, sapphire, silicon) as shown in Figure 7-4. Studying each case separately, Al-Al has the same response as quartz (Figure 7-3) since is a homogeneous material. Now, regarding their moduli of elasticity, inasmuch P/S^2 is inversely proportional to ${E_r}^2$, the response of the systems in ascending scale is: Al-Sapphire, Al-Silicon, Al-Aluminium and Al-Glass. Nanoindentation depths up to 500 nm (coating thicknesses) seem to have a turning point, except for the system Al-Aluminium, due to the influence of substrate's hardness. This can be understood if we compare Al-Aluminium with Al-Glass. Although they demonstrate the same values up until 500 nm, then because glass is harder than aluminium, it has an ascending trend. As a result, in the case of soft on hard, substrate's hardness influences the measurements on indentation test, only when the penetration depths are in the order of film's thickness. In the case of Al-Sapphire and Al-Silicon the trend of the curves is continuously ascending due to the fact of the stiffer substrate.

In summary, the influence of substrate must be considered. It has been shown that the substrate's elastic modulus influences the experimental measurements even at small penetration depths (compared to film thickness), in contrast to substrate's hardness which in the case of soft on hard has a negligible influence on the global response, unless the penetration depth is on the order of coating thickness.

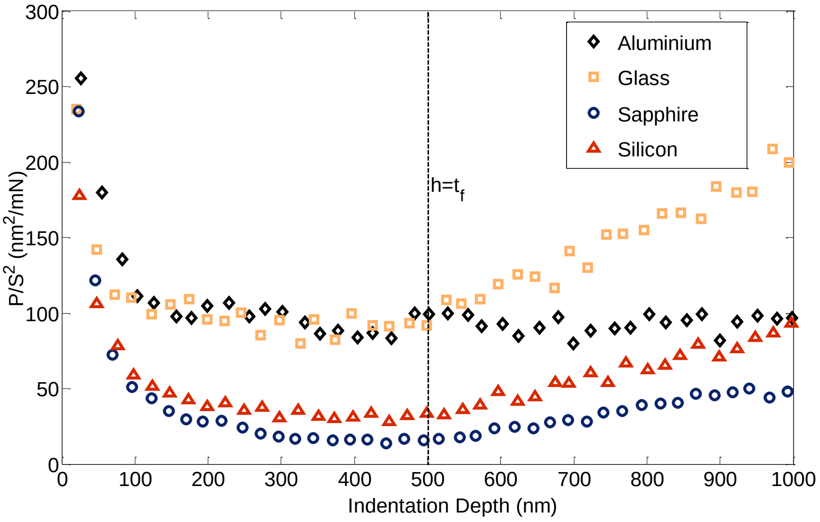

Figure 7-4: P/S^2 of Al films as a function of indentation depth for four different substrate materials [135].

7.2 Models for the Evaluation of Elastic Modulus on Coatings

An important parameter on the indentation of thin films is the radius of contact a. Conical and pyramidal indenters are characterized be self-similarity, which means that the ratio between the circle of contact and depth of penetration a/h remains constant, irrespective of the he applied load increases. Because of that, in the case of thin films, the variable that has the significant control of indentation responses, is either a/t or h/t. For this reason, there was a need to accurately model the indentation on a coated substrate such as to provide the ability to analyze in a quantitative manner all the parameters affecting the response. The most prominent parameters that need to be included are the elastic moduli (E) for the two materials, their Poison's ratio (v), and the film thickness (t).

Many models have been suggested in the literature, some of which have been generated after experimental and theoretical studies [1,136], other through analytical solutions [59,60,137–139], or with the help of finite elements methods [47,48,61,140,141]. In the following sections the models are separated based on the mathematical nature of the resulting equations, these being weighted (a) exponential functions and (b) analytical functions. A third category is also included in this section which relates to equations resulting from computational modeling techniques, in particular the finite element method.

In most cases the following scaling formula is applied:

$$E_{eq} = E_{substrate} + \left(E_{film} - E_{substrate}\right) \Phi(x) \tag{7.3}$$

where Φ is a weight function that relates to the elastic moduli mismatch, the contact radius a, the thickness of the film t and the indentation depth h. When Φ reaches 1, corresponds to small indentation depths ($a/t \rightarrow 0$) and when Φ reaches 0, corresponds to large indentation depths ($a/t \rightarrow \infty$).

7.2.1 Weighted Exponential Functions

Doerner and Nix [1], Menĉík *et al.* [136] and Antunes *et al.* [141] proposed empirical exponential functions, based on their experimental data to determine the elastic modulus of thin films (Vickers – Doerner and Nix, Antunes *et al.*, Berkovich – Menĉík *et al.*). These are concisely presented as follows:

Doerner and Nix model:

$$\frac{\left|1/E_{eq}{}^{*} - 1/E_{f}{}^{*}\right|}{\left|1/E_{f}{}^{*} - 1/E_{s}{}^{*}\right|} = e^{\left(-a_1 \frac{t}{h}\right)} \tag{7.4}$$

Menĉík *et al.* model:

$$\frac{\left|1/E_{eq}{}^{*} - 1/E_{s}{}^{*}\right|}{\left|1/E_{f}{}^{*} - 1/E_{s}{}^{*}\right|} = e^{\left(-a_2 \frac{h}{t}\right)} \tag{7.5}$$

Menĉík *et al.* model:

$$\frac{\left|1/E_{eq}{}^{*} - 1/E_{s}{}^{*}\right|}{\left|1/E_{f}{}^{*} - 1/E_{s}{}^{*}\right|} = e^{\left(-a_3 \frac{h}{t}\right)} \tag{7.6}$$

Antunes *et al.* model:

$$\frac{\left|E_{eq}{}^{*} - E_{f}{}^{*}\right|}{\left|E_{f}{}^{*} - E_{s}{}^{*}\right|} = e^{\left(-a_4 \frac{t}{h}\right)} \tag{7.7}$$

where E^* is the reduced modulus of sample, ${E_f}^*$ is the reduced modulus of film, ${E_s}^*$ is the reduced modulus of substrate, h is the penetration depth, t is the film thickness, $\alpha_{1,2,3,4}$ are empirical fitting constants.

Basically, they represented the system, as two springs in series (coating and substrate) with a weight function which relates the influence of the substrate to the indentation depth. During the process of applying those models in fittings of experimental data, using the least square method as criterion, the values of unknown constant α vary depending on data. Thus, for the appropriate use of those models, since they don't have any physical importance, as they are empirical in origin, the link between ${E_f}^*$ and α must be studied in further detail.

7.2.2 Analytical Functions

Gao *et al* [60] introduced a weight function to determine the elastic modulus of thin films. Their approximation was based on the analytical solution of the contact of a rigid cylindrical punch indenter and an elastic half space. By using an innovative method, they devised a first order perturbation theory to derive closed-form elastic solutions, for the stiffness's contact on a coated substrate. Their function presented as:

$$\frac{\left|{E_{eq}}^* - {E_s}^*\right|}{\left|{E_f}^* - {E_s}^*\right|} = \Phi \equiv \frac{2}{\pi} arctan\left(\frac{t}{a}\right) + \frac{1}{2\pi(1-\nu)}\left[(1-2\nu)\frac{t}{a} ln\left(1+\left(\frac{\alpha}{t}\right)^2\right) - \frac{\frac{\alpha}{t}}{1+\left(\frac{\alpha}{t}\right)^2}\right] \tag{7.8}$$

where Φ = weight function, α = contact radius, ν = samples Poisson's ratio. According to the authors, Equation (7.8) provides good predictions for materials that have elastic moduli mismatch ratio less than 2, because their perturbation analysis was based on a reference homogeneous body, which yields their perturbation results, in a nonhomogeneous body, characterized by a variation of its elastic modulus in indentation's depth direction (two materials, whose mechanical properties don't differ widely).

Jung *et al.* based on Hu's and Lawn's analysis [142] on spherical indentation, they introduced empirical power-law functions [139] to evaluate hardness and elastic modulus on soft films on hard substrates and vice versa, as:

$$E_{eq} = E_s \left(\frac{E_f}{E_s}\right)^{1/\left[1+A(h/t)^C\right]} \tag{7.9}$$

$$H = H_s \left(\frac{H_f}{H_s}\right)^{1/\left[1+B(h/t)^D\right]} \tag{7.10}$$

where A, B, C, D are adjustable coefficients. Although these simple functions demonstrated good agreement on their experimental data, they have excluded important parameters for more "complex" systems: the interaction of Poisson's ratio and the elastic-plastic zones which will yield in significant changes on the values of A, B, C, D.

Another model, which is based on a different weight function, is the model proposed by Perriot and Barthel [59]. Based on an analytical methodology for integral formulation of the elastic contact between an axisymmetric indenter and a coated substrate, they introduced a new weight function to determine the elastic behavior of a coated system. Firstly, they used the results of Li's and Chou's [143] where, by linear elasticity (Hankel transformations) they introduce a relation between the applied normal stress at the surface of the thin film and the normal displacement. Then, due to the fact that they couldn't inverse the problem (from stress-strain to load-displacement) because of the boundary conditions of indentation technique, they used auxiliary fields (Fourier transforms of the Hankel transforms) and they resulted to an integral equation [144]. Thereafter, they applied their equation to an algorithm and given a contact radius a, they introduced force to extract nanoindentation response, in conditions of cone, spherical and flat punch rigid indenters, in frictionless contact with a semi-infinite substrate. They concluded that a sigmoidal behavior is observed in all cases, but the response of E_{eq} is different, depending on the indenter. More specifically, conical and spherical indentation are similar except in high mismatch ratios. Subsequently, for cone indentations, and by changing the mismatch ratio of elastic moduli, they showed that the sigmoidal behavior exists, irrespective of the kind of the system, hard on soft or soft on hard. The only parameter that is altered is the transition from the first plateau to the second one. In the case of soft on hard, the transition point is shifted towards larger values of a/t (see Figure 7-5).

By comparing this result, with Gao's *et al.* function [60], it is observed that they match until mismatch ratios smaller than 2; for bigger mismatch ratios Gao's function is unable to capture the elastic response of the coated system. As mentioned previously, Gao *et al.*

based their analysis on a homogeneous material, but because on indentation testing, the strains under the contact, are distributed inhomogeneously, with consequence the system to be considered as an inhomogeneous.

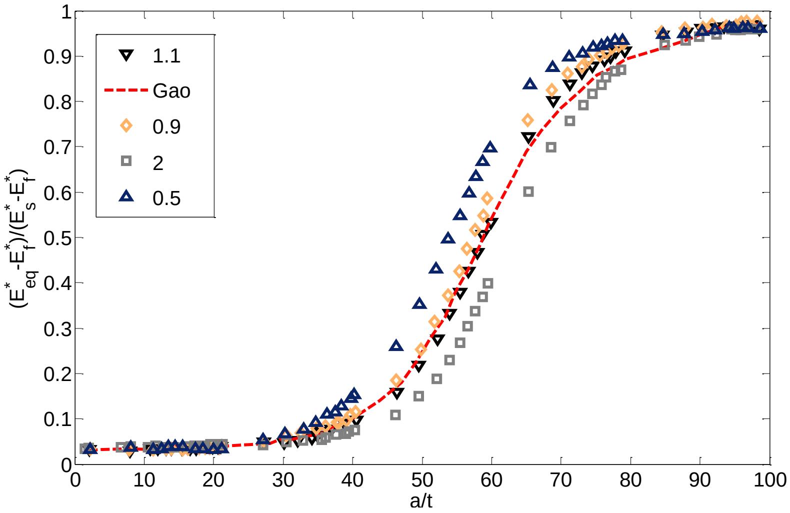

Figure 7-5: Sigmoidal behavior of $\boldsymbol{E_q}^*$ as function of $\boldsymbol{a/t}$ for various mismatch ratio; 0.5, 0.9, 1.1, 1.2, compared with Gao *et al*. function [59].

Continuing from the previous observation, in the case of soft on hard, the film will absorb greater strain than the substrate, which leads to larger contact radius, shifting the transition curve to larger a/t ratios (Figure 7-5). This phenomenon becomes more pronounced with increasing elastic moduli mismatch.

After observing that their theory agrees with Gao's results, they introduce an empirical function, in order to expand Gao's function in larger moduli mismatches:

$$E^*_{eq} = {E_f}^* + \frac{\left({E_s}^* - {E_f}^*\right)}{1 + \left(\frac{tx_0}{\alpha}\right)^n} \tag{7.11}$$

where

$$x_0 = e^{-0.093+0.792\cdot log\left(\frac{{E_s}^*}{{E_f}^*}\right)+0.05\cdot\left[log\left(\frac{{E_s}^*}{{E_f}^*}\right)\right]^2} \tag{7.12}$$

x_0 is related with the position of transition's range. It corresponds to the exact value of a/t for which ${E_{eq}}^* = \left({E_f}^* + {E_s}^*\right)/2$. The adjustable constant n, corresponds to the width of the transition range and is between $1.06 - 1.32$ for various moduli mismatch ratios.

7.2.3 Finite Element Analysis

Clifford and Seah [61] used finite element analysis (FEA) to determine the effect of the Poisson’s ratio between stiff substrates and more compliant coatings. Their motivation for generating this more complex model was the discrepancy existing in the literature between most equations and the shape of experimentally observed curves. Most of the proposed equations contain steep transition gradients which led to low or high elastic modulus fitting values. The new model which has been developed through FEA, assumes that the system is perfectly bonded, and that the penetration occurs by a spherical indenter. The equation is given by:

$$E_{eq}{}^{*} = E_f{}^{*} + \left(E_s{}^{*} - E_f{}^{*}\right)\left(\frac{P\left(\frac{z}{z_0}\right)^n}{1 + P\left(\frac{z}{z_0}\right)^n}\right) \tag{7.13}$$

where

$$\frac{z}{z_0} = \frac{\alpha}{t}\left(\frac{E_f{}^{*}}{E_s{}^{*}}\right)^m \left(\frac{1 - B_s v_s^2}{1 - B_f v_f^2}\right) \tag{7.14}$$

$$\alpha = \frac{2h}{\pi} tan(65{,}3°) \tag{7.15}$$

m = 2/3, B_s = 0.22, B_f = 1.92, P = 2.25, n = 1.5 are fitting parameters.

7.2.4 Critical Comparison of Models

In this section the response of the proposed models to thin film coating systems is critically evaluated for various input variables. Summarizing the previous models, due to the lack of physical significance on exponential and power-law functions, they excluded from the process of comparison. Although their fittings, in any experimental data, are characterized by high values of R-square, however their fitting parameters cannot be controlled and they vary over a wide range, depending on the testing system. In some cases of soft on hard, because of the nature of exponential, these models have the inability to reach the plateau on very small indentation depths, resulting to coatings to have negative values in their moduli of elasticity. Furthermore, they don’t count the effect of moduli mismatch and Poisson’s ratio.

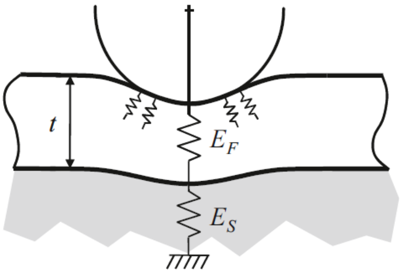

Figure 7-6: Modelling the E_{eq} contribution as a function of indentation stress field [23].

As shown in Figure 7-6, the four exponential functions, as well as Gao's *et al.* function [60], assume that the coating-substrate system operates under the influence of two springs in series. Thus, the substrate's effect begins at small percentages of penetration depth as compared with the coating's thickness. Nevertheless, in nanoindentation experiments, the compressive stress fields are not only in the normal direction with the indenter, but also act in all directions where the surface is in contact with the indenter [59]. As a result, the stress distribution under the contact can't be characterized with accuracy from the above models, so a further study must take place.

We concentrate our discussion on the three most promising models which include the physical mechanisms and behavior during nanoindentation experiments: (a) Gao *et al.*, (b) Perriot and Barthel, and (c) Clifford and Seah. In what follows, a sensitivity analysis of the models to various controlling variables is presented. We first compare the three models in conditions of which the substrate is almost twice as stiff as the coating. The explicit parameters for this simulation and the results are shown in Figure 7-7 (a).

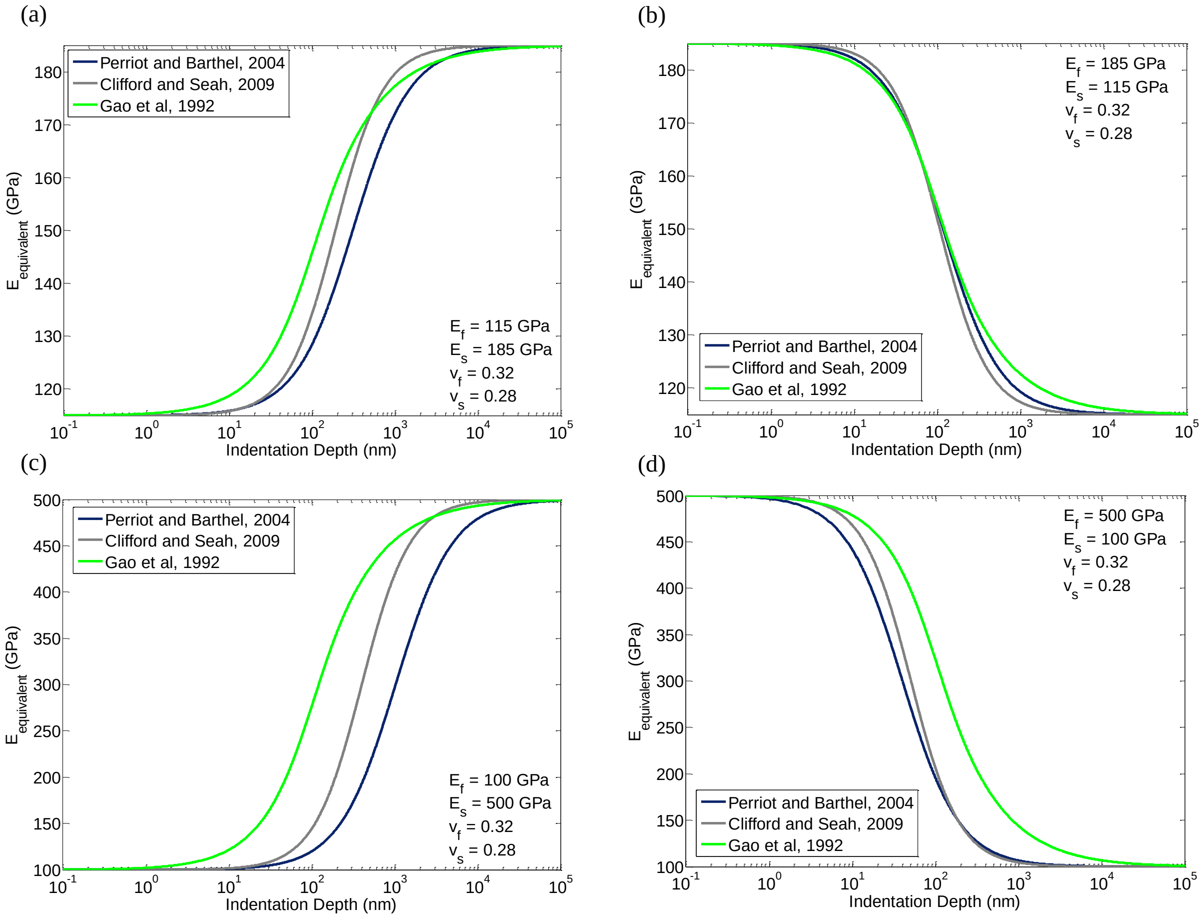

Figure 7-7: Results of the three models under conditions of (a), (c) soft films on hard substrates, (b), (d) hard films on soft substrates, for the evaluation of film's elastic modulus**.**

Perriot's and Barthel's model start the transition range at the same time with Clifford's and Seah's model, but then the reaction of Perriot and Barthel, is slower than Clifford and Seah, since they don't account the influence between Poisson's ratio. Gao's *et al*. model, shows quicker response of the transition range – because of the low sensitivity in the modulus mismatch- as compared with the other two models but during transition range, it seems that exhibit similar response with that of Perriot's and Barthel's model. Overall, however, the three models are in relatively close agreement for this particular mismatch ratio.

As a second comparison, we investigate the response of hard coatings resting on soft substrates. The same mismatch ratio as previously is used, but now reversed. The parameters of this simulation and the results are shown in Figure 7-7 (b). In this comparison, all the models have the same behavior expect at the time that they reach the second plateau. Clifford and Seah model, has the quickest response in contrast to the other two models while the Gao's *et al*. exhibits the slowest response. Based on the previous result, this behavior is expected because of Poisson's ratio, between coating and substrate.

The previous two scenarios concentrated on moduli mismatch ratios which were restricted within 0.5 to 2. The third comparison relates to conditions that the mismatch ratios of elastic modulus between coating and substrate are large. This comparison is separated in two parts: mismatch ratio E_s/E_f = 5 and mismatch ratio E_s/E_f = 1/5. The parameters and results of these simulations are shown in Figure 7-7 (c) and Figure 7-7 (d) respectively.

From Figure 7-7 (c), the three models don't have the same ratio in the transition range, since all models have different behaviors. From Figure 7-7 (d), the Perriot and Barthel model, behaves the same as the Clifford's and Seah's model, with the only difference is on the beginning of the transition range.

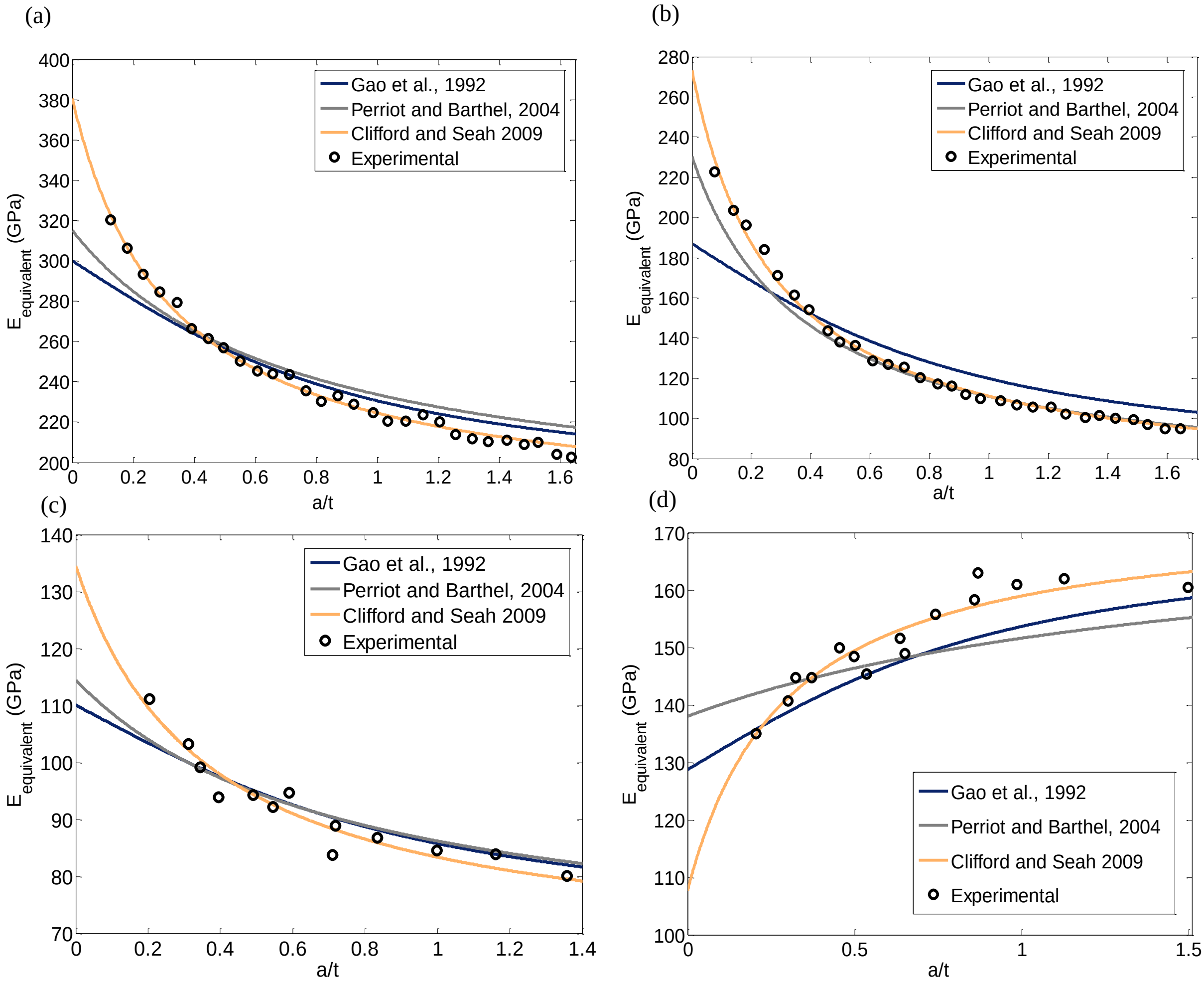

Figure 7-8: Behavior of proposed models to evaluate the elastic modulus of films as a function of a/t. Experimental data extracted from [135,136].

From these four comparisons, the models of Perriot and Barthel and Clifford and Seah exhibit more stable and representative responses for all considered situations. When the mismatch ratio is low the models have similar responses but when the mismatch ratio is high, the model of Gao *et al*., doesn't show the same behavior as the other models. The reason that the Gao's model fails to response rightly in complicated situations, is because of the nature of their weight function; Equation (7.8) excludes the parameter (E_f/E_s), thus the function remains constant for all considered ratios. In order to conclude on the validity of the models in real conditions, they should be contrasted to literature experimental data as shown below in Figure 7-8 while details on the data is presented in Table 7-1.

The models have been examined under circumstances where the elastic moduli between coating and substrate vary. In Figure 7-8 (a) the elastic moduli ratio (thin film/substrate) ~1.5, in Figure 7-8 (b) ~4, in Figure 7-8 (c) ~2 and in Figure 7-8 (d) with ~0.5. In most of cases, the models exhibit high values of R-square. Gao's *et al*. model, demonstrates the poorest response on cases where the elastic-moduli mismatch ratio reaches the value of 4, as expected. Perriot and Barthel function, can't calculate the elastic modulus of (TbFe+Fe) on Silicon, because of the interaction between the Poisson's ratios. As summarized in Table 7-1, Clifford and Seah model, demonstrates the most accurate fittings in all cases which is due to their five fitting parameters which gives more independent behavior on the initial shape of sigmoidal curve, without however any physical basis.

Table 7-1: Experimental parameters and results extracted from Figure 7-8.

Samples	Film t	E_{sub}	v_{film}	v_{sub}	E_f Gao	E_f Perriot	E_f Clifford
Tungsten on Silicon [133]	0.64 μm	174 GPa	0.25	0.25	300 GPa R^2 : 0.8713	315.2 GPa R^2 : 0.8843	380.6 GPa R^2 : 0.9929
Tungsten on Glass [133]	0.5 μm	65 GPa	0.25	0.25	186.9 GPa R^2 : 0.8202	254.1 GPa R^2 : 0.9871	273.1 GPa R^2 : 0.9954
TbFe+Fe on Glass [136]	1.2 μm	65 GPa	0.24	0.3	110.1 GPa R^2 : 0.8431	114.5 GPa R^2 : 0.8475	134.6 GPa R^2 : 0.9291
TbFe+Fe on Silicon [136]	1.2 μm	174 GPa	0.2	0.3	128.7 GPa R^2 : 0.8653	138 GPa R^2 : 0.6972	107.6 GPa R^2 : 0.8919

What one expects and that is not be supported by the above fittings, is that the elastic moduli of the films where to be equal, regardless of the substrate material. The erroneous observation leads to various conclusions, which are analyzed at the end of this chapter. Another significant observation, is based on the fitting results, which differ significantly from the reference values [141] of the elastic moduli of films; E_{Tung} = 410 GPa, $E_{\mathrm{TbFe+Fe}}$ = 130 GPa.

7.3 ISO 14577-4

Given the large available selection of models and the inadequacy of a single model to accurately capture the mechanical response of a wide variety of systems we have resorted to the recently published international standard for guidance. The proposed methodology of ISO 2016 [145] suggests a linear fitting over a region in low depths, where the substrate influence is restricted to small contributions. The ISO requires that all calibrations are performed *a priori* for accurate mechanical measurements. Undoubtedly, this methodology is based on empirical knowledge, without detailed mechanical modeling of the physical mechanisms, but provides accurate results even in complex material systems (coatings, multilayers), by circumventing the non-linear substrate-film interaction regime. Furthermore, as ISO suggested, for more accurate data interpretations, finite element simulations must be applied, especially in materials with non-linear constitutive relationships.

7.4 Chapter Summary

Many of the literature equations for determining the elastic modulus and hardness of thin films through nanoindentation have been presented in this chapter. The best models with the most promising responses, according to our analysis and the work of other researchers, have been examined in detail and analyzed in various parametric conditions. Although some have their basis on analytical and computational results, in a lot of circumstances they fall short to accurately and confidently reflect experimental data.

Firstly, this can be due to the fact of roughness on the surfaces of the tested samples. The presence of roughness can affect the precise measurement of the area of contact. Another parameter can be the adhesion between the coating and substrate, where in all cases, is assumed as perfect. Owing to Y/E mismatch or work hardening exponents, the coating may be subject to delamination processes or in mechanisms which are currently excluded from existing models (cracking, piling-up). The contact which is considered as frictionless and the indenter as rigid, drives in significant errors, especially in cases of stiff coatings. Moreover, the above models don’t take into account the microstructure of the systems, either if they are characterized by porosity, density fluctuations, internal stresses or bluntness of the indenter. Furthermore, material parameters, such as elasto-plasticity, viscoelasticity, viscoplasticity, work-hardening behaviors can affect the indentation response. Lastly, errors can occur from experimental conditions; calibrations, thermal drift, noise. A more extensive study is therefore required (Chapter 8) in order to computationally quantify the effect of several parameters such as to probe their contribution on the overall mechanical response.

Chapter 8

Numerical Evaluation of Hard Coated Systems

As it was discussed in Chapter 7, experimental data on coated systems requires the nanoindentation depth to remain at a small percentage of the film thickness (usually <10%) in order to avoid coating-substrate interactions and enable the usage of traditional bulk materials indentation analysis. With the advent of nanoscale film deposition technologies, the restriction of nanoindentation data into very small depths interferes with instrument's resolution and manufacturing capabilities of the used probe. Therefore, the only option that is left is the precise modelling of the nanoindentation process in order to interpret in a quantitative way the experimental force-displacement ($P - h$) curves on coated systems. The composite response depends on the elastic and plastic properties of the coating and substrate material as well as the nature of the interface. In this study, the finite element method is employed to investigate the indentation response of coated systems. The critical parameters for nanoindentation testing are identified and simulated with the aim to propose improvements of the testing protocols to experimentalists such as to either (a) define testing parameters that circumvent the substrate effect or (b) interpret the indentation data in a way that quantitatively accounts for substrate contributions.

Most models and experimental data (described in Chapter 7) exhibit a “sigmoidal” profile of the composite (or equivalent) modulus of the film/substrate system that is strongly dependent on film thickness and indentation depth or contact radius size, Figure 8-1. The aim of the current study is to examine the proposed models under numerical indentation simulations by varying the elastic moduli mismatch and mechanical response of systems (elastic and elasto-plastic). In addition, we aim to quantify the region of allowable use of the Oliver and Pharr method [2,3] for thin film systems, for rigorous and accurate experimental measurements.

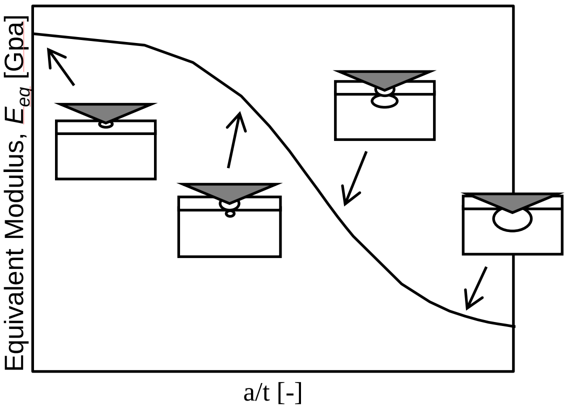

Figure 8-1: Graphical representation of the sigmoidal curve that coating systems exhibit during nanoindentation testing.

8.1 Finite Element Model

Two-dimensional axisymmetric finite element simulations are performed to investigate the mechanical response of coating systems under conical, $\theta = 70.3^o$ indentation. Details of the model geometry are shown in Figure 8-2(a). The ‘semi–infinite’ half space is modeled as a 101×101 μm^2 domain. The indentation simulations were restricted to depths much smaller than the domain such as to avoid any boundary effects. The continuum space is discretized using 4–node axisymmetric, isoparametric elements (CAX4–full integration). The interface between coating and substrate is defined as being perfectly bonded, which means that there is no delamination or slippage. Two identical finite element models have been structured, in order to account two different coating thicknesses: 500 nm and 1000 nm. The element size was continuously refined in five successive regions as approaching the indenter contact region for greater accuracy, Figure 8-2(b).

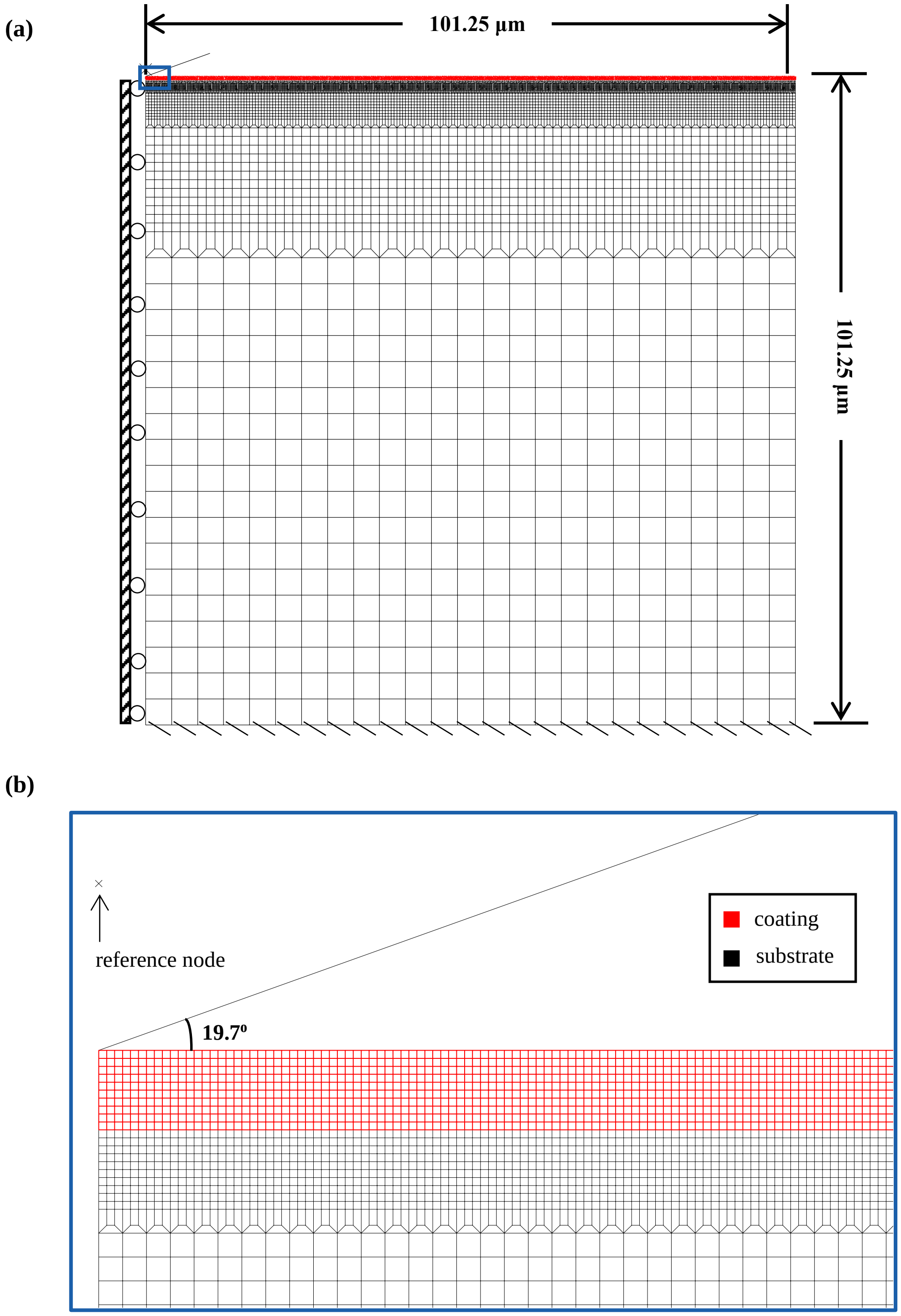

Figure 8-2: (a) Representation of finite element model of coating systems, (b) top portion of finite element mesh showing the details of cone’s geometry and film thickness.

A mesh sensitivity analysis was performed to ensure that the simulations results were insensitive to the mesh size. Roller boundary conditions were applied on the axis of symmetry and fixed boundary conditions on the bottom surface of specimen. We assume that the loading rate is slow enough such as static friction can securely model the interface response. Simulations proceeded in two steps: the indenter was firstly subjected to a ramped vertical displacement, followed by an indenter retraction to the original position which corresponded to complete unloading at zero load. During this process the lower edge of the material was constrained vertically. Axisymmetric boundary conditions were used along the symmetry axis beneath the indenter region [64].

8.2 Indentation Scale Factor for Coating Systems

Numerical parametric studies are being performed and the effect of film thickness and substrate characteristics are quantified on the composite indentation response. An important parameter on the indentation of thin films is the radius of contact a. Conical and pyramidal indenters are characterized by self-similarity, which means that the ratio between the circle of contact and depth of penetration a/h remains constant, irrespective of the magnitude of the applied load. In line with dimensional analysis, the scaling parameter that controls the overall indentation response is either a/t or h/t. Therefore, a set of elastic and elastic-perfect plastic simulations have been performed in order to study their effect (Table 8-1). The mechanical properties of titanium material have been selected to simulate the response of coatings and quartz properties to account for the response of the substrate.

Table 8-1: Input characteristics for the computational analysis of coated systems.

Model Name	E_f [GPa]	E_s [GPa]	v_f [-]	v_s [-]	Y_f [GPa]	Y_s [GPa]	t_f [nm]
N1	115	72	0.32	0.17	-	-	500
N2	115	72	0.32	0.17	-	-	1000
N3	115	72	0.32	0.17	1.2	3.95	500
N4	115	72	0.32	0.17	1.2	3.95	1000

Prior to the analysis of composite thin film systems, we have extracted the $P - h$ response of their bulk counterparts, for benchmarking purposes. The elastic indentation resistance of titanium is higher than that of quartz, Figure 8-3 (a), which relates to the fact that the elastic modulus of titanium is higher. Initially assuming a purely elastic response for both materials (titanium on quartz substrate), we observe a fast transition from the film to the substrate response which remains almost unchanged from $h = 1500$nm onwards (the deviation from the substrate response). When the plastic dissipation capacity of the materials (von-Mises yield law) is taken into consideration, then the response changes drastically. This relates to the fact that the yield stress of titanium is lower than that of quartz which causes a flipping in order for the $P - h$ elastoplastic responses of the bulk counterparts. When the plasticity of the materials are considered, the composite response starts as identical with the softer titanium film indentation response and gradually stiffens (as h~1200nm) until it converges to the substrate response (h~2600nm), see Figure 8-3 (b). It is therefore evident that the behavior of the coated system is load (and subsequently depth) dependent; for low values the titanium properties dominate the response and as the load increases, the mechanical response of quartz (substrate) becomes apparent. An interesting metric characteristic is that for a film of 1000 nm in thickness the indenter "feels" substrate-only properties at a depth of 3× its size.

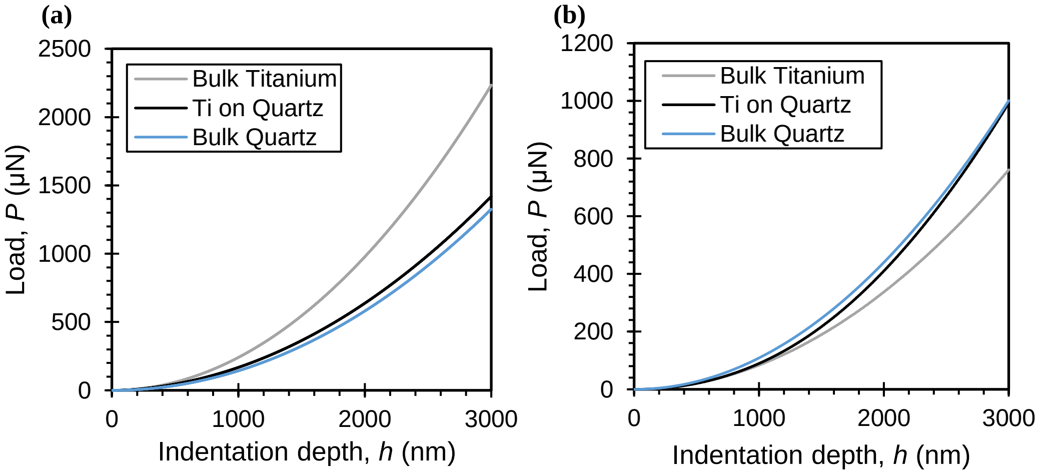

Figure 8-3: Load – displacement responses of simulated titanium coating on quartz titanium for (a) elastic and (b) elastoplastic materials. Their bulk indentation responses are plotted for comparison (only the loading portion of curves is plotted).

Figure 8-4 presents the evolution of equivalent modulus with respect to the two dimensionless characteristics. It is obvious that the function a/t spans the data to a larger range than the h/t, and also appears to be the main ratio that scales the composite response and hence it can be used throughout the remaining studies. Before proceeding it is noteworthy to state that the data scale on a single universal curve irrespective of the film thickness or the material's elastic or elastoplastic response.

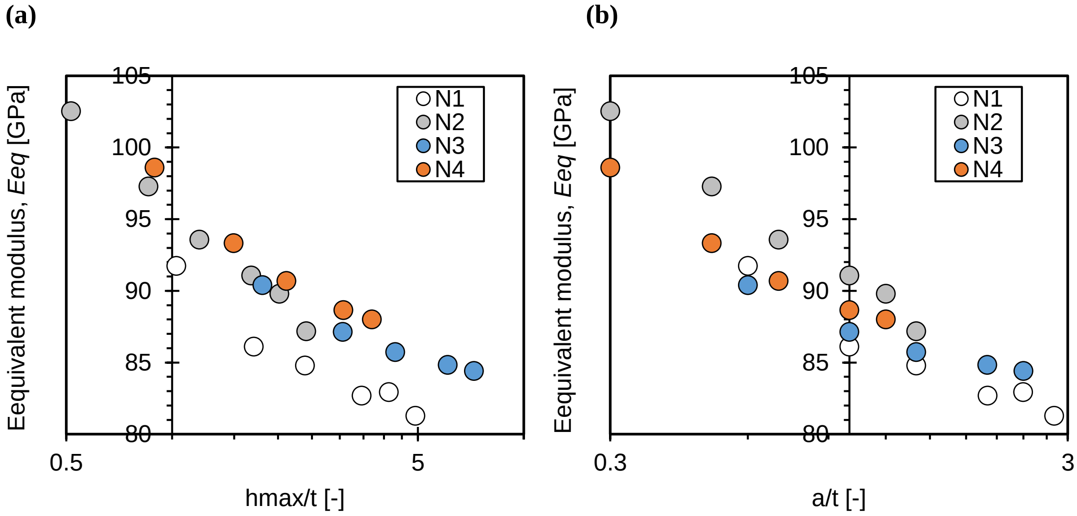

Figure 8-4: Computational results of equivalent modulus as a function of scaling factors (a) $\boldsymbol{h/t}$, (b) $\boldsymbol{a/t}$.

Figure 8-5 shows the evolution of the equivalent elastic modulus in comparison to Equation (7.11). The effect of film thickness and substrate characteristics are quantified on the indentation response. As expected, for small depths the properties of the film are recovered whereas for large indentation depths (compared to the film thickness) the properties of the substrate dominate.

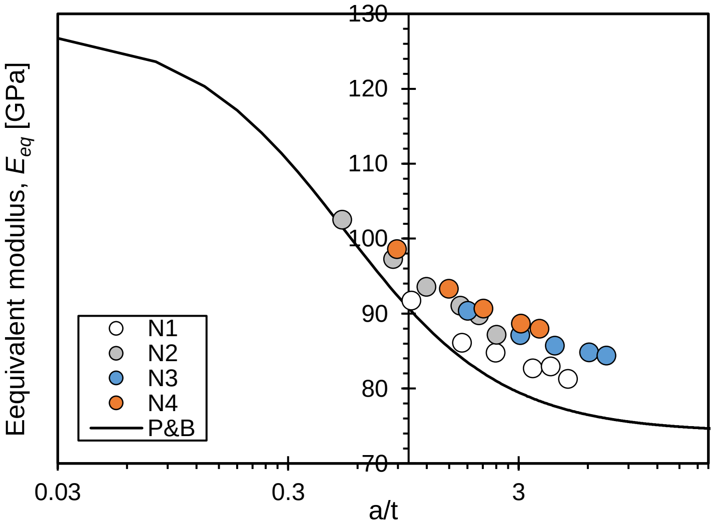

Figure 8-5: Computationally response of hard material on soft substrate. The analytical solution of Perriot and Barthel is illustrated for comparison, Equation (7.11).

It is noted that the computational data cannot approach accurately the sigmoidal analytical solution at the substrate plateau. Even in the case of elastic indentation, which corresponds completely to the constitutive relations used in the P&B analysis, the numerical results exhibit a stiffer behavior (10-15%) as the a/t ratio increases. As it was mentioned in Section 7.2.4, the most crucial parameter in indentation of thin films is the extrapolation of the coating's properties as $a/t \to 0$. The deviation of the models that have been suggested in the literature becomes significant in the initial region of the sigmoidal curve and therefore a more careful numerical study is required. In order to perform such studies, a new finite element model was created (Figure 8-6), which aims for indentation in very low depths; the overall size of the material domain has become smaller, while the minimum element size was set to 5 nm, in order to gain high resolution in small penetration depths.

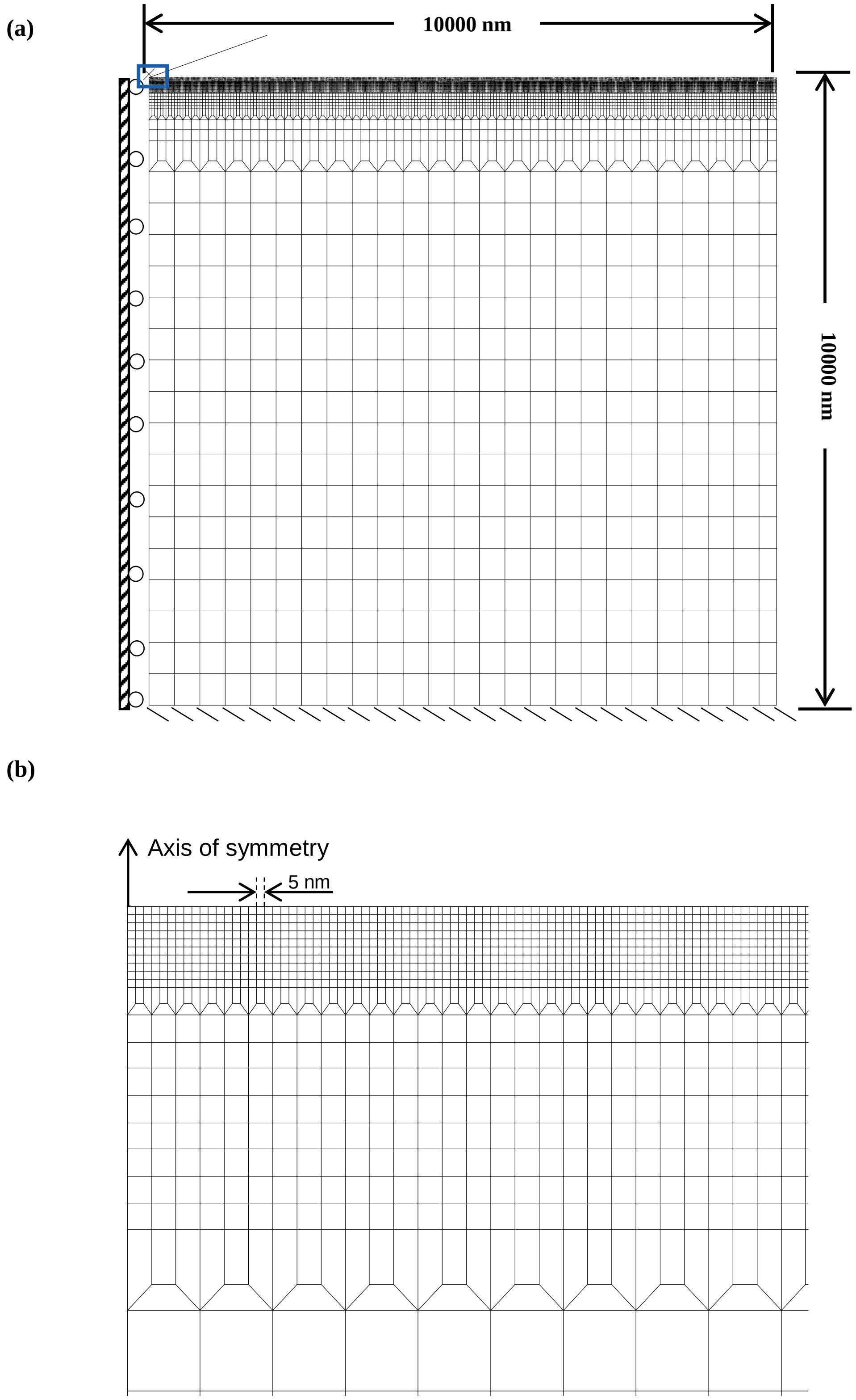

Figure 8-6: (a) Finite element model that targets low indentation depths, (b) portion of the finite element model that describes mesh distribution and size of fine element.

Furthermore, a set of six layers were created with ideal bonding parameters, in order to have the potentials either for varying the thickness of the coating from 50 nm to 1000 nm, or for flexibility in developing multilayer systems, Figure 8-7.

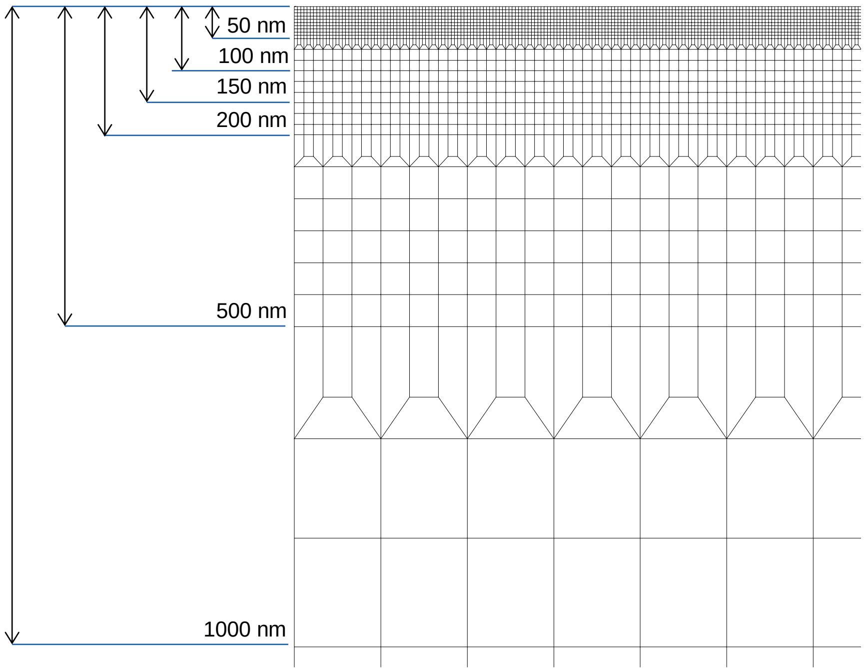

Figure 8-7: Finite element model which takes account multiple layers to be served as different coating thicknesses.

This refined numerical model is identical as that described in Section 2 except from the total size and material properties. In the current study, except from the effect of low indentation depths and film thickness, the effect of elastic moduli mismatch in coating systems was also examined. Details about the input data are provided in Table 8-2, where elastic and elastic-perfect plastic simulations have been performed with the moduli mismatches to be defined for the first group at E_f/E_s = 1.6 and for the second group at E_f/E_s = 5.

Table 8-2: Material properties used to study the effect of moduli mismatch.

Model Name	E_f [GPa]	E_s [GPa]	v_f [-]	v_s [-]	Y_f [GPa]	Y_s [GPa]	t_f [nm]
A1, A2	115	72	0.32	0.17	-	-	500, 1000
A3, A4	115	72	0.32	0.17	1.2	3.95	500, 1000
B1, B2	250	50	0.30	0.25	-	-	500, 1000
B3, B4	250	50	0.30	0.25	5	2	500, 1000

8.3 Parametric Analysis on Film Indentation

8.3.1 Effect of Moduli Mismatch

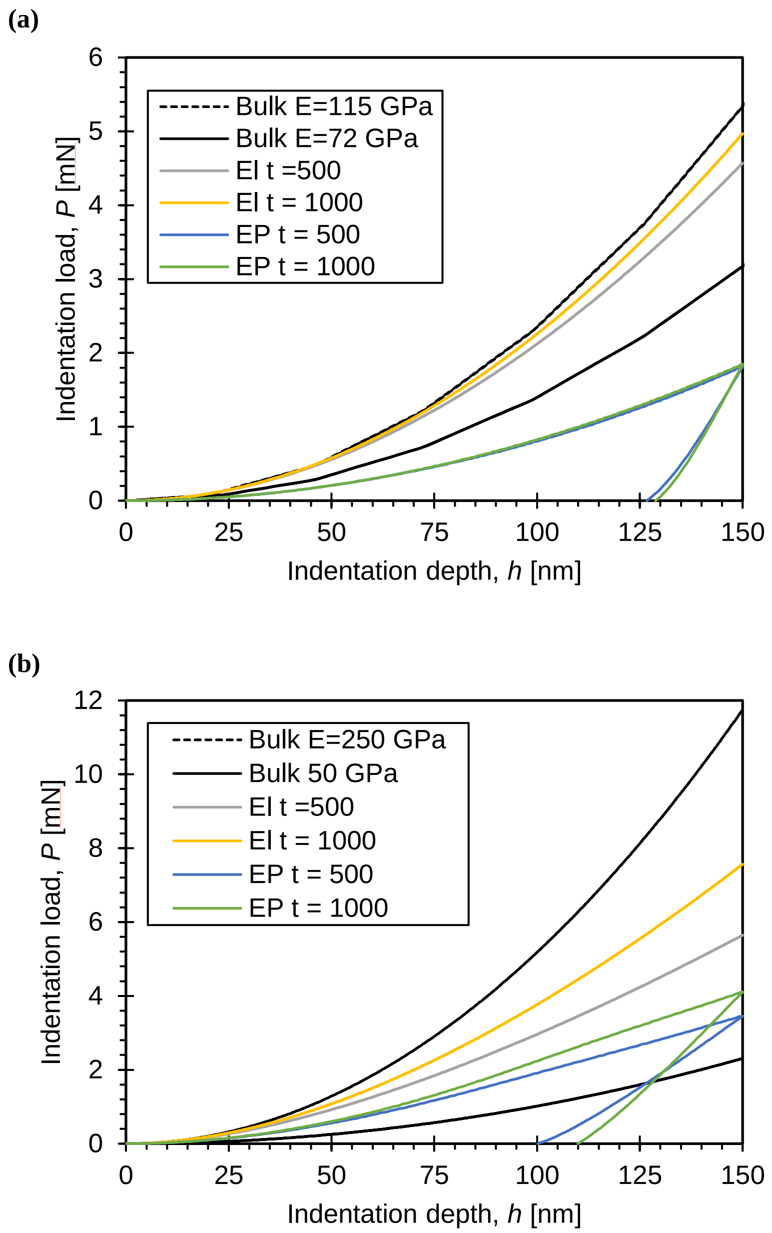

Figure 8-8: Load vs indentation depth curves for coating systems with a fixed elastic mismathch of (a) 1.6 and (b) 5.

Numerical $P - h$ responses for indentation on the coating system with $E_f/E_s = 1.6$ is illustrated in Figure 8-8(a). The response of the bulk counterparts is plotted with black lines for reference. Computational results suggest that the elastic indentation resistance decreases as the film becomes thinner. This behavior is attributed to the substrate effect, since for a fixed indentation depth, thinner coatings will exhibit earlier the substrate contribution on the composite modulus response. For the case of elastic-perfectly plastic simulations the resistance of the system significantly decreases, because of the generated plastic deformations inside the materials. Due to the fact that the selected maximum penetration depth (150 nm) is much lower than the coating thicknesses and that their modulus mismatch is low, the $P - h$ curves for the two films (500 nm and 1000 nm) are almost identical. In Figure 8-8 (b) a similar response on indentation resistance with systems with E_f/E_s = 5 is observed. Here the substrate effect, is even more significant due to the large contrast between the elastic moduli, therefore the elastic resistance of coating with thickness of 500 nm is much lower than that of 1000 nm. Regarding, von-Mises materials the large mismatch ratio plays a dominant role even in relatively small indentation depths.

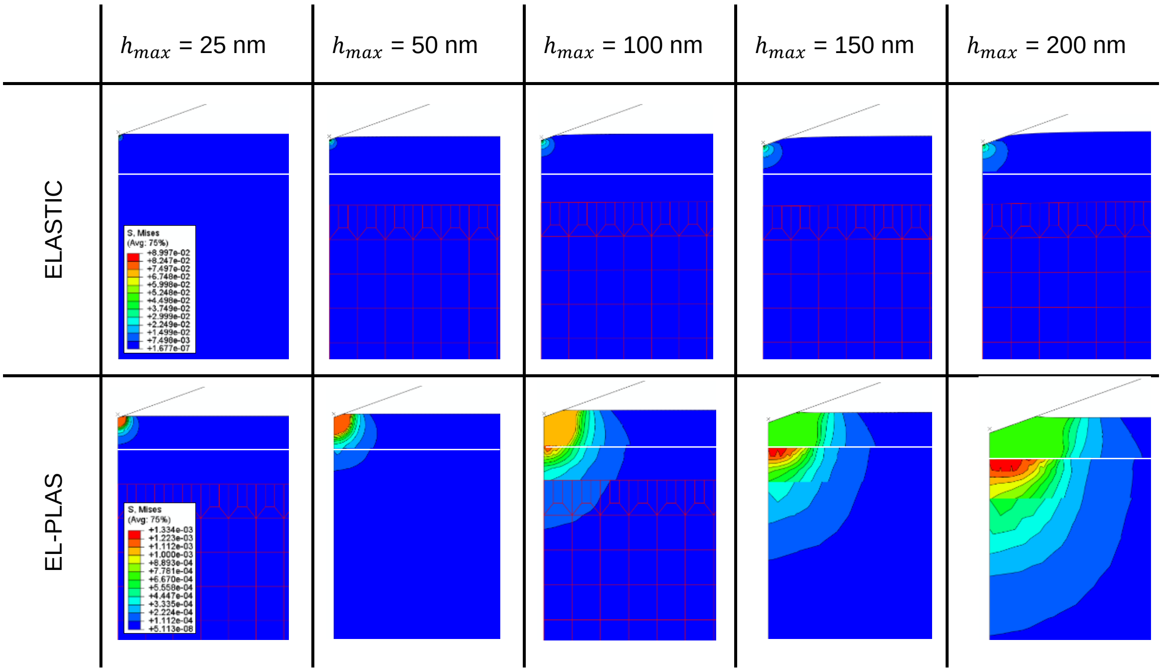

Figure 8-9: von-Mises stress profiles for elastic and elastic-perfect plastic coating systems by varying the maximum penetration depth.

Figure 8-9 captures the von-Mises stress profiles at maximum indentation load for elastic and elasto-plastic coatings. As the depth of penetration increases the generated von Mises stresses propagate into the system. Furthermore, comparing their responses, von Mises stresses are distributed in a larger area under elastoplastic simulations due to the generated plastic flow which is associated with a higher depth of penetration. Associating the contour plot values regarding elastic and elastoplastic responses, it is obvious that elastic material systems exhibit higher von-Mises stresses, due to their high indentation resistance.

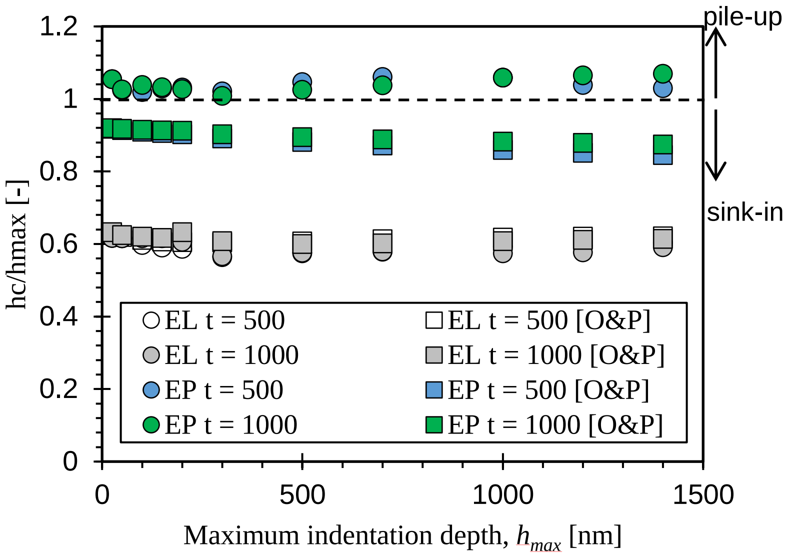

Figure 8-10: Normalized contact depth as a fuction of maximum indentation depth for various coating systems with fixed $\boldsymbol{E_f/E_s}$ = 1.6.

As it was noted in Chapter 2.6 the Oliver and Pharr methodology for calculating the projected area of contact, neglects any pile-up phenomena [2,3]. Therefore, it is crucial to overcome such limitations, which for bulk materials can occur when the ratio between E/Y [108,109] becomes high, while for thin film systems mainly appears when dealing with soft films on hard substrates [146,147]. Any appearance of pile-up leads to an underestimation of the projected contact area as estimated through the O&P method; in fact the estimated contact depth will always be $h_c < h_{max}$. For coatings of E_f/E_s = 1.6, it is shown in Figure 8-10 that numerical elastic-plastic systems exhibit pile-up phenomena and for this reason there is an average deviation of 15% between extracted results and O&P method. For elastic simulations, all the systems exhibit sink-in phenomena and the values of normalized contact depth are in perfect agreement with O&P methodology.

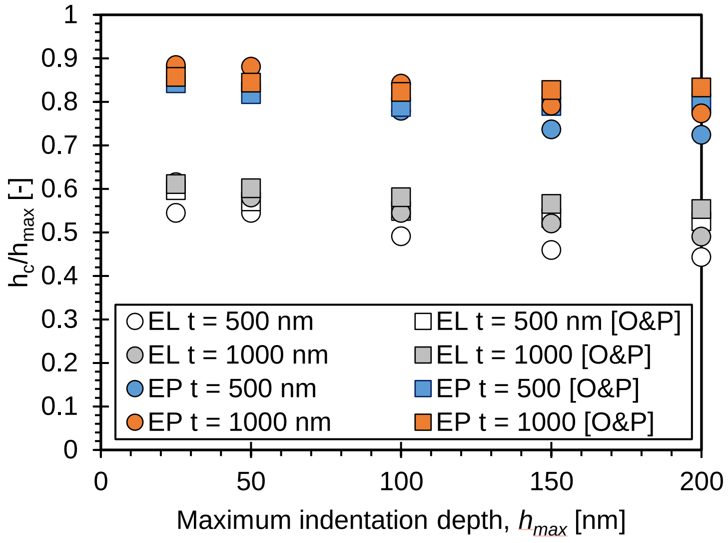

Figure 8-11: Normalized contact depth as a fuction of maximum indentation depth for various coating systems with fixed $\boldsymbol{E_f/E_s}$ = 5.

For thin film systems with E_f/E_s = 5, both elastic and elastic-perfect plastic materials exhibit sink-in behaviour, Figure 8-11. With respect to the Oliver and Pharr method, the deviation between the calculated values remains under 10% for extreme values and as a result this is an additional verification that their methodology is accurate when materials deform either elastically or in a sink-in fashion.

8.3.2 Evaluation of Numerical Results in Sigmoidal Behaviors

Moving on the second part of this study, we here present in Figure 8-12 the calculated composite modulus with respect to a/t for E_f/E_s = 1.6. Numerical results replicate the sigmoidal response that was proposed in the literature [59–61]. Elastic and elastoplastic simulations converge to one single behaviour, underlying the strong dependence on a/t. The recommended equation of Perriot and Barthel [59] has been used in this report for critical comparison with our finite element simulations. The results of numerical data and analytical equation are in good agreement, except at the zone where the substrate effect is very significant – for high indentation depths. In that zone, numerical results seem to exhibit a stiffening behaviour due to the large stresses generated at film’s elements.

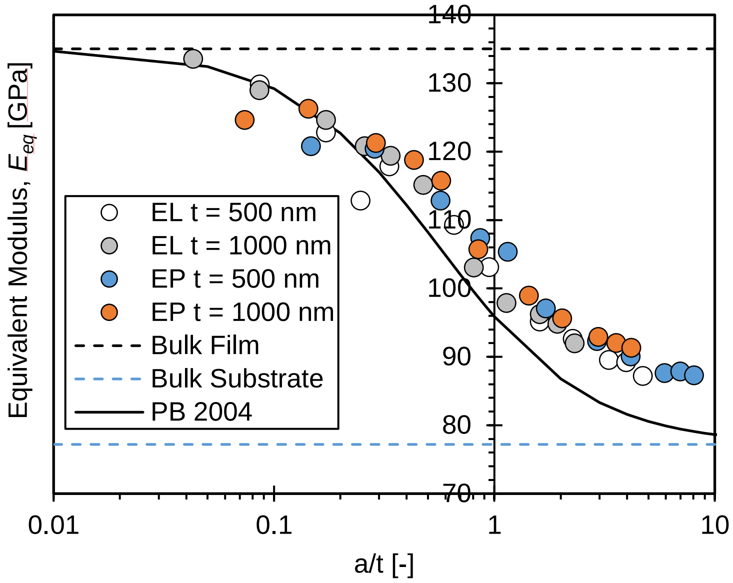

Figure 8-12: Numerical results of equivalent modulus against scaling factor $\boldsymbol{a/t}$ for fixed elastic moduli mismatch equals 1.6. The proposed equation of Perriot and Barthel is plotted for comparison [59].

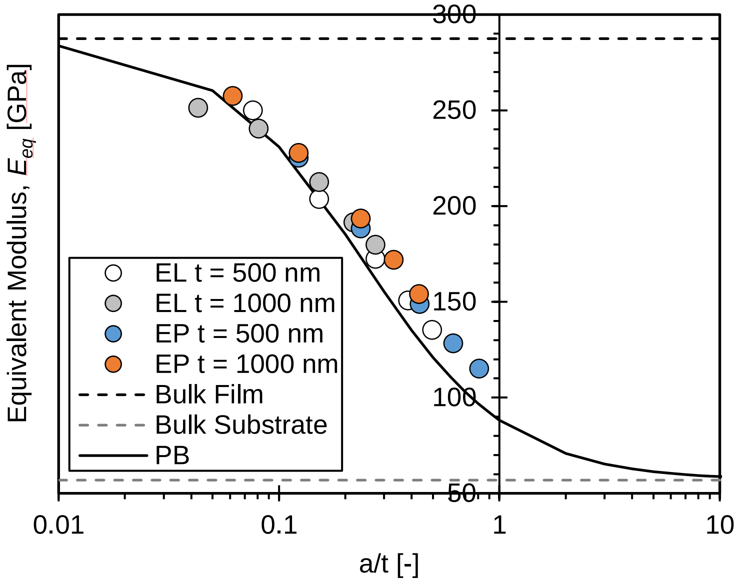

Figure 8-13: Numerical results of equivalent modulus against scaling factor $\boldsymbol{a/t}$ for fixed elastic moduli mismatch equals 5. The proposed equation of Perriot and Barthel is plotted for comparison [59].

Similar response is shown for E_f/E_s = 5, Figure 8-13. Here, data of the final plateau where is the substrate's domain region, have been excluded from the analysis. Although that the moduli mismatch increases, the sigmoidal behaviour between different types of coated systems remains. It must be stated that initial and final values of sigmoidal curve are higher than that of input values (E_f = 250 GPa, E_s = 50 GPa) due that reduced modulus equals is a combination between elastic modulus and Poisson's ratio, as stated in Equation (2.14).

8.3.3 Effect of a Soft Layer Between Coating and Substrate

To the best of our knowledge, the effect of element stiffening when performing numerical simulations on thin films has not been reported in the literature. Due to limitations of ideal bonding between coating and substrate, when indentation depth approaches or exceeds coating's thickness, numerical results will always be affected by the stiffening of compressive elements. This study may be regarded as being of minor importance due that the focus in thin film characterization is the extraction of film's only mechanical properties. Nevertheless, this could provide guidelines to future numerical studies for determining their technical input information. Thus, to study this effect, based on the finite element model with the multilayer's features, we have structured two different elastic models as illustrated in Figure 8-14. First model corresponds to an elastic stiff coating of 150 nm thickness which lays on a softer substrate, while the second model assumes the same conditions with an addition of an elastic thin interlayer with thickness of 50 nm and an elastic modulus of 90% softer than coating's modulus.

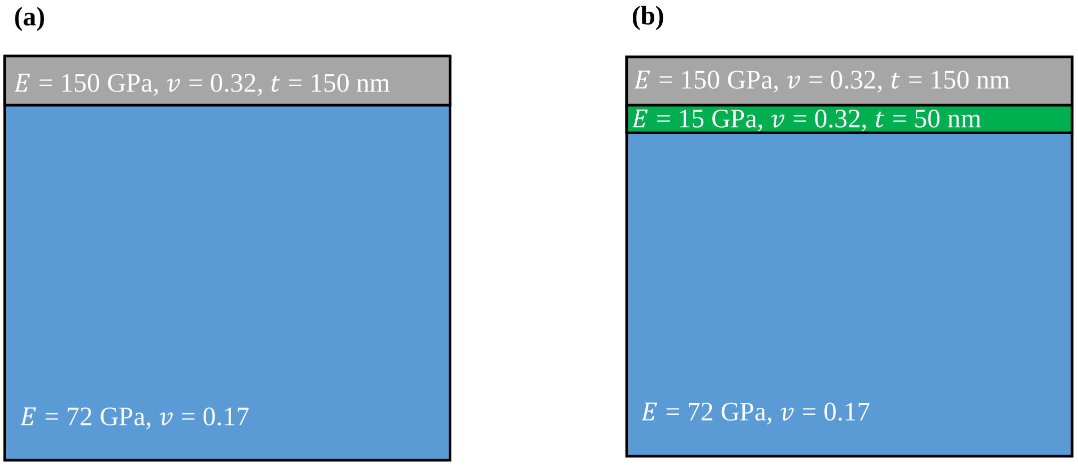

Figure 8-14: Design of numerical models to stufy the effect of a soft intermediate layer, (a) original model without layer, (b) new proposed model with an intermediate layer of 50 nm thickness.

Both models have been indented to a maximum depth of 250 nm which corresponds to almost 2x coating's thickness. Figure 8-15 shows the von-Mises stresses for each system, where the system with the interlayer exhibits lower values in contrast with the single layer. Analysis results concluded that for the case of stiff coating on soft substrate the equivalent modulus is 91.91 GPa with a/t = 2.8, where for the case of soft interlayer between them, E_{eq} = 78.31 GPa with a/t = 2.92. In addition, we performed numerical analysis on an elastic bulk material with properties of that of substrate, in order to contrast them with the response of thin film systems, since of the high penetration depth, the indentation responses must be similar. The analysis yields to an E_r = 77.19 GPa which is very closed with response of soft interlayer. Furthermore, we completed additional simulations for the case of stiff coating to account its response at various a/t ratios. Results show that for a/t = 2.3, E_{eq} = 91.95 GPa, where for a/t = 3.3, E_{eq} = 89.56 GPa, which underlies the large dependency of element stiffening.

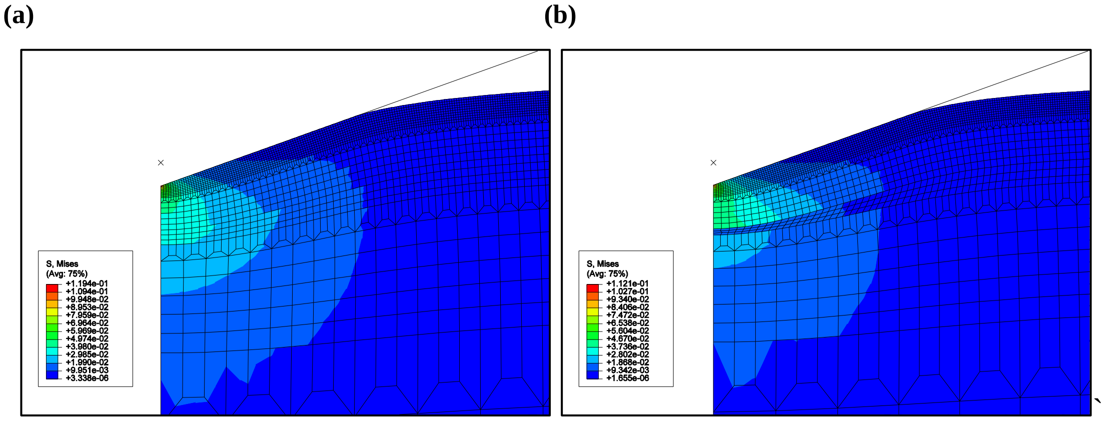

Figure 8-15: von-Mises contour plots for coating system of (a) one layer with thickness of 150 nm, and (b) two layers with thicknesses of 150 nm and 50 nm respectively.

In summary, the addition of a soft interlayer between a stiff coating on soft substrate improves the numerical results in high indentation depths. Although, this soft interlayer must be as thin as possible, in order to have contribution in the "relaxing" mechanism and that not affects the mechanical response of the original system.

8.3.4 Guidance to Design for Experiments Methods

Finally, in order to better illustrate the relation between elastic mismatch and substrate effect, the composite modulus have been normalized for both cases (E_f/E_s = 1.6, 5) in respect to the scaling factor a/t, see Figure 8-16. It appears that as the mismatch on elastic moduli increases, the transition from initial to final plateau, initiates at lower indentation depths. If the O&P method would be used to analyse experimental data on coated systems, and for the case where the percentage error would be restricted to less than 10%, then it can concluded as a general rule that for E_f/E_s = 1.6, maximum indentation depth must be kept under a/t <0.5, while for E_f/E_s = 5, a/t < 0.08 and naturally this restriction will become more stringent as the moduli mismatch ratio increases.

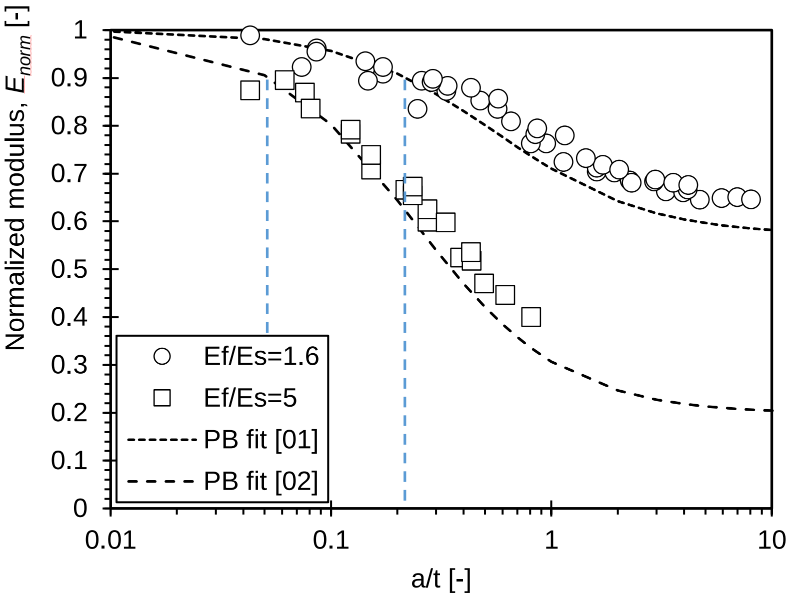

Figure 8-16: Normalized equivalent modulus for a large span of a/t. Blue lines are indicating the limit factor of 10% deviation from thin film's elastic modulus.

8.4 Nanoindentation on Hydrogenated Amorphous Carbon Film

As an application of the FEM model developed herein we have performed a combined experimental numerical investigation in which thin films have been deposited and characterized using a nanoindenter; the experimental data analysis was performed using both analytical and numerical tools.

For very thin films, the restrictions posed by Figure 8-16 might not be experimentally tractable and one is therefore left with the only possibility of concurrently treating the experimental data with computational feedback such as to extract film-only properties. Such an approach is proposed and experimentally verified below on a coated system composed of a hydrogenated amorphous carbon thin film on a silicon substrate. The deposition conditions, characterization process and the proposed coupled computational/experimental methodology for extracting the film's properties follow.

8.4.1 a-C:H Thin Film Deposition

Hydrogenated amorphous carbon (a-C:H) films were deposited using a plasma enhanced chemical vapor deposition (PECVD) system. A schematic of the deposition chamber which is installed at the Research Unit for Nanostructured Materials Systems is presented in Figure 8-17 (a). PECVD was enabled through radio frequency (RF) ion-beam technology, a diagram of which is presented in Figure 8-17 (b). The ion beam source has an external RF antenna that spirals around the plasma tube in the form of a coil. The RF waves emitted by the antenna enter the transparent plasma tube to ionize the gas introduced therein to produce charged ions. The main chamber of the system was pumped down to 10^{-8} mbar (basic pressure) using a roughing and a turbo-molecular pump. The energetic carbon/hydrogen ions generated from this gas-cracking process (methane ($\mathrm{CH_4}$) was used in this study) were accelerated towards the substrate by a voltage applied on a grid located between the plasma source and the substrate material. The voltage applied on the grid related to the kinetic energy of the ions. The transportation of ions from the source to the substrate occurs in line of sight conditions and a working pressure of approximately 10^{-3} mbar, the exact value of which depends on the total gas flow within the discharge tube. The accelerated ion species were deposited on the substrate material to grow hydrogenated amorphous carbon ($\mathrm{a-C:H}$) films. The ion beam arrived at an incidence angle of 30° to the substrate which was located 22 cm away from the ion beam.

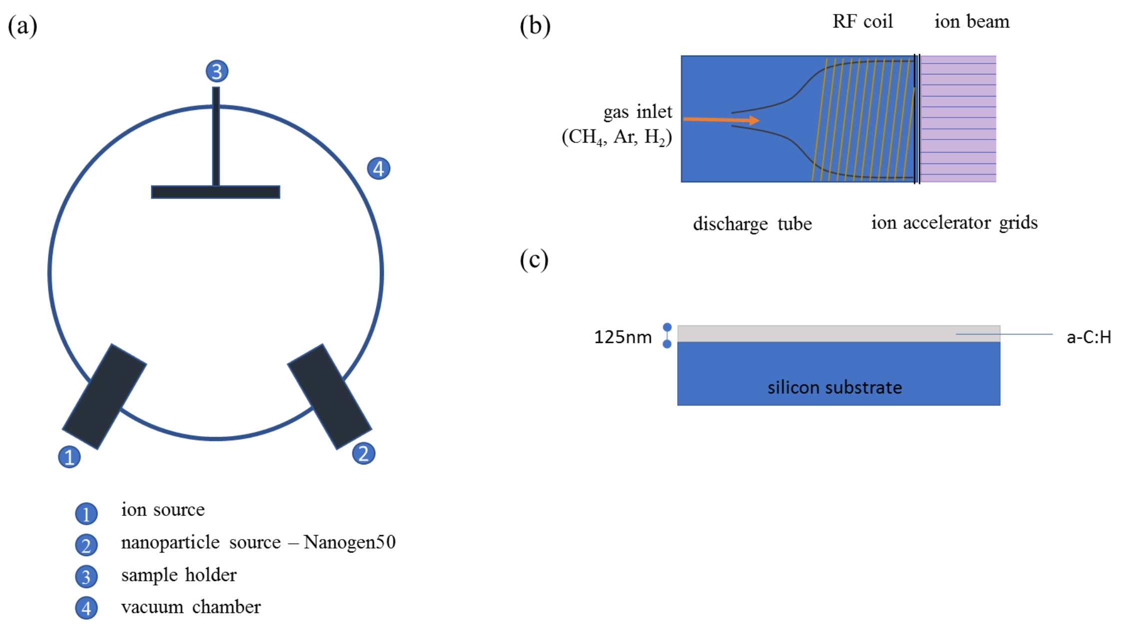

Figure 8-17: (a) Schematic of the hybrid PECVD/PVD system used within this study; Details of (b) the ion source and (c) the deposited film.

8.4.2 Thin Film Characterization

8.4.2.1 X-ray reflectivity

An X-ray diffractometer (Rigaku Ultima IV) was used to measure the specular X-ray reflectivity of the deposited film. The diffractometer was equipped with a Cu tube, operated at 40 kV accelerating voltage and 40 mA emission current. The incidence X-ray beam was collimated into a parallel beam with a 0.03 divergence and additionally monochromatized to Cu Ka (λ=0.15419 nm) by a curved multilayer mirror. Density and thickness values of the thin films were extracted by fitting the respective experimental data to the theoretical reflectivity calculated using Parratt’s formalism [148–150].

8.4.2.2 Raman spectroscopy

The microstructural details of $\mathrm{a-C:H}$ were probed using Raman spectroscopy. This characterization method was employed in order to access the bond characteristics of the deposited $\mathrm{a-C:H}$ films and indirectly link the information with $\mathrm{sp}^2/\mathrm{sp}^3$ configurations, and hydrogen content (i.e., through I_D/I_G and FWHM(G)) [151]. Raman data were collected by a confocal LabRAM from HORIBA Jobin Yvon equipped with a CCD detector and 1800 grooves/mm grating. It is equipped with an Olympus BX41 microscope

(10X, 15X, 40X, 50X and 100X). The 441.1 nm excitation laser beam was provided by a Helium-Cadmium laser. The laser power incident on the sample was 3-4 mW and the accumulation time 15-20 min for each spectrum.

8.4.2.3 Atomic force microscopy

Atomic force microscopy (AFM) was used to quantify the roughness of the resulting films. All measurements were performed in semi-contact mode using a scanning probe microscope (Ntegra Prima, NT-MDT) equipped with an NT-MDT cantilever (NSG10) having a mean force constant of $11.8\ \mathrm{N/m}$ and a tip nominal radius of $6\ \mathrm{nm}$. Images of $3\ \mu\mathrm{m} \times 3\ \mu\mathrm{m}$ and 256×256 data density were collected and subsequently software-analyzed for quantifying the root mean square (RMS) roughness of the deposited $\mathrm{a-C:H}$ surfaces.

8.4.2.4 Nanomechanical testing

The nanomechanical response of the deposited $\mathrm{a-C:H}$ films was tested on an instrumented nanoindentation platform (Micro Materials Ltd, UK) in a load-unload (single depth) mode using a diamond tip of the Berkovich type. During the indentation process the applied load (P) and corresponding depth of penetration (h) were continuously monitored with nanoscale accuracy – $100\ \mathrm{nN}$ for load and $0.1\ \mathrm{nm}$ for displacement. The specimens were probed using a maximum load of 0.5 mN; a 60 s dwell time was introduced at 90% of unloading force in order to collect data for thermal drift corrections. Ten indents ($P - h$ curves) at various locations on the film surface were collected, ensuring reproducibility.

8.4.3 Results and Discussion

Hydrogenated amorphous carbon films of 125 nm (confirmed through XRR reflectivity data) in thickness were deposited on silicon substrates. The root mean square roughness of the films was calculated through AFM scans (Figure 8-18(a)) at 0.4 ± 0.1 nm. The Raman spectra of the a-C:H are presented in Figure 8-18(b) and exhibit the characteristics of amorphous carbon. The cumulative response was deconvoluted to the D-band (~$1350\ \mathrm{cm}^{-1}$) and G-band (~$1550\ \mathrm{cm}^{-1}$) contributions using Gaussian fits. Several important metrics, including the location of the G peak, the intensity ratio of D over G peaks (I_D/I_G) and the full width at half maximum of the G Peak ($\mathrm{FWHM\,(G)}$) were extracted. In general, the D peak is due to the vibration of sp^2 rings and the G peak to the resonance of the sp^2 atoms organized in both rings and chains. Subsequently, the higher the I_D/I_G ratio the higher the sp^2 clustering within an $\mathrm{a-C:H}$ sample. The intensity ratio of $\mathrm{a-C:H}$ yields a value of $I_D/I_G = 0.45$. Empirical relations obtained from experimental data on a large collection of data on hydrogenated amorphous carbon films suggest that this intensity ratio is inversely related to both hydrogen content [151] and (indirectly through the Tauc gap) sp^3 hybridization state [152]. A comparison of this experimentally obtained value with literature data suggests that the $\mathrm{a-C:H}$ film synthesized within this study consists of a hydrogen content of 20-25 at.% and an sp^3 content of approximately 50 at.%. An $\mathrm{a-C:H}$ film with such characteristics is commonly referred to as diamond-like $\mathrm{a-C:H}$ (DLCH) with density values that vary between $1.5\ \mathrm{g/cm^3}$ to $1.8\ \mathrm{g/cm^3}$ and high sp^3 bonds (up to 70 at.%), a significant percentage of which are hydrogenated terminated [153,154]. Indeed, our $\mathrm{a-C:H}$ matrix with a density of $1.7\ \mathrm{g/cm^3}$ (measured through XRR), hydrogen content of ~25 at.% and sp^3 content of ~50 at.% falls within the DLCH category [151]. The $\mathrm{FWHM(G)}$ probes the structural disorder of the sp^2 clustering in amorphous carbon material [152,155]. A lower $\mathrm{FWHM(G)}$ value denotes an $\mathrm{a-C:H}$ with less unstrained sp^2 clustering, whereas a higher $\mathrm{FWHM(G)}$ value suggests a material with an increased disordering in bond lengths and angles for the sp^2 clusters. $\mathrm{FWHM(G)}$, I_D/I_G and G peak position are all consistent with literature results for such films [156–158].

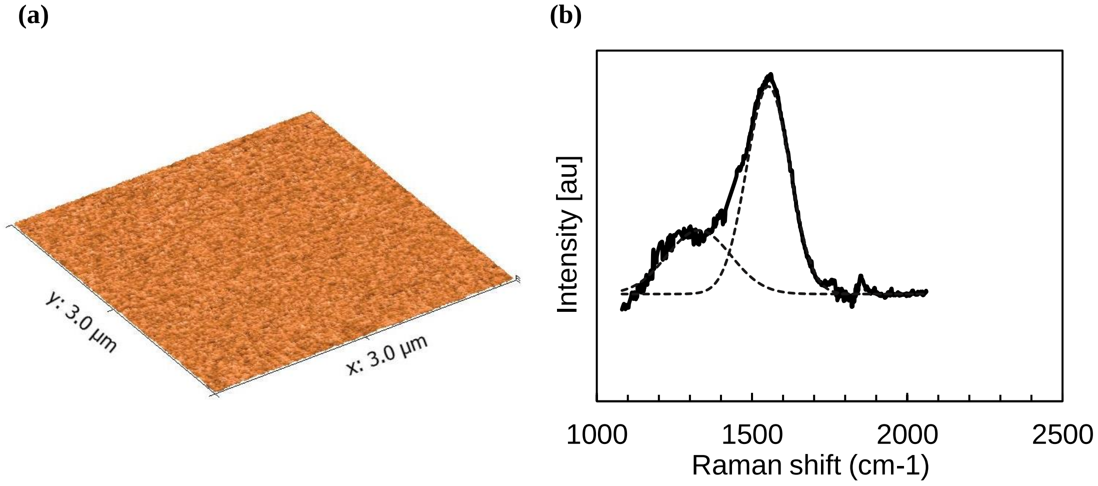

Figure 8-18: (a) AFM image and (b) raman spectra of the deposited a-C:H film.

The mechanical response of the deposited film was measured using nanoindentation at 0.5 mN which resulted in maximum indentation depths of 34-38 nm (very good repeatability). Since the global response at such depths is affected by both the film and the substrate one cannot directly extract the film properties. A comparison of FEM simulation results will be performed in order to identify the optimal film properties that better reflect the experimental data. Before proceeding with such an endeavor two preliminary studies are required to tackle such a problem: (a) a parametric analysis on the effect of the mechanical properties of the film (E and Y) on the overall $P - h$ response is needed that will aid the fitting process, and (b) the exact geometrical characteristics of the used probe are required as this might affect the $P - h$ responses at such small scales (sub-50 nm indents).

8.4.3.1 Effect of E_f and Y_f on $P - h$ response

A series of simulations were performed for investigating the effect of E and Y on the overall response at such small depths and the results are presented in Figure 8-19. The effect of E_f is shown in Figure 8-19 (a) and appears to affect both the unloading slope and peak load, whereas the effect of Y_f is minimally affecting the unloading slope and primarily affects the peak load. These observations allow one to partly decouple the fitting process by concentrating primarily on the unloading slope for identifying the elastic modulus of the film and subsequently quantifying the yield strength based on the peak load resistance of the system. This will be explored in the fitting analysis that will follow.

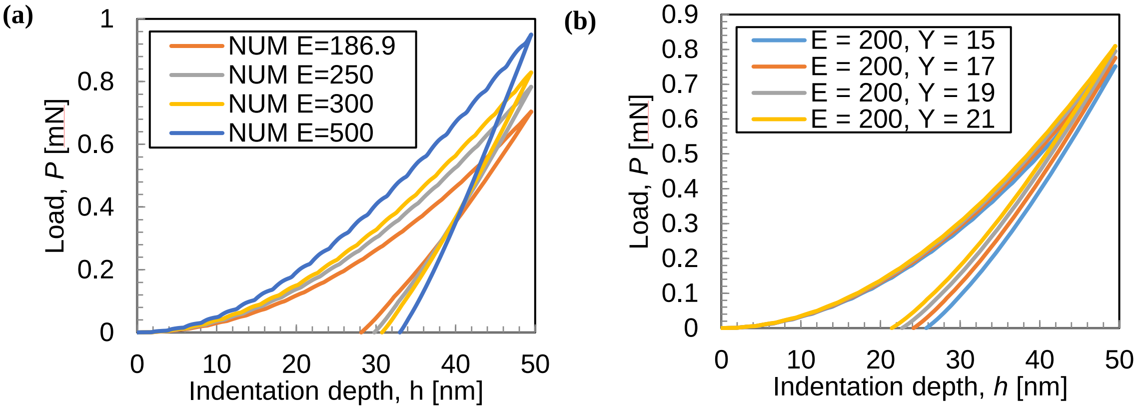

Figure 8-19: Effect of (a) elastic modulus of the film and (b) the yield strength of the film on the simulated $\boldsymbol{P} - \boldsymbol{h}$ response of the layered system, where $\boldsymbol{v_f}$ = 0.15, $\boldsymbol{Y_f}$ = 6.53 GPa, $\boldsymbol{t}$ = 150 nm, $\boldsymbol{E_s}$ = 169.4 GPa, $\boldsymbol{v_s}$ = 0.278 and $\boldsymbol{Y_s}$ = 7 GPa.

8.4.3.2 Effect of Tip Roundness on $P - h$ response

Before proceeding with the fitting process, we wanted to investigate the sensitivity of the results on the exact geometrical details of the tip, due to the very small indentation depths used herein. It is reported in the literature that commercial Berkovich indenters while nominally sharp may contain some bluntness at their very tip that could be approximated with a sphere. We have therefore performed a series of simulations assuming a conospherical geometry rather than a perfect conical geometry, in which the radius of the sphere is systematically altered (R = 100 nm, 200 nm and 500 nm). The simulated $P - h$ results for three different conospheres are shown in Figure 8-20 (a) and the resulting stress and plastic strain fields distributions in Figure 8-20 (b). Interestingly the exact details of the local bluntness can have a significant impact in the overall response; the higher the local radius the higher the indentation resistance that is generated during penetration. This response can be attributed to the more rapid evolution of the contact area with depth expected for a conospherical geometry as compared with an ideal sharp cone. Furthermore, the increased radius leads to an increase in the stress distribution and an extention of the plastic strain fields that might even extend beyond the film domain and tranfer into the substrate.

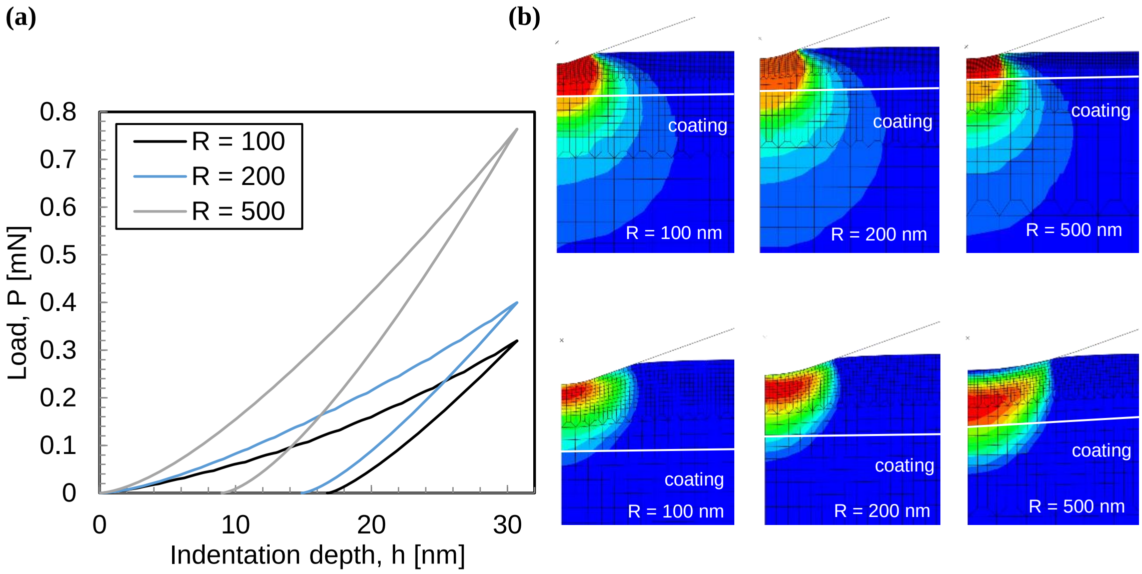

Figure 8-20: (a) Effect of of the local tip radious (a conosphreical indenter is assumed) on the simulated $\boldsymbol{P - h}$ response of the layered system, where $\boldsymbol{E_f}$ = 100 GPa, $\boldsymbol{v_f}$ = 0.17, $\boldsymbol{Y_f}$ = 8 GPa, $\boldsymbol{t}$ = 100 nm, $\boldsymbol{E_s}$ = 169 GPa, $\boldsymbol{v_s}$ = 0.278 and $\boldsymbol{Y_s}$ = 7 GPa. (b) Resulting stress and plastic strain fields for the various consophericalindenters considered herein ($\boldsymbol{R}$ = 100 nm, 200 nm and 500 nm).

Following the above analysis, it was found imperative to account for the potentially present local bluntness of the probe used in these experiments and avoid the propagation of any errors into the fitting process. Therefore, the exact area function of the indenter was obtained by performing a series of multi-depth indents on a material with known elastic modulus (quartz) and back calculating the area of contact using Equation (2.33). The experimental data of the area of contact with contact depth together with theoretical area function of the perfect cone are presented in Figure 8-21(a). It is obvious that the perfect conical geometry approaches the experimental results at higher indentation depths (h>100nm) and for small indentation depths a significant deviation exists which is attributed to the non-ideal geometry. In order to quantify the local tip bluntness, the experimental data at contact depths less than 30 nm were best-fitted to the ideal spherical area function (Figure 8-21(b)) with the resulting radius been 301 nm. It is apparent that the spherical geometry quantifies well the area function below h = 30 nm, and the optimized conospherical geometry is in excellent agreement with experimental data over the whole h = 0-150 nm range (Figure 8-21(a)). For all subsequent calculations therefore the conospherical geometry is used.

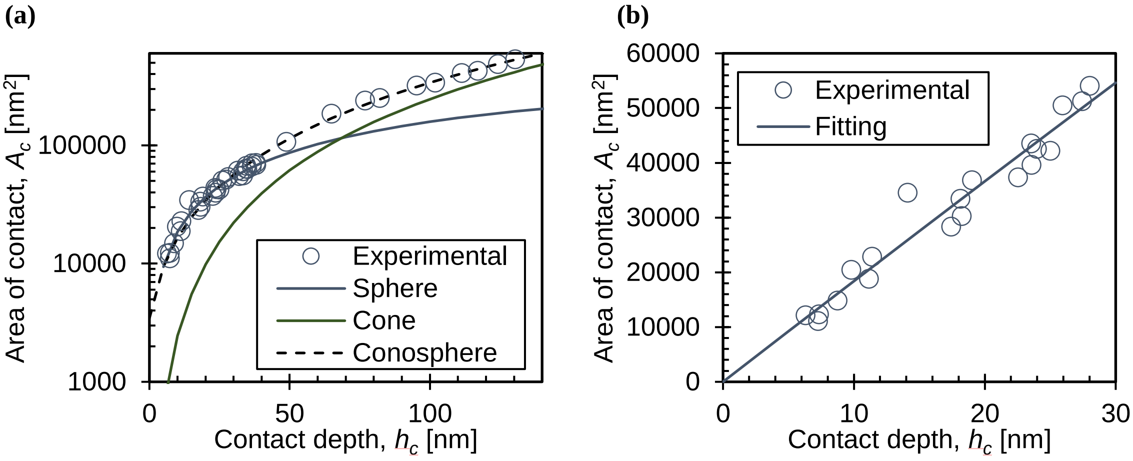

Figure 8-21: (a) Theoretical equations (for perfect sphere and perfect cone) and experimental data on the area function of indenter used in this study. (b) Best-fitted spherical equation (R~300nm) on the sub-30nm experimental data.

8.4.3.3 Calculating the Mechanical Properties of the a-C:H Film

In the following analysis the mechanical properties of the film were kept as variables and were systematically altered until the error between the simulated $P-h$ response and experimental is minimized. Within this process the parametric analysis presented above used for guiding, meaning that the unloading portion of the curve is first fitted and subsequently maximum depth is optimized by varying the yield strength of the film. The results of this optimization process are presented in Figure 8-22 (a) and the film mechanical properties that yielded this response are $E_f = 100$ GPa and $Y_f = 8$ GPa. These properties are close to what is expected for hydrogenated amorphous carbon films of such compositions (sp^3 and H content) and verify the proposed methodology as alternative means for extracting mechanical properties of low dimensional materials. Furthermore, through this numerical methodology, one can obtain useful mechanical information (stress, strain, energy data) that are not available in experiments; Figure 8-22(b) illustrates the von Mises and plastic strain distribution within the a-C:H/Si system for h_{max} = 33.5 nm, the correspondence $P - h$ curve is affected by the substrate's plasticity.

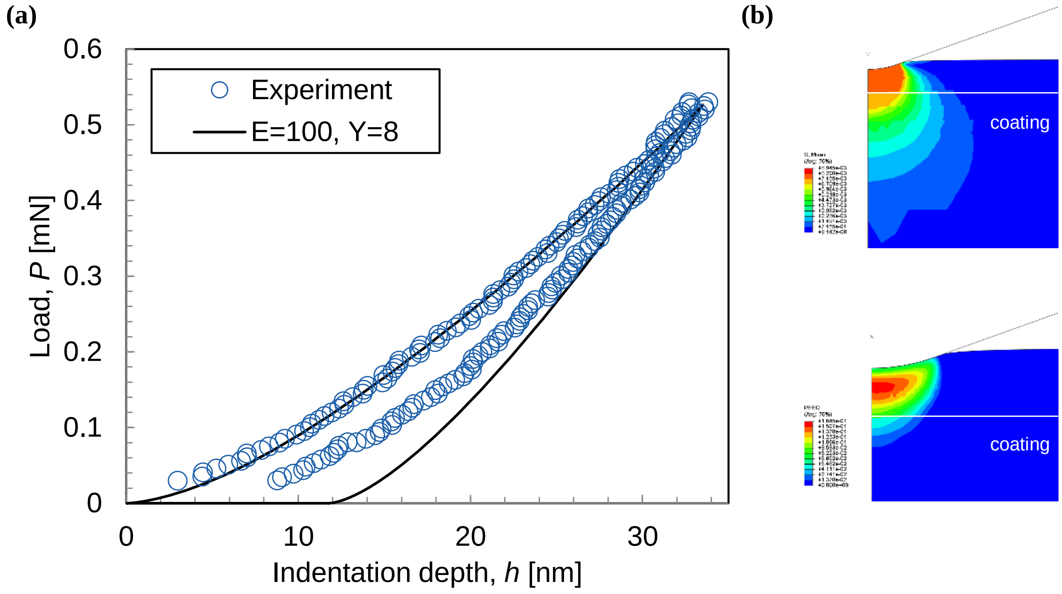

Figure 8-22: (a)Simulated vs experimental $\boldsymbol{P - h}$ curves on the a-C:H film. (b) Contour plots of generated von-Mises stresses and equivalent plastic strains at maximum penetration depth.

8.5 Chapter Summary

Numerical analysis of stiff coatings on soft substrates have been proposed based on elastic and elastic-perfect materials systems. We demonstrated that the plastic deformations generated within the indented film, decrease the indentation resistance of the coated system and depending on the moduli mismatch, the surface may exhibit pile-up phenomena, which may subsequently lead to an overestimation of the calculated mechanical properties of the projected area of contact is calculated using the Oliver and Pharr methodology [2,3]. In addition, numerical modelling is able to capture the sigmoidal behaviour on composite modulus, which is independent from material properties, film thickness and elastic moduli mismatch; a universal curve. Finally, for ulttra thin films a combined experimental-computation methodology is proposed for extracting the mechanical properties of the films which has been demonstrated on a hydrogenated amorphous carbon film deposited on silicon substrate. The importance of tip blunting has been noted and should be included in such type of analyses.

Chapter 9

Indentation Response of Cohesive Frictional Materials

Pressure-sensitive materials like cement-based composites, soils, shales, and bulk metallic glasses have been reported to exhibit enhanced indentation hardness compared to their pressure-insensitive counterparts. While nanoindentation experiments on these materials have been reported in the literature a detailed analysis framework that takes into consideration the peculiarities of their complex mechanical response has not been developed in full. This chapter attempts to contribute towards this end by presenting numerical results of indentation on cohesive-frictional materials, modeled using the Mohr-Coulomb yield criterion. Its' ultimate focus is to explore through nanoindentation simulations the link between hardness of cohesive-frictional materials and strength properties. Dimensional analysis will be employed for the understanding of all governing parameters of these materials, while parametric studies will be performed by varying the cohesion and frictional angle.

9.1 Introductory Remarks

9.1.1 Cohesive-Frictional Materials

Tabor [159], suggested a relationship between hardness over yield strength H/Y = 3 in a fully plastic contact, which corresponds to materials with high ratio of E/Y such as metals. For materials with low E/Y, like ceramics, this ratio is lower at H/Y = 1.5 – 2, [57,160], which relates to the fact that microcracking might be generated during loading that shifts the H/Y ratio at lower values than those of full plasticity. The value of H/Y is commonly used as a rule-of-thumb, either for experimental purposes; extraction of stress–strain curve from indentation data, or computationally; definition of yield point for input parameter to finite element model. Many authors, however, have highlighted that this ratio can drive analysis to inaccurate results for various materials systems like amorphous metallic glasses [161], work-hardening materials [56], cement-based materials [30,162,163] and rigid plastic solids with and without contact friction [164,165]. Specially, for cohesive-frictional materials (soils, shales, amorphous metals, concrete) the ratio between hardness and compressive strength can reach values on the order of $H/Y_c \approx$ 10-30. Thus, the focus of this study is to explore the effect of cohesive strength and frictional angle of Mohr-Coulomb materials under numerical conical indentation simulations and identify their relationship with indentation hardness.

The accurate estimation of the indentation response of those materials is of great importance due to their wide applicability in structural applications. For example, imprecise measurement of the mechanical response of rocks, may lead to failure of drilling wells in oil and gas industry. The major difference between pressure insensitive and cohesive-frictional materials is that the latter class exhibits a shear strength that scales with the hydrostatic pressure of the material; the higher the compressive hydrostatic pressure, the higher its shear strength. A specific characteristic of cohesive-frictional materials is that usually in compression tests exhibit plastic deformation, while in tensile tests display brittle behavior. Hence, due to their large hydrostatic compression strength, nanoindentation testing is the most suitable technique for characterizing the mechanical properties of these materials. Advanced modeling needs to take place in order to capture the mechanical response of cohesive-frictional materials. Some experimental and numerical indentation studies [19,20,166–170] have been performed to correlate the cohesive-frictional strength parameters with indentation hardness, and evaluate computational results with experimental data to obtain scaling relations. Finite element modeling on cohesive-frictional materials showed that the Mohr-Coulomb criterion could accurately represent their indentation response. A special material that is assumed to comply with the Mohr-Coulomb yield criterion is the ultrastructure of bone [171–173].

9.1.2 Dimensional Analysis

Before proceeding to the numerical analysis and given that hardness is the key parameter of the current study, dimensional analysis of conical indentation on a Mohr-Coulomb material will help us develop meaningful expressions. We recall that indentation hardness is defined as the ratio between maximum indentation load P over the projected area of contact A_c and these two dependent quantities can be expressed as:

$$P = f(E, v, c, \theta, \varphi) \tag{9.1}$$

$$A_c = f(E, v, c, \theta, \varphi) \tag{9.2}$$

where E, v, c, φ represent the elastoplastic properties of the cohesive frictional material and θ the half-apex angle of the conical indenter, which for the case of Berkovich equals to 70.32°. From Buckingham Π theorem analysis, Equations (9.1) and (9.2) result in the following two dimensionless relations:

$$\frac{P}{ch^2} = \Pi_7\left(\frac{E}{c}, v, \theta, \varphi\right) \tag{9.3}$$

$$\frac{A_c}{h^2} = \Pi_8\left(\frac{E}{c}, v, \theta, \varphi\right) \tag{9.4}$$

and subsequently, the ratio between them defines another dimensionless relation; the hardness to cohesion ratio:

$$\frac{H}{c} = \frac{\Pi_7}{\Pi_8} = \Pi_9\left(\frac{E}{c}, v, \theta, \varphi\right) \tag{9.5}$$

In 2006, Ganneau *et al.* [19], observed that there is strong dependence between H/c ratio and cone indenter semi-angle θ which due to internal friction angle φ variations. Therefore, they proposed a dual-indentation procedure based on computational yield design theorems (fully plastic, $E/c \to \infty$) and on the relation between H/c and two hardness measurements for Berkovich (θ = 70.32^o) and Corner Cube (θ = 42.28^o) indenters.

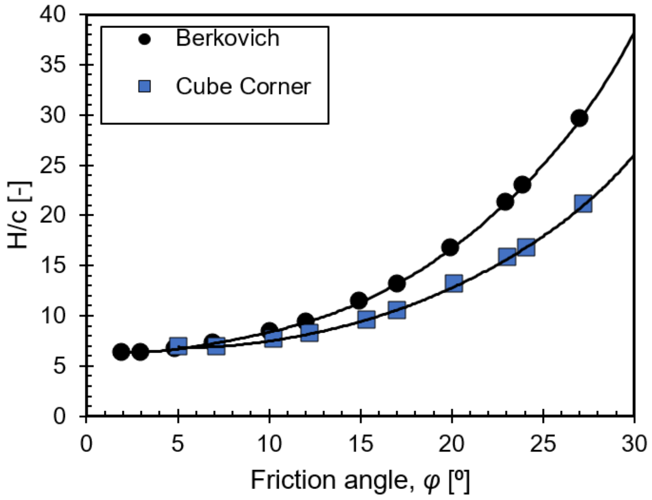

Figure 9-1: Upper bound solutions for $\boldsymbol{H/c}$ ratio for two conical indenter geometries: Berkovich and Cube Corner (data from [19]).

Figure 9-1 illustrates the relation that the H/c obtains as a function of the angle of friction for these two conical indenter angles. It should be noted that for small friction angles, the two curves converge to the value for a Tresca material, given by Tabor as $H/c = 2H/Y \approx$ 5.6. The practical result from the above procedure, is that indentation testing can assess the cohesive-frictional properties of a material provided experiments with two indenters are performed. It becomes apparent that the ratio of the hardness values obtained by two different indenters, here Berkovich and Cube Corner, becomes a unique function of the angle of friction:

$$\frac{H_B}{H_{CC}} = \frac{\Pi_9(\varphi, \theta = 70.32^0)}{\Pi_9(\varphi, \theta = 42.28^0)} \tag{9.6}$$

The numerically calculated dependency of this ratio to the angle of friction is presented in Figure 9-2. It is obvious that the ratio of hardnesses gives access to the internal friction angle of a material through the results presented in Figure 9-2 and the higher the discrepancy in hardness between the two indenters the higher the angle of friction. Once the angle of friction is estimated, the cohesion value can be readily calculated by substituting the friction angle to a single H/c curve shown in Figure 9-1. While this methodology has been proven practical and important, the curves presented in Figure 9-1 and Figure 9-2, neglect the elastic component of the material by assuming fully plastic yield approach. Thus, in the current study we will employ the finite element analysis to quantify the effect of elasticity on the overall response.

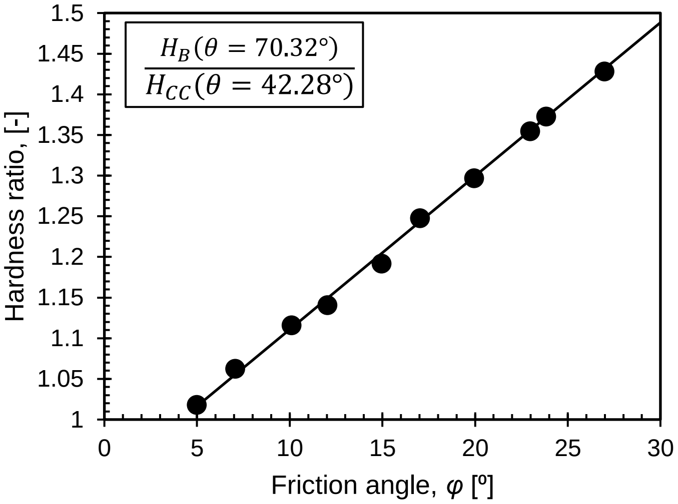

Figure 9-2: Hardness ratio (Berkovich/Cube Corner) as a function of internal friction angle(data from [19]).

9.2 Finite Element Model

9.2.1 Geometry and Mesh Details

Two-dimensional axisymmetric finite element simulations are performed to investigate the elastic-plastic indentation response of cone on cohesive-frictional materials with various cohesion and friction angle values. For the case of conical indentation, the indenter was modeled as a rigid cone with half-apex angle of θ=70.3°. The geometrical details of the finite element model used in this study are the same as the one described in Chapter 3.4. The indentation simulations were restricted to depths up to 939 nm, in order to avoid any boundary effects. The continuum space is discretized using 4–node axisymmetric, isoparametric elements (CAX4–full integration).

Roller boundary conditions were applied on the axis of symmetry and fixed boundary conditions on the bottom surface of specimen. We assume that the loading rate is slow enough such as static friction can securely model the interface response. Simulations proceeded in two steps: the indenter was firstly subjected to a ramped vertical displacement, followed by an indenter retraction to the original position which corresponded to complete unloading at zero load. During this process the lower edge of the material was constrained vertically. Axisymmetric boundary conditions were used along the symmetry axis beneath the indenter region [64].

9.2.2 Mohr-Coulomb Yield Criterion

Materials that display pressure-sensitive plastic behavior can be numerically approached by the Mohr-Coulomb (MC) yield criterion, in which the relation between critical shear strength τ and normal strength σ that defines the pressure-sensitive yield surface is:

$$\tau = c - \sigma \tan\varphi \tag{9.7}$$

where c is the cohesion of the material and φ is the material angle of friction. Figure 9-3 illustrates major yield criteria based on their pressure sensitivity. Tresca and von-Mises criteria used for modeling crystalline metals, which are pressure-insensitive materials. Both criteria are represented by prisms along the hydrostatic pressure axis, where Tresca yield criterion is illustrated by a hexagon prism and von-Mises by cylindrical prism (both open on the hydrostatic axis). On the other hand, Mohr-Coulomb and Drucker-Prager criteria, used for the characterization of pressure-sensitive materials, exhibit a shear strength that scales with hydrostatic pressure. Both criteria are represented by cones along the hydrostatic pressure axis, where Mohr-Coulomb is generated by an irregular hexagon and Drucker-Prager by a circle. The location of the point where the Mohr's circle touches the failure envelope line is defined by the angle 2θ.

In addition, the angle 2θ relates to the frictional angle φ through:

$$\varphi = 2\beta - \frac{\pi}{2} \tag{9.8}$$

The Mohr-Coulomb criterion can be rearranged and stated as a function of the principal stresses:

$$\sigma_1 = 2c\frac{\cos\varphi}{1-\sin\varphi} + \sigma_3\frac{1+\sin\varphi}{1-\sin\varphi} \tag{9.9}$$

where the second term of Equation (9.9) represents the compressive yield strength of a Mohr-Coulomb material Y_c:

$$Y_c = 2c\frac{\cos\varphi}{1-\sin\varphi} \tag{9.10}$$

For the case of φ = 0^o, the Mohr-Coulomb criterion reduces to the Tresca criterion, for which Equation (9.10) predicts that $Y_c = 2c$.

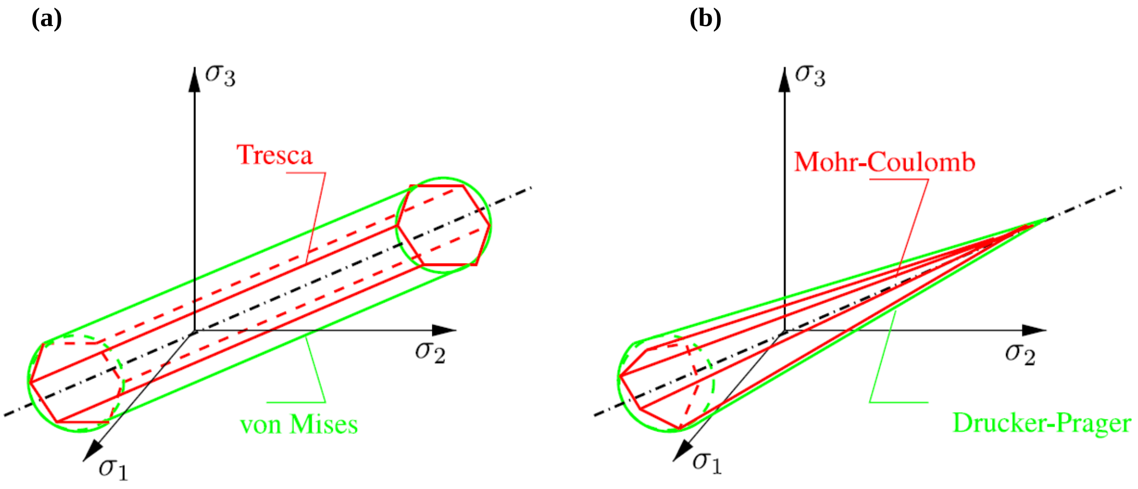

Figure 9-3: Yield criteria in the principal stresses space [174] where (a) represents pressure independent materials; Tresca and von-Mises, (b) represents pressure-sensitive materials; Mohr-Coulomb and Drucker-Prager.

The isotropic form of the Mohr-Coulomb material model is controlled via elastic modulus E, Poisson's ratio v, cohesion strength c and friction angle φ. By varying those properties we have generated parametric studies from the finite element simulations, to correlate the strength of cohesive-frictional materials with hardness values. Generally speaking, through compression testing and via stress-strain curves, the elastic modulus and the yield strength of materials can be calculated. Hence, for this study, the compressive yield strength Y_c and Poisson's ratio v, are assumed to be constant for all numerical studies, in order to investigate how cohesion and friction angle affect the mechanical response of a Mohr-Coulomb material. By setting the initial values of Y_c = 5 GPa, v = 0.17 (based on nanoindentation data for fused quartz) and φ = 0°-30°, and by solving Equation (9.10), the reduced cohesion values have been calculated for each friction angle such as to maintain the same yield strength value, Figure 9-4.

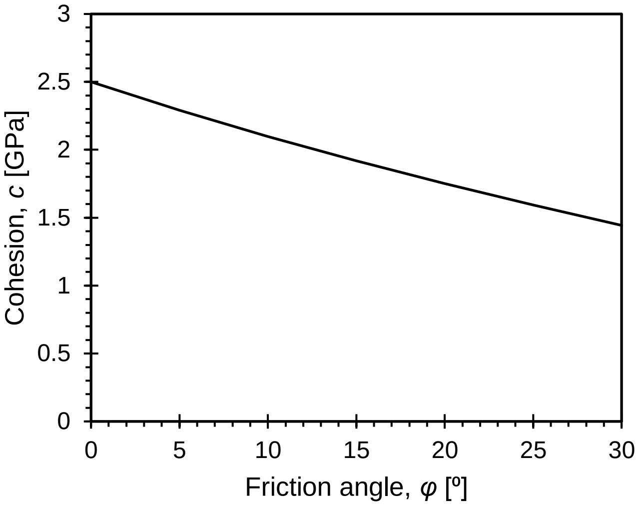

Figure 9-4: Estimation of reduced cohesion for constant compressive yield strength $\boldsymbol{Y_c}$ = 5.

Table 9-1 summarizes the numerical simulations performed in the current study. Please note that selected values may seems unnatural due to their high values, but they scale down due to the self-similarity of conical indentation testing.

Table 9-1: Material properties used for the finite element simulations.

Model Name	c [GPa]	φ [º]	E [GPa]	v [-]	E/c [-]
A: 28.8					
A1	2.50	0	72	0.17	28.8
A2	2.29	5	72	0.17	31.44
A3	2.10	10	72	0.17	34.29
A4	1.92	15	72	0.17	37.5
A5	1.75	20	72	0.17	41.14
A6	1.59	25	72	0.17	45.28
B: 72					
B1	2.50	0	180	0.17	72.0
B2	2.29	5	180	0.17	78.6
B3	2.10	10	180	0.17	85.71
B4	1.92	15	180	0.17	93.75
B5	1.75	20	180	0.17	102.86
B6	1.59	25	180	0.17	113.21
C: 288					
C1	2.50	0	720	0.17	288.0
C2	2.29	5	720	0.17	314.41
C3	2.10	10	720	0.17	342.86
C4	1.92	15	720	0.17	375.0
C5	1.75	20	720	0.17	411.43
C6	1.59	25	720	0.17	452.83
D: 2880					
D1	2.50	0	7200	0.17	2880.0
D2	2.29	5	7200	0.17	3144.10
D3	2.10	10	7200	0.17	3428.57

9.3 Model Validation

Prior to presenting any parametric analysis results the model was benchmarked against experimental data in order to confirm its accuracy and ability to realistically capture the physical response of cohesive-frictional systems. Two benchmarking schemes were used that are presented next.

9.3.1 Benchmark 1: Convergence to the Von-Mises response

Experimental results on fused quartz are plotted against numerical results in Figure 9-5. The derived response of material with $\varphi = 0$ approaches the response of experimental findings and this can be stand as a verification – convergence study, of the finite element model and the selected input values of material's properties.

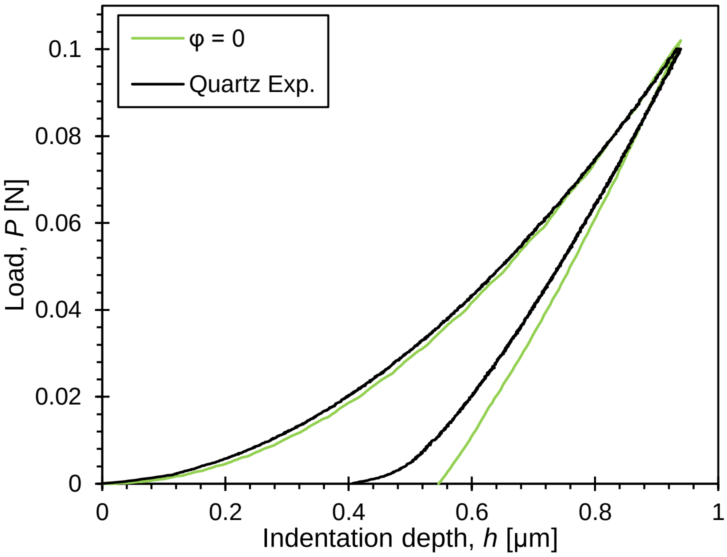

Figure 9-5: Convergence study for estimating input values of Load – displacement response for sharp indentation on fused silica, where the dashed line represents the results of experimental and solid lines indicates the results of numerical findings.

9.3.2 Benchmark 2: Indentation Bulk Metallic Glass

The equilibrium state of a metal is reached when located in its lowest energy state structure and practically is characterized by polycrystallization instead of single crystals, due to varying grain sizes and shapes. A special family of metals, bulk metallic glasses – amorphous alloys, are materials characterised by the absence of crystal structures due to extreme cooling rates from their liquid phase. As a result, grain boundaries and dislocations that are essential in crystalline materials, do not exist and bulk metallic glasses exhibit superior mechanical properties such as: strength-to-weight ratio, large elastic deformation capacity, anti-corrosion resistance and high fracture toughness which considered them today as emerging structural candidates. The first metallic glass was made in 1960 from a binary metallic alloy $Au_{80}Si_{20}$ by cooling rates of over 10^5 K/s [175,176]. At that time, metallic glasses could only be hundreds of microns thick which was too thin for practical applications. In the early 1980s, it was found that the alloying procedure of metals with varying atomic size, reduces the cooling rate and therefore bulk metallic glasses could be formed in larger scales. As a result, amorphous metal alloys became a topic of considerable research for structural and sport equipment applications.

Experimental results of Berkovich indentation data on a commercially available bulk metallic glass $Zr_{41.25}Ti_{13.75}Cu_{12.5}Ni_{10}Be_{22.5}$ (nominal composition in at.%) [169] are illustrated in Figure 9-6 (a). In the current study, we examined the response of the current material under finite element analysis, by assuming either the von-Mises or Mohr-Coulomb criteria and the results are also superimposed in Figure 9-6 (a). Both materials were constructed with equal E = 96 GPa, v = 0.36, Y-c = 834 MPa and φ = 7.4° for Mohr-Coulomb material. It is obvious, that MC model can predict experimental data with high accuracy which confirms its ability to simulate effectively cohesive-frictional material, in contrast with the von-Mises model. The effect of frictional angle plays a major role in the indentation response of a material, since it is influenced by the normal stress and can increases the indentation resistance significantly, here in a factor of 2. Moreover, this increased resistance is demonstrated in Figure 9-6 (b) - (c), where von-Mises material exhibits "softer" response against MC material, due that its surface which is in contact with indenter has been covered by a fully plastic zone.

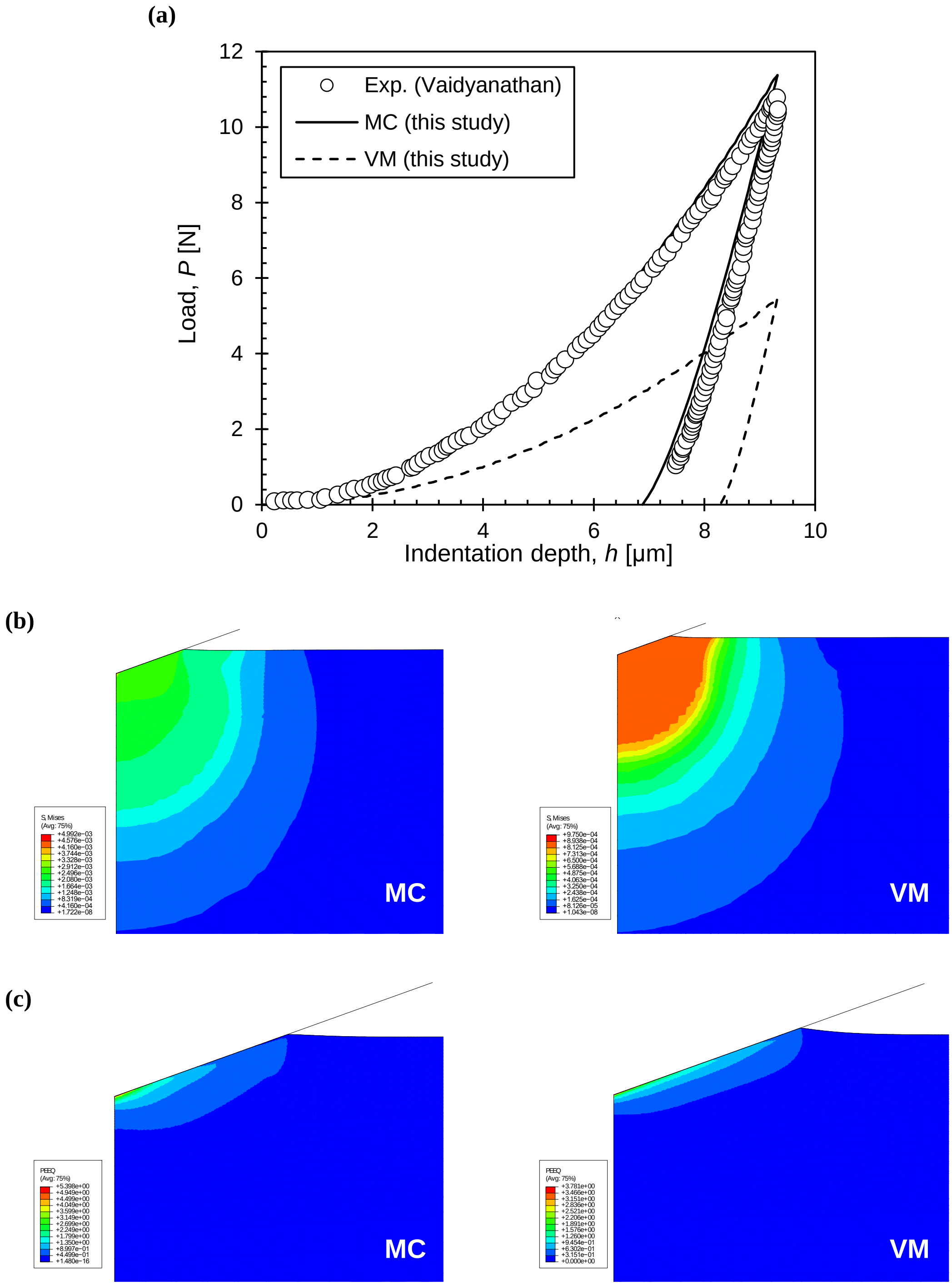

Figure 9-6: (a) Indentation response of bulk metallic glasses, where numerical results of Mohr-Coulomb materials are in excellent agreement with data from literature [169]. In contrast, the effect of frictional angle is demonstrated in terms of (b) stress, where von-Mises material exhibit decreased resistance and in terms of (c) strain, where a fully plastic zone under the contact with conical indenter was predicted for a von-Mises material.

9.4 Numerical Results on Cohesive-Frictional Materials

9.4.1 $P - h$ responses

Numerical $P - h$ curves were extracted from finite element simulations for a cohesive-frictional material with a series of $c - \varphi$ combinations as shown in Table 9-1. Figure 9-7 (a) illustrates the results of A:28.8 group including the experimental data on quartz. It is obvious that any increase of the internal angle of friction leads to an increased resistance to penetration; i.e. cohesive-frictional material shows an enhanced hardness response. If one looks at the stress distributions within the indented materials it becomes apparent that the stress zones increases as φ increases. In addition, larger applied loads are required to overcome the internal friction of a material and generate plastic deformations. As a result, while φ increases, materials exhibit more elastic deformation, and this can be obtained from the trend of the residual final depth h_f which shifts towards the origin for higher φ. Similar, and more enhanced behaviour is extracted for the second group B: 72, Figure 9-7 (b), for which the indentation resistance enhancement is more obvious, due to the higher mismatch between elastic modulus E and cohesion c. As this ratio increases, numerical materials undergo larger plastic deformations and subsequently a higher percentage of the work done is dissipated.

Figure 9-8 presents the computational curves for the larger E/c ratios. In both figures a “wavy” loading curve is obtained, which correlates with the larger E/c mismatch. This is a numerical characteristic which takes place during the loading phase. Every element that meets the rigid indenter, rapidly undergoes plastic deformation, due to the high contact pressure. In addition, Figure 9-8 (b), underlies that each material exhibit fully plastic behavior due that the unloading portion is almost perpendicular with the horizontal plane, suggesting that this category of materials approaches the response of the elastic-perfectly plastic solids.

(a)

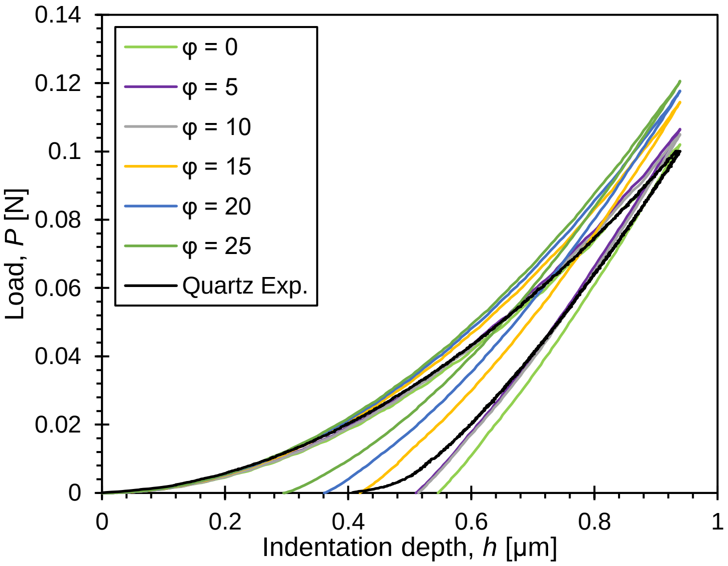

(b)

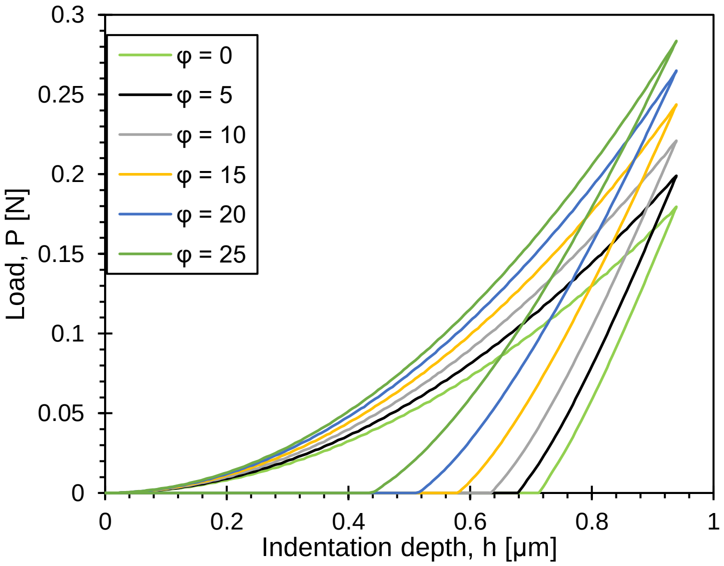

Figure 9-7: Resulting load versus indentation depth curves of simulated data on systems where (a) $\boldsymbol{E/c}$ = 28, (b) $\boldsymbol{E/c}$ = 72, by varying the friction's angle value $\boldsymbol{\varphi}$.

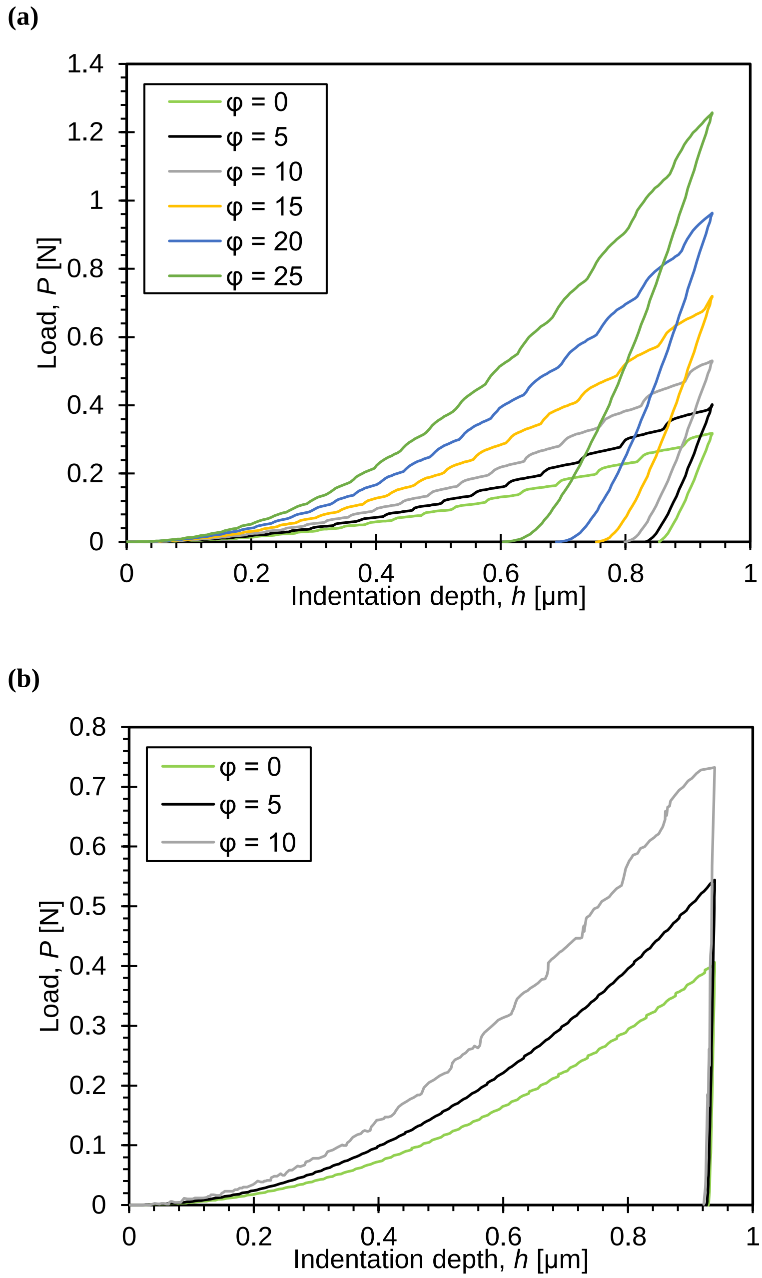

Figure 9-8: Resulting load versus indentation depth curves of simulated data on systems where (a) $\boldsymbol{E/c}$ = 288, (b) $\boldsymbol{E/c}$ = 2880, by varying the friction's angle value $\boldsymbol{\varphi}$.

9.4.2 Area of Contact – Pile-up Phenomena

The projected area of contact at maximum indentation load, is the dominant component (and major source of error) when estimating the mechanical properties of indented material, elastic modulus E and hardness H. The A_c can be determined directly after the unloading step, either through a scanning electron microscope or an atomic force microscope. Exporting the contact area for materials that exhibit high elastic recovery may lead to overestimated mechanical properties values. Furthermore, analytical approaches have been suggested in the literature, while the one proposed by Oliver and Pharr [2] is the most popular and can capture the area of contact with high precision, assuming that sink-in response takes place. Figure 9-9 illustrates the deformation profiles of the indented materials for all numerical groups. The contact depth h_c, which is defined as the vertical distance from maximum penetration depth h_{max} until the point the material's surface is in contact with the indenter, tends to increase as E/c increases. The first two groups exhibit sink-in behaviour, while in the last two groups, the material beneath cone turns to pile-up for all internal friction angles. The deviation between deformed curves for each group, is attributed to the elastic-plastic deformation which is driven by the value of friction angle.

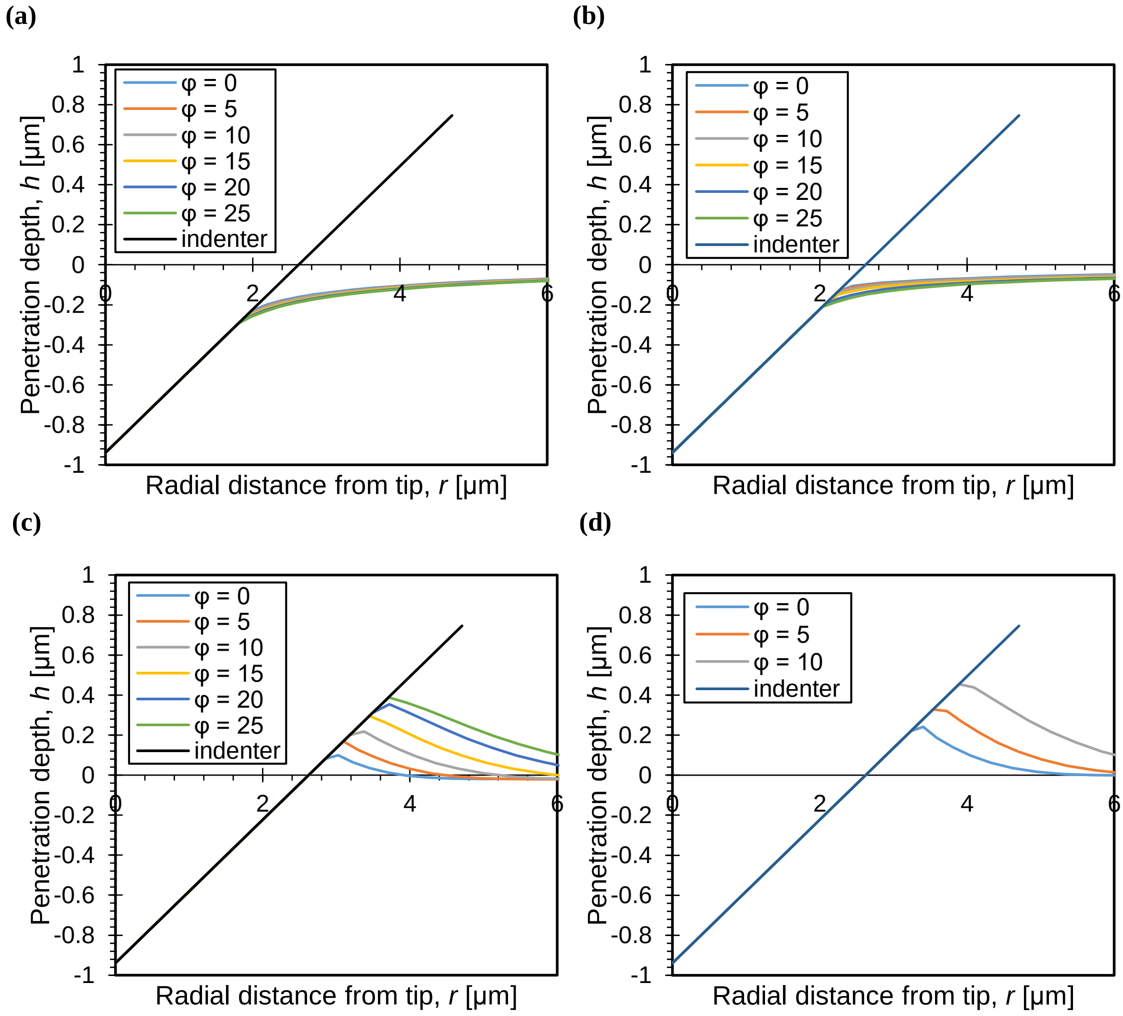

Figure 9-9: Deformation profiles in fully loaded configuration for all simulated groups.

Figure 9-10 shows the displacement profiles for the unloaded configuration of all numerical studies. Here, the elastic recovery is very distinct for the first two groups of E/c materials. Again, as the internal friction angle increases, elastic deformation is the dominant phase of material’s behaviour. This elastic work, as it can be observed from Figure 9-10 (a)-(b), by following the trend of imprint, aims to cause a curved profile response as friction angle increases. As a result, the surface that is close to the contact area, tends to pile up after the retraction of indenter to its initial position. This behaviour implies plastic deformation during unloading phase which has not been mentioned earlier in the literature and will be examined later.

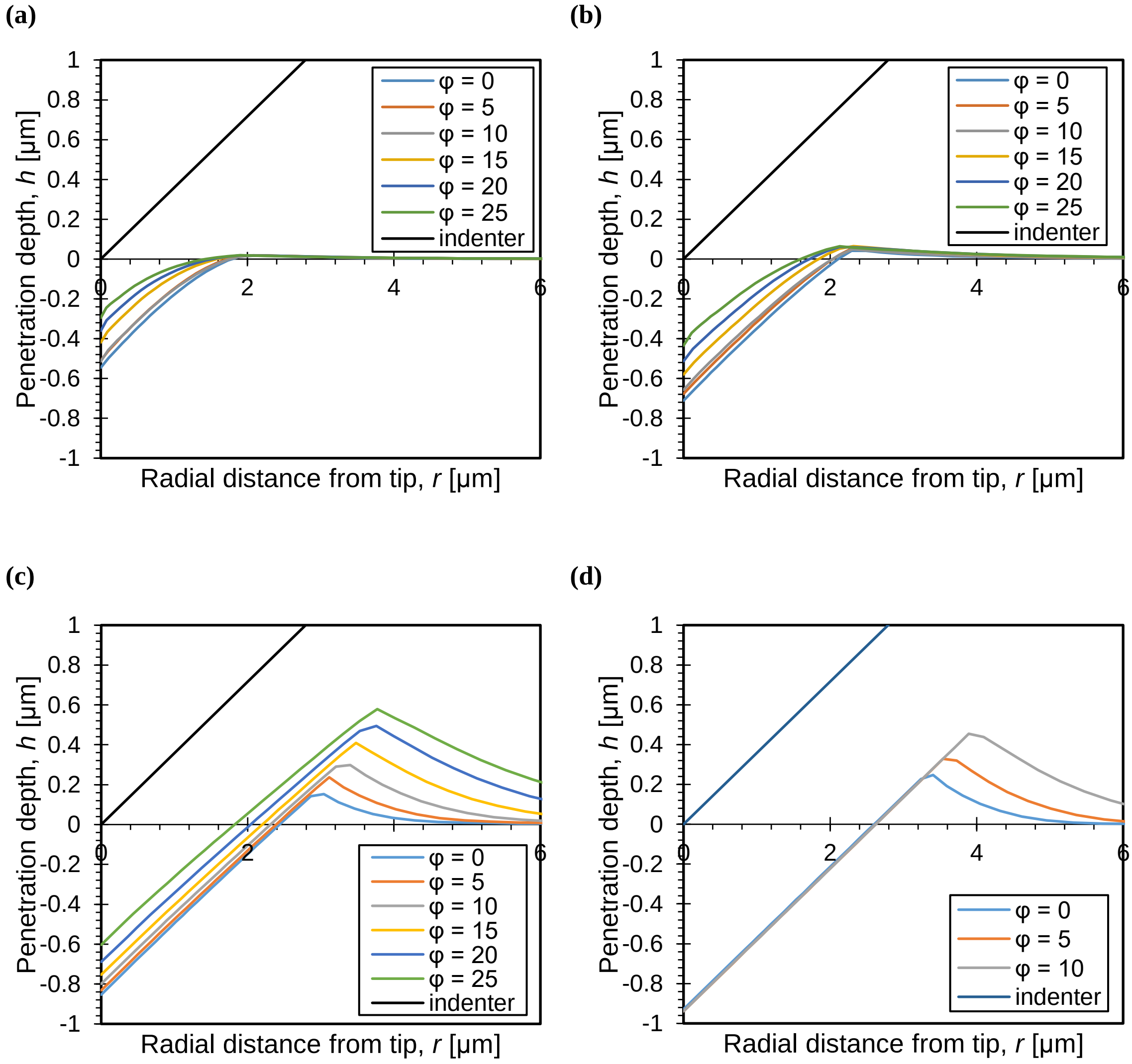

Figure 9-10: Deformation profiles in fully unloaded configuration for all simulated groups.

As E/c increases, Figure 9-10 (c)-(d), pile-up exists which corresponds to large plastic deformation. Although for materials with E/c = 288 exhibit combined elastic-plastic deformation, since they show elastic recovery depending on friction angle value. For the case of E/c = 2880 the undeformed profiles are identical except from the value of contact depth, which relates to the deviation of applied load and friction angle. That response indicates fully plastic deformation.

We have proved in Section 3.7.1, by applying Equation (3.5) that a von-Mises material with mismatch ratio of $E/Y > 100$, displays pile-up phenomena and in such cases the use of the Oliver and Pharr methodology is not recommended, due to the underestimation of the contact depth and the projected area values. Similar dimensional analysis as Equation (3.5) for cohesive-frictional material results:

$$\frac{h_c}{h} = \Pi_{10}\left(\frac{c}{E}, \varphi, v, \theta\right) \tag{9.11}$$

Figure 9-11 (a) shows the numerical results of dimensional group Π_{10} as a function of internal friction angle. Furthermore, results from Equation (2.42) are plotted against numerical findings, where both are in excellent agreement since material exhibit sink-in behaviour, for $c/E > 0.1$. As this ratio decreases (which corresponds to values larger than E/c = 250), the contact depth is higher than the maximum depth. Inside the indented material, large plastic zones are generated and as a result material volume around contact tends to move outside the contact surface, resulting in pile-up phenomena. Under these conditions, Equation (2.42) fails to obtain the true contact depth, which has its origin on an elastic contact problem formulation.

The effect of accurate contact depth is illustrated in Figure 9-11 (b), where the error in estimating the projected contact area is plotted for a range of c/E mismatches. The Oliver and Pharr methodology is in good agreement with computational results for values of $c/E > 0.01$. For pile-up behaviour, the deviation between the two methodologies is significant (up to 65%) and for this case where experimentalists use O&P procedure, they overestimate the indentation hardness and modulus of indented material.

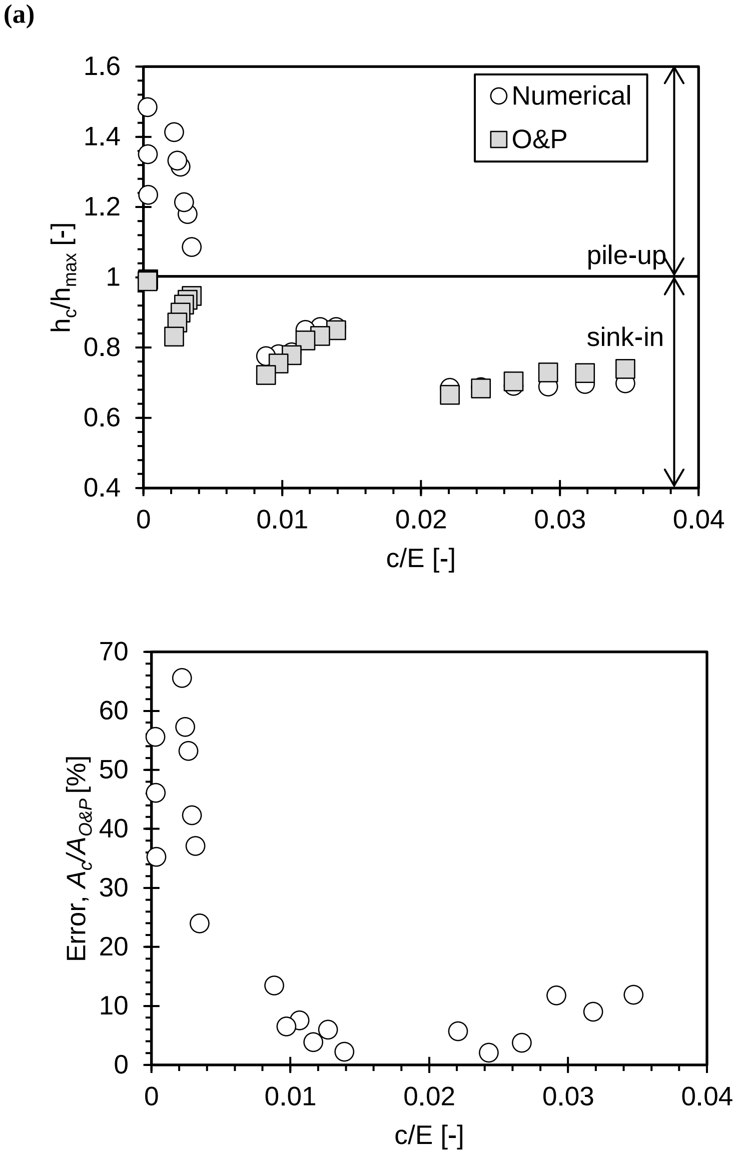

Figure 9-11: (a) Contact depth as obtained using numerical techniques and Oliver and Pharr method for all simulated groups. (b) Error in contact error estimation between the two methods. For $c/E < 0.01$ the percentage error in the estimation of projected contact area ranges from 15 – 65%.

As described in Chapter 2, although Equation (2.4) has been derived for conical indenters on linear elastic materials, it can be accurately use for any axisymmetric indenter and even elasto-plastic materials (Von-Mises type) provided the area of contact is properly accounted for [3,22]. The validity of the equation in the case of cohesive-frictional materials has not been tested. Rearranging Equation (2.4) it can result in a general relationship between elastic modulus E, Poisson's ratio v, contact radius a, at maximum indentation depth h_{max} (assuming rigid indenter):

$$\frac{1-v^2}{Ea}\frac{dP}{dh}\bigg|_{h=h_{max}} = 2 \tag{9.12}$$

Cheng and Cheng [109] through finite element simulations on work hardening materials under conical indentation ($\theta = 68^o$) shown that Equation (9.12) remains constant and equals to 2.16 over a wide range of Y/E, strain-hardening exponents and pile-up phenomena. This greater than 2.0 value, can be credited to the wrong semi-angle θ used in their calculations. Figure 9-12 illustrates the numerical indentation response of Equation (9.12) as a function of c/E for cohesive-frictional materials. Impressively, the dimensionless parameter appears to be independent from the cohesion-to-stiffness ratio, the internal friction angle and unaffected from pile-up or sink-in phenomena, suggesting that Equation (2.4) is a universal equation of indentation analysis that continue to hold true even for cohesive-frictional materials.

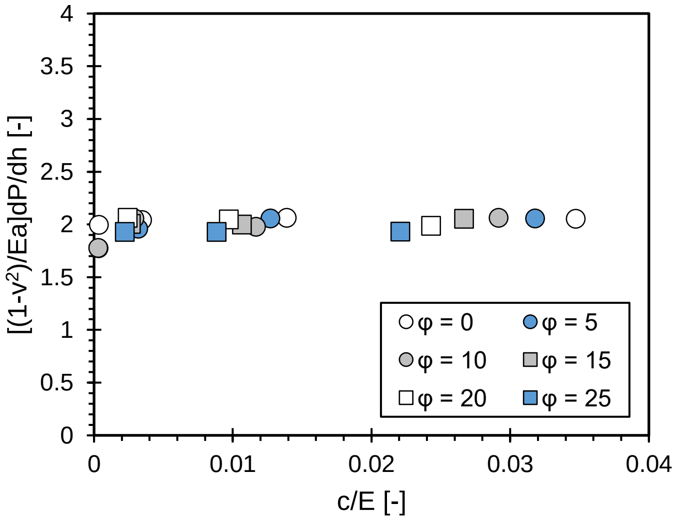

Figure 9-12: Numerical results of frictionless conical indentation on an elasto-plastic cohesive-frictional material. The dimensionless parameter $[(\mathbf{1}-\boldsymbol{v}^2)/\boldsymbol{Ea}]\boldsymbol{dP}/\boldsymbol{dh}$, appears to be independent of the cohesion-to-stiffness $\boldsymbol{c}/\boldsymbol{E}$, the friction angle $\boldsymbol{\varphi}$ and piling-up or sinking-in phenomena.

9.4.3 Work of Indentation

The mechanical response of indented materials can also be estimated from the information contained in the $P - h$ curve, without the need of calculating the projected area of contact [134,177,178]. The area under the loading curve defines the total work done during indentation testing W_t, which is the result of absorbed energies by elastic and plastic deformations; W_e and W_p, see Chapter 3.3.3. By applying dimensional analysis, Cheng *et al.* [56,62] proposed a linear relationship between the ratio of hardness to modulus H/E^* and the ratio of plasticity index (W_p/W_t). Through finite element simulations they have shown that this linear correlation accounts for a wide range of Y/E, Poisson's ratio and strain-hardening exponents. In Figure 9-13, computational results of Mohr-Coulomb materials for friction angles of 0^o and 5^o and a variety of E/c exhibit this linear relationship between H/E^* (an index of tribological behaviour) and plasticity index.

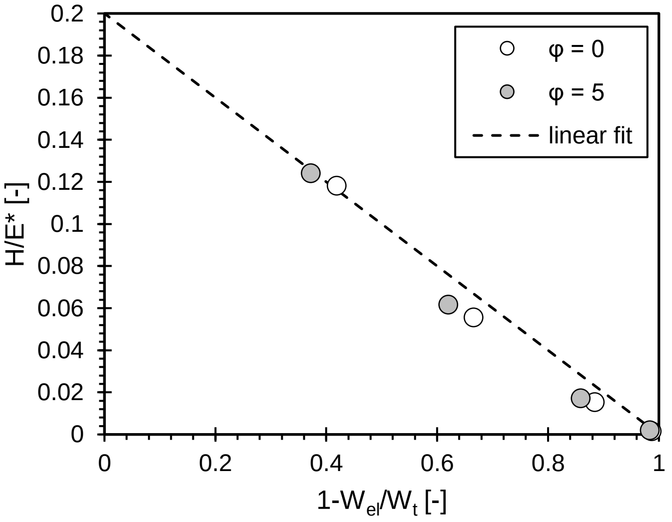

Figure 9-13: Numerical relationship between $\boldsymbol{H/E^*}$ and [1-$\boldsymbol{Wel/Wt}$] for internal frictional angles $\boldsymbol{\varphi}$ = 0^0, 5^0 and various $\boldsymbol{E/c}$, for cohesive-frictional material.

Although, while internal friction angle increases, there is a linear deviation trend ($10 \leq \varphi \leq 25$) that is independent from the mismatch between elastic modulus-to-cohesion ratio, Figure 9-14 (a). Therefore, the response of material which are characterized by a high-pressure sensitivity response, must be considered and analysed with all other parameters that may affect its behaviour, before trying to extract their mechanical properties from energy-based methods. This behaviour is better illustrated in Figure 9-14 (b), where the evolution of plasticity index is plotted with respect of frictional angles. For $\varphi \geq 10$, it seems that the generated plastic zone during indentation contact is eliminating due that elastic response is the dominant phase of such material. Furthermore, as E/c decreases this behaviour becomes more aggressive.

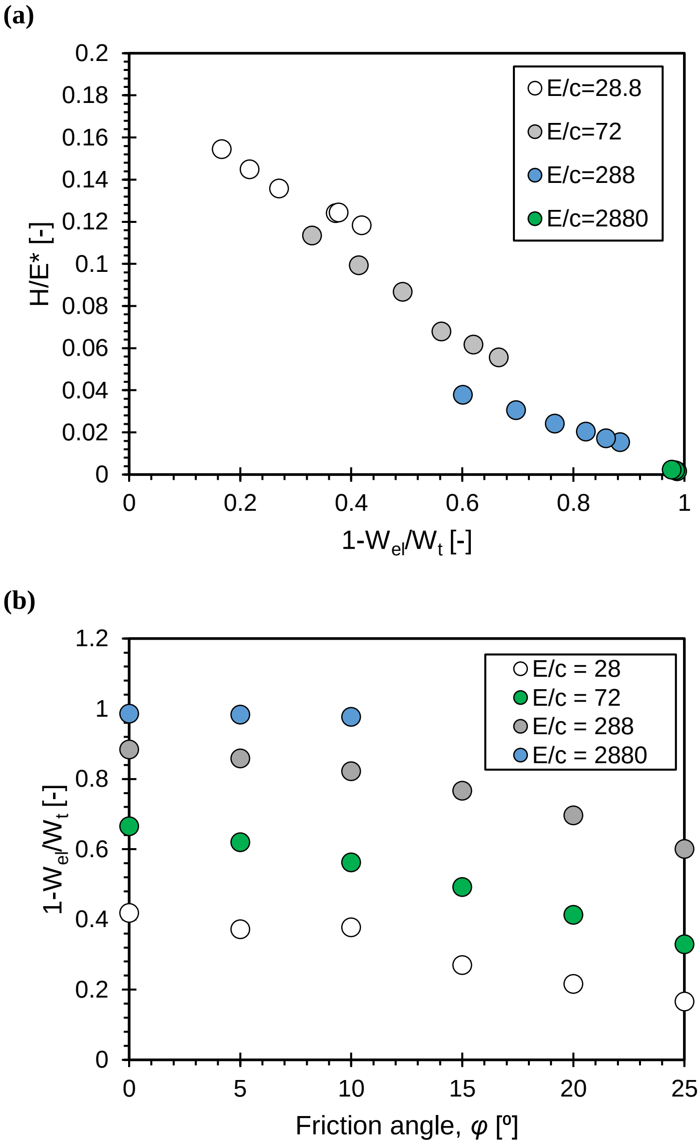

Figure 9-14: (a) Numerical correlation between H/E^* and [1-Wel/Wt] for various E/c cohesive-frictional materials. (b) Evolution of plasticity index for a wide range of frictional angles.

In addition, Cheng *et al.* [56,62] have proposed a dimensionless relation between plasticity index and the ratio of the final-imprint depth h_f to the maximum indentation depth h_{max}. They have shown that their computational results are independent of indenter geometry θ and mechanical properties. It has been proved in Chapter 6.3 that this relation is also valid for auxetic materials by applying finite element simulations under three different indenter geometries. In Figure 9-15, results on this relationship are plotted for a wide range of E/c. In addition, Equation (6.4) which has been proposed by Lawn and Howes [127] is in great agreement with the numerical results. Hence, plasticity index over h_f/h_{max} is independent of elastic-to-cohesion ratio, internal friction angle, pile-up or sink-in phenomena.

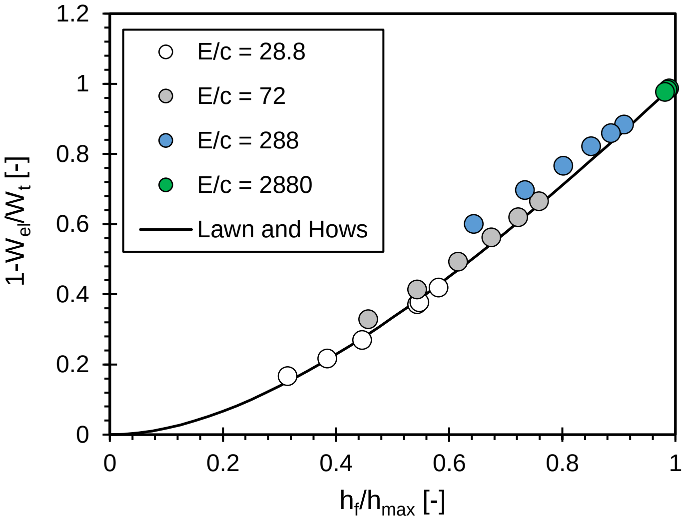

Figure 9-15: Plasticity index as a fuction of dimensionless parameter $\boldsymbol{h_f/h_{max}}$ for cohesive frictional materials.

9.4.4 Hardness Enhancement

Computational response of hardness-to-cohesion has been extracted as a function to friction angle, in order to be compared with the numerical study of Ganneau *et al.* [19] and is demonstrated in Figure 9-16. Their study was based on numerical yield design, which corresponds to fully plastic zones. For E/c = 28.8 an almost smooth transition from φ = 0°-25° is obtained which states that if a Mohr-Coulomb material exhibits an almost elastic indentation response, its pressure sensitivity behaviour will not affect its mechanical properties. As E/c increases, plastic strains are generated inside the indented material and the hardness-to-cohesion is dependent extremely on friction angle value. For E/c= 72 the hardness-to-cohesion enhancement equals to 3.0 from φ = 0°-25°. This enhancement in H/c is increasing as E/c increases; for E/c = 288, H/c = 3.65 from φ = 0º - 25º. In addition, if ones focuses on individual frictional angles, he/she will observe that the discrepancy between H/c is increasing with the increase of frictional angle. As the material becomes more plastic, i.e., large E/c, the divergence on hardness-to-cohesion is minimized due that the plasticity index of indentation data is approaching unity, $W_p/W_t \rightarrow 1$. Furthermore, comparing results of this study with Ganneau *et al.* results, it is noticeable that while E/c increases, numerical results are approaching the results of yield design (fully plastic). For friction angles up to 10º the two methodologies are in excellent agreement and for $\varphi > 10$º, where due to high friction angles, the strength of materials is increasing significant, the two methodologies start to deviate.

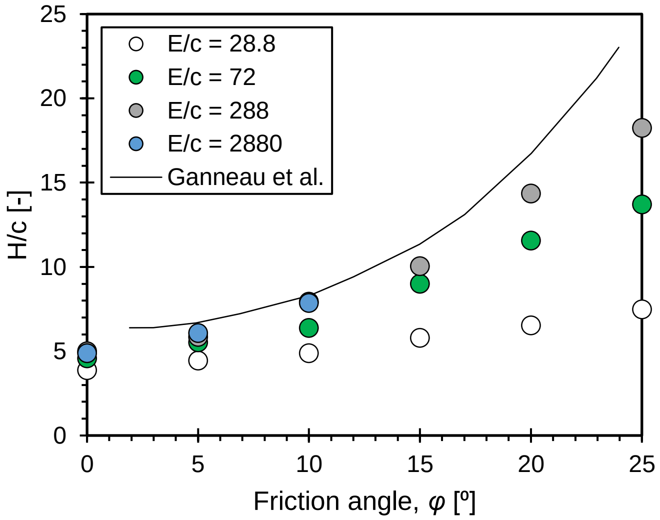

Figure 9-16: Solutions for the hardness-to-cohesion ratio of Mohr-Coulomb elastic-plastic materials for a wide range of internal friction angles.

At this point, we want to state again that through an indentation test, the elastic modulus of material is extracted from the slope of unloading curve at maximum indentation depth, due that the retraction of indenter is always assumed to be elastic. Although, as mentioned in Figure 9-10 the unloading curve of materials with relatively low E/c mismatches, seems to exhibit plastic deformations. For that reason, the plasticity dissipation energy has been extracted during indentation simulations, Figure 9-17. At low profile values (initial contact) the plastic dissipation is zero, due that early contact is elastic. While the penetration depth increases towards its maximum predefined value (corresponds to value 1 in numerical profile) the plastic dissipation increases too. Now, for numerical profiles from 1 -2 which describe the unloading portion, one is expecting that the plastic zone inside the material will be constant, as performed in Figure 9-17 (b), for material of E/c = 2880 and φ = 5. However, for low E/c ratios, Figure 9-17 (a), the plastic dissipation during unloading increases linearly until the complete retraction of the indenter, at a value of ~1.4 in numerical profile.

(a)

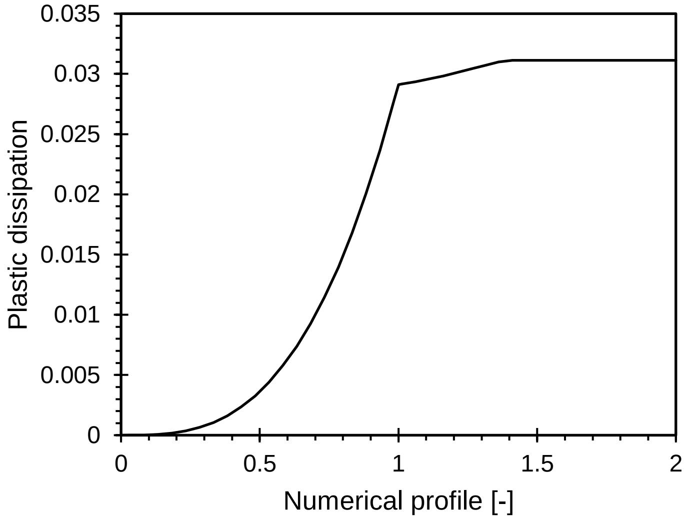

(b)

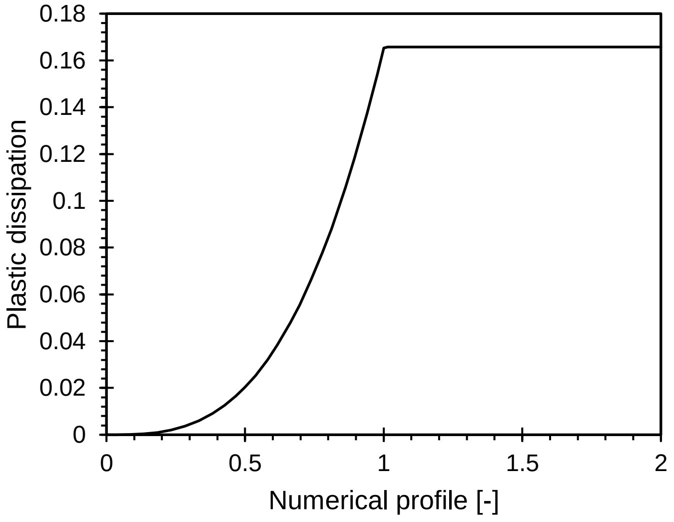

Figure 9-17: Evolution of numerical plastic dissipation response during numerical profile; 0 – 1 corresponds to loading profile at maximum indentation depth, 1 – 2 links the unloading profile, for cohesive-frictional materials (a) $\boldsymbol{E/c}$ = 72 and $\boldsymbol{\varphi}$ = 5, (b) $\boldsymbol{E/c}$ = 2880 and $\boldsymbol{\varphi}$ = 5.

In order to better capture this behavior, the plastic zone boundaries were derived from computational solutions, in which equivalent plastic strains for a Mohr-Coulomb material are defined as:

$$\varepsilon_{pl} = \frac{1}{c}\int \sigma : d\varepsilon_{pl} \tag{9.13}$$

Figure 9-18 displays the equivalent plastic strains that are generated in the material of E/c = 72 and φ = 5. The maximum value of ε_{pl} contour legend, has been downgraded in order to enhance its sensitivity on lower values in order to investigate any changes in distribution during unloading step. Figure 9-18 (a) states the plastic strains shape at fully indentation load. In Figure 9-18 (b) (c) (d), indenter has been retracted at 40%, 80% and 100%, respectively. Although the major distribution under the area of contact remains virtually unaffected, plastic equivalent strains are generated near the contact radius and expand until full unloading is achieved. This can be explained, that during unloading, the large strain energy that is imposed during indenter's penetration, drives material response in regions near to contact area to be deformed plastically.

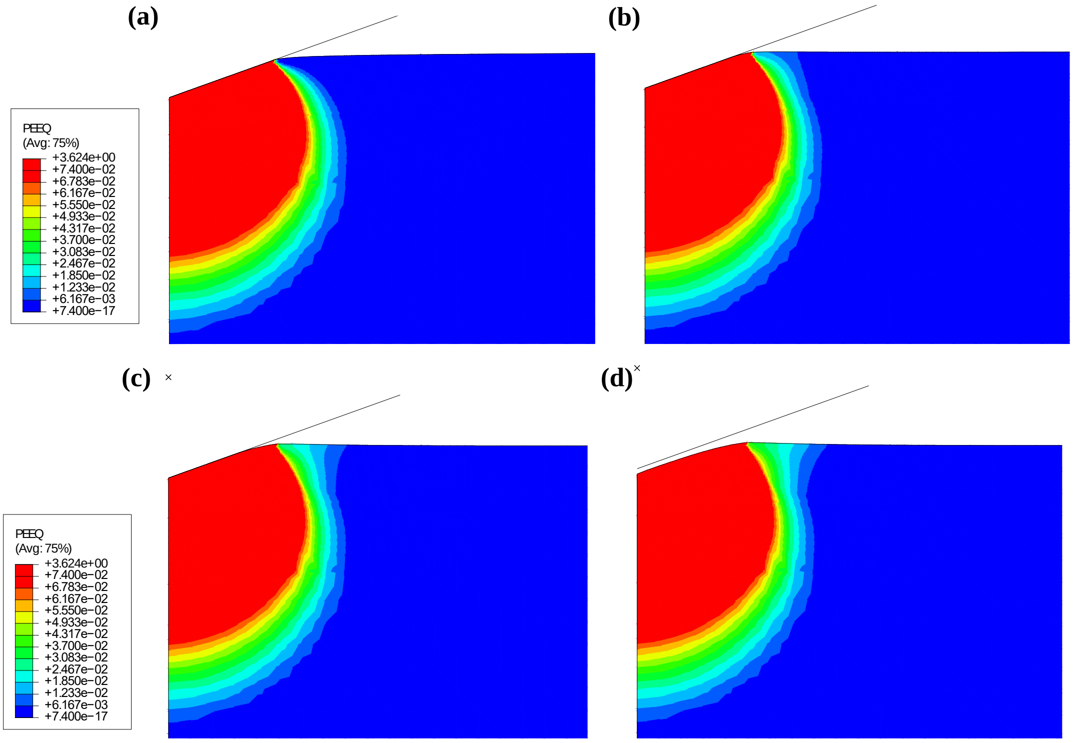

Figure 9-18: Equivalent plastic strain-profiles for $\boldsymbol{E/c}$ = 72 and $\boldsymbol{\varphi}$ = 5. The maximum contour value was downgraded in order to show the effect of generated strains during unloading; (a) fully loaded condition, (b) retraction of 40%, (c) retraction of 80%, (d) fully unloaded condition.

9.5 Chapter Summary

Numerical data presented in this chapter provides quantitate links between indentation hardness and strength properties of cohesive-frictional materials. Compressive yield strength was kept constant for all numerical studies in order to investigate the influences on cohesion and frictional angles for a large span of E/c ratio. Dimensional analysis yielded characteristic relationships of this class of materials regarding indentation analysis; dimensionless parameter $[(1-v^2)/Ea]dP/dh$ appears to be independent of c, φ and pile-up or sink-in phenomena, plasticity index maintains its relationship with h_f/h_{max} as for elastic and von-Mises materials. The results of hardness-to-cohesion ratio for a wide range of frictional angles are in excellent agreement with results from literature. In addition, through this study we captured the elastoplastic response of this parameter in order to understand the mechanisms based on the plasticity extend inside the material. This technique holds great promise for performing similar numerical studies under Cube Corner indentation and then combining both results for extracting the cohesion and friction-angle of Mohr-Coulomb materials. Finally, numerical data suggest that plastic deformation can even occur during unloading which is something that has been overlooked in the literature and could be significant in certain circumstances; this phenomenon was attributed to the plastic flow that might occur after the redistribution of strain energy upon unloading.

Part V

CONCLUSIONS AND PERSPECTIVES

Chapter 10

Concluding Remarks

The aim of this thesis was to explore and resolve various open issues regarding nanoindentation testing using finite element modeling. Furthermore, it aimed in obtaining contact mechanics relationships for the understanding and modeling of the indentation response of several emerging material systems. This chapter summarizes the main results and contributions that resulted from this study. Based on these results, some future research perspectives are proposed, and preliminary numerical results are presented.

10.1 Summary of Results

Finite element studies of nanoindentation on advanced material systems have revealed several contact mechanics relationships and aimed the thorough understanding of underlying physics at stake in each system. Numerical models have been tailored and utilized over several parametric studies and a variety of material responses in order to propose protocols to experimentalists for design of experiments and investigate the indentation response, to introduce new methodologies and correction factors for the accurate calculation of mechanical properties. The most important results are summarized below by topic:

10.1.1 Auxetic Materials

- Through numerical modeling we have shown that the increase in indentation resistance can be traced to the shear stiffening and the reduction of that contact area that auxetic materials exhibit when compared to conventional materials.
- The rapid amplification of hardness observed into the negative regime (auxetic materials) for which a seven-fold enhancement for the lowest ν simulated in this study ($H_{\nu=\text{-0.9}}/H_{\nu=0}= 7.13$) is observed under conical indentation of θ = 70.3°, while for spherical indentation a maximum six-fold increase was extracted at ν = -0.9.
- Adhesive indentation contact in both cases (cone, sphere) leads to a minor increase of the indentation resistance of auxetic materials due to the decrease of area of contact, while the decrease of indenter's angle up to θ = 60° results to a 12-fold enhancement of hardness for material with ν = -0.9.
- For elastoplastic auxetic materials, any existence of plastic deformation starts to weaken this advanced characteristic and for high plasticity index values, materials undergo softening. Hence, any enhancement on hardness, depends entirely on the elastic response of auxetic materials and needs to be maintained under various loading conditions if one is to ensure these enhanced characteristics.
- In order to analyze indentation experiments on auxetic materials one must correct the analytical solution with the proposed correction factors.

10.1.2 Coating Systems

- A critical literature review showed that indentation data on coating systems is required to cover the first plateau of sigmoidal curve in order to eliminate any misleading fitting on film's extrapolated properties.
- Finite element studies on hard coatings show that plastic deformations during indentation experiments eliminate the resistance of these systems.
- Pile-up phenomena may appear for various moduli mismatches, which can lead to overestimation of the mechanical properties for the case of the projected contact area as extracted by the Oliver and Pharr methodology.
- Computational results on the indentation of coated systems suggest that the sigmoidal behaviour of composite moduli (coating and substrate) scales with a/t

in a universal fashion and independently from material properties, film thickness and elastic moduli mismatch.

- For the analysis through the Oliver and Pharr methodology of indentation data on thin films, ones must calculate the allowable region based on the moduli mismatch as proposed in Figure 8-16.
- A combined numerical-experimental methodology is proposed for calculating the mechanical properties of thin films (demonstrated on an a-C:H/Si system). The exact details of the indenter geometry can play a pivotal role in the response and should be included in the analysis when sub-50 nm indents are considered.

10.1.3 Cohesive-Frictional Materials

- Computational results provide indentation relationships between hardness and strength properties of cohesive-frictional materials.
- Combined parametric studies of cohesion and frictional angles have been performed by letting the compressive yield strength of materials constant through all studies.
- Dimensional analysis lead to characteristics indentation relationships which are in excellent agreement with literature.
- Effect of pile-up phenomena have been examined and quantified for Mohr-Coulomb materials.
- The results of hardness-to-cohesion ratio for a wide range of frictional angles are in excellent agreement with results from literature.
- Numerical elastoplastic response of hardness-to-cohesion has been studied in order to quantify the effect of the size of plastic region inside the material.
- Finally, numerical data exhibit plastic deformation during unloading path and that behavior is attributed to plastic flow response after the release of strain energy for low E/c ratios.

10.2 Future Perspectives

Several ideas have been generated through the implementation of this thesis that will serve as the basis for future investigations. Some of those are separately discussed below:

10.2.1 Computational Fracture Mechanics on Coating Applications

A parameter of investigation can be the adhesion between coating and substrate, where in almost all cases in literature, it is assumed to be perfectly bonded [48,179–181]. Owing to Y/E mismatch or work hardening exponents, the coating may subject to delamination process or in mechanisms where excluded in existing models (cracking, piling-up). As well as the contact which is considered as frictionless and the indenter as rigid, drives in significant errors, in cases of stiff coatings. Hence frictional effects in the indenter–material interface can be included in the analysis through an isotropic Coulomb model. As future work, one can introduce fracture elements between the interface of the thin film and substrate. As a result, delamination processes can be investigated and compared to experimental results (Figure 10-1).

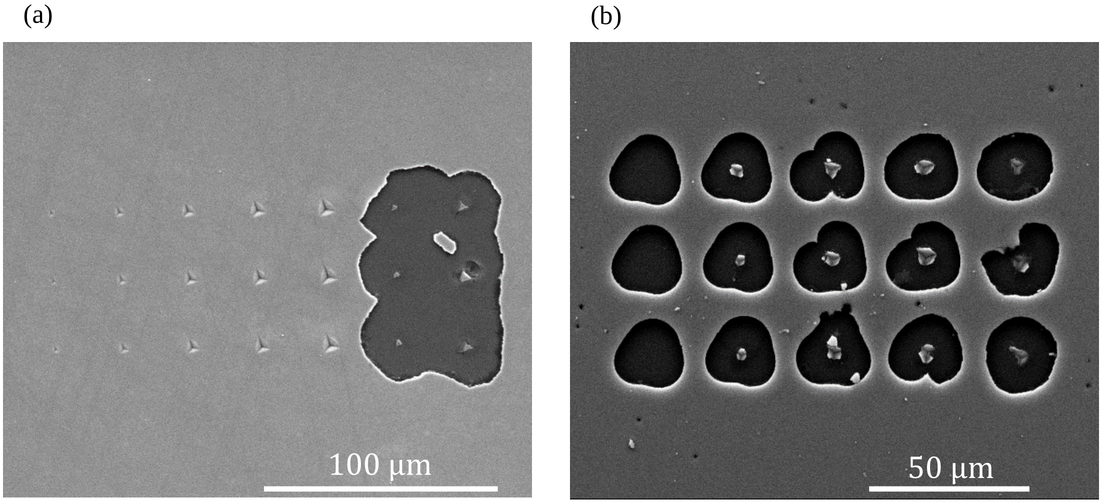

Figure 10-1: SEM images of secondary electron mode show cracks on the surface of (a) titanium alloy, (b) pure niobium, films on silicon substrates, due on indenter's load.

10.2.2 Super Hard Materials/Films

During indentation on very hard materials the response might be influenced by the mechanical characteristics of the indenter. In the majority of nanoindentation tests a diamond indenter is used which for most practical applications can be safely considered as rigid and any deformation could be neglected during the analysis. In cases of very hard materials ($H > 30$ GPa) the elastic and in some cases plastic characteristics of the diamond probe should be included in the analysis.

It has been reported in the literature that hard materials with mechanical properties in the order of elastic modulus of 550 GPa and of hardness of 60-100 GPa [182–186] have been synthesized and characterized. These “innovative” materials turned the attention of research community into the synthesis technique and also to their mechanical analysis. A critical review paper, that was published in 2012 [187] states a variety of errors that could have been performed in analysis. According to Fischer-Cripps, their major errors derived from; values of instrument compliance and initial penetration depth, fixed value for the power law exponent in $P-h$ curves, correlation of Knoop hardness with Martens hardness, the value of area of contact and arbitrary constraint factor ($C \equiv H/\sigma_y$).

The assumption of rigid indenter when it penetrates into superhard materials may also lead to miscalculated mechanical properties. The effect of indenter’s deformation is a major key, to be able to characterize material’s properties. We here relax this assumption and perform preliminary parametric analysis of the indentation process using the diamond’s mechanical characteristics. Hence, we developed a numerical axisymmetric model (Figure 10-2), CAX4 elements, with the potential of a deformable indenter. The ‘semi–infinite’ half space is modeled as a 101×101 μm^2 domain.

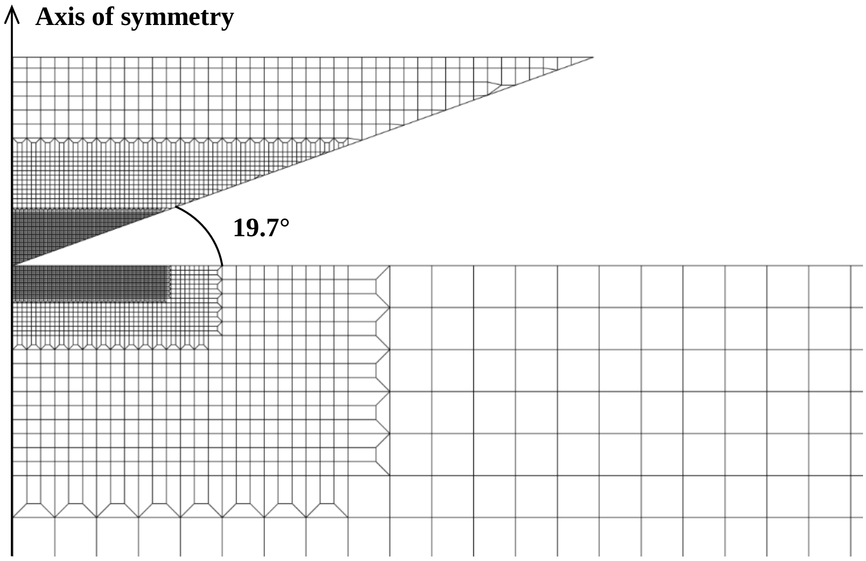

Figure 10-2: Finite element model for the study of supehard materials, in where indenter is modeled as axisymmetric deformable solid with semi angle 70.3°.

In Figure 10-3, we present our preliminary results for elastic indenter (E = 1141 GPa, v = 0.07) and elastic-perfectly plastic materials (E = 500 GPa, v = 0.3, Y = 0.5, 1 GPa).

Simulations were performed in a displacement driven approach until the maximum predefined depth is reached. As shown in Figure 10-3 a material with Y = 1 GPa results in minimum penetration depth than other material. This attributes to the elastic deformation that indenter materials undergo, Figure 10-3 (b). Although for these selected values indenter's deformation may assumed as minimal, for larger yield stresses values would play a significant role in the overall indentation response of superhard materials. As future study, we want to apply parametric studies through various indented materials; auxetics, cohesive-frictional materials and evaluate Hertz's Equation (2.13) in such extreme cases.

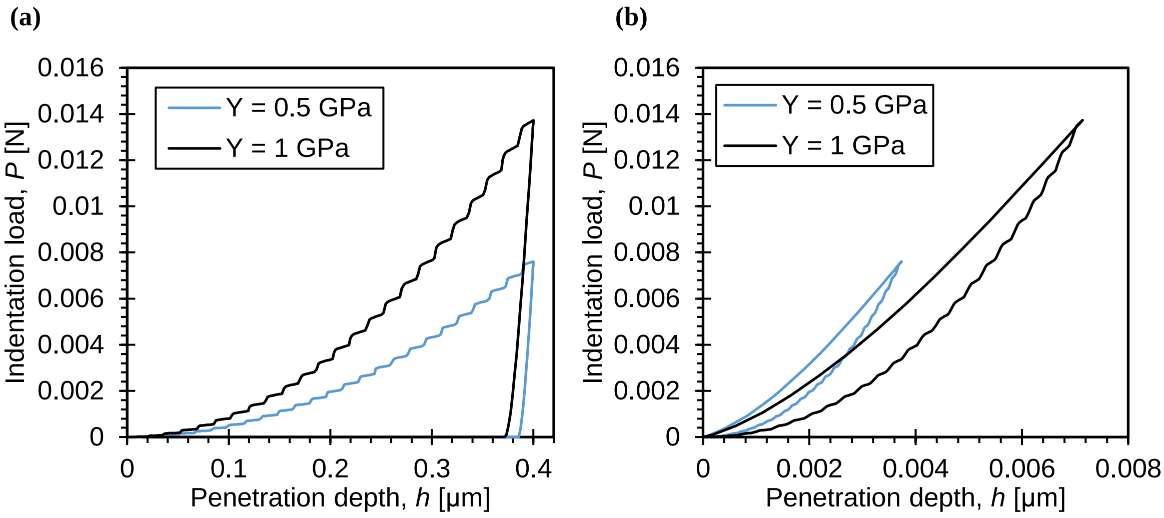

Figure 10-3: Primary $\boldsymbol{P-h}$ results on superhard materials for deformable indenter where (a) corresponds to the response of von-Mises materials and (b) to the indentation response of conical indenters.

10.2.3 Auxetic Structures for Biomedical Applications

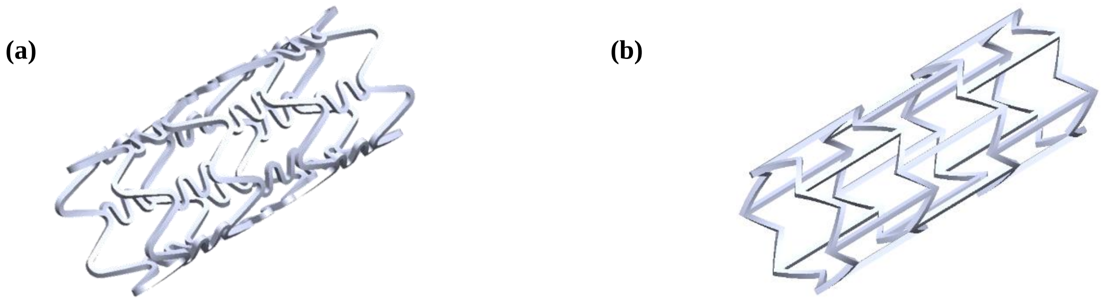

Figure 10-4: (a) Conventional stent structure, (b) auxetic honeycomb stent structure, which were design in SolidWorks software, Dassault Systemes.

From an application perspective, one can study the numerical strength of auxetic structures and design a tailored structure for stent applications, see Figure 10-4. A stent is a small medical structure comprising an expandable mesh-like tubular geometry. As mentioned in Chapter 5, auxetic materials have the ability to contract under compressive stresses and to expand laterally under tension. Therefore, not only auxetic stents will enhance the mechanical properties of conventional stents but will also minimize any tissue adhesion damage.

10.2.4 Numerical response of cohesive-frictional materials under Cube Corner indentation

Dual indentation approach that has been developed by Ganneau *et al.*, [19] it is implemented in many studies for extracting experimentally the mechanical properties of pressure-sensitive materials. In this thesis, we have performed numerical indentation studies by assuming the geometry of a Berkovich indenter (Chapter 9). Hence, in order to provide practical knowledge to experimentalists, similar studies must be performed with Cube Corner indenter, to extract new hardness-to-cohesion curves that can deliver the elastoplastic behavior and mechanical properties (c, φ) of Mohr-Coulomb materials.

10.3 Concluding Remarks

We have presented in this thesis a numerical approach for assessing the mechanical properties of advanced materials under nanoindentation simulations. We have calculated the existence of crucial scale parameters that must lead the indentation response of corresponding systems. Furthermore, we proposed correction factors or methods for eliminating any inaccuracies and correct the elastic theory based on the behavior of those structures. It is our hope that results of this thesis will contribute to the field of small scale mechanical testing and form the basis for further developments in the fields of instrumented indentation, auxetic materials testing and design, thin film mechanics and testing of cohesive-frictional materials, ultimately leading to new and tailored-made optimized materials/structures.

REFERENCES

1. Doerner, M.F.; Nix, W.D. A method for interpreting the data from depth-sensing indentation instruments. *A method Interpret. data from depth-sensing indentation instruments* **1986**, *01*, 601–609.
2. Oliver, W.C.; Pharr, G.M. Improved technique for determining hardness and elastic modulus using load and displacement sensing indentation experiments. *J. Mater. Res.* **1992**, *7*, 1564–1580.
3. Oliver, W.C.; Pharr, G.M. Measurement of hardness and elastic modulus by instrumented indentation: Advances in understanding and refinements to methodology. *J. Mater. Res.* **2004**, *19*, 3–20.
4. Beake, B.D.; Smith, J.F.; Gray, A.; Fox-Rabinovich, G.S.; Veldhuis, S.C.; Endrino, J.L. Investigating the correlation between nano-impact fracture resistance and hardness/modulus ratio from nanoindentation at 25–500 °C and the fracture resistance and lifetime of cutting tools with Ti1−xAlxN (x=0.5 and 0.67) PVD coatings in milling operations. *Surf. Coatings Technol.* **2007**, *201*, 4585–4593.
5. Bhakhri, V.; Klassen, R.J. Investigation of high-temperature plastic deformation using instrumented microindentation tests. Part IThe deformation of three aluminum alloys at 473 K to 833 K. *J. Mater. Sci.* **2006**, *41*, 2259–2270.
6. Constantinides, G.; Tweedie, C.A.; Savva, N.; Smith, J.F.; Van Vliet, K.J. Quantitative Impact Testing of Energy Dissipation at Surfaces. *Exp. Mech.* **2009**, *49*, 511–522.
7. Constantinides, G.; Tweedie, C.A.; Holbrook, D.M.; Barragan, P.; Smith, J.F.; Van Vliet, K.J. Quantifying deformation and energy dissipation of polymeric surfaces under localized impact. *Mater. Sci. Eng. A* **2008**.
8. Constantinides, G.; Ravi Chandran, K.S.; Ulm, F.-J.; Van Vliet, K.J. Grid indentation analysis of composite microstructure and mechanics: Principles and validation. *Mater. Sci. Eng. A* **2006**, *430*, 189–202.
9. Sorelli, L.; Constantinides, G.; Ulm, F.-J.; Toutlemonde, F. The nano-mechanical signature of Ultra High Performance Concrete by statistical nanoindentation techniques. *Cem. Concr. Res.* **2008**, *38*, 1447–1456.

10. Constantinides, G.; Kalcioglu, Z.I.; McFarland, M.; Smith, J.F.; Van Vliet, K.J. Probing mechanical properties of fully hydrated gels and biological tissues. *J. Biomech.* **2008**, *41*, 3285–3289.

11. Hertz, H. Ueber die Berührung fester elastischer Körper. *J. fur die Reine und Angew. Math.* **1882**, *1882*, 156–171.

12. Sneddon, I.N. Boussinesq's problem for a rigid cone. *Math. Proc. Cambridge Philos. Soc.* **1948**, *44*, 492–507.

13. Sneddon, I.N. The relation between load and penetration in the axisymmetric boussinesq problem for a punch of arbitrary profile. *Int. J. Eng. Sci.* **1965**, *3*, 47–57.

14. Loubet, J.L.; Georges, J.M.; Marchesini, O.; Meille, G. Vickers Indentation Curves of Magnesium Oxide (MgO). *J. Tribol.* **1984**, *106*, 43–48.

15. Pethica, J.; Hutchings, R.; Oliver, W.C. Philos. Mag. A48. **1983**, 593.

16. Bulychev, S.I.; Alekhin, V.P.; Shorshorov, M.K.; Ternovskii, A.P.; Shnyrev, G.D. Determination of Young's modulus according to the indentation diagram. *Ind. Lab.* **1975**, 1409–1412.

17. Borodich, F.M.; Keer, L.M. Contact problems and depth-sensing nanoindentation for frictionless and frictional boundary conditions. *Int. J. Solids Struct.* **2004**, *41*, 2479–2499.

18. Tabor, D. *The Hardness of Metals*; Oxford Classic Texts, 2000;

19. Ganneau, F.P.; Constantinides, G.; Ulm, F.-J. Dual-indentation technique for the assessment of strength properties of cohesive-frictional materials. *Int. J. Solids Struct.* **2006**, *43*, 1727–1745.

20. Cariou, S.; Ulm, F.-J.; Dormieux, L. Hardness–packing density scaling relations for cohesive-frictional porous materials. *J. Mech. Phys. Solids* **2008**, *56*, 924–952.

21. Pharr, G.M.; Oliver, W.C.; Brotzen, F.R. On the generality of the relationship among contact stiffness, contact area, and elastic modulus during indentation. *J. Mater. Res.* **1992**, *7*, 613–617.

22. Cheng, C.-M.; Cheng, Y.-T. On the initial unloading slope in indentation of elastic-

plastic solids by an indenter with an axisymmetric smooth profile. *Appl. Phys. Lett.* **1997**, *71*, 2623.

23. Fischer-Cripps, A.C. *Nanoindentation*; 3rd ed.; Springer New York: New York, 2011;

24. Oliver, W.C.; Pharr, G.M. Nanoindentation in materials research: Past, present, and future. *MRS Bull.* **2010**, *35*, 897–907.

25. Schuh, C.A. Nanoindentation studies of materials. *Mater. Today* **2006**, *9*, 32–40.

26. Lawn, B.R. Indentation of Ceramics with Spheres : A Century after Hertz. **1998**, *94*, 1977–1994.

27. VanLandingham, M.R.; Villarrubia, J.S.; Guthrie, W.F.; Meyers, G.F. Nanoindentation of polymers: an overview. *Macromol. Symp.* **2001**, *167*, 15–44.

28. Tweedie, C.A.; Constantinides, G.; Lehman, K.E.; Brill, D.J.; Blackman, G.S.; Van Vliet, K.J. Enhanced stiffness of amorphous polymer surfaces under confinement of localized contact loads. *Adv. Mater.* **2007**, *19*, 2540–2546.

29. Vandamme, M.; Tweedie, C.A.; Constantinides, G.; Ulm, F.-J.; Van Vliet, K.J. Quantifying plasticity-independent creep compliance and relaxation of viscoelastoplastic materials under contact loading. *J. Mater. Res.* 2012, *27*, 302–312.

30. Constantinides, G.; Ulm, F.-J.; Van Vliet, K.J. On the use of nanoindentation for cementitious materials. *Mater. Struct.* 2003, *36*, 191–196.

31. Constantinides, G.; Smith, J.F.; Ulm, F.-J. Nanomechanical explorations of cementitious materials: recent results and future perspectives. In *Nanotechnology in Construction 3*; Bittnar, Z., Bartos, P.J.M., Němeček, J., Šmilauer, V., Zeman, J., Eds.; Springer, 2009; pp. 63–69 ISBN 978-3-642-00979-2.

32. Němeček, J.; Králík, V.; Vondřejc, J. Micromechanical analysis of heterogeneous structural materials. *Cem. Concr. Compos.* **2013**, *36*, 85–92.

33. Williams, S.R. *Hardness and hardness measurements*; American society of metals: Cleveland, Ohio, 1942;

34. Brinell, J.A. Memoire sur les epreuves a bille en acier. *Congr. Int. des Methodes d*

Essai des Mater. Constr. **1901**, *Tome 2*, 83–94.

35. Meyer, E. Investigations of hardness testing and hardness. *Phys. Z.* **1908**, *9*.
36. Ludwick, P. *Die Kegelprobe—Ein neues Verfahren zur Härtebestimmung von Materialien*; Springer: Berlin, 1908;
37. Rockwell, S.P. Testing metals for hardness. *Trans. Am. Soc. Steel Treat.* **1922**, *2*, 1013–1033.
38. Mott, B.A. *Micro-Indentation Hardness Testing*; Butterworths, London, 1956;
39. Newey, D.; Wilkins, M.A.; Pollock, H.M. An ultra-low-load penetration hardness tester. *J. Phys. E.* **1982**, *15*, 119–122.
40. Ternovskii, A.P.; Alekhin, V.P.; Shorshorov, M.K.; Khrushchov, M.M.; Skvortsov, V.N. Micromechanical Testing of Materials by Depression. *Zavod. Lab.* **1974**, *39*, 1242–1247.
41. Johnson, K.L. *Contact Mechanics*; Press, C.U., Ed.; Cambridge University Press, 1985; Vol. 37; ISBN 0521347963.
42. Lee, E.H.; Radok, J.R.M. The Contact Problem for Viscoelastic Bodies. *J. Appl. Mech.* **1960**, *27*, 438.
43. Sneddon, I.N. *Fourier Transforms*; Dover Publications, 2010;
44. Hay, J.C.; Bolshakov, A.; Pharr, G.M. A critical examination of the fundamental relations used in the analysis of nanoindentation data. **1999**, *14,* 2296–2305.
45. King, R.B. Elastic analysis of some punch problems for a layered medium. *Int. J. Solids Struct.* **1987**, *23*, 1657–1664.
46. Kim, N.-H. *Introduction to Nonlinear Finite Element Analysis*; Springer US: New York, NY, 2015; ISBN 978-1-4419-1745-4.
47. King, R.B. Elastic analysis of some punch problems for a layered medium. *Int. J. Solids Struct.* **1987**, *23*, 1657–1664.
48. Bhattacharya, A.K.; Nix, W.D. Analysis of elastic and plastic deformation associated with indentation testing of thin films on substrates. *Int. J. Solids Struct.* **1988**, *24*, 1287–1298.

49. Larsson, P.-L.; Giannakopoulos, A.E.; SÖderlund, E.; Rowcliffe, D.J.; Vestergaard, R. Analysis of Berkovich indentation. *Int. J. Solids Struct.* **1996**, *33*, 221–248.

50. Bolshakov, A.; Pharr, G.M. Influences of pileup on the measurement of mechanical properties by load and depth sensing indentation techniques. *J. Mater. Res.* **1998**, *13*, 1049–1058.

51. Bolshakov, A.; Oliver, W.C.; Pharr, G.M. Influences of stress on the measurement of mechanical properties using nanoindentation: Part II. Finite element simulations. *J. Mater. Res.* **1996**, *11*, 760–768.

52. Hay, J.L.; Wolff, P.J. Small correction required when applying the Hertzian contact model to instrumented indentation data. *J. Mater. Res.* **2001**, *16*, 1280–1286.

53. Poon, B.; Rittel, D.; Ravichandran, G. An analysis of nanoindentation in linearly elastic solids. *Int. J. Solids Struct.* **2008**, *45*, 6018–6033.

54. Xu, Z. Effects of indenter geometry and material properties on the correction factor of Sneddon's relationship for nanoindentation of elastic and elastic–plastic materials. *Acta Mater.* **2008**, *56*, 1399–1405.

55. Dao, M.; Chollacoop, N.; Van Vliet, K.J.; Venkatesh, T.A.; Suresh, S. Computational modeling of the forward and reverse problems in instrumented sharp indentation. *Acta Mater.* **2001**, *49*, 3899–3918.

56. Cheng, Y.-T.; Cheng, C.-M. Scaling, dimensional analysis, and indentation measurements. *Mater. Sci. Eng. R* **2004**, *44*, 91–149.

57. Feng, G.; Qu, S.; Huang, Y.; Nix, W.D. An analytical expression for the stress field around an elastoplastic indentation/contact. *Acta Mater.* **2007**, *55*, 2929–2938.

58. Sarris, E.; Constantinides, G. Finite element modeling of nanoindentation on C–S–H: Effect of pile-up and contact friction. *Cem. Concr. Compos.* **2013**, *36*, 78–84.

59. Perriot, A.; Barthel, E. Elastic contact to a coated half-space: Effective elastic modulus and real penetration. *J. Mater. Res.* **2004**, *19*, 600–608.

60. Gao, H.; Cheng-Hsin, C.; Jin, L. Elastic contact versus indentation modeling of multi-layered materials. *Int. J. Solids Struct.* **1992**, *29*, 2471–2492.

61. Clifford, C.A.; Seah, M.P. Nanoindentation measurement of Young’s modulus for compliant layers on stiffer substrates including the effect of Poisson’s ratios. *Nanotechnology* **2009**, *20*, 145708.

62. Cheng, Y.-T.; Li, Z.; Cheng, C.-M. Scaling relationships for indentation measurements. *Philos. Mag. A Phys. Condens. Matter, Struct. Defects Mech. Prop.* **2002**, *82*, 1821–1829.

63. Hibbitt, K.& S. *ABAQUS: Theory Manual*; 6.13.; Dassault Systèmes, 1992;

64. Sarris, E.; Constantinides, G. Finite element modeling of nanoindentation on C–S–H: Effect of pile-up and contact friction. *Cem. Concr. Compos.* **2013**, *36*, 78–84.

65. Shuman, D. Atomic Force Microscope Indentation Measurement Software. In *Nanoscale Calibration Standards and Methods*; Wiley-VCH Verlag GmbH & Co. KGaA: Weinheim, FRG, 2006; pp. 463–480.

66. Lee, J.H.; Pharr, G.M.; Gao, Y. Corrections to the stiffness relationship in 3-sided and conical indentation problems. *Int. J. Solids Struct.* **2019**, *166*, 154–166.

67. Greaves, G.N.; Greer, A.L.; Lakes, R.S.; Rouxel, T. Poisson’s ratio and modern materials. *Nat. Mater.* **2011**, *10*, 823–37.

68. Evans, K.E. Auxetic polymers: a new range of materials. *Endeavour* **1991**, *15*, 170–174.

69. Keskar, N.R.; Chelikowsky, J.R. Negative Poisson ratios in crystalline SiO2 from first-principles calculations. *Nature* **1992**, *358*, 222–224.

70. Grima, J.N.; Gatt, R.; Alderson, A.; Evans, K.E. An alternative explanation for the negative Poisson’s ratios in α-cristobalite. *Mater. Sci. Eng. A* **2006**, *423*, 219–224.

71. Alderson, A.; Evans, K.E. Rotation and dilation deformation mechanisms for auxetic behaviour in the $α$-cristobalite tetrahedral framework structure. *Phys. Chem. Miner.* **2001**, *28*, 711–718.

72. Yeganeh-Haeri, A.; Weidner, D.J.; Parise, J.B. Elasticity of α-Cristobalite: A Silicon Dioxide with a Negative Poisson’s Ratio. *Science (80-.).* **1992**, *257*, 650–652.

73. Love, A.E.H. *A Treatise on the Mathematical Theory of Elasticity*; New York Public Library: Dover, New York, 1892;

74. Baughman, R.H.; Shacklette, J.M.; Zakhidov, A.A.; Stafstrom, S. Negative Poisson's ratios as a common feature of cubic metals. *Nature* **1998**, *392*, 362–365.

75. Grima, J.N.; Jackson, R.; Alderson, A.; Evans, K.E. Do Zeolites Have Negative Poisson's Ratios? *Adv. Mater.* **2000**, *12*, 1912–1918.

76. Grima, J.N.; Gatt, R.; Zammit, V.; Williams, J.J.; Evans, K.E.; Alderson, A.; Walton, R.I. Natrolite: A zeolite with negative Poisson's ratios. *J. Appl. Phys.* **2007**, *101*.

77. Gatt, R.; Zammit, V.; Caruana, C.; Grima, J.N. On the atomic level deformations in the auxetic zeolite natrolite. *Phys. Status Solidi* **2008**, *245*, 502–510.

78. Li, Y. The anisotropic behavior of Poisson's ratio, Young's modulus, and shear modulus in hexagonal materials. *Phys. Status Solidi* **1976**, *38*, 171–175.

79. Gunton, D.J.; Saunders, G.A. The Young's modulus and Poisson's ratio of arsenic, antimony and bismuth. *J. Mater. Sci.* **1972**, *7*, 1061–1068.

80. Williams, J.L.; Lewis, J.L. Properties and an anisotropic model of cancellous bone from the proximal tibial epiphysis. *J. Biomech. Eng.* **1982**, *104*, 50–6.

81. Lees, C.; Vincent, J.F. V.; Hillerton, J.E. Poisson's Ratio in Skin. *Biomed. Mater. Eng.* **1991**, *1*, 19–23.

82. Veronda, D.R.; Westmann, R.A. Mechanical characterization of skin-finite deformations. *J. Biomech.* **1970**, *3*, 111–24.

83. Frolich, L.M.; LaBarbera, M.; Stevens, W.P. Poisson's ratio of a crossed fibre sheath: the skin of aquatic salamanders. *J. Zool.* **1994**, *232*, 231–252.

84. Baughman, R.H. Auxetic materials: avoiding the shrink. *Nature* **2003**, *425*, 667.

85. Gibson, L.J.; Ashby, M.F. *Cellular Solids*; Cambridge University Press: Cambridge, 1997; ISBN 9781139878326.

86. Lakes, R. Deformation mechanisms in negative Poisson's ratio materials: structural aspects. *J. Mater. Sci.* **1991**, *26*, 2287–2292.

87. Grima, J.N.; Evans, K.E. Auxetic behavior from rotating squares. *J. Mater. Sci.*

Lett. **2000**, *19*, 1563–1565.

88. Grima, J.N.; Evans, K.E. Auxetic behavior from rotating triangles. *J. Mater. Sci.* **2006**, *41*, 3193–3196.

89. Grima, J.N.; Chetcuti, E.; Manicaro, E.; Attard, D.; Camilleri, M.; Gatt, R.; Evans, K.E. On the auxetic properties of generic rotating rigid triangles. *Proc. R. Soc. A Math. Phys. Eng. Sci.* **2012**, *468*, 810–830.

90. Grima, J.N.; Gatt, R.; Ellul, B.; Chetcuti, E. Auxetic behaviour in non-crystalline materials having star or triangular shaped perforations. *J. Non. Cryst. Solids* **2010**, *356*, 1980–1987.

91. Grima, J.N.; Alderson, A.; Evans, K.E. Negative Poisson’s ratios from rotating rectangles. *Comput. Methods Sci. Technol.* **2004**, *10*, 137–145.

92. Grima, J.N.; Gatt, R.; Farrugia, P.-S. On the properties of auxetic meta-tetrachiral structures. *Phys. status solidi* **2008**, *245*, 511–520.

93. Grima, J.N.; Gatt, R.; Alderson, A.; Evans, K.E. On the origin of auxetic behaviour in the silicate α-cristobalite. *J. Mater. Chem.* **2005**, *15*, 4003.

94. Grima, J.N.; Manicaro, E.; Attard, D. Auxetic behaviour from connected different-sized squares and rectangles. *Proc. R. Soc. A Math. Phys. Eng. Sci.* **2011**, *467*, 439–458.

95. Alderson, K.L.; Pickles, A.P.; Neale, P.J.; Evans, K.E. Auxetic polyethylene: The effect of a negative poisson’s ratio on hardness. *Acta Metall. Mater.* **1994**, *42*, 2261–2266.

96. Chan, N.; Evans, K.E. Indentation Resilience of Conventional and Auxetic Foams. *J. Cell. Plast.* **1998**, *34*, 231–260.

97. Toronjo, A. Articles of apparel including auxetic materials 2018.

98. Cross, T.M.; Hoffer, K.W.; Jones, D.P.; Kirschner, P.B.; Langvin, E.; Meschter, J.C. Auxetic structures and footwear with soles having auxetic structures 2016.

99. Cross, T.M. Footwear with flexible auxetic sole structure 2017.

100. Alderson, A.; Rasburn, J.; Ameer-Beg, S.; Mullarkey, P.G.; Perrie, W.; Evans, K.E. An auxetic filter: A tuneable filter displaying enhanced size selectivity or

defouling properties. *Ind. Eng. Chem. Res.* **2000**, *39*, 654–665.

101. Alderson, A.; Rasburn, J.; Evans, K.E.; Grima, J.N. Auxetic polymeric filters display enhanced de-fouling and pressure compensation properties. *Membr. Technol.* **2001**, *2001*, 6–8.

102. Rasburn, J.; Mullarkey, P.G.; Evans, K.E.; Alderson, A.; Ameer-Beg, S.; Perrie, W. Auxetic structures for variable permeability systems. *AIChE J.* **2001**, *47*, 2623–2626.

103. Ali, M.N.; Busfield, J.J.C.; Rehman, I.U. Auxetic oesophageal stents: structure and mechanical properties. *J. Mater. Sci. Mater. Med.* **2014**, *25*, 527–553.

104. Ali, M.N.; Rehman, I.U. An Auxetic structure configured as oesophageal stent with potential to be used for palliative treatment of oesophageal cancer; development and in vitro mechanical analysis. *J. Mater. Sci. Mater. Med.* **2011**, *22*, 2573–2581.

105. Kuribayashi, K.; Tsuchiya, K.; You, Z.; Tomus, D.; Umemoto, M.; Ito, T.; Sasaki, M. Self-deployable origami stent grafts as a biomedical application of Ni-rich TiNi shape memory alloy foil. *Mater. Sci. Eng. A* **2006**, *419*, 131–137.

106. Gifford, K.; Sprinkle, A.; Citkowski, P.C. Auxetic stents 2011.

107. Burriesci, G.; Bergamasco, G. Annuloplasty prosthesis with an auxetic structure 2005.

108. Cheng, Y.-T.; Cheng, C.-M. Scaling relationships in conical indentation of elastic-perfectly plastic solids. *Int. J. Solids Struct.* **1999**, *36*, 1231–1243.

109. Cheng, Y.-T.; Cheng, C.-M. Analysis of indentation loading curves obtained using conical indenters. *Philos. Mag. Lett.* **1998**, *77*, 39–47.

110. Troyon, M.; Huang, L. Correction factor for contact area in nanoindentation measurements. *J. Mater. Res.* **2011**, *20*, 610–617.

111. Argatov, I.I.; Guinovart-Díaz, R.; Sabina, F.J. On local indentation and impact compliance of isotropic auxetic materials from the continuum mechanics viewpoint. *Int. J. Eng. Sci.* **2012**, *54*, 42–57.

112. Argatov, I.I.; Sabina, F.J. Small-scale indentation of an elastic coated half-space:

Influence of Poisson's ratios on the substrate effect. *Int. J. Eng. Sci.* **2014**, *81*, 33–40.

113. Alderson, K.L.; Fitzgerald, A.; Evans, K.E. The strain dependent indentation resilience of auxetic microporous polyethylene. *J. Mater. Sci.* **2000**, *5*, 4039–4047.

114. Borodich, F.M.; Keer, L.M. Evaluation of elastic modulus of materials by adhesive (no-slip) nano-indentation. *Proc. R. Soc. A Math. Phys. Eng. Sci.* **2004**, *460*, 507–514.

115. Mossakovskii, V.I. Compression of elastic bodies under conditions of adhesion (Axisymmetric case). *J. Appl. Math. Mech.* **1963**, *27*, 630–643.

116. Spence, D.A. Self Similar Solutions to Adhesive Contact Problems with Incremental Loading. *Proc. R. Soc. A Math. Phys. Eng. Sci.* **1968**, *305*, 55–80.

117. Borodich, F.M.; Keer, L.M. Contact problems and depth-sensing nanoindentation for frictionless and frictional boundary conditions. *Int. J. Solids Struct.* **2004**, *41*, 2479–2499.

118. Collin, J.-M.; Mauvoisin, G.; El Abdi, R. An experimental method to determine the contact radius changes during a spherical instrumented indentation. *Mech. Mater.* **2008**, *40*, 401–406.

119. Collin, J.-M. Correction factor for contact radius in spherical indentation measurements. *Mech. Mater.* **2012**, *50*, 47–52.

120. Photiou, D.; Prastiti, N.; Sarris, E.; Constantinides, G. On the conical indentation response of elastic auxetic materials: Effects of Poisson's ratio, contact friction and cone angle. *Int. J. Solids Struct.* **2016**, *81*.

121. Yoffe, E.H. Modified Hertz theory for spherical indentation. *Philos. Mag. A* **1984**, *50*, 813–828.

122. Photiou, D.; Prastiti, N.; Sarris, E.; Constantinides, G. On the conical indentation response of elastic auxetic materials: Effects of Poisson's ratio, contact friction and cone angle. *Int. J. Solids Struct.* **2016**, *81*, 33–42.

123. Tuck, J.R.; Korsunsky, A.M.; Bull, S.J.; Davidson, R.I. On the application of the work-of-indentation approach to depth-sensing indentation experiments in coated systems. *Surf. Coatings Technol.* **2001**, *137*, 217–224.

124. Zhou, L.; Yao, Y. Single crystal bulk material micro/nano indentation hardness testing by nanoindentation instrument and AFM. *Mater. Sci. Eng. A* **2007**, 95–100.

125. Jha, K.K.; Suksawang, N.; Agarwal, A. A new insight into the work-of-indentation approach used in the evaluation of material's hardness from nanoindentation measurement with Berkovich indenter. *Comput. Mater. Sci.* **2014**, *85*, 32–37.

126. Jha, K.K.; Zhang, S.; Suksawang, N.; Wang, T.-L.; Agarwal, A. Work-of-indentation as a means to characterize indenter geometry and load–displacement response of a material. *J. Phys. D. Appl. Phys.* **2013**, *46*.

127. Lawn, B.R.; Howes, V.R. Elastic recovery at hardness indentations. *J. Mater. Sci.* **1981**, *16*, 2745–2752.

128. Thomson, T. Magnetic properties of metallic thin films. *Met. Film. Electron. Opt. Magn. Appl.* **2014**, 454–546.

129. Photiou, D.; Panagiotopoulos, N.T.; Koutsokeras, L.; Evangelakis, G.A.; Constantinides, G. Microstructure and nanomechanical properties of magnetron sputtered Ti − Nb films. *Surf. Coatings Technol.* **2016**, *302*.

130. Doerner M.F., Nix, W.D. A method for interpreting the data from depth-sensing indentation instrumentso Title. *J. Mater. Res.* **1986**, *1*, 601–609.

131. Bull, S.J. Nanoindentation of coatings. *J. Phys. D. Appl. Phys.* **2005**, *38*, R393–R413.

132. Buckle, H. The Science of Hardness Testing and its Research Applications. In *American Society for Metals*; Westbrook, J.W., Conrad, H., Eds.; Ohio, 1973; pp. 453–491.

133. Saha, R.; Nix, W.D. Effects of the substrate on the determination of thin film mechanical properties by nanoindentation. *Acta Mater.* **2002**, *50*, 23–38.

134. Joslin, D.L.; Oliver, W.C. A new method for analyzing data from continuous depth-sensing microindentation tests. *J. Mater. Res.* **1990**, *5*, 123–126.

135. Saha, R.; Nix, W.D. Effects of the substrate on the determination of thin film mechanical properties by nanoindentation. *Acta Mater.* **2002**, *50*, 23–38.

136. Menčík, J.; Munz, D.; Quandt, E.; Weppelmann, E.R.; Swain, M. V. Determination

of elastic modulus of thin layers using nanoindentation. *J. Mater. Res.* **1997**, *12*, 2475–2484.

137. Ogilvy, J.A. A parametric elastic model for indentation testing of thin films. *J. Phys. D. Appl. Phys.* **1993**, *26*, 2123–2131.
138. Tricoteaux, A.; Duarte, G.; Chicot, D.; Le Bourhis, E.; Bemporad, E.; Lesage, J. Depth-sensing indentation modeling for determination of Elastic modulus of thin films. *Mech. Mater.* **2010**, *42*, 166–174.
139. Jung, Y.-G.; Lawn, B.R.; Martyniuk, M.; Huang, H.; Hu, X.Z. Evaluation of elastic modulus and hardness of thin films by nanoindentation. *J. Mater. Res.* **2004**, *19*, 3076–3080.
140. Bhattacharya, A.K.; Nix, W.D. Finite element analysis of cone indentation. *Int. J. Solids Struct.* **1991**, *27*, 1047–1058.
141. Antunes, J.M.; Fernandes, J.V.; Sakharova, N.A.; Oliveira, M.C.; Menezes, L.F. On the determination of the Young's modulus of thin films using indentation tests. *Int. J. Solids Struct.* **2007**, *44*, 8313–8334.
142. Hu, X.Z.; Lawn, B.R. A simple indentation stress–strain relation for contacts with spheres on bilayer structures. *Thin Solid Films* **1998**, *322*, 225–232.
143. Li, J.; Chou, T.-W. Elastic field of a thin-film/substrate system under an axisymmetric loading. *Int. J. Solids Struct.* **1997**, *34*, 4463–4478.
144. Huguet, A.S.; Barthel, E. Surface forces and the adhesive contact of axisymmetric elastic bodies. *J. Adhes.* **2000**, *74*, 143–175.
145. 14577-4:2016, I. Metallic materials -- Instrumented indentation test for hardness and materials parameters -- Part 4: Test method for metallic and non-metallic coatings. In.
146. Randall, N.X. Direct measurement of residual contact area and volume during the nanoindentation of coated materials as an alternative method of calculating hardness. *Philos. Mag. A* **2002**, *82*, 1883–1892.
147. Tsui, T.Y.; Pharr, G.M. Substrate effects on nanoindentation mechanical property measurement of soft films on hard substrates. *J. Mater. Res.* **1999**, *14*, 292–301.

148. Parratt, L.G. Surface studies of solids by total reflection of x-rays. *Phys. Rev.* **1954**, *95*, 359–369.

149. Photiou, D.; Panagiotopoulos, N.T.; Koutsokeras, L.; Evangelakis, G.A.; Constantinides, G. Microstructure and nanomechanical properties of magnetron sputtered Ti−Nb films. *Surf. Coatings Technol.* **2016**, *302*, 310–319.

150. Constantinou, M.; Pervolaraki, M.; Koutsokeras, L.; Prouskas, C.; Patsalas, P.; Kelires, P.; Giapintzakis, J.; Constantinides, G. Enhancing the nanoscratch resistance of pulsed laser deposited DLC films through molybdenum-doping. *Surf. Coat. Technol.* **2017**, *330*, 185–195.

151. Casiraghi, C.; Ferrari, A.C.; Robertson, J. Raman spectroscopy of hydrogenated amorphous carbons. *Phys. Rev. B - Condens. Matter Mater. Phys.* **2005**, *72*, 1–14.

152. Ferrari, A.C.; Robertson, J. Raman spectroscopy of amorphous, nanostructured, diamond-like carbon, and nanodiamond. *Philos. Trans. A. Math. Phys. Eng. Sci.* **2004**, *362*, 2477–2512.

153. Ferrari, A.C.; Libassi, A.; Tanner, B.K.; Stolojan, V.; Yuan, J.; Brown, L.M.; Rodil, S.E.; Kleinsorge, B. Density , sp 3 fraction , and cross-sectional structure of amorphous carbon films determined by x-ray reflectivity and electron energy-loss spectroscopy. *Phys. Rev. B - Condens. Matter Mater. Phys.* **2000**, *62*, 89–103.

154. Ferrari, A.C.; Robertson, J. Resonant Raman spectroscopy of disordered, amorphous, and diamondlike carbon. *Phys. Rev. B* **2001**, *64*, 075414.

155. Ferrari, A.C.; Robertson, J. Interpretation of Raman spectra of disordered and amorphous carbon. *Phys. Rev. B - Condens. Matter Mater. Phys.* **2000**, *61*, 14095–14107.

156. Baba, K.; Hatada, R.; Flege, S.; Ensinger, W. Preparation and Properties of Ag-Containing Diamond-Like Carbon Films by Magnetron Plasma Source Ion Implantation. *Adv. Mater. Sci. Eng.* **2012**, *2012*, 1–5.

157. Qiang, L.; Zhang, B.; Zhou, Y.; Zhang, J. Improving the internal stress and wear resistance of DLC film by low content Ti doping. *Solid State Sci.* **2013**, *20*, 17–22.

158. Wu, Y.; Chen, J.; Li, H.; Ji, L.; Ye, Y.; Zhou, H. Preparation and properties of Ag/DLC nanocomposite films fabricated by unbalanced magnetron sputtering.

Appl. Surf. Sci. **2013**, *284*, 165–170.

159. Tabor, D. A simple theory of static and dynamic hardness. *Proc. R. Soc. London. Ser. A. Math. Phys. Sci.* **1948**, *192*, 247–274.

160. Swain, M. V; Hagan, J.T. Indentation plasticity and the ensuing fracture of glass. *J. Phys. D. Appl. Phys.* **1976**, *9*, 2201–2214.

161. Schuh, C.A.; Nieh, T.G. A survey of instrumented indentation studies on metallic glasses. *J. Mater. Res.* **2004**, *19*, 46–57.

162. Kholmyansky, M.; Kogan, E.; Kovler, K. On the hardness determination of fine grained concrete. *Mater. Struct.* **1994**, *27*, 584–587.

163. Igarashi, S.; Bentur, A.; Mindess, S. Characterization of the microstructure and strength of cement paste by microhardness testing. *Adv. Cem. Res.* **1996**, *8*, 87–92.

164. Lockett, F.J. Indentation of a rigid/plastic material by a conical indenter. *J. Mech. Phys. Solids* **1963**, *11*, 345–355.

165. Chitkara, N.R.; Butt, M.A. Numerical construction of axisymmetric slip-line fields for indentation of thick blocks by rigid conical indenters and friction at the tool-metal interface. *Int. J. Mech. Sci.* **1992**, *34*, 849–862.

166. Bobko, C.P.; Gathier, B.; Ortega, J.A.; Ulm, F.-J.; Borges, L.; Abousleiman, Y.N. The nanogranular origin of friction and cohesion in shale-A strength homogenization approach to interpretation of nanoindentation results. *Int. J. Numer. Anal. Methods Geomech.* **2011**, *35*, 1854–1876.

167. Han, Y.; Abousleiman, Y.N.; Hull, K.L.; Al-Muntasheri, G.A. Numerical Modeling of Elastic Spherical Contact for Mohr-Coulomb Type Failures in Micro-Geomaterials. *Exp. Mech.* **2017**, *57*, 1091–1105.

168. Palkovic, S.D.; Kupwade-Patil, K.; Yip, S.; Büyüköztürk, O. Random field finite element models with cohesive-frictional interactions of a hardened cement paste microstructure. *J. Mech. Phys. Solids* **2018**, *119*, 349–368.

169. Vaidyanathan, R.; Dao, M.; Ravichandran, G.; Suresh, S. Study of mechanical deformation in bulk metallic glass through instrumented indentation. *Acta Mater.* **2001**, *49*, 3781–3789.

170. Rodríguez, M.; Molina-Aldareguía, J.M.; González, C.; LLorca, J. Determination of the mechanical properties of amorphous materials through instrumented nanoindentation. *Acta Mater.* **2012**, *60*, 3953–3964.

171. Tai, K.; Ulm, F.-J.; Ortiz, C. Nanogranular Origins of the Strength of Bone. *Nano Lett.* **2006**, *6*, 2520–2525.

172. Mitarai, N.; Nori, F. Wet granular materials. *Adv. Phys.* **2006**, *55*, 1–45.

173. Wang, X.; Allen, M.R.; Burr, D.B.; Lavernia, E.J.; Jeremić, B.; Fyhrie, D.P. Identification of material parameters based on Mohr–Coulomb failure criterion for bisphosphonate treated canine vertebral cancellous bone. *Bone* **2008**, *43*, 775–780.

174. Keryvin, V. Indentation as a probe for pressure sensitivity of metallic glasses. *J. Phys. Condens. Matter* **2008**, *20*, 114119.

175. Klement, W.; Willens, R.H.; Duwez, P. Non-crystalline Structure in Solidified Gold–Silicon Alloys. *Nature* **1960**, *187*, 869–870.

176. He, Y.; Schwarz, R.B.; Mandrus, D.; Jacobson, L. Elastic moduli, density, and structural relaxation in bulk amorphous Zr41.2Ti13.8Cu12.5Ni10Be22.5 alloy. *J. Non. Cryst. Solids* **1996**, *205–207*, 602–606.

177. Hainsworth, S. V.; Chandler, H.W.; Page, T.F. Analysis of nanoindentation load-displacement loading curves. *J. Mater. Res.* **1996**, *11*, 1987–1995.

178. Cheng, Y.-T.; Cheng, C.-M. Relationships between hardness, elastic modulus, and the work of indentation. *Appl. Phys. Lett.* **1998**, *73*, 614–616.

179. Pelletier, H.; Krier, J.; Mille, P. Characterization of mechanical properties of thin films using nanoindentation test. *Mech. Mater.* **2006**, *38*, 1182–1198.

180. Csanádi, T.; Németh, D.; Lofaj, F. Mechanical Properties of Hard W-C Coating on Steel Substrate Deduced from Nanoindentation and Finite Element Modeling. *Exp. Mech.* **2017**, *57*, 1057–1069.

181. Lofaj, F.; Németh, D. The effects of tip sharpness and coating thickness on nanoindentation measurements in hard coatings on softer substrates by FEM. *Thin Solid Films* **2017**, *644*, 173–181.

182. He, J.L.; Veprek, S. Finite element modeling of indentation into superhard

coatings. *Surf. Coatings Technol.* **2003**, *163–164*, 374–379.

183. Veprek, S. Recent search for new superhard materials: Go nano! *J. Vac. Sci. Technol. A Vacuum, Surfaces, Film.* **2013**, *31*, 050822.

184. Veprek, S.; Argon, A.S. Towards the understanding of mechanical properties of super- and ultrahard nanocomposites. *J. Vac. Sci. Technol. B Microelectron. Nanom. Struct.* **2002**, *20*, 650.

185. Niederhofer, A.; Nesládek, P.; Männling, H.-D.; Moto, K.; Vepřek, S.; Jílek, M. Structural properties, internal stress and thermal stability of nc-TiN/a-Si3N4, nc-TiN/TiSix and nc-(Ti1−yAlySix)N superhard nanocomposite coatings reaching the hardness of diamond. *Surf. Coatings Technol.* **1999**, *120–121*, 173–178.

186. Veprek, S.; Mukherjee, S.; Karvankova, P.; Männling, H.-D.; He, J.L.; Moto, K.; Prochazka, J.; Argon, A.S. Limits to the strength of super- and ultrahard nanocomposite coatings. *J. Vac. Sci. Technol. A Vacuum, Surfaces, Film.* **2003**, *21*, 532.

187. Fischer-Cripps, A.C.; Bull, S.J.; Schwarzer, N. Critical review of claims for ultra-hardness in nanocomposite coatings. *Philos. Mag.* **2012**, *92*, 1601–1630.

188. Liu, Y.; Wang, B.; Yoshino, M.; Roy, S.; Lu, H.; Komanduri, R. Combined numerical simulation and nanoindentation for determining mechanical properties of single crystal copper at mesoscale. *J. Mech. Phys. Solids* **2005**, *53*, 2718–2741.

189. Bressan, J.D.; Tramontin, A.; Rosa, C. Modeling of nanoindentation of bulk and thin film by finite element method. *Wear* **2005**, *258*, 115–122.

190. Lee, H.; Haeng Lee, J.; Pharr, G.M. A numerical approach to spherical indentation techniques for material property evaluation. *J. Mech. Phys. Solids* **2005**, *53*, 2037–2069.

APPENDIX A Sample Input File

This is a general description of an input file, that used on this thesis for modelling nanoindentation technique:

A1. Mesh Generation

```
** Mesh definition
*Node, nset=komvoi
Node number, x-coordinate, y-coordinate
…
*node, nset=ref_point (definition of reference point for rigid surface – indenter)
Node number, x-coordinate, y-coordinate
*Element, type=CAX4, ELSET= indented material [definition of element family]
Element number, node 1, node 2, node 3, node 4
…
*Solid section, elset=indented material, material=halfspace, controls=HGC
*Section controls, Name=HGC, HOURGLASS=stiffness
```

A2. Materials

```
**Material Property Definition
**elastic properties
*ELASTIC
<Emod>, <pois>
**yielding properties
**von Mises
*plastic
*<ys>
**Mohr Coulomb material
*Mohr coulomb
<Phi>, <Psi>
*Mohr coulomb hardening
<c>
```

A3. Boundary Conditions

```
**Axisymmetric condition for the side elements dx=0
*Boundary
```

```
side elements, 1
** Boundary for the restriction of indenter dx=0 and drz=0
*Boundary
reference node assigned name, 1
reference node assigned name, 6
** Fixed condition for the bottom elements dx=0 and dy =0
*Boundary
bottom elements, 1, 2
**
```

A4. Contact Definition

```
** definition of the elements that may be in contact with rigid analytical surface of indenter
*…
*Surface, type=ELEMENT, name=target
Name of the contact elements
*Surface, type=segments, name=indenter
start, coordinates x, y
line, coordinates x, y
** if indenter is sphere, then the command is circle instead of line
*RIGID BODY, REF NODE=name of reference node, ANALYTICAL SURFACE=indenter
*CONTACT PAIR, INTERACTION=ROUGH
target, indenter
*SURFACE INTERACTION, NAME=ROUGH
**Definition of friction contact between indenter and material
*friction
<fric>
```

A5. Definition of loading step

```
*Step, name=Step-1, nlgeom=YES, inc=10000, UNSYMM=YES
punch
*Static
**Definition of time steps; initial increment, minimum increment and maximum increment
0.000015, 1., 1e-05, 0.005
*BOUNDARY
Reference node location, <penetration>
** where penetration defines the maximum indentation depth
```

```
*controls,parameters=field
0.05,0.1
**output print information
*Restart, write, frequency=1,overlay
*PRINT,CONTACT=YES
*CONTACT CONTROLS, FRICTION ONSET=DELAY
*CONTACT PRINT, SLAVE=target
*NODE PRINT, FREQUENCY=1
U
*OUTPUT, FIELD,F REQUENCY=1
*NODE OUTPUT
U
*node output, nset=bottom elements
RF
*node output, nset=reference point
U
*ELEMENT OUTPUT
S
PEEQ
*OUTPUT, HISTORY, FREQUENCY=10
*CONTACT OUTPUT, nset = contact elements
*ENERGY OUTPUT, VARIABLE=PRESELECT
*End Step
```

A6. Definition of unloading step

```
*Step, name=Step-2, nlgeom=YES, inc=1000, UNSYMM=YES
return to original position
*Static
0.00015, 1., 1e-05, 0.005
*BOUNDARY, OP = MOD
Reference node location, 0.0
**output print information
*Restart, write, frequency=1,overlay
*PRINT,CONTACT=YES
*CONTACT CONTROLS, FRICTION ONSET=DELAY
*CONTACT PRINT, SLAVE=target
*NODE PRINT, FREQUENCY=1
U
```

```
*OUTPUT, FIELD, FREQUENCY=1
*NODE OUTPUT
U
*node output, nset=bottom elements
RF
*node output, nset=reference point
U
*ELEMENT OUTPUT
S
PEEQ
*OUTPUT, HISTORY, FREQUENCY=10
*CONTACT OUTPUT, nset = contact elements
*ENERGY OUTPUT, VARIABLE=PRESELECT
*End Step
```

APPENDIX B Mesh Information

The region area beneath the indenter experiences large strain distribution and numerically speaking is the most important parameter that need to be defined. This region should be meshed fine enough to capture the mechanical response of the contact and to obtain accurate generated distribution of stresses and strains inside the material. In addition, a coarser mesh must be used further away from the indenter tip in order to reduce the computational time. A mesh sensitivity study should be performed to determine the appropriate size and number of elements. A variety of mesh sensitivity studies have been proposed in the literature [188–190], where they either compare the load-displacement curves for different element sizes, or they study pile-up changes by increasing the number of elements in the contact region.

In this thesis, two mesh sensitivity analysis were carried out; the first by minimizing the element size near to the area of contact, to investigate the desired size that captures the indentation response within minimal computational time and high accuracy of results. As illustrated in Figure B-1, the value of maximum indentation load is kept constant for element size values smaller than 200 nm. Furthermore, in our case we wanted to compare numerical results with experiments of h_{max} = 500 nm, and thus we have set the minimum element size to 50 nm in order to collect enough data for analyzing P - h curves.

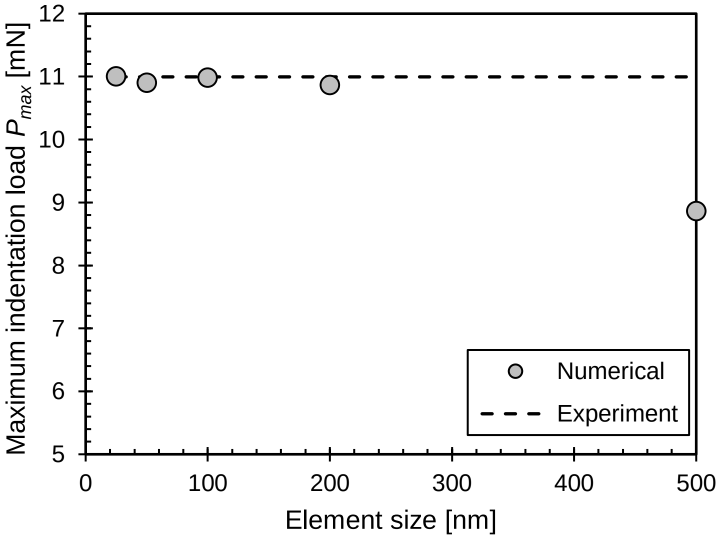

Figure B-1: Convergence study by minimizing the element size near to the area of contact. Material was modeled as elastic-perfect plastic; E = 115 GPa, v = 0.32, Y = 500 MPa.

The second convergence study was performed by comparing the variation of load-displacement curves for different element sizes as shown in Figure B-2. While the two numerical models characterized be a deviation of 10 regarding their element size, both exhibit identical indentation response; the deviation of the maximum indentation load is lower that 3% and the deviation of the resulting elastic modulus of the material is lower than 1%, which verify the accuracy of our finite element results. Here, it must be stated that the minimum element size in nanoindentation simulations must be related with the maximum indentation depth. As was explained in Chapter 8.3.3, in cases of elastic or elastic-perfect plastic materials, surface materials may undergo numerical stiffening in large indentation depths and therefore larger element sizes must be used in that case.

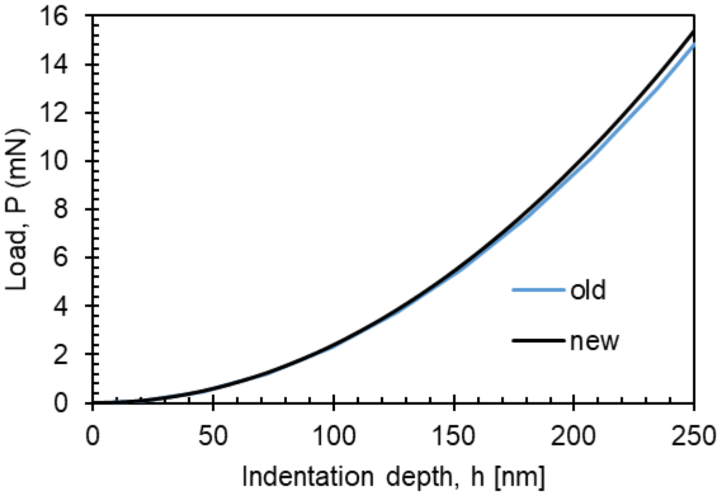

Figure B-2: Mesh sensitivity study to investigate the effect in $P - h$ curves.

Furthermore, we have studied the influence of mesh refinement on two different numerical models (see Figure 3-3 – bulk model and Figure 8-2 – coating model) with the same minimum element size and different partition pattern, through the numerical indentation response of an elastic auxetic material with E = 100 GPa and v = -0.9. Analysis results are presented in Table B-1 where illustrate that the two models are in excellent agreement in relation with their contact response. Hence, for numerical efficiency purposes (memory and computational time) we have chosen the bulk model.

Table B-1: Analysis results of the two numerical models.

Model	P_{max} [N]	P [%]	h_c [μm]	h_c [%]	γ [-]	γ [%]	Size [GB]	Time [s]
Bulk	0.5316	1.36	0.2978	0.05	1.121	1.13	0.475	545
Coating	0.5245		0.2979		1.108		3.5	4227

Table B-2 summarizes mesh information regarding the three different finite element models that have been used in this thesis.

Table B-2: Technical information of numerical models.

Model	Total Nodes	Total Elements	Minimum Element Size	Average CPU Time [s]
Bulk	7352	7142	50	400
Coating	55722	54625	50	1900
Multilayer	32030	30970	5	1400

APPENDIX C Dissemination and Awards

C1: Journal Publications

Published Papers

1. **D. Photiou**, E. Sarris, G. Constantinides, Erratum to ‘On the elastic conical indentation response of auxetic materials: effects of Poisson’s ratio, contact friction and cone angle’ [Int. J. Solids Struct. 81(2016) 33-42], International Journal of Solids and Structures, 2017.
2. N. Kostoglou, J. Lukovic, B. Babic, B. Matovic, **D. Photiou**, G. Constantinides, K. Polychronopoulou, V. Ryzkhov, B. Grossman, C. Mitterer, C. Rebholz, ‘Few-step synthesis, thermal purification and structural characterization of porous boron nitride nanoplatelets’, Materials and Design, 110, 540-548, 2016.
3. **D. Photiou**, N.T. Panagiotopoulos, L. Koutsokeras, G.A. Evangelakis, G. Constantinides, ‘Microstructure and nanomechanical properties of magnetron sputtered Ti-Nb films’, Surface and Coatings Technology, 302, 310-319, 2016.
4. **D. Photiou**, N. Prastiti, E. Sarris, G. Constantinides, ‘On the elastic conical indentation response of auxetic materials: effects of Poisson’s ratio, contact friction and cone angle’, International Journal of Solids and Structures, 81, 33-42, 2016.

Working Papers

5. **D. Photiou**, E. Sarris, G. Constantinides, ‘Spherical indentation on auxetic materials: elastic and elastoplastic response’, in preparation
6. **D. Photiou**, E. Sarris, G. Constantinides, ‘Indentation hardness enhancement of auxetic materials: effect of plasticity’, in preparation
7. **D. Photiou**, E. Sarris, G. Constantinides, ‘Finite element results on the indentation on cohesive-frictional materials’, in preparation
8. **D. Photiou**, E. Sarris, G. Constantinides, ‘On the universality of the BASh/O&P method for indentation analysis’, in preparation

9. **D. Photiou**, E. Sarris, G. Constantinides, ‘Indentation response of superhard materials: finite element study’, in preparation

C2: Conference Presentations

1. **D. Photiou**, E. Sarris and G. Constantinides, Finite Element Modeling of Nanoindentation on Thin Films, XXXIII Panhellenic Conference on Solid State Physics and Materials Science, Nicosia, Cyprus, 17-19 September 2018. (podium)
2. **D. Photiou**, E. Sarris and G. Constantinides, Finite Element Modeling of Nanoindentation on Superhard Materials, XXXIII Panhellenic Conference on Solid State Physics and Materials Science, Nicosia, Cyprus, 17-19 September 2018. (poster)
3. **D. Photiou**, E. Sarris and G. Constantinides, Indentation Resistance of Elastic and Elastic-plastic Auxetic Materials: A Finite Element Study, 13th International Conference on Nanosciences and Nanotechnologies – NN16, Thessaloniki, Greece, 5-8 July, 2016. (podium)
4. **D. Photiou**, N. Prastiti, E. Sarris and G. Constantinides, Indentation Resistance Enhancement of Auxetic Materials: A Numerical Investigation, XXXI Panhellenic Conference on Solid State Physics and Materials Science, Thessaloniki, Greece, 20-23 September 2015. (podium)
5. **D. Photiou**, N.T. Panagiotopoulos, L. Koutsokeras, G.A. Evangelakis, G. Constantinides, Nanomechanics of Magnetron Sputtered Ti-Nb Films, XXXI Panhellenic Conference on Solid State Physics and Materials Science, Thessaloniki, Greece, 20-23 September 2015. (poster)
6. N.T. Panagiotopoulos, **D. Photiou**, G.Constantinides, G.A.Evangelakis, A.R. Yavari, ‘Ti-Nb and Ti-Hf thin films’, 21st International Symposium on Metastable, Amorphous and Nanostructured Materials (ISMANAM 2014), Cancún, México, 29 June to 4 July, 2014. (podium)
7. **D. Photiou**, G. Constantinides, ‘Experimental and computational nanomechanics of biomedical coatings’, Training School COST Action NAMABIO MP1005, 14 –17 October 2014, Frederick University, Nicosia, Cyprus. (podium)
8. **D. Photiou**, N.T. Panagiotopoulos, M. Constantinou, G.A. Evangelakis, G. Constantinides, ‘Nanomechanics of binary and ternary Ti-Nb-Hf films for biomedical applications’, 12th MML European Nanomechanical User Group Meeting, University of Malta, Malta, 24-25 October, 2012 (poster).
9. **D. Photiou**, N.T. Panagiotopoulos, M. Constantinou, G.A. Evangelakis, G. Constantinides, ‘Nanomechanics of binary and ternary Ti-Nb-Hf films for biomedical

applications', 9th International Conference on Nanosciences and Nanotechnologies – NN12, Thessaloniki, Greece, 3-6 July, 2012 (poster).

C3: Awards

1. 1st prize praise for the competition FOITO, "Nanomechanics of Titanium alloy films for biomedical applications", Research Promotion Foundation, Cyprus, 2013
2. 5th place for the Competition: Present around the World, oral presentation "Nanomechanics of Ti-Alloy films for biomedical applications", Europe, Middle East and Africa Network of IET (Institution of Engineering and Technology), Paris, France, 2012
3. 1st place for the Competition: Present around the World, oral presentation "Nanomechanics of Ti-Alloy films for biomedical applications", Cyprus Network of IET (Institution of Engineering and Technology), Limassol, Cyprus, 2012